

**Synthesis, Characterisation and 3D  
Printing of a Light-Curable Degradable  
Polymer for Craniofacial Bone  
Regeneration**

**Taleen Sally Shakouri  
BSc (Hons)**

Thesis submitted to University College London in fulfilment of the  
requirements for the degree of Doctor of Philosophy

Division of Biomaterials and Tissue Engineering, Eastman Dental Institute, UCL

**2021**

## **Declaration**

I, Taleen Sally Shakouri confirm that the work presented in this thesis is my own. Where information has been derived from other sources, I confirm that this has been indicated in the thesis.

Signature:

Date: 27<sup>th</sup> August 2021

## Dedication

*In dedication to my family; past, present and future...*

## **Acknowledgments**

First and most importantly, I would like to express my sincere gratitude to my supervisors, Professor Jonathan Knowles and Dr Elena García-Gareta who supported me throughout my PhD journey with an incredible amount of guidance and motivation. Your achievements and supervision pushed me to work harder than I thought would ever be possible and I am truly thankful for the belief you put in me and your ongoing support. None of this would be possible without you.

Sincere appreciation goes to the department of Biomaterials and Tissue Engineering at the Eastman Dental Institute for offering great facilities to make this research achievable. I would like to gratefully acknowledge the ITREN team at Dankook University of South Korea for collaborating with me on the polymer synthesis and would also like to thank RAFT for generously providing the funding for this project.

I would like to extend my gratitude to Dr George Georgiou, Dr Graham Palmer, Dr Nicola Mordan and Dr Isabel Kingston for their endless technical advice and being true friends during my time at the Eastman. A heartfelt thank you to Dr David Chau for the years of guidance you have given me as an academic and a friend.

No research is done in isolation; therefore, I would like to thank my friends and colleagues from the Eastman: Dr Mayda Arshad, Dr Nazanin Owji and Dr Zalike Keskin-Erdogan who made my journey easier and were always there for me during my breakthroughs and my breakdowns.

I would like to acknowledge and show my gratitude to my closest friends who have seen me grow as a scientist and have always been there when I needed a laugh and an escape. James Fortune, Peter Haddow, Lydia Collins, Adam Itani, Dallal Itani, Samir Itani, Sophia Grilli, Jay Russell, Liz Grilli, Lauren Baker, Melanie Knott, Abi Wade and Lorna Storey, your friendships are truly invaluable.

Finally, I am exceptionally grateful to my family who have always encouraged and believed in me. To my parents, Rita and Salam Shakouri, thank you for all that you have sacrificed for me to achieve my best in education and out. Thank you for always being there. Thank you to Jane and Martin Roche for supporting me and providing wisdom and guidance no matter what. Lastly, a very special thank you to my partner, Liam Roche, who has stood by me throughout my academic journey and supported me through my highs and lows. I hope this makes you immensely proud forever.

## **Abstract**

A surgeon's options for correcting congenital deformities, removing oral tumours and reconstructing the head and neck region are typically restricted by the equipment available to restore bone function and appearance for the patient. New production techniques and implants with improved osseointegration performance are urgently needed to meet the growing demand for effective implants at a reasonable price. Non-degradable materials are used widely for bone repair; however, they will stay in the body indefinitely until removed surgically. Metals, such as titanium, can be used for three-dimensional (3D) printing of scaffolds.

3D printing has the potential to enhance the creation of anatomically fitting patient-specific devices with highly effective delivery in a cost-effective manner. However, metal implants have the disadvantage that they can release traces of material over time and induce immunological responses. Non-degradable polymers, such as poly (methyl methacrylate), have the disadvantages that they undergo highly exothermic polymerisation, are prone to infection and lack osseointegration. Ceramics, such as calcium phosphates, have also been studied for use in craniofacial bone regeneration, however, they have poor fracture toughness, brittleness and excessive stiffness.

In view of the disadvantages associated with several of the known 3D printable materials, this thesis takes you through the development of an improved material that addresses some of the disadvantages discussed above.

In this study, the synthesis of the new material referred to as "CSMA-2" is investigated along with its mechanical properties and the effects of the addition of different ratios of calcium phosphate fillers to the isosorbide-based, light-

curable, degradable polymer. A comparison between two different photoinitiator systems is carried out throughout this study to ultimately find the most suited formulation for the 3D printing of the resin.

Mechanical tests showed the modulus values to be between 1.7-3 kN/mm<sup>2</sup> in CSMA-2 and its composites dependant on the photoinitiator system used. *In vitro* cell culture studies, using human bone osteosarcoma cells and human adipose-derived stem cells confirmed cytocompatibility of the material. Finally, Digital Light Processing 3D printing, allowed a direct photo-polymerisation of the resin to form bone- like scaffolds ready to be implanted *in vivo*.

## Impact Statement

Craniofacial reconstruction surgery is a result of defects caused by traumatic incidents, congenital disorders and cancerous tumours leading to tissue resection. Around 1 in 700 babies in the UK are born with cleft lip or palate which can ultimately lead to difficulties in feeding and in speaking as well as a long-term risk of dental issues. The most common treatment for these congenital disorders is surgery to correct the deformities. Further to this, approximately 125,000 people sustain serious facial injuries in traumatic incidents in the UK alone. 15,000 of these are said to go on to receive treatment for their craniofacial defects (Hutchison *et al.*, 2019). Oral cancers are the 6<sup>th</sup> most common cancer in the world. In the UK, 8,300 individuals develop oral cancer every year and the majority of treatment focusses on the removal of tissue and resection.

Over the years, attempts in restoring defects in the craniofacial region have proven difficult due to the complexity of the tissue structure as well as the lack of functionality post-surgery. The degree and extent of the defect determine the clinical approaches for treating bone healing deficiencies. Surgical reconstruction is required for critically damaged tissues that cannot restore by the conservative method of self-repair. The current most popular options for surgical procedures in the craniofacial region include the use of autologous, allogeneic and alloplastic bone grafts. However, there are many associated complications and drawbacks with using these grafting methods such as an increased risk of infection, severe pain and discomfort for the patient, rejection of the implanted material and a high cost. As a result of these drawbacks, many attempts have been made to find an ideal bone implant that can offer the same benefits as already proven grafting



methods, whilst limiting the complications and risk. Over the years, the increased research in the field of bone tissue engineering has led to new and successful techniques for the reconstruction and correction of defects in this region.

The main aim of this study is to expand on current tissue engineering approaches to find a good alternative to current treatment options for craniofacial and maxillofacial surgery. The specific objectives are to produce a novel, light-curable, degradable polymeric system which can be combined with calcium phosphates to promote the regrowth of previously damaged craniofacial tissues. These polymeric systems will be mechanically and chemically modified to use as resins for 3D printing to allow the creation of personalised custom-fit implants for patients to ultimately positively impact patients' quality of life and offer them a new approach to restore their abilities and deformities whilst taking into consideration their aesthetic requirements.

## Publications

- **Shakouri, Taleen**, Cha, Jae-Ryung, Owji, Nazanin et al. 'Comparative study of photoinitiators for the synthesis and 3D printing of a light-curable, degradable polymer for custom- fit hard tissue implants.' *Biomedical Materials*, vol. 16, issue 1, (2020), pp: 015007
- Owji, Nazanin, Aldaadaa, Alaa, Cha, Jae-Ryung, **Shakouri, Taleen** et al. 'Synthesis, Characterization, and 3D Printing of an Isosorbide-Based, Light-Curable, Degradable Polymer for Potential Application in Maxillofacial Reconstruction.' *ACS Biomater. Sci. Eng.* 2020, 6, 5, 2578–2587.

## Conference Posters and Presentations

- T. Shakouri, E. García-Gareta, JR. Cha, HW. Kim, J. Knowles (2019)  
Maxillofacial implants from the synthesis of a novel 3D-Printable polymer  
*Eastman Dental Institute Research Away Day*
- T. Shakouri, E. García-Gareta, JR. Cha, HW. Kim, J. Knowles (2019)  
Maxillofacial implants from the synthesis of a novel 3D-Printable polymer  
*5<sup>th</sup> London Polymer Group Symposium*

# Contents

|  |           |
|--|-----------|
| <b><i>Declaration</i></b> .....                                    | <b>2</b>  |
| <b><i>Dedication</i></b> .....                                     | <b>3</b>  |
| <b><i>Acknowledgments</i></b> .....                                | <b>4</b>  |
| <b><i>Abstract</i></b> .....                                       | <b>6</b>  |
| <b><i>Impact Statement</i></b> .....                               | <b>8</b>  |
| <b><i>Publications</i></b> .....                                   | <b>10</b> |
| <b><i>Symbols</i></b> .....  | <b>16</b> |
| <b><i>Abbreviations</i></b> .....                                  | <b>18</b> |
| <b><i>Index of Tables</i></b> .....                                | <b>24</b> |
| <b><i>Index of Figures</i></b> .....                               | <b>25</b> |
| <b><i>Index of Equations</i></b> .....                             | <b>39</b> |
| <b><i>Chapter 1 : Introduction and Literature Review</i></b> ..... | <b>40</b> |
| <b>1.1 Human Bone</b> .....  | <b>41</b> |
| 1.1.1 Cortical and Cancellous Bone .....                           | 42        |
| <b>1.2 Bone Composition</b> .....                                  | <b>45</b> |
| 1.2.1 Inorganic Matrix .....                                       | 45        |
| 1.2.2 Osteoblasts and Osteoclasts.....                             | 46        |
| 1.2.3 Organic Matrix .....   | 47        |
| <b>1.3 Bone Formation</b> .....                                    | <b>51</b> |

|   |            |
|---|------------|
| 1.3.1 Intramembranous Ossification.....                         | 51         |
| 1.3.2 Endochondral Ossification.....                            | 52         |
| <b>1.4 Osseointegration .....</b>                               | <b>55</b>  |
| 1.4.1 The Success and Failure of Osseointegrated Implants ..... | 57         |
| 1.4.2 Osteoconductive vs. Osteoinductive .....                  | 58         |
| <b>1.5 Craniofacial Reconstruction .....</b>                    | <b>59</b>  |
| 1.5.1 Congenital Disorders .....                                | 60         |
| 1.5.2 Traumatic Incidents .....                                 | 61         |
| 1.5.3 Cancers .....   | 62         |
| <b>1.6 Materials Currently In Use .....</b>                     | <b>62</b>  |
| 1.6.1 Autologous Bone Grafts .....                              | 65         |
| 1.6.2 Allogeneic Bone Grafts.....                               | 67         |
| 1.6.3 Xenografts .....  | 69         |
| 1.6.4 Alloplastic Grafts .....                                  | 70         |
| 1.6.5 Metals .....  | 86         |
| <b>1.7 Additive Manufacturing .....</b>                         | <b>87</b>  |
| 1.7.1 3D Printing Materials and Techniques .....                | 90         |
| 1.7.2 Photopolymerisation.....                                  | 99         |
| 1.7.3 3D Printing in Tissue Engineering .....                   | 107        |
| <b>1.8 Clinical Need for New Materials .....</b>                | <b>108</b> |
| <b>1.9 Aims and Objectives.....</b>                             | <b>109</b> |

## **Chapter 2 : Synthesis and 3D printing of a light-curable degradable**

|  |            |
|--|------------|
| <b>polymeric system (CSMA-2).....</b>          | <b>111</b> |
| <b>2.1 Introduction.....</b>                   | <b>112</b> |
| <b>2.2 Materials and Methodology .....</b>     | <b>120</b> |
| 2.2.1 Materials .....                          | 120        |
| 2.2.2 Synthesis of BHIS .....                  | 121        |
| 2.2.3 Synthesis of CSMA-2 .....                | 123        |
| 2.2.4 Photoinitiator systems .....             | 125        |
| 2.2.5 Material Characterisation .....          | 125        |
| 2.2.6 Composite Preparation.....               | 127        |
| 2.2.7 Computer-Aided Design .....              | 131        |
| 2.2.8 Optimisation of Settings .....           | 131        |
| 2.2.9 3D Printing.....                         | 134        |
| 2.2.10 Post Curing.....                        | 136        |
| 2.2.11 Scanning Electron Microscopy (SEM)..... | 137        |
| 2.2.12 Computed Tomography (CT) .....          | 138        |
| <b>2.3 Results.....</b>                        | <b>139</b> |
| 2.3.1 Polymer Synthesis.....                   | 139        |
| 2.3.2 Material Characterisation .....          | 142        |
| 2.3.3 3D Printed Constructs .....              | 152        |
| 2.3.4 SEM Analysis .....                       | 155        |
| 2.3.5 CT Analysis .....                        | 156        |

|  |            |
|--|------------|
| 2.4 Discussion.....  | 159        |
| 2.5 Conclusion .....   | 166        |
| <b>Chapter 3 : Mechanical Properties and Degradation Studies .....</b> | <b>167</b> |
| 3.1 Introduction.....  | 168        |
| 3.2 Materials and Methodology .....                                    | 172        |
| 3.2.1 Materials .....  | 172        |
| 3.2.2 Mechanical testing.....  | 172        |
| 3.2.3 Remineralisation Properties .....                                | 175        |
| 3.2.4 Degradation Studies.....   | 176        |
| 3.2.5 Statistical Analysis.....  | 178        |
| 3.3 Results.....   | 178        |
| 3.3.1 Mechanical testing.....  | 178        |
| 3.3.2 Comparing CQ Vs. BAPO Mechanically .....                         | 187        |
| 3.3.3 Remineralisation Properties .....                                | 194        |
| 3.3.4 Degradation Studies.....   | 200        |
| 3.4 Discussion.....  | 208        |
| 3.5 Conclusion .....   | 216        |
| <b>Chapter 4 : Biological Exploration .....</b>                        | <b>217</b> |
| 4.1 Introduction.....  | 218        |
| 4.2 Materials and Methodology .....                                    | 222        |
| 4.2.1 Materials .....  | 222        |
| 4.2.2 Cell Culture.....  | 222        |

|   |                   |
|---|-------------------|
| 4.2.3 Cell Metabolic Activity .....                               | 224               |
| 4.2.4 Phalloidin and DAPI Staining .....                          | 227               |
| 4.2.5 Real-Time Polymerase Chain Reaction .....                   | 228               |
| 4.2.6 Angiogenesis Assessment .....                               | 236               |
| 4.2.7 Statistical Analysis .....                                  | 239               |
| <b>4.3 Results.....</b>   | <b>239</b>        |
| 4.3.1 Cytocompatibility Studies .....                             | 239               |
| 4.3.2 Osteogenic Differentiation .....                            | 251               |
| 4.3.3 Differentiation Studies (qPCR) .....                        | 259               |
| 4.3.4 Angiogenic Response (CAM) .....                             | 267               |
| <b>4.4 Discussion.....</b>  | <b>274</b>        |
| <b>4.5 Conclusion .....</b>                                       | <b>288</b>        |
| <b><i>Chapter 5 : General Discussion and Conclusion .....</i></b> | <b><i>289</i></b> |
| <b>5.1 Discussion.....</b>  | <b>290</b>        |
| <b>5.2 Future Work.....</b>                                       | <b>300</b>        |
| <b>5.3 Conclusion .....</b>                                       | <b>301</b>        |
| <b><i>Bibliography.....</i></b>                                   | <b><i>302</i></b> |

## Symbols

|            |                       |
|------------|-----------------------|
| <b>μg</b>  | Microgram             |
| <b>μL</b>  | Microlitre            |
| <b>μm</b>  | Micrometre            |
| <b>a.u</b> | Arbitrary unit        |
| <b>Ca</b>  | Calcium               |
| <b>cm</b>  | Centimetre            |
| <b>d</b>   | Day                   |
| <b>Δ</b>   | Delta                 |
| <b>E</b>   | Modulus of elasticity |
| <b>g</b>   | Gram                  |
| <b>J</b>   | Joule                 |
| <b>L</b>   | Litre                 |
| <b>m</b>   | Mass                  |
| <b>M</b>   | Molarity              |
| <b>mg</b>  | Milligram             |
| <b>Min</b> | Minute                |
| <b>mL</b>  | Millilitre            |
| <b>mm</b>  | Millimetre            |



|                       |                         |
|-----------------------|-------------------------|
| <b>mM</b>             | Millimolar              |
| <b>m<sub>w</sub></b>  | Molecular weight        |
| <b>N</b>              | Newton                  |
| <b>N</b>              | Sample number           |
| <b>nm</b>             | Nanometre               |
| <b>O</b>              | Oxygen                  |
| <b>P</b>              | Phosphorus              |
| <b>ppm</b>            | Parts per million       |
| <b>S</b>              | Flexural strength       |
| <b>s</b>              | Seconds                 |
| <b>Si</b>             | Silica                  |
| <b>T</b>              | Temperature             |
| <b>t</b>              | Time                    |
| <b>T<sub>s</sub></b>  | Sample thickness        |
| <b>V</b>              | Volume                  |
| <b>V<sub>0</sub></b>  | Initial volume          |
| <b>V<sub>dt</sub></b> | Volume at a given point |
| <b>w</b>              | Week                    |
| <b>y</b>              | Year                    |

## Abbreviations

|                               |  |
|-------------------------------|--|
| <b>3D</b>                     | Three-dimensional                                    |
| <b><math>\alpha</math>TCP</b> | $\alpha$ -Tricalcium phosphate                       |
| <b><math>\beta</math>TCP</b>  | $\beta$ -Tricalcium phosphate                        |
| <b>ABS</b>                    | Acrylonitrile butadiene styrene                      |
| <b>ACP</b>                    | Amorphous calcium phosphate                          |
| <b>AM</b>                     | Additive manufacturing                               |
| <b>ATR</b>                    | Attenuated total reflection                          |
| <b>BAPO</b>                   | Phenylbis(2,4,6-trimethylbenzoyl)<br>phosphine oxide |
| <b>BF</b>                     | Bifurcation  |
| <b>BFM</b>                    | Biaxial flexural modulus                             |
| <b>BFS</b>                    | Biaxial flexural strength                            |
| <b>BG</b>                     | Bioactive glass                                      |
| <b>BHIS</b>                   | bis(2-hydroxyethyl) isosorbide                       |
| <b>BSE</b>                    | Bovine spongiform<br>encephalopathy                  |
| <b>CAD</b>                    | Computer-aided design                                |

|               |   |
|---------------|---|
| <b>CAM</b>    | Chorioallantoic membrane  |
| <b>CaP</b>    | Calcium phosphate   |
| <b>cDNA</b>   | Complimentary DNA   |
| <b>CI</b>     | Confidence interval   |
| <b>COL1A1</b> | Collagen type I   |
| <b>CSMA-2</b> | <p>((((((((((3R,3aR,6S,6aR) -</p> <p>hexahydrofuro[3,2-b] furan-3,6-diyl)</p> <p>bis(oxy)) bis(ethane-2,1-diyl))bis(oxy))</p> <p>bis(carbonyl))bis(azanediy))bis</p> <p>(3,3,5 - trimethylcyclohexane - 5,1-</p> <p>diyl))bis(azanediy))bis(carbonyl))</p> <p>bis(oxy))bis(ethane - 2, 1 - diyl)</p> <p>bis(2-methylacrylate)</p> |
| <b>CT</b>     | Computed tomography   |
| <b>CQ</b>     | Camphorquinone  |
| <b>DBTDL</b>  | Dibutyltin dilaurate  |
| <b>DC</b>     | Degree of conversion  |
| <b>DCPA</b>   | Dicalcium phosphate anhydrous<br>(monetite)   |

|              |   |
|--------------|---|
| <b>DCPD</b>  | Dicalcium phosphate dihydrate<br><br>(brushite) |
| <b>DLP</b>   | Digital light processing                        |
| <b>DMA</b>   | Dynamic mechanical analysis                     |
| <b>DMEM</b>  | Dulbecco's modified eagle medium                |
| <b>DNA</b>   | Deoxyribonucleic acid                           |
| <b>E</b>     | Young's Modulus                                 |
| <b>EBM</b>   | Electron beam melting                           |
| <b>ECM</b>   | Extra cellular matrix                           |
| <b>ED</b>    | Embryonic development                           |
| <b>EDI</b>   | Eastman Dental Institute                        |
| <b>FBS</b>   | Foetal Bovine Serum                             |
| <b>FDA</b>   | Food and drug administration                    |
| <b>FDM</b>   | Fused deposition modelling                      |
| <b>FTIR</b>  | Fourier-transform infrared<br><br>spectroscopy  |
| <b>GAPDH</b> | Glyceraldehyde 3-phosphate<br><br>dehydrogenase |
| <b>gDNA</b>  | Genomic DNA                                     |

|              |                                 |
|--------------|---------------------------------|
| <b>GPa</b>   | Gigapascal                      |
| <b>H</b>     | Hydrogen                        |
| <b>HA</b>    | Hydroxyapatite                  |
| <b>hADSC</b> | Human adipose-derived stem cell |
| <b>HEMA</b>  | (Hydroxyethyl)methacrylate      |
| <b>HV</b>    | Vickers Pyramid Number          |
| <b>IPDI</b>  | Isophorone diisocyanate         |
| <b>MPa</b>   | Megapascal                      |
| <b>MRI</b>   | Magnetic resonance image        |
| <b>NMR</b>   | Nuclear magnetic resonance      |
| <b>OCN</b>   | Osteocalcin                     |
| <b>OCP</b>   | Octacalcium phosphate           |
| <b>OPN</b>   | Osteopontin                     |
| <b>PBS</b>   | Phosphate buffered saline       |
| <b>PC</b>    | polycarbonate                   |
| <b>PCL</b>   | Poly-caprolactone               |
| <b>PCR</b>   | Polymerase chain reaction       |
| <b>PEEK</b>  | Polyether ether ketone          |
| <b>PGA</b>   | Polyglycolide                   |

|                 |   |
|-----------------|---|
| <b>PLA</b>      | Poly-lactic acid                                      |
| <b>PLGA</b>     | Poly(lactic-co-glycolic acid)                         |
| <b>PLGA-nHA</b> | Poly(lactic-co-glycolic acid)/<br>nano hydroxyapatite |
| <b>PMMA</b>     | Poly(methyl methacrylate)                             |
| <b>PPSF</b>     | polyphenylsulfone                                     |
| <b>qPCR</b>     | Real-time PCR   |
| <b>RNA</b>      | Ribonucleic acid                                      |
| <b>RPM</b>      | Rotations per minute                                  |
| <b>RUNX2</b>    | Runt-related transcription factor 2                   |
| <b>SEM</b>      | Scanning electron microscope                          |
| <b>SLA</b>      | Stereolithography                                     |
| <b>SLS</b>      | Selective laser sintering                             |
| <b>STL</b>      | Standard tessellation language                        |
| <b>TCP</b>      | Tricalcium phosphate                                  |
| <b>TEGDMA</b>   | Triethylene glycol dimethacrylate                     |
| <b>TTCP</b>     | Tetracalcium phosphate                                |
| <b>UV</b>       | Ultraviolet   |
| <b>VEGF</b>     | Vascular endothelial growth factor                    |

|            |                           |
|------------|---------------------------|
| <b>WCA</b> | Water contact angle       |
| <b>WHO</b> | World health organisation |
| <b>XRD</b> | X-ray powder diffraction  |

## Index of Tables

|   |            |
|---|------------|
| <i>Table 1-1: Various types of calcium phosphates with their abbreviations and chemical formula are arranged in order of ascending calcium (Ca) to phosphorous (P) ratio. ....</i>  | <i>76</i>  |
| <i>Table 1-2: Current commercially available polymers for use in craniofacial reconstruction surgery, highlighting their melting points, Young's modulus and tensile strength. ....</i>   | <i>84</i>  |
| <i>Table 1-3: A summary of 3D printing techniques used for craniofacial reconstruction applications along with the suitable materials for each printing method. ....</i>  | <i>91</i>  |
| <i>Table 2-1: Description of the two photoinitiators used in the study, CQ and BAPO, with the appropriate nomenclature, abbreviation, chemical structure and molecular mass in g/mol. ....</i>  | <i>115</i> |
| <i>Table 2-2: A table displaying the polymer to calcium phosphate filler wt % ratios for the composite polymer discs used in this study. ....</i>   | <i>129</i> |
| <i>Table 2-3: A table explaining the several steps taken in the production of the starting monomer, Bis(2-hydroxyethyl) isosorbide (BHIS) with all the varying quantities of catalyst used throughout the process along with their outcomes. ....</i>   | <i>141</i> |
| <i>Table 2-4: The results from the numerical CT scan analysis carried out on the log-pile structure highlighting the accuracy of the 3D printing. 4 orthogonal faces were chosen and measured for their area-equivalent circle diameter as well as their cross-sectional area to compare to the original STL file dimensions (last row). ....</i> | <i>158</i> |
| <i>Table 3-1: Comparison of mechanical strength and Young's modulus values for trabecular and cortical bone compared to CSMA-2. ....</i>  | <i>209</i> |
| <i>Table 4-1: Table representing the components of the QuantiNova Reverse Transcription Kit used for the synthesis of cDNA. The protocol was interpreted from Qiagen's procedural guide. ....</i>   | <i>231</i> |
| <i>Table 4-2: Reverse-transcription thermal cycle protocol followed. ....</i>   | <i>232</i> |



*Table 4-3: Table representing the forward and reverse primer sequences used for qPCR highlighting the species acquired from and the annealing temperature for each gene. .... 233*

*Table 4-4-4: Table representing the forward and reverse primer sequences used for qPCR highlighting the species acquired from and the annealing temperature for each gene. .... 233*

## **Index of Figures**

*Figure 1-1: Structure of bone showing a) long bone and (b) cortical bone formation. Image taken from Robles-Linares, J.A.; Ramírez-Cedillo, E.; Siller, H.R.; Rodríguez, C.A.; Martínez-López, J.I. Parametric Modeling of Biomimetic Cortical Bone Microstructure for Additive Manufacturing. *Materials* **2019**, *12*, 913. <https://doi.org/10.3390/ma12060913> ..... 44*

*Figure 1-2: A schematic diagram showing the development of endochondral bone. Reprinted from: Rosy Setiawati and Paulus Rahardjo (December 14th, 2018). *Bone Development and Growth, Osteogenesis and Bone Regeneration*, Haisheng Yang, IntechOpen, DOI: 10.5772/intechopen.82452. Available from: <https://www.intechopen.com/chapters/64747> (Setiawati and Rahardjo, 2019). ..... 53*

*Figure 1-3: The possible areas of craniofacial reconstruction in a human. The diagram was created using BioRender.com ..... 60*

*Figure 1-4: A flow chart showing the three main classifications of bioceramics; bioinert, bioactive and bioresorbable with examples of each group. .... 71*

*Figure 1-5: Image (A) shows a PMMA customised implant commercially available through Stryker and Image (B) showing a commercially available PEEK milled implant available through DePuy Synthes. Image (A) reprinted from Stryker Corporation, Kalamazoo, MI, United States. <https://cmf.stryker.com/products/pmma-customized-implant> with permission from Stryker. Image (B) reprinted from DePuy Synthes Companies, Raynham, MA, United States. <https://www.jnjmedicaldevices.com/en-EMEA/service-details/peek-milled-implants> with permission from DePuy Synthes. .... 81*

*Figure 1-6: A schematic of extrusion based 3D bioprinting. Image reprinted from (Vanaei et al., 2021)*

*Vanaei, S., Parizi, M. S., Vanaei, S., Saleemizadehparizi, F. and Vanaei, H. R. (2021). 'An Overview on Materials and Techniques in 3D Bioprinting Toward Biomedical Application' Engineered Regeneration. Elsevier, 2, pp. 1-18. Doi: <https://doi.org/10.1016/j.engreg.2020.12.001>..... 94*

*Figure 2-1: Chemical structures showing the production of bis(2-hydroxyethyl) isosorbide (BHIS). ..... 122*

*Figure 2-2: An image of the column set up for the final purification of the initial starting monomer, BHIS. Silica beads were used as a separation material and a mixture of methanol: ethyl acetate with a 1:9 ratio was used for the mobile phase. The column was then left to dry at 60°C for 24 hours under vacuum to obtain high-purity BHIS. .... 123*

*Figure 2-3: Preparation of (((((((((((((3R,3aR,6S,6aR)-hexahydrofuro[3,2-b]furan-3,6-diyl)bis(oxy))bis(ethane-2,1 diyl))bis- (oxy))bis(carbonyl))bis(azanediy))bis(methylene))bis(3,3,5-trimethylcyclohexane-5,1-diyl))bis(azanediy))bis(carbonyl))bis- (oxy))bis(ethane-2,1-diyl)bis(2-methylacrylate). ..... 124*

*Figure 2-4: An example of the manual method to produce composite-polymer discs by placing the polymer/ filler paste onto a metal circlip disc, layering it with an acetate sheet and light-curing with a 450-470nm blue light diode for 40 seconds each side ..... 128*

*Figure 2-5: A screenshot image of the settings page from the standard options on the XYZ Nobel Superfine 3D printer. As seen, the curing settings include the curing time, power intensity and power level which are critical steps in the printing process. The peeling settings include the speed of which the construct is peeled off the platform and the distance it travels. The platform settings highlight the speed and distance of which the build platform ascends and descends when creating the construct layers. ... 132*

*Figure 2-6: Images taken of the XYZ Nobel Superfine DLP 3D printer used in this study. Image (A) shows the printer itself with its red cover to eliminate light, (B) shows the build platform at the top of the moving axis and (C) shows the resin tank ready to be filled with the appropriate material. .... 135*

*Figure 2-7: A schematic showing how the DLP 3D printer used in this study works beginning with the laser source emitting UV light at 450 nm which is transmitted via a mirrored projector screen onto the*

resin tank which is pre-filled with the required material. The build platform descends the moving axis, and the model is built layer by layer until it is complete, when the build platform will ascend back up to the top and allow the release of the model. .... 136

Figure 2-8: The XYZ Printing UV Chamber for the purpose of post curing the 3D printed models. Image (A) shows the chamber closed, with a solid red exterior to prevent any additional light emitting the chamber. Image (B) shows the chamber open, with the platform that the item is placed upon. .... 137

Figure 2-9:  $^1\text{H}$  NMR spectra highlighting the chemical bond formation of BHIS. The synthesis is confirmed by the proton signal at 3.58~3.73 ppm, which represents the  $\text{H}_2\text{-C-C-H}_2$  protons and correspond to the ethylene group in BHIS. On the spectra 1= withdrawing electron density from O-, 2= Alkane, 3= Ethylene group and 4= Hydroxyl group. .... 143

Figure 2-10:  $^1\text{H}$  NMR spectra highlighting the chemical bond formation of BHIS with a focus on the integrals investigated throughout the spectra. The area under the NMR resonance is proportional to the number of hydrogens which that resonance represent. .... 144

Figure 2-11:  $^{13}\text{C}$  NMR analysis of the monomer BHIS. The spectrum here shows 10 visible carbon environments which represent the 10 carbon environments seen in the structure of BHIS. .... 145

Figure 2-12:  $^1\text{H}$  NMR spectra highlighting the chemical bond formation of CSMA-2. The synthesis is confirmed by the three singlets present at 6.14, 5.59 and 1.96 ppm corresponding to the protons of the methacryl group ( $\text{CH}_2=\text{C-CH}_3$ ). The signals seen between 0.8 and 1.2 ppm correspond to the protons of the isophorone cycle. On the spectra 1= Alkene, 2=Methacrylate, 3= Ester bonds and 4=Isophorone cycle. .... 146

Figure 2-13:  $^1\text{H}$  NMR spectra highlighting the chemical bond formation of CSMA-2 with a focus on the integrals investigated throughout the spectra. The area under the NMR resonance is proportional to the number of hydrogens which that resonance represents. .... 147

Figure 2-14:  $^{13}\text{C}$  NMR analysis of CSMA-2. The spectrum here shows 19 visible carbon environments which represent the 19 carbon environments seen in the structure of CSMA-2. .... 148

*Figure 2-15: FTIR spectrum of CSMA-2 with 2% CQ photoinitiator showing the percentage of reacted monomers post curing; 65% of polymerisation was achieved in this formulation after exposure to blue light for 40 seconds. Absorbance profiles were received at  $1320 \pm 1 \text{ cm}^{-1}$  (C–O stretch bond) and  $1335 \pm 2 \text{ cm}^{-1}$  was set as the baseline. .... 150*

*Figure 2-16: FTIR spectrum of CSMA-2 with 2% BAPO photoinitiator showing the percentage of reacted monomers post curing; 72% of polymerisation was achieved in this formulation after exposure to blue light for 40 seconds. Absorbance profiles were received at  $1320 \text{ cm}^{-1}$  (C–O stretch bond) and  $1335 \pm 2 \text{ cm}^{-1}$  was set as the baseline. .... 151*

*Figure 2-17: FTIR spectrum of CSMA-2 representing the rate of reaction to show the start time of the reaction (4.65 seconds) ..... 152*

*Figure 2-18: 3D printed composite-polymer discs of 10 mm X 1 mm containing 0, 5 or 10 wt% hydroxyapatite, printed via the XYZ Nobel Superfine DLP printer and post cured via the methanol and UV curing chamber method. .... 153*

*Figure 2-19: 3D printed porous scaffolds containing CSMA-2 + 2 wt% BAPO photoinitiator and either 0 wt% HA (left image) 5 wt% HA (middle image) and 10 wt% HA (right image). All scaffolds were designed using AutoCAD and are 6 mm in diameter and 3 mm thick with pores of 0.5 mm. .... 154*

*Figure 2-20: Images taken of the log-pile structure symbolising cortical bone, on the left and trabecular bone construct on the right. Both scaffolds were designed using AutoCAD and 3D printed using CSMA-2 with 2 wt% BAPO photoinitiator using the XYZ Nobel Superfine DLP Printer. .... 154*

*Figure 2-21: Image (A) shows a 3D printed matrix utilising CSMA-2 and 2% BAPO photoinitiator, followed by a matrix viewed via a SEM at 25 X magnification with highlighted dimensions (B). .... 155*

*Figure 2-22: Images of the log-pile structure reoriented using the Bruker MicroCT DataViewer programme to display the faces of the cylinders orthogonal to the perspective of direction. The sliced CAD image (A) displays the faces of the cylinders, whereas (B) shows the faces of the cylinders. .... 156*

*Figure 3-1: A graphical representation for the comparison of bend strength results from the biaxial flexural test done via the Shimadzu for composite-polymer discs with 2 wt% CQ and a range of 0-5 wt%*

HA. The highest recorded value was 84.07 N/mm<sup>2</sup> for CSMA-2 with 2 wt% CQ and no added HA. The lowest value recorded was 75.46 N/mm<sup>2</sup> for the 5 wt% HA composite polymer which was statistically significant with the result of the CSMA-2 polymer composite by itself. (\*p < 0.05)..... 179

Figure 3-2: A graphical representation for the comparison of bend strength results from the biaxial flexural test done via the Shimadzu for composite-polymer discs with 2 wt% CQ and a range of 0-50 wt% HA. The highest recorded value was again, 84.07 N/mm<sup>2</sup> for CSMA-2 with 2 wt% CQ and no added HA. This was statistically significantly different to the value recorded for 30 wt% HA (65.31 N/mm<sup>2</sup>), 40 wt% (63.50 N/mm<sup>2</sup>) and the lowest value recorded which was 59.51 N/mm<sup>2</sup> for the 50 wt% HA composite polymer (\*p < 0.05). ..... 180

Figure 3-3: A graphical representation for the comparison of Young's Modulus results from the biaxial flexural test done via the Shimadzu for composite-polymer discs with 2 wt% CQ and a range of 0-5 wt% HA. The highest recorded value was 2.44 kN/mm<sup>2</sup> for CSMA-2 with 2 wt% CQ and no added HA. This was statistically significantly different to the lowest value recorded which was 1.96 kN/mm<sup>2</sup> for the 5 wt% HA composite polymers as well as the result for the 3 wt% HA composite-polymer sample which had a result of 2.02 kN/mm<sup>2</sup> (\*p < 0.05)..... 181

Figure 3-4: A graphical representation for the comparison of Young's Modulus results from the biaxial flexural test done via the Shimadzu for composite-polymer discs with 2 wt% CQ and a range of 0-50 wt% HA. The highest recorded value was 2.44 kN/mm<sup>2</sup> for CSMA-2 with 2 wt% CQ and no added HA. This was statistically significantly different to the lowest value recorded which was 1.76 kN/mm<sup>2</sup> for the 40 wt% HA composite polymers as well as the result for the 50 wt% HA composite-polymer sample which had a result of 1.89 kN/mm<sup>2</sup> (\*p < 0.05). ..... 183

Figure 3-5: A graphical representation for the comparison of hardness results from the Vickers Hardness test done via the Wallace Micro-Hardness Tester for composite-polymer discs with 2 wt% CQ and a range of 0-5 wt% HA. The lowest recorded value was 7.54 g/mm<sup>2</sup> for CSMA-2 with 2 wt% CQ and no added HA. The highest value recorded was 8.04 g/mm<sup>2</sup> for the 5 wt% HA composite polymer which was statistically significant with the result of the CSMA-2 polymer composite by itself. (\*p < 0.05)..... 184

Figure 3-6: A graphical representation for the comparison of hardness results from the Vickers Hardness test done via the Wallace Micro-Hardness Tester for composite-polymer discs with 2 wt% CQ and a range of 0-50 wt% HA. The lowest recorded value was 7.54 g/mm<sup>2</sup> for CSMA-2 with 2 wt% CQ and no added HA. The highest value recorded was 21.47 g/mm<sup>2</sup> for the 50 wt% HA composite polymer which was statistically significant with the result of the CSMA-2 polymer composite by itself as well as the values for all the HA-incorporated composites 10-40 wt%. (\*p < 0.05)..... 185

Figure 3-7: Water contact angle measurements investigating the hydrophilicity of the polymer with no added HA compared to HA incorporated composite discs: a direct correlation can be observed between hydrophilicity and addition of CaP fillers. The 50 wt% formulation showed the most hydrophilic behaviour (however not statistically significant, \*P > 0.05, from the 10-40 wt% formulation) but statistically significantly different to CSMA-2 alone which had the highest contact angle measurement of 59 ° showing the least hydrophilic behaviour out of the composites but still exhibiting hydrophilicity as the angle is smaller than 90 °. (\*p < 0.05). ..... 187

Figure 3-8: A graphical representation for the comparison of flexural strength results from the biaxial flexural test done via the Shimadzu for composite-polymer discs with 2 wt% CQ (red) and a range of 0-10 wt% HA vs. composite-polymer discs with 2 wt% BAPO (blue) and a range of 0-10 wt% HA. The highest recorded value was 135.49 N/mm<sup>2</sup> for CSMA-2 with 2 wt% BAPO and no added HA. All CQ values were significantly lower than their respective BAPO incorporated values (\*p < 0.05). ..... 189

Figure 3-9: A graphical representation for the comparison of Young's Modulus results from the biaxial flexural test done via the Shimadzu for composite-polymer discs with 2 wt% CQ (red) and a range of 0-10 wt% HA vs. composite-polymer discs with 2 wt% BAPO (blue) and a range of 0-10 wt% HA as well as comparing the Young's modulus results from the DMA test. The highest recorded value was 2.44 kN/mm<sup>2</sup> for CSMA-2 with 2 wt% CQ and no added HA. This was statistically significantly different to the respective values with BAPO and the BAPO formulations carried out via DMA (\*p < 0.05). ..... 190

Figure 3-10: A graphical representation for the comparison of hardness results from the Vickers Hardness test done via the Wallace Micro-Hardness Tester for composite-polymer discs with 2 wt% CQ (green) and a range of 0-10 wt% HA vs. composite-polymer discs with 2 wt% BAPO (white) and a range of 0-10 wt%

HA. The CQ values ranged from 7.54-8.09 g/mm<sup>2</sup> for CSMA-2 which compare to the BAPO values which ranged from 8.21-9.79 g/mm<sup>2</sup>. All CQ incorporated formulations had significantly lower hardness values than their respective BAPO incorporated formulations (\*p < 0.05). ..... 192

Figure 3-11: A graphical representation for the comparison of the contact angle measurements for the purpose of investigating the hydrophilicity of the composite-polymer discs with 2 wt% CQ (purple) and a range of 0-10 wt% HA vs. composite-polymer discs with 2 wt% BAPO (white) and a range of 0-10 wt% HA. The CQ values range from 54°-59° which compare to the BAPO values which ranges from 54°- 55°. A direct correlation can be observed between the hydrophilicity and the addition of CaP fillers. (\*p < 0.05) ..... 194

Figure 3-12: SEM images highlighting the surface remineralisation of 0-50 wt% HA incorporated composite-polymer discs. Deposition of HA particles can be clearly observed on the surface of the discs as the quantity increased. The first image, CSMA-2 alone with no added HA, showed a clear surface with no particles attached. By 50 wt% HA, there was a significantly greater amount of HA particles dispersed on the surface of the discs which are shown to be a continuous layer of merged crystals. .... 196

Figure 3-13: X-Ray Diffraction analysis of calcium phosphate precipitation in the 0-50 wt% HA with 2 wt% CQ composite-polymer specimens. Hydroxyapatite diffraction peaks began to be observed in the 10 wt% HA specimens (purple) then increased in size as the quantity of HA increased up to 50 wt% HA (orange). ..... 198

Figure 3-14: X-Ray Diffraction analysis of calcium phosphate precipitation in the 0-10 wt% HA with 2 wt% BAPO composite-polymer specimens. Hydroxyapatite diffraction peaks began to be observed in the 5 wt% HA specimens (red) and the 10 wt% HA specimens (blue). ..... 199

Figure 3-15: pH values of a glass control disc in comparison with CSMA-2 with 2 wt% BAPO photoinitiator, 5 wt% HA and 10 wt% HA incorporated composite discs post 24-hour immersion in a neutral culture media. All samples showed acidic behaviour with the values ranging from 6-7.4. The 10 wt% HA formulations exhibited the highest pH at 7.4, however all the groups remained in the acidic-basic range. (\*p<0.05) ..... 200

Figure 3-16: Representation of the cumulative percentage mass change across a 6-month incubation period at the set physiological temperature 37°C. Equation 2-4 allowed calculation of the rate of degradation with respect to the initial dry weight percentage mass change of CSMA-2 compared to the CaP incorporated composite discs in phosphate buffered saline: the highest rate of mass change is observed in the 10 wt% CaP discs with a 8% drop in weight (blue), while the lowest value was exhibited by the CSMA-2 polymer by itself which had a 6% drop in weight over the 6-month period (black). ..... 202

Figure 3-17: Representation of the cumulative percentage mass change across a 6-month incubation period at a set temperature of 60°C. Equation 2-4 allowed calculation of the rate of degradation with respect to the initial dry weight percentage mass change of CSMA-2 compared to the CaP incorporated composite discs in phosphate buffered saline: the highest rate of mass change is observed in the 10 wt% CaP discs with a 10 % drop in weight (blue), while the lowest value was exhibited by the CSMA-2 polymer by itself which had a 9% drop in weight over the 6-month period (black). ..... 203

Figure 3-18: A graphical representation for the comparison of bend strength results from the biaxial flexural test done via the Shimadzu for composite-polymer discs with 2 wt% BAPO and a range of 0-5 wt% HA across 6 months of incubation time to assess the degradation properties. The highest recorded value was 137.54 N/mm<sup>2</sup> for CSMA-2 with 2 wt% BAPO and no added HA after 1 month of incubation in PBS. The lowest recorded value for CSMA-2 with no added HA was at the 6-month time point giving a bend strength value of 88.21 N/mm<sup>2</sup>. The lowest value recorded throughout the experiment was 57.21N/mm<sup>2</sup> for the 10 wt% HA composite polymer after 6 months of incubation in PBS. The results for the 4,5 and 6-month time points were statistically significantly different compared to the results from 0-3 months incubation for all 3 formulations. (\*p < 0.05)..... 205

Figure 3-19: A graphical representation for the comparison of Young's modulus results from the biaxial flexural test done via the Shimadzu for composite-polymer discs with 2 wt% BAPO and a range of 0-5 wt% HA across 6 months of incubation time to assess the degradation properties. The highest recorded value was 2.62 kN/mm<sup>2</sup> for CSMA-2 with 2 wt% BAPO and no added HA after 1 month of incubation in PBS. The lowest recorded value for CSMA-2 with no added HA was at the 6-month time point giving a modulus value of 1.20 kN/mm<sup>2</sup>. The lowest value recorded throughout the experiment was 0.944 kN/mm<sup>2</sup> for the 10 wt% HA composite polymer after 6 months of incubation in PBS. The results for the



4,5 and 6-month time points were statistically significantly different compared to the results from 0-3 months incubation for all 3 formulations. (\*p < 0.05)..... 207

Figure 4-1: Diagram representing the process for the metabolic activity alamarBlue assay. Interpreted from the alamarBlue assay user guide provided by ThermoFisher Scientific. The diagram was created using BioRender.com..... 225

Figure 4-2: Diagram highlighting the steps involved in RNA isolation via the conventional TRIzol® method. The protocol was interpreted from the TRIzol® user guide provided by ThermoFisher Scientific. The diagram was created using BioRender.commet..... 228

Figure 4-3: Observation of (A) successful embryo transfer with an intact egg yolk and live embryo on embryonic development day 3. (B) An unsuccessful embryo transfer with a live embryo. (C) Successful embryo transfer with an intact egg yolk but a dead embryo as the heart is not beating..... 237

Figure 4-4: An image taken from above the ex-ovo culture on embryonic development day 9 showing the implantation of CSMA-2 composite-polymer porous scaffolds that were prepared via SLA 3D printing along with the positive and negative controls which were all sterilised using ethanol before implantation on the CAM..... 238

Figure 4-5: Metabolic activity of MG-63 cells on 0, 5 and 10 wt% HA incorporated composite discs with either CQ or BAPO (BP) photoinitiator at 1, 4 and 7 days post incubation. The values are compared to cells grown on tissue culture plastic (TCP) control in this experiment. As seen in the graph, the discs containing BAPO (BP) initiator have higher fluorescence intensity values, suggesting a higher metabolic activity on those samples. The control is significantly different to all the samples in the day 4 and 7 cultured experiment at (\*p < 0.05)..... 240

Figure 4-6: Fluorescence imaging results for DAY 1 using DAPI and phalloidin (blue and green respectively) to assess the proliferation and morphology of MG-63 osteosarcoma cells on the surface of the tissue culture plastic control (A) compared to CSMA-2 prepared with 2 wt% CQ photoinitiator (B), CSMA-2 with 2 wt% BAPO photoinitiator (C), CSMA-2 with 2 wt% CQ and 5 wt% HA (D), CSMA-2 with 2 wt% CQ and 10 wt% HA (E) and CSMA-2 with 2 wt% BAPO and 10 wt% HA (G). Scale Bar = 100µm..... 243

Figure 4-7: Fluorescence imaging results for DAY 4 using DAPI and phalloidin (blue and green respectively) to assess the proliferation and morphology of MG-63 osteosarcoma cells on the surface of the tissue culture plastic control (A) compared to CSMA-2 prepared with 2 wt% CQ photoinitiator (B), CSMA-2 with 2 wt% BAPO photoinitiator (C), CSMA-2 with 2 wt% CQ and 5 wt% HA (D), CSMA-2 with 2 wt% CQ and 10 wt% HA (E) and CSMA-2 with 2 wt% BAPO and 10 wt% HA (G). Scale Bar = 100µm..... 244

Figure 4-8: Fluorescence imaging results for DAY 7 using DAPI and phalloidin (blue and green respectively) to assess the proliferation and morphology of MG-63 osteosarcoma cells on the surface of the tissue culture plastic control (A) compared to CSMA-2 prepared with 2 wt% CQ photoinitiator (B), CSMA-2 with 2 wt% BAPO photoinitiator (C), CSMA-2 with 2 wt% CQ and 5 wt% HA (D), CSMA-2 with 2 wt% CQ and 10 wt% HA (E) and CSMA-2 with 2 wt% BAPO and 10 wt% HA (G). Scale Bar = 100µm..... 245

Figure 4-9: Metabolic activity of hADSCs on 0, 5 and 10 wt% HA incorporated composite discs with BAPO photoinitiator at 1, 4 and 7 days post incubation. The values are compared to cells grown on the surface of a control glass. As seen in the graph, the discs containing 10 wt% HA have significantly higher fluorescence intensity values when comparing them to the 0 and 5 wt% HA samples, suggesting a higher metabolic activity for that formulation. The control is significantly higher than the other formulations for all of the time points except for day 4 where the control and 10 wt% HA formulations are not significantly different. (\*p < 0.05). ..... 247

Figure 4-10: Fluorescence imaging results for DAY 1 using DAPI and phalloidin (blue and green respectively) to assess the proliferation and morphology of hADSCs on the surface of a control glass coverslip (A) compared to CSMA-2 prepared with 2 wt% BAPO photoinitiator and no added HA (B), CSMA-2 with 2 wt% BAPO and 5 wt% HA (C) and CSMA-2 with 2 wt% BAPO and 10 wt% HA (D). Scale Bar = 200µm ..... 249

Figure 4-11: Fluorescence imaging results for DAY 4 using DAPI and phalloidin (blue and green respectively) to assess the proliferation and morphology of hADSCs on the surface of a control glass coverslip (A) compared to CSMA-2 prepared with 2 wt% BAPO photoinitiator and no added HA (B), CSMA-2 with 2 wt% BAPO and 5 wt% HA (C) and CSMA-2 with 2 wt% BAPO and 10 wt% HA (D). Scale Bar = 200µm ..... 250

Figure 4-12: Fluorescence imaging results for DAY 7 using DAPI and phalloidin (blue and green respectively) to assess the proliferation and morphology of hADSCs on the surface of a control glass coverslip (A) compared to CSMA-2 prepared with 2 wt% BAPO photoinitiator and no added HA (B), CSMA-2 with 2 wt% BAPO and 5 wt% HA (C) and CSMA-2 with 2 wt% BAPO and 10 wt% HA (D). Scale Bar = 200µm ..... 251

Figure 4-13: Metabolic activity of hADSCs cultured in either SM or OM on 0, 5 and 10 wt% HA incorporated composite discs with BAPO photoinitiator at 1, 7, 14, 21 and 29 days post incubation. The values are compared to cells grown on the surface of a control glass disc. As seen in the graph, after 7 days of culture, the cells grown in OM had a higher metabolic activity and this trend remained the same throughout. The SM groups were compared statistically to the OM groups where all the timepoints from day 7 onwards showed significant differences. The highest metabolic activity was seen in the OM-0% HA group, although this was not significantly different to the OM control or the 5 and 10 wt% HA formulations, suggesting promotion of cell metabolic activity throughout. Data are presented as Mean ± SD, n=3. (\*p < 0.05) where \* represents significant difference to the SM control sample and # represents significant difference to the OM control sample. .... 252

Figure 4-14: Fluorescence imaging results for DAY 7 using DAPI and phalloidin (blue and green respectively) to assess the proliferation and morphology of hADSCs on the surface of the composite-polymer specimens prepared in either standard media or osteogenic supplemented media. The left hand side images are the results for the standard media, and they're compared to the right hand side images which are the osteogenic supplemented specimens. Scale Bar= 100µm. .... 255

Figure 4-15: Fluorescence imaging results for DAY 14 using DAPI and phalloidin (blue and green respectively) to assess the proliferation and morphology of hADSCs on the surface of the composite-polymer specimens prepared in either standard media or osteogenic supplemented media. The left hand side images are the results for the standard media, and they're compared to the right hand side images which are the osteogenic supplemented specimens. Scale Bar= 100µm. .... 256

Figure 4-16: Fluorescence imaging results for DAY 21 using DAPI and phalloidin (blue and green respectively) to assess the proliferation and morphology of hADSCs on the surface of the composite-

*polymer specimens prepared in either standard media or osteogenic supplemented media. The left hand side images are the results for the standard media, and they're compared to the right hand side images which are the osteogenic supplemented specimens. Scale Bar= 100µm. .... 257*

*Figure 4-17: Fluorescence imaging results for DAY 28 using DAPI and phalloidin (blue and green respectively) to assess the proliferation and morphology of hADSCs on the surface of the composite-polymer specimens prepared in either standard media or osteogenic supplemented media. The left hand side images are the results for the standard media, and they're compared to the right hand side images which are the osteogenic supplemented specimens. Scale Bar= 100µm. .... 258*

*Figure 4-18: Runt-related transcription factor 2 (RUNX2) gene expression quantification by qPCR of hADSCs grown on 3D printed CSMA-2 discs with either 0, 5 or 10 wt% HA incorporated at day 7, 14 and 21. The gene expression was normalised against the housekeeping gene, GAPDH expression and using the expression on TCP as a baseline control. A high upregulation of RUNX2 expression occurred on all specimens at day 7 which reduced by day 21 as RUNX2 is an early marker. The osteogenic samples had a better upregulation throughout, with the 0 wt% HA and 10 wt% HA showing the highest expression of RUNX2 when compared to the control. Data are shown as Mean ± SD, n=3. (\*p < 0.05) (\*\*p<0.01) ..... 260*

*Figure 4-19: Collagen type 1 (COL1A1) gene expression quantification by qPCR of hADSCs grown on 3D printed CSMA-2 discs with either 0, 5 or 10 wt% HA incorporated at day 7, 14 and 21. The gene expression was normalised against the housekeeping gene, GAPDH expression and using the expression on TCP as a baseline control. The early timepoints displayed an upregulation of COL1A1 expression as it is an early marker of osteoblast. Downregulation of COL1A1 expression occurred by day 21. The osteogenic formulations gave a significantly higher level of expression in comparison to the standard media formulations and in comparison, to the control. Data are shown as Mean ± SD, n=3. (\*p < 0.05) (\*\*p<0.01) ..... 262*

*Figure 4-20: Osteocalcin (OCN) expression quantification by qPCR of hADSCs grown on 3D printed CSMA-2 discs with either 0, 5 or 10 wt% HA incorporated at day 7, 14 and 21. The gene expression was normalised against the housekeeping gene, GAPDH expression and using the expression on TCP as a baseline control. Day 7 did not display much expression as the later timepoints as OCN is a late onset*

marker. Day 14s results display an upregulation in gene expression, particularly for the osteogenic formulations which compared significantly with the control. A high upregulation of OCN expression occurred on all specimens at day 21 however, the standard 0 wt% formulation was significantly lower than the remainder of the group. The osteogenic samples had a better upregulation throughout, with the 10 wt% HA showing the highest expression of OCN. Data are shown as Mean  $\pm$  SD, n=3. (\*p < 0.05) (\*\*p<0.01) ..... 263

Figure 4-21: Osteopontin (OPN) expression quantification by qPCR of hADSCs grown on 3D printed CSMA-2 discs with either 0, 5 or 10 wt% HA incorporated at day 7, 14 and 21. The gene expression was normalised against the housekeeping gene, GAPDH expression and using the expression on TCP as a baseline control. Day 7 and day 14 showed a small gene expression but not a high amount of expression as the later timepoints as OPN is a late onset marker. A high upregulation of OPN expression occurred on all specimens at day 21 with the highest expression being seen in the 10 wt% formulations which significantly compare to the remaining groups. The 5 wt% formulation was not as consistent as other genes explored but still had significant expression of OPN throughout. Data are shown as Mean  $\pm$  SD, n=3. (\*p < 0.05) (\*\*p<0.01) ..... 265

Figure 4-22: The results from the control groups for the CAM assay. The left hand side represents the positive control sample, filter paper soaked in VEGF and the right hand side images represent the negative control sample, filter paper soaked in PBS. Images taken of the control sample, (b) grey-scale prepared image for analysis and (c) binary image. Scale bar = 1 mm. .... 268

Figure 4-23: The results from the CAM assay assessing angiogenesis on CSMA-2 with 0, 5 or 10 wt% HA composite scaffolds. The left-hand side images represent the results for 0% HA, CSMA-2 by itself. The middle set of images represent the results for 5 wt% HA and the right-hand side images represent the results for 10 wt% HA samples. Images (a) show the first standard image of the excised sample that was tested. The differences were observed in the vascular infiltration of the different composites as indicated by the growth of blood vessels seen in red (Scale bar = 1 mm). Images (b) show the grey-scale prepared image on Microsoft PowerPoint to allow for ImageJ analysis and images (c) show the binary images on ImageJ which allow a detailed edge of the scaffold to be identified and newly formed blood vessels shown in black. .... 269

Figure 4-24: Graphical representation of the vascular density for the control samples and each composite-polymer material scaffold calculated after the CAM assay. The positive control had the highest vascular area at 15.15%. However, this was not significantly different to the results for 0 and 10 wt% HA which had vascular area results of 11.95 % and 13.32 % respectively. The negative control gave a vascular area of 9.35 % which is significantly different to all the formulations, apart from the 5 wt% group. The 5 wt% HA composites had a lower vascular density with only 8.79 % which compared significantly with the 0 and 10 wt% groups as confirmed by the digital images. Data are presented as Mean  $\pm$  SD, n=3. (\*p < 0.05) ..... 271

Figure 4-25: Graphical representation of the bifurcation points for the control samples and each composite-polymer material scaffold calculated after the CAM assay. The 10 wt% HA composite had the highest number of BF points at 40 which compared significantly to the 5 wt% HA formulations at 22 BF. All groups were significantly higher than the negative control group which only displayed 18 BF points. All Data are presented as Mean  $\pm$  SD, n=3. (\*p < 0.05)..... 273

## Index of Equations

|   |            |
|---|------------|
| <i>Equation 2-1: Equation used to calculate the rate of monomer conversion; where C is the conversion, A<sub>0</sub> is the initial absorbance peak and A<sub>f</sub> is the final absorbance peak. ....</i>  | <i>127</i> |
| <i>Equation 3-1: Equation showing how to calculate the Young's modulus where E represents the Young's modulus in pressure units, <math>\sigma</math> represents uniaxial stress, or uniaxial force per unit surface in pressure units and <math>\epsilon</math> represents the strain, or proportional deformation and is dimensionless. ....</i> | <i>173</i> |
| <i>Equation 3-2: The Vickers pyramid number (HV) is an equation for determining the hardness of a material, where F is the force applied to the diamond in kg-force (kgf) and A is the surface area of the resulting indentation in square millimetres (mm<sup>2</sup>). ....</i>   | <i>174</i> |
| <i>Equation 3-3 : Equation showing how the percentage mass change was calculated for degradation studies. ....</i>  | <i>177</i> |
| <i>Equation 3-4: Wenzel's equation stating the relationship between surface roughness and wettability where <math>\Theta_m</math> is the measured contact angle, <math>\Theta_Y</math> is Young's contact angle and r is the roughness ratio. ....</i>  | <i>212</i> |
| <i>Equation 4-1: Normalisation step to calculate the <math>\Delta Ct</math>. ....</i>   | <i>235</i> |
| <i>Equation 4-2: Calibration step to set a value for the baseline ....</i>  | <i>235</i> |
| <i>Equation 4-3: Showing the final form of the <math>2^{-\Delta\Delta Ct}</math> equation, the derivation of which has been reported previously by Livak and colleagues (Livak and Schmittgen, 2001). ....</i>  | <i>235</i> |
| <i>Equation 4-4: Expanded relative quantification where the equation may be used to compare the gene expression in two different samples (sample A and sample B); each sample is related to an internal control gene. ....</i>  | <i>236</i> |

# **Chapter 1 : Introduction and Literature Review**



## 1.1 Human Bone

The human body is composed of around 270 bones from birth which decreases to around 213 bones by adulthood as bones become fused. The human skeleton can be divided into the axial skeleton (containing approximately 74 bones) which is formed by the skull, vertebral column and the rib cage and the appendicular skeleton (containing approximately 126 bones) which is made up of the shoulder girdle, pelvic girdle and upper and lower limb bones. During a human lifetime, all of a human's bones have the capacity to repair and remodel themselves (Widmaier, E. P., Raff, H. & Strang, 2006). This enables the bones to adjust to changing biomechanical stresses while also assisting in the removal of old and damaged bone and the replacement of new, stronger bone (Langdahl, Ferrari and Dempster, 2016).

The human skeleton performs a number of critical roles, including providing structural support for the body, allowing for movement, protecting key organs, and maintaining mineral homeostasis (Clarke, 2008) as well as harbouring bone marrow.

Human bone can be classified into three types according to its morphology. These include long bones, short bones and flat bones. Long bones are typically longer than they are wide, and cartilaginous predecessors form them. The tibia and femur are examples of long bones. The epiphysis, metaphysis, and diaphysis are the three segments that make up long bones (Clarke, 2008). The epiphysis is the bone's outermost layer, which surrounds the joints. It is mostly made up of compact bone, which gives it good mechanical qualities. Between the epiphysis and the diaphysis is the metaphysis. It is composed of thin compact bone on top

and thick cancellous bone underneath. The metaphysis area carries the growth plates and blood vessels and is the region where fractures occur most frequently (Inoue *et al.*, 2018). The diaphysis is made up of cortical bone and usually contains bone marrow. A diaphysis' central section is made up of thick compact bone and thin cancellous bone that surrounds the marrow cavity. This is where primary ossification occurs, also known as the remodelling process (Inoue *et al.*, 2018).

Short bones are another classification of bone. They are seen as cuboidal shaped and are as wide as they are long. Their major purpose is to provide support and stability while allowing for minimal mobility. Carpals in the wrists and tarsals in the ankles are examples of short bones. Flat bones are present in the cranium, pelvis, and rib cage, and are made up of two thin layers of compact bone surrounding a variable amount of cancellous bone between them. The primary role of flat bones is to protect internal organs, and most red blood cells are generated in flat bones in adult humans (Garzón-Alvarado, González and Gutiérrez, 2013). Finally, irregular bones can vary in shape and structure hence not fitting into any of the three classifications. They have a complex shape which helps protect internal organs such as the vertebrae which has a vital role of protecting the spinal cord.

### **1.1.1 Cortical and Cancellous Bone**

There are two types of bones: compact cortical bone and cancellous (trabecular) bone. The adult human skeleton is composed of 80% cortical bone and 20%

cancellous bone. Varying skeletal sites within the body have different ratios of cortical to cancellous bone.

Cortical bone is dense and compact, and it forms the hard exterior of bones. The cortical bone is also responsible for giving bone its white and smooth solid look. Cortical bone facilitates the bones main functions such as protecting organs, storing and releasing chemical elements such as calcium, supporting the whole body and providing ability for movement. Cortical bone consists of multiple microscopic columns referred to as osteons. A central canal known as the Haversian canal is surrounded by many layers of osteoblasts and osteocytes in each column. The haversian canal is a network of microscopic tubes through which blood vessels and neurons can pass. The blood vessels and nerves are connected throughout the compact bone via canals known as 'Volkmann's canals'. The columns are metabolically active, and the type of the cells within the osteon will alter as bone is reabsorbed and formed (Kim *et al.*, 2015). Osteocytes occupy various areas known as lacunae that are dispersed throughout the bone lamella. Osteocytes are matured bone cells that are derived from osteoblasts.

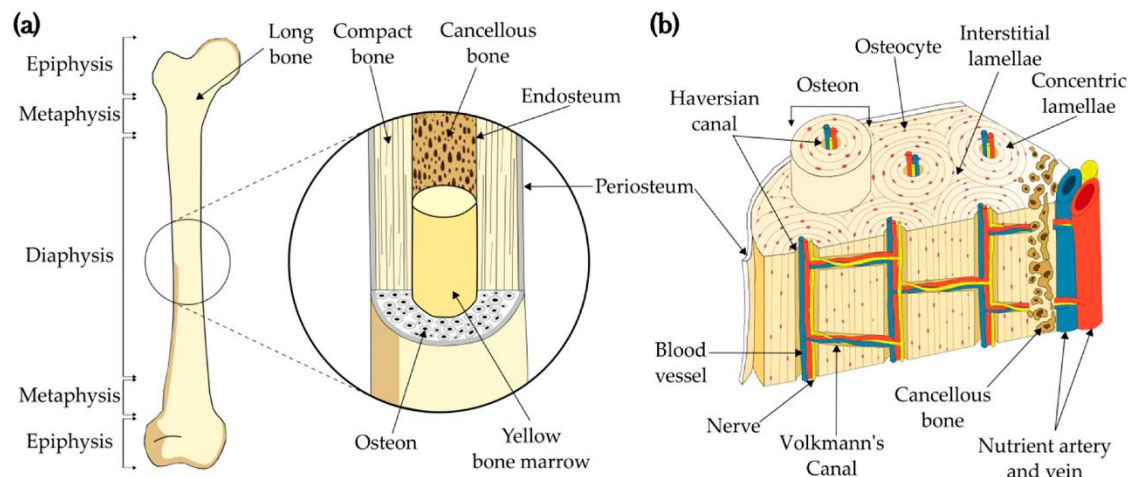


Figure 1-1: Structure of bone showing a) long bone and (b) cortical bone formation. Image taken from Robles-Linares, J.A.; Ramírez-Cedillo, E.; Siller, H.R.; Rodríguez, C.A.; Martínez-López, J.I. Parametric Modeling of Biomimetic Cortical Bone Microstructure for Additive Manufacturing. *Materials* **2019**, *12*, 913. <https://doi.org/10.3390/ma12060913>

Cancellous bone/trabecular bone is the internal tissue of the skeletal bone and is an open porous network. Cancellous bone has a larger surface-area-to-volume ratio than cortical bone and is substantially less dense and not as organised (Hart *et al.*, 2017). Due to this, cancellous bone tends to be weaker and more flexible rather than rigid and dense. Cancellous bone is typically found at joints in the core of the vertebrae and at the extremities of longer bones. Because it contains red bone marrow, cancellous bone is extremely vascular and frequently serves as a location for the generation of blood cells. The main functional area of cancellous bone is the trabecula. The trabecula is a small tissue element that supports areas of the body and organs. Trabecula is usually composed of collagenous tissues and cancellous bone is formed from grouping trabeculated bone tissue together. Overall, cancellous/ trabecular bone accounts for 20% of total bone mass but has ten times the surface area of cortical bone (Doblaré, García and Gómez, 2004).

## 1.2 Bone Composition

Bone is a strong, mineralised connective tissue that is dense and calcified. Minerals, organic matrix, cells, and water make up the majority of bone tissue. The mineral (inorganic) portion makes up around 65%, the organic matrix makes up about 35% and is mostly made up of collagen fibres, while the rest of the bone tissue is made up of cells like osteoblasts and osteocytes. Osteoclasts and bone lining cells, for example, are involved in the production and mineralisation of bone (Florencio-Silva *et al.*, 2015).

### 1.2.1 Inorganic Matrix

Minerals, primarily calcium and phosphate ions that join together to create hydroxyapatite ( $\text{Ca}_{10}(\text{PO}_4)_6(\text{OH})_2$ ), make up the inorganic composition of bone tissue (the mineral) (Shaker and Deftos, 2018). Hydroxyapatite makes up at least 90% of the total mineral weight in bone tissue. The mineral matrix begins as an unmineralised osteoid, which is later mineralised by osteoblasts secreting vesicles containing alkaline phosphatase, which cleaves phosphate groups and serves as calcium and phosphate deposition foci. The vesicles then break, forming a crystal growth centre (Bottini *et al.*, 2018).

Osteoblasts create the bone mineral hydroxyapatite in organised groups of linked cells, which is deposited in a carefully regulated manner into the organic matrix, generating a strong and dense mineralised tissue.

### 1.2.2 Osteoblasts and Osteoclasts

Osteoblasts make up 4-6% of all bone cells and are found on the surface of the bones. These cells are responsible for the bone forming function and show characteristics of protein synthesising cells. Osteoblasts are terminally differentiated products of mesenchymal stem cells (MSC's). Stem cells have the ability to differentiate into a variety of cell types (Maher *et al.*, 2015) which can lead to the creation of pre-osteoblasts and the synthesis of restricted intercellular substances (Dallas, Prideaux and Bonewald, 2013). Finally, mature osteoblasts are in charge of osteoid production (extracellular matrix). Multinucleated cells, or osteoclasts, are large cells with 4 to 40 nuclei. Osteoclasts are bone resorption and bone removal cells that originate from the marrow monocyte-macrophage lineage (Boyle, Simonet and Lacey, 2003). Osteoclasts are the only cells in the body capable of absorbing extracellular bone matrix, a process critical for the healing of skeleton microdamage and the adaptability of bone to mechanical changes (Florencio-Silva *et al.*, 2015).

Human bone undergoes growth, modelling and remodelling during life. Bone remodelling is a complex process in which old bone is replaced by new bone in a cycle of three phases. The first phase is the initiation of bone resorption by osteoclasts, the second is the reversal period from resorption to new bone forming and the third phase is the bone formation by osteoblasts. Bone remodelling is an important occurrence in humans to allow for fracture healing and adaptation to mechanical use as well as for calcium homeostasis (Feng and McDonald, 2011). However, having an imbalance of bone resorption and formation can result in bone disease. A study by Khosla and colleagues (Khosla, Oursler and Monroe, 2012) explored a scenario in which excessive resorption by

osteoclasts without the matching amount of newformed bone by osteoblasts contributed to significant bone loss and osteoporosis, whereas the contradictory may result in osteopetrosis (Crockett *et al.*, 2011). Due to this, it is vital that there is equilibrium between bone formation and resorption, but this could depend on several factors such as hormones, biochemical stimulations, chemokines and cytokines.

### **1.2.3 Organic Matrix**

The organic matrix, which is made up of collagenous and non-collagenous proteins, accounts for about 35% of bone mass. The collagenous proteins represent about 90% of the bone matrix in which type I collagen is the most abundant protein. Bone's elasticity and tensile strength are due to the organic matter's unique three-dimensional structure. The remainder of the organic bone matrix (10%) is made up of non-collagenous proteins which play a vital role in bone remodelling. The non-collagenous proteins include; osteonectin, osteocalcin, osteopontin, proteoglycans and bone sialoproteins (Persikov, Ramshaw and Brodsky, 2005).

#### **1.2.3.1 Collagen**

Collagen is known as the main structural protein in the extracellular matrix of the bone and is the main component of connective tissues making it the most abundant protein in mammals (Di Lullo *et al.*, 2002). Over 90% of collagen in the human body is type I collagen mineralised with hydroxyapatite crystals (Hadjidakis and Androulakis, 2006) and it has a major role in bone health and function. Type I collagen is an interstitial matrix collagen organised in fibrils, which

are essential for the competence of several tissues. The effects of type I collagen have been studied by several researchers for years to understand how it works with a variety of cells, its effectiveness in different tissues and its overall role for bone health in the body of mammals. According to McNerny and collaborators (McNerny *et al.*, 2015), collagen crosslinking may have a critical role in bone health, particularly in bones with a high risk of fracture. Furthermore, a study conducted by Wang and co-workers (Wang *et al.*, 2012) explored if type I collagen may initiate and direct the formation of carbonated apatite mineral in the absence of any other extracellular matrix components.

### **1.2.3.2 Glycoproteins**

Glycoproteins are the most common non-collagenous protein components in bone matrix. Cell proliferation, hydroxyapatite deposition mediation, and cell control are all functions of these molecules, which are generated by the binding of carbohydrates to a protein core (Polo-Corrales, Latorre-Esteves and Ramirez-Vick, 2014).

### **1.2.3.3 Osteonectin**

Osteonectin is a calcium-binding glycoprotein found in bones. Osteonectin is a non-collagenous organic protein produced in vast quantities by osteoblasts and fibroblasts which initiates mineralisation and promoting mineral crystal formation. (Rosset and Bradshaw, 2016). Osteonectin is found in relatively large amounts in immature bone and promotes mineralisation of collagen, hydroxyapatite and



calcium due to the presence of glutamate bonds which enable the conjugation of ions and molecules.

#### **1.2.3.4 Osteocalcin**

Osteocalcin is a non-collagenous protein hormone found in bone similar to osteonectin. Osteocalcin is a hormone produced by osteoblasts that helps regulate the body's metabolism (Lee *et al.*, 2007). A study carried out by Neve and collaborators (Neve, Corrado and Cantatore, 2013) explores the role of osteocalcin and its role in human bone. They explain that osteocalcin is vitamin K-dependent and has a high affinity for calcium ions due to a unique arrangement of Gla proteins in its structure that aids in hydroxyapatite absorption. Their findings also imply that osteocalcin plays a beneficial role in bone metabolism and osteogenesis. More research is being done on the involvement of osteocalcin in the skeleton's endocrine functions. A study undertaken by Rossi and colleagues (Rossi *et al.*, 2019) investigated the ability of osteoclasts to affect the decarboxylation of osteocalcin and glucose metabolism, as well as male fertility and cognitive skills, using animal models. Furthermore, a study led by Moser and co-researchers (Moser and van der Eerden, 2019) explains the functions of osteocalcin in human bone and the evidence that osteocalcin is not only involved in bone remodelling but also plays a vital role in physiological processes.

#### **1.2.3.5 Osteopontin**

Osteopontin is a phosphorylated glycoprotein found in a variety of tissues with a strong affinity for hydroxyapatite. Osteopontin plays a part in a number of critical

roles in the body, including immunological response, cell adhesion and migration, and carcinogenesis (Zhao *et al.*, 2018). Some studies, such as one carried out by De Fusco and co-researchers (De Fusco *et al.*, 2017), suggest that osteopontin has a contribution in pathogenesis of various disease states such as obesity and osteoporosis. Due to osteopontin being a protein primarily expressed in cells with effects on bone remodelling and because it is known as being one of the most overexpressed genes in the adipose tissue of the obese which contributes to osteoporosis. Furthermore, studies have suggested that osteopontin could play a role of a link between inflammation and cancer as osteopontin is a mediator of tumour-associated inflammation and facilitates metastasis (Lamort *et al.*, 2019).

#### **1.2.3.6 Bone Sialoprotein**

Bone sialoprotein is a component of mineralised tissues such as bone, cementum and dentin. Bone sialoprotein is a component of the bone extracellular matrix and studies suggest that it constitutes approximately 8% of all non-collagenous proteins found in bone and cementum. Whilst the function of bone sialoprotein in these mineralised tissues remains unknown, studies have suggested that bone sialoprotein can act as a nucleus for the formation of hydroxyapatite crystals (Hunter and Goldberg, 1994). Furthermore, additional roles of bone sialoprotein are angiogenesis and the potential protection in cell lysis (Ogata, 2008).

### **1.2.3.7 Proteoglycans**

Proteoglycans are a significant protein component of the extracellular matrix, consisting of protein molecules linked to long sequences of polysaccharides and glycosaminoglycans. The major function of proteoglycans is to maintain structural integrity as well as acting as a local reservoir for cytokines and growth factors and as mediators of cell-signalling pathways (Kram and Young, 2013). Proteoglycans are potential nucleators for the precipitation of hydroxyapatite in human bone due to their presence in an osteoid (Blair *et al.*, 2017).

## **1.3 Bone Formation**

Osteogenesis, also known as ossification, is the process of bone development and creation. It starts with bone replacing collagenous mesenchymal tissue, resulting in the creation of a primitive type of bone with randomly organised collagen fibres that is later remodelled into mature lamellar bone with regular collagen rings (Akter and Ibanez, 2016). This lamellar bone constantly undergoes remodelling by osteoclasts and osteoblasts. The intramembranous ossification and the endochondral ossification processes are the two types of bone development (Setiawati and Rahardjo, 2019).

### **1.3.1 Intramembranous Ossification**

Intramembranous ossification is a bone growth process in which undifferentiated mesenchymal stem cells' connective tissue membrane transforms into bone and matrix bone cells. An ossification centre forms in the connective tissue membrane

to start the process. Mesenchymal stem cells clump together and start to differentiate into specialised cells, some of which become capillaries and others become osteogenic or osteoblasts (Setiawati and Rahardjo, 2019). Osteoblasts are cells that are responsible for the mineralisation of the bone matrix and can release proteoglycan proteins that trap calcium ions. The unmineralised bone matrix composed of type I collagen and glycosaminoglycans is formed as a result of this process. The skull and mandible bones are produced at this period. During the sixth week of pregnancy, the mandible shows the first signs of intramembranous ossification of the skull (Long and Ornitz, 2013).

Within a few days, the osteoid is produced within the fibrous membrane and mineralised, prompting trapped osteoblasts to become osteocytes. When osteoblasts continue to deposit osteoid, the encased cells mature into osteocytes. Between embryonic blood vessels, which form a random network of trabeculae, the osteoid is laid down. As the bone matrix forms, trabeculae also form and connects to each other to create cancellous bone (Breeland, Sinkler and Menezes, 2021). At the end of the intramembranous ossification process, the formed cancellous/trabecular bone is substituted by cortical bone.

### **1.3.2 Endochondral Ossification**

Endochondral ossification is a process of bone development in which the tissue that will become bone is firstly formed from cartilage (Karaplis, 2002). Firstly, it is separated from the joint and epiphysis and surrounded by perichondrium which then forms the periosteum. Dependant on the location of mineralisation, this part of bone development can be divided into perichondral ossification and

enchondral ossification. Both types of ossification play important roles in the formation of long bones however, only enchondral ossification occurs in the formation of short bones (Setiawati and Rahardjo, 2019). Perichondral ossification begins in the perichondrium where mesenchymal stem cells from the tissue differentiate into osteoblasts, surrounding the bony diaphyseal before enchondral ossification, indirectly affects its direction (Dennis *et al.*, 2015).

Once the cartilage model has been established, cells from the centre and periphery can infiltrate it, generating primary and secondary ossification centres. These centres gradually develop in different directions, eventually replacing cartilage with bone as seen in figure 1-2 below.

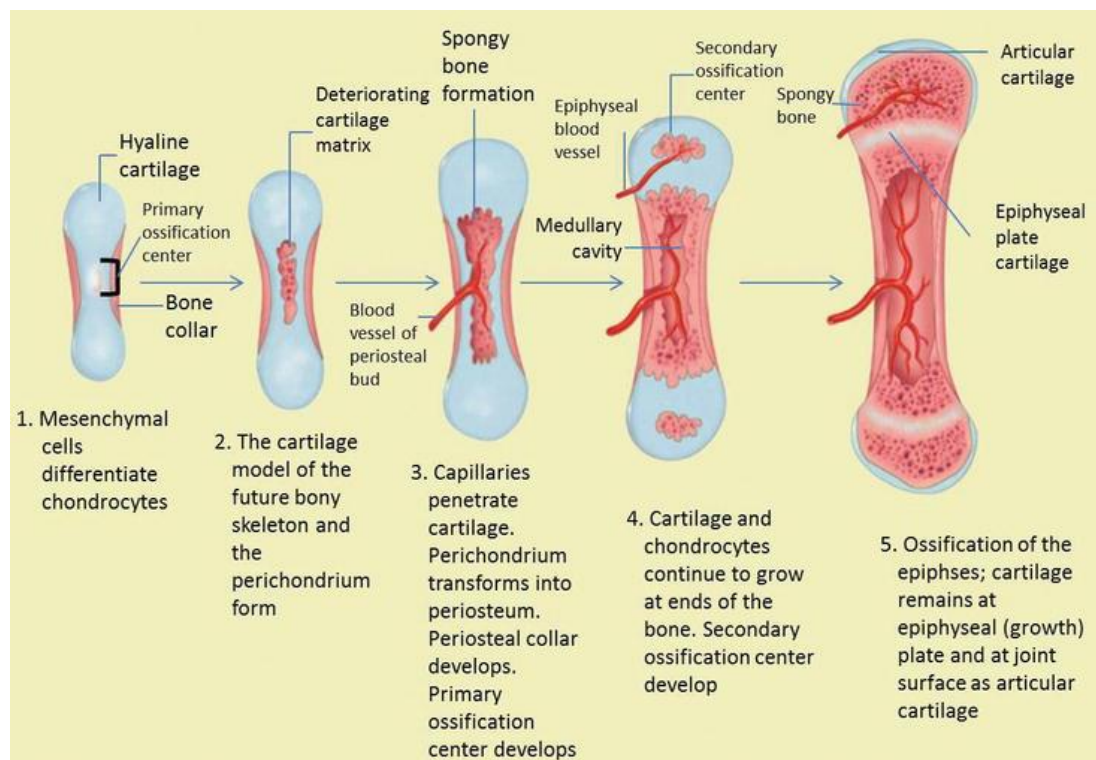


Figure 1-2: A schematic diagram showing the development of enchondral bone. Reprinted from: Rosy Setiawati and Paulus Rahardjo (December 14th, 2018). *Bone Development and Growth, Osteogenesis and Bone Regeneration*, Haisheng Yang, IntechOpen, DOI: 10.5772/intechopen.82452. Available from: <https://www.intechopen.com/chapters/64747> (Setiawati and Rahardjo, 2019).

Endochondral ossification occurs in the long bones at two separate sites: the diaphyseal (main) and epiphyseal (secondary). The diaphyseal site is where bone production begins, whereas the epiphyseal site, which is under autonomous control, is ossified later in the process. As a result, a layer of differentiation will occur between the two ossification centres, known as the epiphyseal plate, which may be found between the diaphysis and epiphysis (Breeland and Menezes, 2019). Metaphysis is an area which is formed due to the fusion between diaphysis and epiphysis that can occur during bone growth (Mencio and Swiontkowski, 2014).

At the primary centre area, chondrocytes segregate to allow local calcification to occur. Because of the slow diffusion and poor nutritional supply throughout the bone, chondrocyte death can occur (Stoddart *et al.*, 2018). Despite many theories connecting the death of chondrocytes with apoptosis, the most recent studies explain that hypertrophic chondrocyte death occurs because of a mechanism that is morphologically distinct from apoptosis but has not yet been characterised (Ahmed *et al.*, 2007). As a result of highly distributed vascularisation (which occurs due to the formation of thin walled lacunae being broken leaving holes for vascularisation), some of the cells go on to become osteoblasts. As a result of the deposition of both calcium and phosphate as hydroxyapatite with the help of other proteins and alkaline phosphatase expressed by osteoblasts, new bone matrix is created in the central area, resulting in the replacement of the majority of the central cartilage (Blair *et al.*, 2017).

At this stage, osteoblasts play the main role in new bone formation. They allow for the formation of trabecular bone on the cartilage remnant. Osteoclasts begin to degrade bone in the core area while bone growth continues to the two outer

ends, leaving a hole that is eventually filled with red bone marrow (Ortega, Behonick and Werb, 2004).

The secondary ossification also has the help of epiphyseal vascularisation in development. The secondary centres, on the other hand, do not resorb, and the bone in the epiphysis does not resorb in the future. Furthermore, the hyaline cartilage, which can be found commonly in the ribs, nose, larynx and trachea, is totally changed into bone during diaphysis, however in the epiphysis, it is not completely replaced into bone, leaving a trace of cartilage known as the epiphyseal plate, which will ossify in early adulthood (Emons *et al.*, 2009).

#### **1.4 Osseointegration**

Osseointegration has been defined in several ways by a variety of researchers through the years. It is believed that back in 1940, Bothe and his collaborators were the first researchers to implant titanium into an animal and observe how it fused to the bone (Buser, Sennerby and De Bruyn, 2017). However, osseointegration was later described by Gottlieb Leventhal in 1951 after placing titanium screws in rat femurs and stating how by the end of the 16 weeks the screws were so tight in the femur that when an attempt was made to remove it the femur was fractured (Leventhal, 1951). This led to the final discovery and naming of osseointegration in 1952 by physician Per-Ingvar Brånemark who implanted a titanium chamber in rabbit bone to study blood flow. At the end of the experiment when it came time to remove the chambers from the rabbit bone, it was discovered that the bone was so integrated to the implant that the chamber could not be removed, leading to the term 'osseointegration' (Branemark, 1983). As a result of Brånemark's work, implantation in dental medicine began in the

mid 1960's as he embarked on the first experiment placing dental implants into a human who had a cleft palate defect (Sandor, 2006).

Osseointegration is now seen as a highly common treatment mode which allows for the establishment of a direct interface between an implant and bone without the need for soft tissue intervention. It's the structural and functional link between living bone and the surface of a load-bearing artificial implant such as joint replacements, dental implants, or prosthetics (Jayesh and Dhinakarsamy, 2015).

Any lesion of the pre-existing bone matrix is known to induce direct bone healing in osseointegration, defects, and primary fracture healing. When the matrix is exposed to extra cellular fluids, non-collagenous proteins and growth factors are set free and activate bone repair (Wubneh *et al.*, 2018). Once bone repair is activated, osseointegration follows 3 stages. These are; the incorporation by woven bone formation, the adaptation of bone mass to load and the adaptation of bone structure to load, also known as remodelling (Parithimarkalaignan and Padmanabhan, 2013).

Implants have become a highly prevalent therapy in dentistry for both restoring missing teeth and correcting abnormalities for aesthetic reasons. As introduced by Brånemark in 1965, the favourable clinical performance of dental implants has been attributed to their firm osseointegration.

Bone regeneration related to dental implants in a healthy specimen is a complicated process that can take up to several weeks to occur. After implantation, bone regeneration is regulated by growth and differentiation factors that are released in the implant area (Shah, Thomsen and Palmquist, 2019). Bone regeneration is formed either on the implant's surface; known as contact



osteogenesis, or from the surrounding bone around the implant's surface; known as distance osteogenesis. The final step is bone remodelling which occurs by replacing immature bone with mature bone at the site of implant. This can provide mechanical stability for the implant insertion process (Alghamdi, 2018).

#### **1.4.1 The Success and Failure of Osseointegrated Implants**

Although osseointegration is thought to be the foundation of a successful endosseous implant, there are several elements that influence its success or failure. Firstly, the exploration of the bone-implant interface is important to understand as many studies have concluded that the strength of the interface between bone and implant increases soon after the implant placement (within 12 weeks). This is vital as the strength may be described as being related to the amount of bone surrounding the implant surfaces. Also, the biophysical stimulation and time allowed for healing of the implants may affect the strength of the bone-implant interface over time (Parithimarkalaignan and Padmanabhan, 2013).

Next, the implant compatibility is an important factor to explore as the implant needs to have biocompatibility properties to allow a good resistance and lack of toxicity to the body. Commercially, pure titanium has been widely used for several years as the material of choice for dental implants due to its resistance to corrosion which is down to the titanium alloys reacting with oxygen in the air to form titanium oxide which protects it from corrosion, its biocompatibility and mechanical properties (Özcan and Hämmerle, 2012).

The implant surface characteristics are also an important factor in determining the success and failure of osseointegrated implants. Especially in the oral region, the surface quality will determine the tissue reaction to the implant. The hardness of the implant relates closely to the potential stresses in the surface of the oral cavity which may result in increased corrosion rate and a higher chance of the implant wearing. The wear can be caused by the hardness of the material but also the surface roughness of the implant (Barfeie, Wilson and Rees, 2015).

These factors can heavily influence the osseointegration process which needs to be successful for functional implants. However, materials are always changing, and new technologies are always appearing so osseointegration properties are constantly being adapted to suit the implant's purpose. The main points to address in order to create osseointegration are; a minimal amount of remaining bone should be removed; the retention of the original bone should be maintained and the basic topography of the region should not be changed (Jayesh and Dhinakarsamy, 2015).

#### **1.4.2 Osteoconductive vs. Osteoinductive**

Osteoinduction is the process by which osteogenesis is stimulated and is commonly found in any form of bone healing process. Osteoinduction involves the stimulation of osteoprogenitor cells such as bone morphogenetic proteins, to develop into osteoblasts, which subsequently initiate the production of new bone. A bone graft material that is both osteoconductive and osteoinductive will not only act as a scaffold for existing osteoblasts, but it will also stimulate the creation of new osteoblasts, allowing the graft to integrate more quickly. In a bone healing

situation such as a fracture, the majority of bone healing is dependent on osteoinduction (Polo-Corrales, Latorre-Esteves and Ramirez-Vick, 2014).

Bone grafting is a surgical procedure which is commonly used in implants to replace missing bone or to repair bone fractures. Osteoconduction, osteoinduction and osteogenesis are the biologic mechanisms that provide the rationale for bone grafting to occur. All bone grafted materials should be osteoconductive.

Osteoconduction means that bone grows on a surface. Osteoconduction occurs when the bone graft material serves as a scaffold for new bone growth that is perpetuated by the native bone. Osteoblasts from the margin of the defect that is being grafted utilise the bone graft material as a framework upon which to spread and generate new bone (Dym and Pierse, 2011).

## **1.5 Craniofacial Reconstruction**

The craniofacial region encompasses the portions of the head that surround the brain, as well as the face and neck structures formed from the embryonic pharynx (Morriss-Kay, 2016). The craniofacial area is made up of a variety of tissue types, including bone, cartilage, muscles, ligaments, and skin, as well as important supporting structures like blood arteries and nerves (Visscher *et al.*, 2016). Many diseases, injuries, and deformities in the head, neck, face, jaw, and the hard and soft tissues of the oral region are treated through oral and maxillofacial surgery. In the United Kingdom alone, around 60,000 craniofacial reconstruction procedures are performed each year (Laub, 2015). Trauma, such as vehicle accidents, tumour removal surgery, or the correction of congenital deformities in

babies and children born with cleft lip and palate, necessitate these operations. Reconstructive surgery may be required in some cases to correct the conditions.

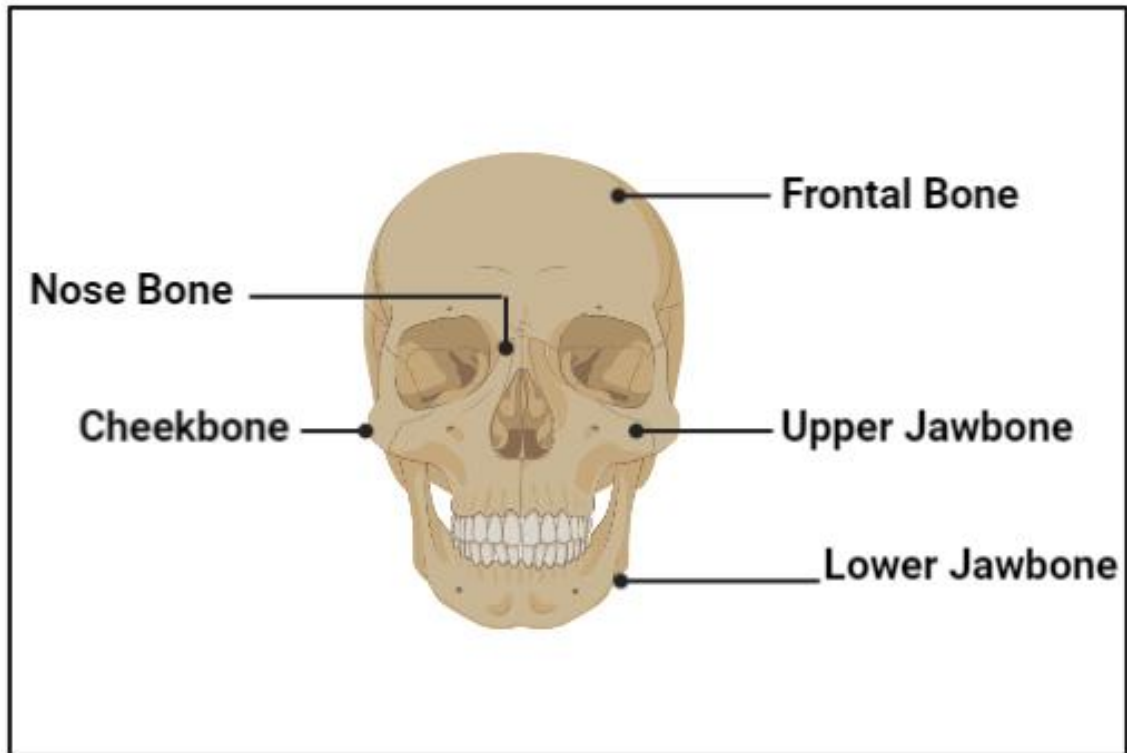


*Figure 1-3: The possible areas of craniofacial reconstruction in a human. The diagram was created using BioRender.com*

### **1.5.1 Congenital Disorders**

Alongside cleft lip and palate, the most common facial abnormalities young children are born with, there are several other conditions that require facial reconstruction surgery known as craniofacial dysostosis. Craniofacial dysostosis is used to describe a variety of problems involving the overgrowth and undergrowth of the head and face structures. Couzon syndrome, Apert syndrome, and Pfeiffer syndrome are examples of craniofacial dysostosis. Children suffering with these conditions will frequently have aberrant facial growth and will require surgery to reposition their facial bones forward (Tan *et al.*, 2016).

'LeFort osteotomies' are operations that relocate the facial bones forward and are numbered according to the level in the face where they are performed. LeFort I- exclusively moves the upper jaw's tooth-bearing portion. LeFort II advances the upper jaw's tooth-bearing section and the nose forward, while LeFort III moves the entire upper jaw, nose, cheek bones, and eye sockets forward (Kashani and Rasmusson, 2016). Prior to LeFort osteotomies there is a long period of orthodontic preparation in which the teeth are moved into positions that will make it suitable for surgery. During surgery, facial bones are moved and usually fixed in a suitable position by a combination of bone grafts and metal screws (Buchanan and Hyman, 2013).

Reconstruction of congenital defects, which account for major tissue loss in infants, present significant challenges in the process of providing suitable aesthetic and functional outcomes for the patients (Shand, 2018).

### **1.5.2 Traumatic Incidents**

Motor vehicle accidents, sports injuries, violent assaults, falls, and collisions during recreational activities are all common causes of traumatic occurrences. All of these reasons can severely damage the craniofacial region in the human body leading to the need for maxillofacial surgery to help correct parts of the bones and tissues that have been injured. Injuries to parts of the face can cause long term damage to a patient such as a disturbance in jaw movement, blindness and breathing difficulties which could, although rare, lead to death (Jose *et al.*, 2016).

Motor vehicle accidents are the most common cause of maxillofacial trauma and fractures in a vast number of countries around the world, according to studies. A study undertaken by Yadollahi and co-workers (Yadollahi, Behzadi Seyf-abadi

and Pazhuheian, 2019) looked at the various types, causes and incidents associated with maxillofacial fractures and found that motor vehicle collisions were the most common. However, recent studies, such as one carried out by Lello and associates (Lello, Allen and Haig, 2015), discussed how in recent years, over 60% of severe facial injuries are a result of domestic abuse and assaults. Furthermore, over 13,000 burns occur every year in England and Wales alone which can be serious enough to require craniofacial surgery including but not limited to, skin grafts, tissue grafts and bone replacement (Stylianou, Buchan and Dunn, 2015).

### **1.5.3 Cancers**

The craniofacial region can be significantly impacted by the effect of over 30 different types of cancers which can lead to deformation of the bony constructs in that part of the body. In removal of large cancerous tumours in the craniofacial region, defects in the mouth, throat or neck may need to be repaired. This is usually done by a skin graft if the area is small and compatible. However, to repair larger defects, more tissue may be needed which recent advances in facial prosthesis and reconstructive surgery offers patients to align and correct missing bone tissue and help with speech issues or swallowing issues that may have been caused by the removal of the tumour (Gou *et al.*, 2018).

## **1.6 Materials Currently In Use**

The reconstruction of bone defects following congenital disorders, traumatic incidents and the removal of cancerous tumours is a critical procedure requiring a suitable implant material which will offer the correct properties and functions,

including but not limited to, aesthetic restoration, optimum support, structural integrity and functional rehabilitation (Neumann and Kevenhoerster, 2009). A good material should also promote the formation of new bone as well as osteoconductive and osteoinductive properties. Furthermore, the suitable material should not cause pain, infection or any adverse reactions for the body as well as adhering to the composition and structure of the native bone tissue (Koons, Diba and Mikos, 2020).

The foreign body reaction occurs when any foreign material is implanted into the body and causes an inflammatory and fibrotic response. When a foreign object is implanted into a tissue, immune system cells become drawn to it and attempt to break it down. If the substance does not degrade, fibroblasts encircle it and establish a physical barrier to keep it isolated from the rest of the body. The cellular response breaks the contact between the implant and its target tissue, making long-term implantation of medical devices difficult (Carnicer-Lombarte *et al.*, 2021). The slow onset of this body-induced reaction, as well as its dynamic character (beginning with an acute inflammatory onslaught and progressing to a long-term fibrotic response), make it difficult to predict and test for during implant device design and development. Optimisation of implanted technology for good function over a period of days to weeks following implantation is a common subject of research. Clinical devices must have the ability to be implanted in human patients for years or decades, even though it is impractical to test new technologies for extended lengths of time at each phase. It is critical to examine the effects of foreign body reactions on both the implanted device and the surrounding tissue in order to improve bench-to-bedside translation of novel technologies (Xu and Siedlecki, 2007).

According to their mechanism, regenerative bone materials are divided into four categories: osteogenic materials, which directly stimulate bone cells to synthesise bone tissue; osteoinductive materials, which induce the differentiation of mesenchymal cells into osteoblasts, improving bone formation in orthotopic and heterotopic sites; and osteoconductive materials, which aid cell proliferation, migration, and the formation of new bone; osteo-promotive materials, which serve as a substrate for bone cells to grow on (Rodella, Favero and Labanca, 2011).

Tissue engineering and regenerative techniques for the reconstruction of the craniofacial region have received a lot of attention in recent decades. Although bone has the ability to grow on its own, when a significant lesion surpasses the tissue's regeneration capability, clinical intervention in the form of bone repair operations may be required (Smith *et al.*, 2015).

Bone grafting has been a technique used in the craniofacial reconstruction field for centuries. The first successful bone grafting procedure was documented in the 17th century by Dutch surgeon Job Van Meekeren, who transplanted a fragment of bone from a dog's skull into a cranial deformity in a human soldier (Fernandez de Grado *et al.*, 2018). Furthermore, in the 19th century, Van Merren reported of the first ever autogenous graft success. Allogenic grafts were also reported around the 19th century and by 2001 bone grafting had become so popular that there were more than 2 million procedures recorded in the world (Campana *et al.*, 2014).

Over the centuries, a persistent effort has been made in this field to identify new graft materials to offer promising developments of new implants for patients needing facial reconstruction surgery. Several methods have been implemented



in this field for many years to try and keep up with a cost-efficient, customisable, osteoconductive, readily available and durable properties (Meyer *et al.*, 2020).

### **1.6.1 Autologous Bone Grafts**

Autologous (or autogenous) bone grafts involve using bone from the same individual receiving the graft. The bones can be harvested from non-essential bones like the iliac crest region, but in craniofacial surgery, they are most typically harvested from the chin area and are obtained from a preserved bone flap that was removed during a prior procedure (Meyer *et al.*, 2020).

Grafts have been fundamental for regenerating and repairing bone tissue around the head and neck region. For bone regeneration, a variety of space-filling biomaterials have been tested, and the material chosen is mostly determined by the application site. Because of its osteogenic, osteoinductive, and osteoconductive properties, autologous materials have been used for bone regeneration since 1978 and are still considered the gold standard in bone transplants (Matassi *et al.*, 2011).

Many researchers, such as Fillingham and associates (Fillingham and Jacobs, 2016), have suggested that autologous bone grafts can be divided into non-vascularised and vascularised grafts to suit both cortical and cancellous bone regions. Several studies, such as one carried out by Yadla and colleagues (Yadla *et al.*, 2011) have explored the significance of the autologous bone grafting method and confirm why it is the most frequently used grafting method around the world due to its low infection rate. Due to the harvested graft originating from the same individual, it is believed to be a grafting approach free of immunological rejection, reducing external risks (Osorio *et al.*, 2020).

Autologous grafts, also referred to as autografts are known to be osteoactive materials, having both osteoinductive and osteoconductive properties allowing it to be able to promote the differentiation of mesenchymal stem cells into osteoblasts, resulting in bone formation (García-Gareta, Coathup and Blunn, 2015).

#### **1.6.1.1 Cancellous Autografts**

The most prevalent type of autologous bone graft is cancellous autografts. Despite ischemic conditions during transplantation, a large number of mesenchymal stem cells survive, helping to retain the osteogenic potential and ability to produce new bone from the graft (Bhatt and Rozental, 2012). Furthermore, the large surface area of a cancellous autograft aids improved revascularisation and graft assimilation into the host bone. Inflammation and hematoma form quickly in the early phases of autograft transplantation, with the recruitment of mesenchymal stem cells to generate fibrous granulation tissue, but the necrotic graft tissue is being removed by macrophages, generating neovascularisation (Wang and Yeung, 2017). Furthermore, osteoid are produced by osteoblasts around necrotic tissue during autograft integration, which happens at the same time as the production of new bone by accumulating hematopoietic cells within the transplanted bone. This process leads to the complete resorption and replacement of the graft (Roberts and Rosenbaum, 2012).

#### **1.6.1.2 Cortical Autografts**

Cortical bone autografts have a limited number of osteoprogenitor cells leading them to be mechanically supportive and to possess great structural integrity (Roberts and Rosenbaum, 2012). In contrast to the cancellous autograft, the

substitution of cortical autograft is triggered by osteoclasts after the formation of hematoma as well as the inflammatory response in the early phase of bone regeneration, since the revascularisation and remodelling processes are impeded by the dense architecture of the bone (Gross *et al.*, 1991). Following osteoclast resorption, the major method of incorporating the cortical autograft is to increase bone development over a necrotic core. However, depending on the state of the implantation site as well as the size and shape of the graft, this procedure can take many years (Goldberg and Akhavan, 2005).

### **1.6.2 Allogeneic Bone Grafts**

Allogeneic bone grafts, or allografts, are a common form of bone grafting material that are from one individual, usually a human donor and are transplanted into a different individual. As autologous bone transplants have several drawbacks, such as the requirement for a second surgical site and greater surgery time, allografts are considered as the best alternative especially for patients with poor healing potential (Goldberg and Akhavan, 2005). Allografts are considered osteoconductive materials in the same way that autogenous grafts are, however their osteogenic capacity is lesser (Kumar, Vinitha and Fathima, 2013). Allografts can be customised and therefore can be available in cortical and cancellous bone options. They can also be produced in a variety of sizes for augmentation procedures and are sterilised with approval by the Food and Drug Administration (FDA) although the risk of cross infection remains the most significant drawback after allograft implantation (Roberts and Rosenbaum, 2012). Allografts have been reported to be immunogenic and have a higher failure rate than autografts, which is due to the activation of major histocompatibility complex antigens (Wang and Yeung, 2017).

Although the specific mechanism of immune response in allograft incorporation is unknown, multiple studies have demonstrated that when immunogenicity is minimised by altering the allograft to narrow histocompatibility discrepancies, allografts are more tolerated (Goldberg and Akhavan, 2005).

#### **1.6.2.1 Cancellous allografts**

Cancellous allografts are the most commonly used types of commercial allografts and have been seen to be supplied mainly in the form of cuboidal blocks. Due to their mechanical properties and their poor healing promoting ability, cancellous autografts are mainly applied in spinal fusion augmentation and filler materials for cavitary skeletal defects (Khan *et al.*, 2005). In comparison to autografts, the incorporation process of allografts follows a similar pattern of events; however, osseointegration is predominantly slowed by the host's inflammatory response, which can result in the creation of fibrous tissue around the graft. Meanwhile, several years after transplantation, allografts might become entrapped and never totally resorbed.

#### **1.6.2.2 Cortical allografts**

Cortical allografts are mainly applied in spinal augmentation to fill large skeletal defects where immediate load-bearing resistance is needed (Orti *et al.*, 2016). Most commonly, frozen or freeze-dried products that are free of blood and marrow are transplanted into patients. Furthermore, the cortical allograft is incorporated through a process known as creeping substitution, similarly to the autogenous grafts, which is when the cortical bone is incorporated and mediated by osteoclasts as opposed to osteoblasts (Huang *et al.*, 2014). The osteoclastic

resorption initiates the cortical allografting process, which is followed by the creation of new bone via osteoconduction (Temple and Malinin, 2008).

### **1.6.3 Xenografts**

Heterologous materials, also known as xenografts are made from the bones of several animal species, with bovine bone being the most prevalent (Temple and Malinin, 2008). Bovine bone xenografts have been successfully used to treat a variety of bone abnormalities (Mardas, Chadha and Donos, 2010). The bone skeletal tissues are deproteinated to produce inorganic bone scaffolds. The organic components of the bone are normally extracted using ethylene diamine during the deproteination process (Thuaksuban, Nuntanaranont and Pripatnanont, 2010). Many authors have confirmed the osteoconductive properties of xenografts (Carlino *et al.*, 2008). However, according to the Food and Drug Administration (FDA), there is always a risk of transmission of Bovine Spongiform Encephalopathy (BSE) when utilising xenografts (Sogal and Tofe, 1999). BSE is a neurodegenerative disease of cattle which has been referred to more commonly as 'mad cow disease'. Commercial xenografts such as Peppen-P15 or Bio-Oss are organic-free composition grafts and because they are predominantly composed of calcium phosphate, their chemical characteristics are comparable to those of the mineral component found in natural bone (Sartori *et al.*, 2003). Several investigations have revealed that commercial xenografts, like the ones presented here, are often porous materials with porosity similar to that of human cancellous bone. Xenografts are employed in a range of situations, from minor bone defects in dentistry to more sophisticated surgical procedures like maxillary sinus augmentation (Mardas, Chadha and Donos, 2010) and the majority of cases show great promise in a clinical scenario in regards to bone

growth. However, there are ongoing ethical debates about xenograft materials that may prevent them being used in medical applications. A case study by Rodriguez and co-researchers (Rodriguez and Nowzari, 2019), investigated the long-term risks and late clinical complications of bovine-derived xenografts in patients that had been referred due to bone augmentation complications. The results of their case study showed a variety of concerns with the bone-derived graft materials such as implant failure, foreign body reactions, sinus and maxillary bone pathoses, displacement of the material, chronic inflammation and many more complications which affect the long-term safety of the xenografts.

#### **1.6.4 Alloplastic Grafts**

Alloplastic is a synthetic substance that's utilised to repair bone tissue and is the most frequently used type of bone graft in the implant industry due to its osteoconductive properties, making it compatible with the patient's own bone. They have been introduced in this industry to overcome the disadvantages of using natural bone substitutes such as autografts, allografts and xenografts (AlGhamdi, Shibly and Ciancio, 2010). Alloplastic grafts can be produced with varying physiochemical properties and can be customised with varying levels of porosity and pore sizes. Bioceramics, polymers, and biocomposites are three different types of alloplastic materials (Sheikh, Sima and Glogauer, 2015). Over the years, ongoing studies have been proving that these synthetic bone substitutes should be able to meet the optimal specifications of supporting the newly formed bone and should essentially be biodegradable (Giannoudis, Dinopoulos and Tsiridis, 2005).

### 1.6.4.1 Bioceramics

Bioceramics are ceramic materials that are biocompatible and used commonly in the medical and dental field for implant materials to replace hard tissue in the body such as bone and teeth (Best *et al.*, 2008). Bioceramics are classified as bioinert, bioactive, or bioresorbable depending on the type of bioceramics utilised and their interactions with tissue, as indicated in the flow chart diagram below (figure 1-4).

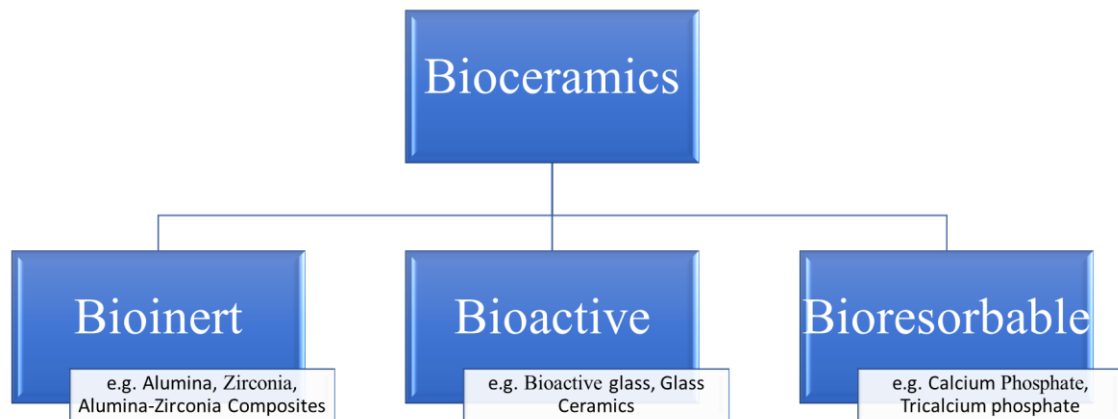


Figure 1-4: A flow chart showing the three main classifications of bioceramics; bioinert, bioactive and bioresorbable with examples of each group.

#### **Bioinert**

Zirconia ( $ZrO_2$ ) and Alumina ( $Al_2O_3$ ) are categorised as being bioinert. These materials have stable physiochemical properties which make good compatibility with the hard tissues. Therefore, when these materials are implanted into the body, there is little chance of there being a physiological reaction as well as no chance of there being an immunological rejection by the tissue (Kumar, Dehiya and Sindhu, 2018). The bioinert materials also have good strength to resist

fractures and they are applied as a structural-support implant in places such as bone plates and bone screws (Hench and Wilson, 1993). Zirconia has been used as an implant material since the early 1960s, and alumina was first used as an implant material in the early 1970s. Both alumina and zirconia have predominantly been used in dental applications, bone spacing implants and in orthopaedic joint replacements (Jayaswal *et al.*, 2010). With the increasing usage of both alumina and zirconia implants, a desire for a novel material with the combined characteristics of  $\text{Al}_2\text{O}_3$  and  $\text{ZrO}_2$  arose. This novel material should have the biocompatibility of both alumina and zirconia, as well as the strength of  $\text{ZrO}_2$  and the long-term *in vivo* stability of  $\text{Al}_2\text{O}_3$  (Apratim *et al.*, 2015). To overcome all the present limitations, new  $\text{ZrO}_2$  -  $\text{Al}_2\text{O}_3$  composites have been studied and investigated to find better properties for implant materials. These composites have shown to be less prone to ageing than  $\text{ZrO}_2$  and to have a higher fracture toughness than  $\text{Al}_2\text{O}_3$  (Sequeira *et al.*, 2017). There are two different composites containing two possible compositions of zirconia and alumina. If the composite has a richer side of  $\text{ZrO}_2$  it is known as an Alumina-Toughened Zirconia composite, on the other hand if the composite has a richer side of  $\text{Al}_2\text{O}_3$ , it is known as a Zirconia-Toughened Alumina composite. Both of the types of composites display higher mechanical property values of toughness, hardness and strength than zirconia or alumina alone (Kurtz *et al.*, 2014).

### **Bioactive**

In 1969, the discovery of four-component glasses which could bond to living tissues was made by Hench (Hench, 2006). Bioactive materials have been used since the discovery. It was shown that it is possible for certain materials to evoke



a controlled action and reaction in the physiological environment (Shirtliff and Hench, 2003). Bioactive materials were being employed clinically in a number of dental and orthopaedic applications by the mid-1980s, including a variety of compositions of ceramics, bioactive glasses, glass-ceramics and composites (Fernandes *et al.*, 2018).

Bioactive materials have a positive effect on living tissues and have the ability to induce a response that can help in the regeneration and repair of body tissues (Kumar, Dehiya and Sindhu, 2018). A specific biological response is produced when a bioactive material enters the body which begins to form chemical bonds between the interface of the material and the body's tissue. Bioactive glasses (BGs) and glass ceramics are examples of bioactive materials. After decades of reviewing the work in this field, in 1993 Rawlings (Rawlings, 1993) described the key features and properties of BGs alongside glass ceramics. After extensive research, the BG concept was in the spotlight with the discovery of Bioglass® 45S5 which had extraordinary interfacial bond properties between implants and bone (Fernandes *et al.*, 2017). Bioglass® 45S5 is composed of 45 wt% SiO<sub>2</sub>, 24.5 wt% CaO, 24.5 wt% Na<sub>2</sub>O, and 6.0 wt% P<sub>2</sub>O<sub>5</sub> (Tulyaganov *et al.*, 2020). The 45S5 designation denotes glass with a SiO<sub>2</sub> content of 45% and a calcium-to-phosphorous molar ratio of 5:1 (Rahaman *et al.*, 2011). As low ratios of Ca:P do not bond freely to bone, the high ratio of Ca:P in Bioglass® 45S5 promotes the formation of apatite crystals which explains why it is ideal for a variety of biological applications due its comparable composition to hydroxyapatite, the mineral component of bone (Jones, 2013).

Traditional melt-quench or sol-gel techniques, in which a number of chemicals combine and solidify as glass, are used to make glass ceramics. The glass

structure is made up of a network of  $\text{Si}^{4+}$ ,  $\text{B}^{3+}$ , and  $\text{P}^{3+}$  ions, each of which contributes to the creation of intermediate oxides and network modifiers. The next step of controlled heat treatment is important to obtain glass crystallisation forming glass-ceramics (Fernandes *et al.*, 2017).

### **Bioresorbable**

Calcium phosphates (CaPs) are resorbable bioceramics and due to their outstanding biocompatibility, osteoconduction, and osseointegration capabilities, are frequently used in bone regeneration. CaP was commercially made available in the 1980s for the advantages it carries when assimilated by the human body, however, the history of CaPs in the medical field began in 1769 when the first evidence of its existence in bone tissue was discovered (Dorozhkin, 2012). Furthermore, the attempt to treat various diseases with CaPs dates way back to the 1790s with the original intention to treat rickets (Eliaz and Metoki, 2017). Since then, there has been a surge in interest in researching CaPs, especially in the field of bone tissue engineering. Various CaPs have been studied and used in bone regeneration and are displayed in table 1-1 with their abbreviations, chemical formulas and calcium phosphate : phosphorous ratios (Mehdawi and Young, 2015).

Tricalcium phosphate's (TCP) chemical formula is  $\text{Ca}_3(\text{PO}_4)_2$ . It is a porous calcium phosphate that occurs in two different crystalline forms known as  $\alpha$ TCP or  $\beta$ TCP which both have Ca/P molar ratios of 1.5 (Tamimi, Sheikh and Barralet, 2012). Studies, such as one by Zima and colleagues (Zima *et al.*, 2017), carried out tests on  $\alpha$ TCP to see how the effect of modified hydroxyapatite influences the physiochemical properties and cytocompatibility of  $\alpha$ TCP bone cements. The study led to show promising properties for  $\alpha$ TCP as a fracture site filler. Like

$\alpha$ TCP,  $\beta$ TCP has also proven popular for use as a filler and has shown positive and acceptable results in several clinical studies. A study by Rojbani and co-workers (Rojbani *et al.*, 2011) evaluated the osteoconductivity of both  $\alpha$ TCP and  $\beta$ TCP in animals and reported a higher degradation rate in  $\alpha$ TCP which allows more bone formation to occur in a shorter amount of time when compared to  $\beta$ TCP and sintered HA. Furthermore, studies, such as one carried out by Yuan and collaborators (Yuan *et al.*, 2010), have shown  $\beta$ TCP to have high osteoinductive potential and therefore  $\beta$ TCP has been highly favourable in the study and discovery of bone graft materials.

In contrary, many studies have presented drawbacks associated with the application of TCP such as the production of fibrous tissue rather than bone during the healing process post-surgery, as well as the lack of mechanical strength of TCP as a whole (Jeong *et al.*, 2019).

Table 1-1: Various types of calcium phosphates with their abbreviations and chemical formula are arranged in order of ascending calcium (Ca) to phosphorous (P) ratio.

| Name                                     | Abbreviation  | Chemical Formula   | Ca:P Ratio |
|--|---------------|--|------------|
| Monocalcium phosphate monohydrate        | MCPM          | $\text{Ca}(\text{H}_2\text{PO}_4)_2 \cdot \text{H}_2\text{O}$    | 0.5        |
| Dicalcium phosphate dihydrate (brushite) | DCPD          | $\text{CaHPO}_4 \cdot 2\text{H}_2\text{O}$                       | 1.0        |
| Dicalcium phosphate anhydrate (monetite) | DCPA          | $\text{CaHPO}_4$   | 1.0        |
| Octacalcium phosphate                    | OCP           | $\text{Ca}_8\text{H}_2(\text{PO}_4)_6 \cdot 5\text{H}_2\text{O}$ | 1.33       |
| $\beta$ -Tricalcium phosphate            | $\beta$ -TCP  | $\text{Ca}_3(\text{PO}_4)_2$                                     | 1.5        |
| Amorphous calcium phosphate              | ACP           | $\text{Ca}_3(\text{PO}_4)_2 \cdot n\text{H}_2\text{O}$           | 1.5        |
| $\alpha$ -Tricalcium phosphate           | $\alpha$ -TCP | $\alpha\text{-Ca}_3(\text{PO}_4)_2$                              | 1.5        |
| Hydroxyapatite                           | HA            | $\text{Ca}_{10}(\text{PO}_4)_6(\text{OH})_2$                     | 1.67       |
| Tetracalcium phosphate                   | TTCP          | $\text{Ca}_4(\text{PO}_4)_2\text{O}$                             | 2.0        |

Hydroxyapatite (HA) is a naturally occurring mineral type of calcium apatite with the formula of  $\text{Ca}_{10}(\text{PO}_4)_6(\text{OH})_2$ . It accounts for almost half of the weight of the bone and has excellent osteoconductive and osteointegrative capabilities (Eliaz and Metoki, 2017). In human bone, HA is present in combination with other common ions such as  $\text{F}^-$ ,  $\text{CO}_3^{2-}$  or  $\text{Na}^+$ . Owing to its chemical similarities to natural bone, HA is frequently employed as a bone substitute (Kattimani, Kondaka and Lingamaneni, 2016). HA can be synthetically manufactured as well as produced in different forms such as in a porous non-resorbable form, a solid non-resorbable form or a resorbable non-ceramic and porous form (Sheikh, Sima and Glogauer, 2015). The synthesis of the HA form and shape is aided by heat. Work carried out by Sheikh and co-researchers (Sheikh, Sima and Glogauer, 2015) investigated how applying a high temperature during the production process can result in the formation of a non-resorbable sintered dense form of HA. However, the development of resorbable porous HA may be caused by a lower fabrication temperature. Furthermore, several studies have been undertaken to test the biological effect of HA in the healing of bone defects as an implant material. These studies all showed promising clinical results such as one carried out by Foster and co-researchers (Foster *et al.*, 2016), which studied the effects and complications of utilising HA as a filler for the correction of bone defects in patients undergoing retromastoid craniectomy (a surgery to remove part of the skull to relieve pressure in that area) procedures. The study concluded that HA was successful in offering a positive alternative to titanium cranioplasty. The use of HA in the field of tissue engineering and craniofacial reconstruction offers a number of benefits and drawbacks. Due to its biological features, such

as biocompatibility, bioactivity, osteoconduction, osteoinduction, and osteointegration, HA has been widely used as an artificial bone substitute (Kattimani, Kondaka and Lingamaneni, 2016). With a Ca:P ratio of 1.67, HA is one of the most stable and less-soluble calcium phosphate bioceramics (Dorozhkin, 2009). Furthermore, HA only contains calcium and phosphate ions which is why there have been no adverse local or systemic toxicity reported in any study using HA biologically. Further studies have also proven that the surface of HA supports the adhesion of osteoblastic cells and promotes growth and differentiation (Ohgushi *et al.*, 1993). Brittleness, low tensile strength, and fracture toughness are some of the downsides of HA. Because of its low mechanical qualities, HA cannot be used in bulk for load bearing applications (Family *et al.*, 2012). Moreover, research has shown that pure HA is low in viscosity and has proven to be difficult to make complex shapes with, which is why a lot of additive manufacturing techniques have been adapted for the use of HA (Garagiola *et al.*, 2016).

#### **1.6.4.2 Polymers**

As many polymeric materials are biocompatible and biodegradable, they are frequently employed in bone tissue engineering. Polymeric materials are also extremely adaptable due to their controlled copolymerisation, implying that they may be manufactured with a variety of biodegradation rates (Song *et al.*, 2018). Polymethylmethacrylate (PMMA) is the most often used polymer in craniofacial reconstructive surgery nowadays. PMMA is made up of fine pre-polymerized resin particles combined with methyl methacrylate (Fernandes da Silva *et al.*, 2014), with low postoperative irritation, provides a protective and defect-filling substitute (Unterhofer *et al.*, 2017). A popular commercially available PMMA based polymer used for cranioplasty is Cranioplastic™ from DePuy Synthes, Raynham, MA, United States of America.

The polymerisation process of PMMA starts by the reaction between the benzoyl peroxide and N- dimethyl-p-toluidine. The polymerisation reaction is highly exothermic, and the temperature of the PMMA material can reach 80°C. However, It is currently well tolerated and supports bone formation on its surface allowing it to be osteoconductive (Fernandes da Silva *et al.*, 2014). A study by Abdo-Filho and colleagues (Abdo Filho *et al.*, 2011) explored the use of PMMA in craniofacial surgery and discussed its advantages. It was said that PMMA releases about 3-5% of monomer residues typically within 5 minutes of polymerisation and can decrease to 1.2% over a prolonged period of time. This suggests that the monomer's toxicity should vanish completely in around 4 hours. Furthermore, investigations have demonstrated that after PMMA implantation, no monomer fragments are produced and no PMMA toxicity occurs 48 and 78 months after the reconstructive procedure (Lu *et al.*, 2002).

A case study by Simon and associates (Simon *et al.*, 2014) looked at the challenging reconstruction of complex geometric shaped large cranial defects and the need for a light weight, adaptable and easy to fit implant. They explained that using PMMA for the implant was safe and easy as well as providing a better economic alternative. Their study reported no post-operative complications and excellent cosmetic results in the patient.

Some disadvantages of using PMMA for reconstruction of bony facial contour deficiencies after facial trauma should be discussed such as the possibility of infection and the lack of incorporation and vascularisation into adjacent bone. However, when prefabricated, PMMA still holds several advantages including but not limited to, shortening of operative times, complete polymerisation resulting in no permeability to body fluids and the improvement of physical properties of the implanted material (Abdo Filho *et al.*, 2011).

Polyetheretherketone (PEEK), a semi-crystalline thermoplastic with mechanical characteristics similar to human bone, is another extensively used polymer in bone tissue engineering. PEEKs characteristics such as its low Young's modulus (3-4 kN/mm<sup>2</sup>), its tensile strength (90-100 N/mm<sup>2</sup>) and its robustness, all properties that could provide better protection when used in craniofacial surgery (Lethaus *et al.*, 2012). Along with its mechanical properties, PEEK can be easily sterilised through gamma irradiation, which is an advantage to help reduce the risk of infection in the body. Furthermore, when comparing PEEK to PMMA, several studies recorded similar success rates and complications rates for cranioplasty using the two polymeric materials. The comparison between the two is not clear, however, some studies recorded a greater damage to the surrounding tissues with PMMA than with PEEK (Nguyen *et al.*, 2018).



As advantageous as PEEK is in the field of cranioplasty, it also has its own limiting drawbacks that need to be considered. PEEK is a bioinert material which is prone to deficient osteogenic properties, limiting its ability to be used in a variety of applications (Johansson *et al.*, 2016).

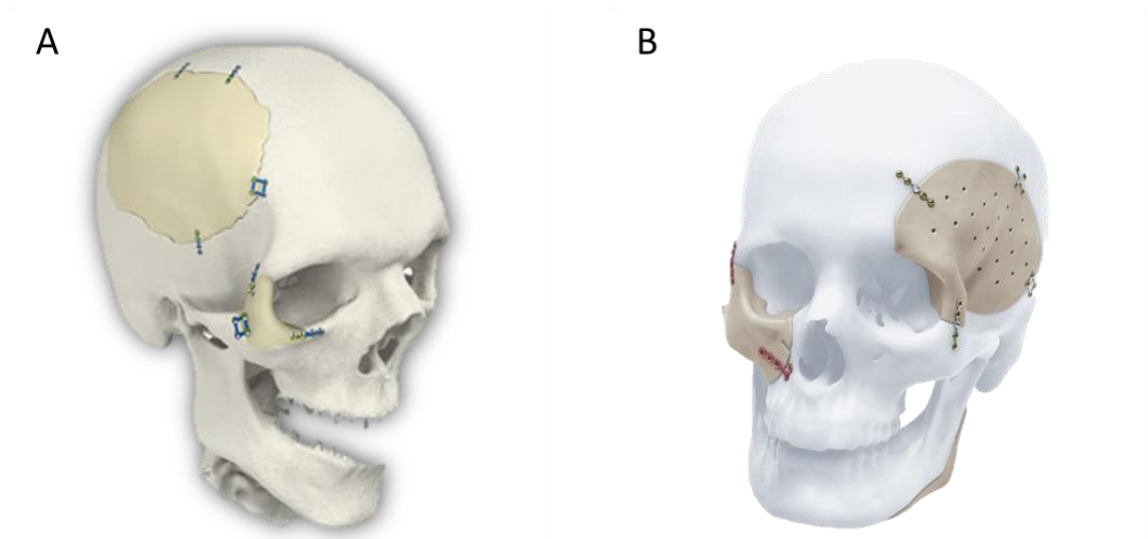


Figure 1-5: Image (A) shows a PMMA customised implant commercially available through Stryker and Image (B) showing a commercially available PEEK milled implant available through DePuy Synthes.

Image (A) reprinted from Stryker Corporation, Kalamazoo, MI, United States.

<https://cmf.stryker.com/products/pmma-customized-implant> with permission from Stryker. Image (B)

reprinted from DePuy Synthes Companies, Raynham, MA, United States.

<https://www.jnjmedicaldevices.com/en-EMEA/service-details/peek-milled-implants> with permission from DePuy Synthes.

Polylactic acid (PLA), polyglycolic acid (PGA), and polycaprolactone (PCL) are polyhydroxyesters that have also been explored for bone tissue engineering. PLA is used widely in clinical applications today (Borkotoky, Dhar and Katiyar, 2018) mainly due to its elastic modulus being similar to that of human bone, making it ideal for bone scaffolds and implants (Grémare *et al.*, 2018). PLA has the

advantage of biodegradability, however, an ideal biomaterial should have perfect biocompatibility, improved bioactivity, a customised degradation rate, non-toxic degradation products, and great mechanical performance, yet PLA does not meet all of these requirements (Murariu and Dubois, 2016). PLA has the disadvantages of limited cell adherence and a slow disintegration rate due to its hydrophobicity, as well as inflammation *in vivo* due to the acidic nature of the degradation products (Liu *et al.*, 2020). PGA is a hydrophilic, highly crystalline polymer that degrades at an advanced rate. PLA and PGA are mostly employed in bioceramics and allografts as binders or conjugators (Gentile *et al.*, 2014).

PCL is an aliphatic semi-crystalline polymer used often as bone scaffolds in bone tissue engineering due to its superior mechanical properties including high strength, toughness and elasticity. It is non-toxic and generally tissue compatible, and it degrades over a period of 2-3 years (Anderson and Shive, 1997). PCL as a polymer has also been studied as it is known for its osteogenic property. Many studies, such as one carried out by Shkarina and fellow researchers (Shkarina *et al.*, 2018) tested its use in conjunction with other bioceramics such as hydroxyapatite and tricalcium phosphate to form scaffolds and suggested good bone growth properties.

All polymers have varying mechanical and physical properties leading some to be more effective than others in different scenarios. Some polymers such as poly(DL-lactide) (PDLLA) are amorphous. They have a glass transition temperature above which they can flow but have no melting point. Table 1-2 below displays the main properties of the most commonly used, commercially available, polymers in bone tissue engineering and craniofacial reconstruction

surgeries. The table highlights their melting point ranges, the young's modulus and tensile strength of each polymer.

Table 1-2: Current commercially available polymers for use in craniofacial reconstruction surgery, highlighting their melting points, Young's modulus and tensile strength.

| <u>Polymer</u>                          | <u>Chemical Formula</u> | <u>Melting Point (°C)</u> | <u>Modulus (GPa)</u> | <u>Tensile Strength (MPa)</u> |
|---|-------------------------|---------------------------|----------------------|-------------------------------|
| <b>Poly(methyl methacrylate) (PMMA)</b> | $(C_5O_2H_8)_n$         | ≈ 160                     | ≈ 2.8                | ≈ 70                          |
| <b>Polyether ether ketone (PEEK)</b>    | $(C_{19}H_{16}O_3)_n$   | ≈ 343                     | ≈ 3-4                | ≈ 90-100                      |
| <b>Poly-lactic acid (PLA)</b>           | $(C_3H_4O_2)_n$         | ≈ 150-160                 | ≈ 2.7                | ≈ 37                          |
| <b>Poly(glycolic acid) (PGA)</b>        | $(C_2H_2O_2)_n$         | ≈ 225-230                 | ≈ 6                  | ≈ 60-120                      |
| <b>Polycaprolactone (PCL)</b>           | $(C_6H_{10}O_2)_n$      | ≈ 60                      | ≈ 0.4                | ≈ 16                          |

### **1.6.4.3 Biocomposites**

Biocomposites are materials made up of several different materials, such as a polymer-polymer combination, ceramic-ceramic, or ceramic-polymer. Combining more than one material can help to improve biological and mechanical properties of a scaffold to hopefully be a better substitute for allografts or autografts (Yunus Basha, Sampath and Doble, 2015). There are a variety of different biocomposites available, but a popular option is the self-reinforced polymers such as PLA and poly(lactic-co-glycolic acid) (PLGA) with calcium phosphate. A study by Sokolova and fellow researchers (Sokolova *et al.*, 2020) looked at the combination of PLGA with nano-hydroxyapatite (PLGA-nHA) to form spheres that were then thermally sintered to porous scaffolds for use in bone substitution. Their scaffold porosity was approximately 50% volume and *in vitro studies* demonstrated high cytocompatibility with the scaffolds. The PLGA-nHA composites were further investigated using DNA-loaded calcium-phosphate nanoparticles, which demonstrated good gene transfection capability using enhanced green fluorescent protein as a model protein which suggests potential enhanced bone growth around the implanted scaffold.

Biocomposites were created to address the disadvantages of utilising polymers and bioceramics separately by combining the flexibility of a polymer with the hardness of bioceramics to create a new material with greater qualities than the two components separately (Baino, Novajra and Vitale-Brovarone, 2015).

### 1.6.5 Metals

Metals and alloys are also commonly used materials for maxillofacial surgery but choosing which metals is also a challenge as they require specific mechanical properties and characteristics including tensile strength, elasticity and shear stress. The first alloy to be used for maxillofacial surgery was Vitallium composing of 65% cobalt, 30% chromium and 5% molybdenum. Vitallium has been used in dentistry since 1929 (Pacifici, DE Angelis, *et al.*, 2016). It has been well tolerated in oral and maxillofacial surgery and during the 1990s there were no significant reporting's of complications with the use of this alloy.

Gold and stainless-steel implants were also introduced relatively early. In facial nerve paresis-induced lagophthalmos, gold implants were specially employed in craniofacial surgery for middle ear and upper lid closure. The inability to close the eyelid, whether on a blink, gently or forcefully, is known as lagophthalmos (Gilardino, Chen and Bartlett, 2009). Inlays, on lays, crowns, bridges, periodontal splints, and post and cores are just a few of the dental prostheses that have been treated with gold (Bladen, Norris and Malhotra, 2012). However, due to the high cost of gold, it is no longer a popular choice in prosthesis, and these sorts of implants have been replaced by materials that are less expensive and more biocompatible (Saini *et al.*, 2015).

Stainless steel has adequate mechanical properties and bio-compatibility for most maxillofacial implant applications. It is also known to be relatively easy and cheap to manufacture and therefore is used in many implant devices. However, stainless steel is amongst those metals which are known to be problematic due

to their corrosion as well as potential allergic reactions from some patients due to the nickel present in stainless steel alloys.

The use of titanium in maxillofacial surgery was established in 1967, and it revolutionised the area (Saini *et al.*, 2015). Titanium has mechanical qualities that make it a good material for internal hard attachment, and when combined with its biocompatibility, it is deemed appropriate for use in this field. For these reasons, as well as overcoming any defects that were caused by previous metals used, titanium has become the gold standard material in use for maxillofacial reconstruction (Pacifici, De Angelis, *et al.*, 2016). However, just like all materials currently in use, titanium also has its drawbacks such as the release of traces of metal over time and the potential stimulation of an immunological response (Kim *et al.*, 2019).

### **1.7 Additive Manufacturing**

Three-dimensional (3D) printing, also known as additive manufacturing (AM), is a method for creating three-dimensional objects by layering basic materials such as polymers, ceramics, and metals. The 3D printable objects are usually produced from a computer-aided design (CAD) drawings, or from a computed tomography (CT) scan or even from a magnetic resonance image (MRI) (Paul *et al.*, 2018). The process of 3D printing has become increasingly popular over the last few years as it is an easily repeatable process, as well as accurate and cost-effective, allowing reliable production of customisable parts (Sidambe, 2014).

Despite the fact that AM techniques have been discussed and employed in many manufacturing activities such as the aerospace, construction, and automotive industries since the 1980s, it has only lately become a field of study in the

technological and medicinal applications (Gu *et al.*, 2015). In the medical field, 3D printing can allow for pre-operative surgical planning. Surgeons can use 3D models to assist them in studying a patient's impaired organs prior to operations as well as allowing them to explore the condition of the patient and giving them a better understanding in comparison to a 2D image. This alone could shorten the operation time and ultimately improve the outcome of the operation for the patient and the surgeon (Paul *et al.*, 2018).

Throughout the medical field, the 3D printing process begins with an anatomical scan using an MRI or CT image. Following that, the scan is transformed into a standard tessellation language (STL) file to allow the creation of the model layer by layer to achieve its final structure. The suitable printing method is chosen based on the application's objective. The material will need to undergo sterilisation before implantation to prevent any unwanted reactions post-implantation. Sterilisation techniques could include carrying out the production of the implant material in aseptic standards or simply sterilising in alcohol and under UV light, which was the chosen method used in this study. This technique was chosen due to its simplicity to reproduce in larger quantities, as well as the cost of the alcohol used and the availability of the UV light. Another method for sterilisation is gamma irradiation which has been used over the last 40 years as one of the most common methods to eliminate microorganisms from medical devices and bone grafts (Harrell *et al.*, 2018). Amongst a variety of advantages for the use of gamma irradiation, there has been ongoing concerns surrounding the exposure of gamma rays and the effect on patients.

Ethylene oxide (EtO) is also used commonly for sterilisation in the medical field as the advantages include high efficiency to destroy resistant microorganisms,



working under low temperature and not being corrosive to metals, plastics and rubber materials. However, disadvantages of using EtO are important to consider. These include a detrimental hazardous effect on personnel handling it as acute exposures to EtO gases can result in respiratory irritation and lung injury as well as other side effects. Furthermore, chronic exposure has been associated with the occurrence of cancer, reproductive effects and neurotoxicity. Aside from health concerns, EtO sterilisation has lengthy cycle times and is expensive to run often (Lewis *et al.*, 2011).

The three main strategies that can benefit from 3D printing in the medical field are reconstruction, rehabilitation, and regeneration. Reconstruction processes, such as tissue grafting, is the main procedural approach for plastic surgery. The use of 3D printing in plastic and reconstructive surgeries has become very popular in the hope of helping to restore normal aesthetics and symmetry with patients with mandibular defects, craniosynostosis, tumours or complex syndromes (Dumas *et al.*, 2019). One sector that has been heavily influenced by the recent developments in 3D printing is the craniofacial region. Evolving 3D printing technologies have enabled more effective and personalised treatments of complex craniofacial defects (Tao *et al.*, 2019). Rehabilitation involves prosthesis with complex structures being created to replace previous damaged tissues to enhance the aesthetics for the patient. Finally, in regards to tissue regeneration, 3D printing allows the production of custom-fit scaffolds to restore various defects which could be related to the bone, muscle, skin or cartilage (Nyberg *et al.*, 2017). When in combination, these 3D printing strategies can aid in the development of personalised treatments for patients and allow acceptable

aesthetic and functional outcomes in the craniofacial reconstruction field (Gougoutas *et al.*, 2015).

### **1.7.1 3D Printing Materials and Techniques**

There are many examples of 3D printing techniques that are used frequently in the medical industry at present. Digital light processing (DLP), stereolithography (SLA), selective laser sintering (SLS), fused deposition modelling (FDM), inkjet bioprinting, extrusion bioprinting, and electron beam melting (EBM) are examples of these techniques.

Sterilisation is required for medical equipment and implants because the presence of microorganisms can result in life-threatening infections. Also, any substance that will come into contact with tissue must be biocompatible, that is, it must not be hazardous to living tissue or cause detrimental reactions in biological systems. Implants must be made of materials that recipients' bodies are likely to absorb. Corrosion resistance is also crucial, as the bodies' fluids can be quite corrosive over time. Further to this, implants need to stand up to heavy long-term use, therefore, these materials must be strong, durable and lightweight. Modern 3D printers, fortunately, are compatible with a variety of polymers and metals that suit these requirements. A few of the most regularly used 3D printed materials for the medical industry are listed below in table 1-3, highlighting the printing methods, applications and suitable materials.

Table 1-3: A summary of 3D printing techniques used for craniofacial reconstruction applications along with the suitable materials for each printing method.

| Treatment   | Printing Applications  | Printing Methods   | Suitable Materials  | References   |
|---|--|--|---|--|
| <b>Reconstruction</b><br>( <i>Tissue grafting</i> )                                   | <ul style="list-style-type: none"> <li>○ Surgical positioning</li> <li>○ Custom-fit implants</li> <li>○ Bone reconstruction</li> </ul>                       | <ul style="list-style-type: none"> <li>○ SLA</li> <li>○ FDM</li> <li>○ SLS</li> </ul>  | <ul style="list-style-type: none"> <li>○ PMMA</li> <li>○ HA</li> <li>○ PEEK</li> <li>○ BGs</li> <li>○ Titanium</li> </ul> | <ul style="list-style-type: none"> <li>• Tappa <i>et al.</i>, 2017</li> <li>• Han <i>et al.</i>, 2019</li> </ul>     |
| <b>Tissue Regeneration</b><br>( <i>Rebuild native tissue structure and function</i> ) | <ul style="list-style-type: none"> <li>○ Composite craniofacial tissues</li> <li>○ Scaffold regeneration</li> <li>○ Bone, skin, cartilage, muscle</li> </ul> | <p><b><u>Bioprinting</u></b></p> <ul style="list-style-type: none"> <li>○ Inkjet</li> <li>○ Extrusion</li> <li>○ SLS</li> <li>○ SLA</li> </ul> | <ul style="list-style-type: none"> <li>○ Gelatine</li> <li>○ Alginate</li> <li>○ Fibrinogen</li> </ul>                    | <ul style="list-style-type: none"> <li>• Shen <i>et al.</i>, 2020</li> <li>• Tarafder <i>et al.</i>, 2015</li> </ul> |
|   |  | <p><b><u>Acellular</u></b></p> <ul style="list-style-type: none"> <li>○ SLS</li> <li>○ FDM</li> </ul>  | <ul style="list-style-type: none"> <li>○ CaPs</li> <li>○ PCL</li> </ul>   |  |
| <b>Prosthetic Rehabilitation</b><br>( <i>Patient aesthetics</i> )                     | <ul style="list-style-type: none"> <li>○ Surgical guides</li> <li>○ Moulds for casting</li> <li>○ Printed prosthesis</li> </ul>                              | <ul style="list-style-type: none"> <li>○ FDM</li> <li>○ Inkjet</li> </ul>  | <ul style="list-style-type: none"> <li>○ PMMA</li> <li>○ PDMS</li> </ul>  | <ul style="list-style-type: none"> <li>○ Mills <i>et al.</i>, 2017</li> </ul>  |

### **1.7.1.1 Fused Deposition Modelling**

The most commonly used 3D printing process worldwide is FDM. To create a 3D construct, FDM printers use a thermoplastic filament that is heated to its melting point and then extruded layer by layer. Scott Crump created the technology behind FDM in the 1980s. Since then, several 3D printing companies have adopted comparable technologies under various names. FDM printers can handle several print heads, allowing them to print a variety of materials at once. Typically, one of the print heads in these multi-head printers has a supporting filament that can be readily removed or dissolved in water. FDM's most common printing material in most industries is acrylonitrile butadiene styrene (ABS), a basic thermoplastic that's found in many products. PLA, nylon, polycarbonate (PC), and polyvinyl alcohol (PVA) are some other common printing fibres. Because of their biocompatibility and biodegradability, lactic acid-based polymers such as PLA and PCL are also frequently used in medical and pharmaceutical applications (Tappa and Jammalamadaka, 2018).

In medicine, FDM is used to create individualised patient-specific medical devices such implants, prostheses, anatomical models, and surgical guidance (Mills *et al.*, 2017). Due to its accessibility and affordability, in the medical industry, FDM 3D printing is now most commonly utilised with plastics such as PEEK due to its biocompatibility and high-performance, making it suitable for the creation of dental implants (Han *et al.*, 2019). L-lactide/-caprolactone (PLC) and poly(-caprolactone)/bioactive glass (PCL/BAG), which are highly biocompatible with fibroblasts, are also key biocompatible polymers utilised to create scaffolds via FDM (Korpela *et al.*, 2013).

### **1.7.1.2 Extrusion Based Printing**

In this method, materials are extruded via a print head utilising pneumatic pressure or mechanical force. Materials are constantly put in layer-by-layer way, similar to FDM, until the desired shape is achieved. Because this method does not require any heating, it is most typically employed to create tissue engineering constructions containing cells and growth hormones (Tappa and Jammalamadaka, 2018). Bioinks are biomaterials that have been infused with cells and other biological materials and are utilised in 3D printing. This 3D printing approach allows for the accurate deposition of small units of cells while causing minimal cell harm.. This technology may be used to 3D print a wide range of materials with varying viscosities and high cell density aggregates. Bioinks for 3D printing usually contain natural polymers such as collagen (Rhee *et al.*, 2016), gelatin, alginate (Markstedt *et al.*, 2015), and hyaluronic acid, as well as synthetic polymers like as PVA and polyethylene glycol (PEG). These bioinks are commonly post-processed with chemical or UV crosslinking to improve the mechanical properties of the scaffolds. Depending on the type of polymer used in the bioink, various biological tissues and scaffolds can be generated (Tarafer *et al.*, 2015).

With this technology, many print heads holding different types of cell lines can be used to create a complex multicellular construct. A study carried out by Lee and co-workers (Lee *et al.*, 2014) used extrusion-based 3D printing to regenerate the auricular cartilage and fat tissue of an ear. They 3D printed using PCL and a cell-laden hydrogel as the main part of the construct, using PEG as the sacrificial layer for support. They explored chondrogenesis and adipogeneses of the cell-printed structure and concluded that 3D printing technology can be utilised for ear regeneration as it allowed significant tissue formation and satisfied geometry and anatomy expectations. Despite

all of this progress, bioprinting material selection and mechanical strength remain a serious challenge. Fabricating vascularisation within a complex tissue is still a difficulty that this technology hasn't solved (Askari *et al.*, 2021).

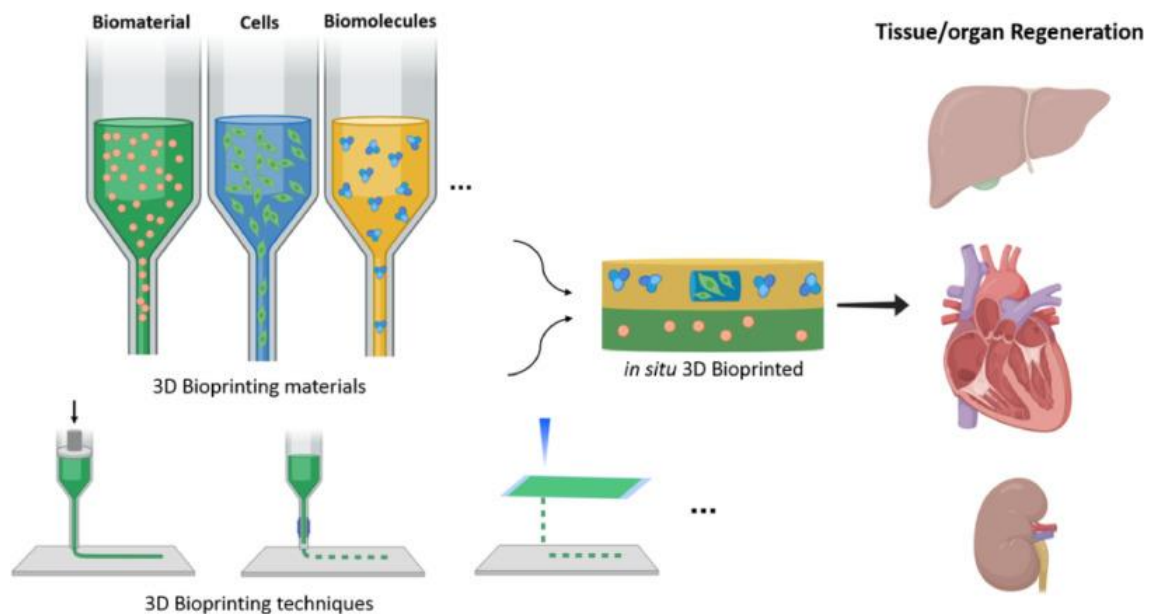


Figure 1-6: A schematic of extrusion based 3D bioprinting. Image reprinted from (Vanaei *et al.*, 2021) Vanaei, S., Parizi, M. S., Vanaei, S., Salemizadehparizi, F. and Vanaei, H. R. (2021). 'An Overview on Materials and Techniques in 3D Bioprinting Toward Biomedical Application' *Engineered Regeneration*. Elsevier, 2, pp. 1-18. Doi: <https://doi.org/10.1016/j.engreg.2020.12.001>

### 1.7.1.3 Electron Beam Melting

To create high-precision prints, the EBM technique uses high-speed electron beams to melt the metal powder layer by layer. This technology is particularly well suited to the manufacturing of complex orthopaedic implants. EBM produces parts in a vacuum environment, which increases melting efficiency, allows for stacking, and minimises the need for post-heat treatment, all of which lowers costs for the user. Materials commonly used in EBM 3D printing include titanium, cobalt and chrome alloys (Ni *et*

*al.*, 2019). Orthopaedic implants made with EBM technology operate exceptionally well and have porous structures comparable to those seen in natural bone tissue, resulting in improved osseointegration. This suggests EBM's potential use in other areas of tissue engineering and regenerative medicine (Lv *et al.*, 2021).

#### **1.7.1.4 Selective Laser Sintering**

SLS is a 3D printing technique that employs a laser, rather than an electron beam, as the power source to melt and fuse powders, which are then stacked layer by layer to build a printed item based on 3D model data (Gan *et al.*, 2020). SLS is widely utilised in the medical field. SLS may theoretically use any material that can be turned into powder and sintered with heat. In practise, seven commercially accessible materials are frequently utilised, including wax, polycarbonate, nylon and acrylic. In tissue engineering applications, bioceramics, like HA can also be sintered to create custom-fit implants for bone tissue restoration (Comesaña *et al.*, 2011). The mechanical properties, density, and surface texture of sintered objects can be affected by the type of laser used. Powdered materials for SLS should have the right particle sizes and flowability for spreading on the SLS machine's component bed. As well as its use in tissue engineering scaffolds, SLS is frequently employed in the fabrication of 3D devices for drug incorporation and delivery (Duan and Wang, 2011).

SLS provides the ability to create bone regeneration implants with the added benefit of allowing for the creation of complicated structures that are extremely strong once cured (Liu *et al.*, 2013). Unfortunately, a restricted range of materials can be employed due to the high laser temperature necessary during the curing process (Colasante *et al.*, 2016). PCL polymer, polyether ketone, hydroxyapatite (HA), and biocompatible

polymers such as polyetheretherketone (PEEK), poly(vinyl alcohol) (PVA), polycaprolactone (PCL), and poly(L-lactic acid) (PLLA) are among the materials that can be used in SLS 3D printing to create tissue engineering scaffolds (Wiria *et al.*, 2007).

#### **1.7.1.5 Stereolithography**

SLA was the first technology used in reconstructive surgery. The process involves using a light source, such as UV light or a laser to selectively polymerise a liquid, photosensitive resin (Mondschein *et al.*, 2017). In the early 1980s, Kodama (Kodama, 1981) published the first study on the fabrication of 3D structures using UV light to photopolymerise liquid-based resins. He devised two methods: one using a mask for each layer to do the exposure through, and the other using an optical fibre to selectively cure the photopolymer. Controlling fibre movement along the x and y axes resulted in a pre-set design. In 1986, Hull (Hull and Arcadia, 1984) added to this by using movement along the z-axis to create 3D scaffolds using UV light in a layer by layer technique. Light selectively polymerises the resin in an SLA system using a CAD model. The platform is lowered after the first layer is formed, and a new resin material is added to polymerise and build the second layer.

SLA has a number of advantages over other approaches. When many objects are being printed, each layer is printed at the same time, and the overall printing time is only determined by the structural thickness. Printing time is greatly reduced as a result of this. SLA can also perfectly regulate the scaffold's outward geometry and interior architecture due to a high resolution advantage of precision and the light source's narrow and tightly controlled width. As a result, a complicated scaffold can be readily



constructed. The biggest problem is that there are just a few biocompatible materials that can be used to make tissue engineering scaffolds using SLA (Colasante *et al.*, 2016).

Common photo-crosslinked macromolecules used as scaffolds in SLA 3D tissue engineering include poly(propylene fumarate) (PPF), photocurable synthetic polymer versions of poly(ethylene glycol)/poly(D,L-lactide) (PEG-PL) hydrogel, and gelatin methacrylate (GelMA). GelMA demonstrates high pore interconnectivity useful in the uniform distribution and proliferation of human umbilical vein endothelial cells in the human umbilical vein. PPF has been successfully used in rabbit cranial reconstruction; PEG-PL has been shown to promote human mesenchymal stem cell adherence and proliferation; and PPF has been shown to promote human mesenchymal stem cell adherence and proliferation (Gauvin *et al.*, 2012).

#### **1.7.1.6 Digital Light Processing**

A similar technique to SLA, DLP 3D printing relies on the use of light, typically in the UV region of 380-405 nm to cure photosensitive viscous resins. Each layer is projected by DLP, resulting in an illuminated plane where photopolymerisation can take place. As opposed to SLA, the minute the light hits the resin, it is not limited to a single spot. Instead, the entire layer is created at the same time. To produce the required form for each layer, patterning of the light is necessary. This is achieved with a “mask” produced by a digital micromirror device (DMD). It sits between the optical path of the UV-emitting lamp and the resin. Furthermore, A DLP projector has a DLP chip with millions of mirrors inside it. These mirrors are incredibly small, measuring less than a sixth of the width of a human hair. A single pixel is represented by each mirror. They

swivel back and forth, reflecting light as needed to produce a highly detailed grayscale image. The light is routed through a colour wheel that spins. To create the final projected image, the wheel synchronises with the DLP chip.

Thousands of micrometre-sized LEDs are used as light sources in modern DLP printers. Some DLP printers replace the DMD with an LCD screen, which has a significant price impact. A DLP projector has a DLP chip with millions of mirrors inside it. These mirrors are incredibly small, measuring less than a sixth of the width of a human hair.

It's only logical that the resins for SLA and DLP are similar, given their common basic way of functioning. Both require a photodegradable initiator material (or a combination of them) that creates highly reactive species when exposed to light (free radicals, cations, or carbene-like compounds). In both circumstances, the size of the monomer molecules will aid in determining the object's stiffness. Short chain monomers tend to make items that are more rigid, whereas long chain monomers are more flexible. The difference in speed between SLA and DLP is significant. SLA is often slow due to the very confined nature of its polymerisation technique. SLA 3D printers compensate for this weakness by sweeping the infill regions of an object faster than the outer shells. This can reduce time during the printing process, but to ensure the components to be more structurally stable, a UV-curing post-processing stage is frequently recommended.

DLP has the inherent advantage of being able to cure the entire surface of a layer at once. Because there is no distinction between the outline and the inside sections, post-

curing is not required. For the same 3D file, a 30-minute print on a DLP printer can take 4 hours on a SLA printer (Wu and Hsu, 2015).

DLP 3D printing typically employs a free radical photosensitive resin. The following are some of the reasons why cationic photopolymerization should not be used: firstly, cationic photoinitiator can barely function under 405 nm irradiation, some cationic photoinitiator could work under 405 nm, however, the price is too high to constrain its application and second, the DLP 3D printing light intensity is insufficient to photolysis the cationic photoinitiators, preventing photopolymerisation from occurring (Quan *et al.*, 2020).

A study conducted by Zhang and co-researchers (Zhang *et al.*, 2012) investigated the fabrication of a 3D extracellular matrix via DLP, to assess the difference between 2D and 3D cell culture systems. The lithography material used to create the microwell-array structure in this study was poly (ethylene glycol) diacrylate (PEGDA), a commonly used biomaterial. The scaffolds' ability to influence cell proliferation and cell–cell interactions was thought to be possible with this fine structure design with variable feature sizes (Liu and Yan, 2018).

### **1.7.2 Photopolymerisation**

Photopolymerisation occurs when a polymer is exposed to light, usually in the visible or ultraviolet range of the electromagnetic spectrum. These changes often lead to structural differences, for example affecting the hardness and stiffness of the material post-exposure to light. Printable materials in photochemistry-based 3D printing include primarily monomers, oligomers, and photoinitiators. Starting species are formed during the 3D printing process by a photochemical reaction in a photoinitiating system

under controlled light irradiation, and then react with monomer and oligomer units. As a result, light-induced polymerisation is ideal for 3D printing polymer-based items (Zhang and Xiao, 2018). Photopolymerisation-based 3D printing techniques have been a popular area of research for material scientists, engineers and polymer chemists due to the environmental, economic and production benefits (Chatani, Kloxin and Bowman, 2014).

A photoinitiator, monomer, and potential additives and fillers make up a typical photopolymer system. When photoinitiators are subjected to visible light, they produce reactive species. They decompose in the presence of UV, visible and IR light. Several commercial photoinitiators can be used in the process of 3D printing and all carry different advantages and disadvantages depending on the system they are used in.

There are two main systems used in photopolymerisation mechanisms for 3D printing: radical and cationic systems. Radical polymerisation is a method in which a polymer is formed by the successive addition of free-radical building blocks. The free radicals are usually formed by different mechanisms that usually involve separating initiator molecules. The initiating free radical then adds non-radical monomer units to allow the growth of a polymeric chain. (Nguyen *et al.*, 2020)

For DLP based printing specifically, a variety of initiators have been explored (Bagheri and Jin, 2019). Camphorquinones, benzophenones, and thioxanthenes are the most often utilised photoinitiators because they can perform hydrogen-abstraction or electron-transfer processes in the presence of co-initiators such tertiary amines (Fouassier *et al.*, 2010). Lithium acyl phosphinate (Lithium phenyl-2,4,6-trimethylbenzoylphosphinate) is a free radical photoinitiator that causes free radical

chain polymerisation when exposed to light. It is often coupled with GelMA to create a photopolymer that can be utilised in bioprinting. However, many studies have shown lithium acyl phosphinate to be cytotoxic to mammalian cells, therefore research is still taking place to advance it for wider uses (Nguyen *et al.*, 2020).

### **1.7.2.1 Methacrylate Based Photocurable Systems**

Methacrylate based monomers are often used for 3D photopolymerisation processes via a radical system. The three fundamental processes of radical systems are generation, initiation, and propagation. Under light irradiation, radical generation occurs, and a photoinitiator is responsible for converting photolytic energy into active species to commence photopolymerisation. Under light irradiation, the majority of commercially available photoinitiators undergo the Norrish type I $\alpha$ -cleavage reaction and create radical fragments. The incident light required to produce the cleavage varies in wavelength and intensity which changes depending on the chemical structures of the photoinitiators (Eibel, Fast and Gescheidt, 2018). Benzil ketals, such as 2-hydroxy-2-methyl-1-phenylpropan-1-one (Irgacure 1173) and 2,2-dimethoxy-2-phenylacetophenone (DMPA; Irgacure651), absorb light in the UV region, making them appropriate for SLA based 3D printing applications. Phosphine oxide containing photoinitiators, such as phenylbis(2,4,6-trimethylbenzoyl)phosphine oxide (BAPO; Irgacure 819) present lower energy levels leading to higher wavelengths, which is preferable for the DLP-based systems (Ligon *et al.*, 2017).

Methacrylate-based resins are compatible with different types of commercially available 3D printers and have been employed in a variety of applications, including 3D printing of shape memory polymers, a siloxane-based hybrid polymer network,

extremely stretchy photopolymers, and functional materials for biological applications. A study carried out by Gou and colleagues (Gou *et al.*, 2014) investigated the use of 3D printed PEG-derived hydrogels for the purpose of a liver-inspired detoxification device to replace the traditional methods of intravenously administered nanoparticles. Their 3D printed hydrogel scaffold allowed toxins to be collected and removed within the liver-biomimetic construct leading to novel alternative detoxification treatment platforms.

Although methacrylate-based resins have shown to be effective in 3D photopolymerisation, they do have some drawbacks. During the polymerisation process, these resins tend to shrink. Depending on the functionality of the monomer utilised, pure methacrylate resins tend to gel at low conversions. Usually, this event would result in a relatively limited flow of uncured resin. With each newly created bond, further photopolymerisation would result in an increase in shrinkage stress which is not ideal for these systems (Boddapati *et al.*, 2011). Shrinkage and associated stress can result in deformation during the layer-by-layer 3D printing process; hence the material of choice needs to have less shrinkage properties (Kim, Kim, J W and Kim, 2006). Another disadvantage of methacrylate free radical polymerisation is the oxygen inhibition. A review by Moad and co-workers (Moad, Rizzardo and Thang, 2008) establishes a solution to tackle this problem by suggesting the incorporation of additives such as tertiary amines to lessen the oxygen-oxygen inhibition in the 3D printing system. However, the use of tertiary amines could potentially discolour the cured monomer (Ganster *et al.*, 2008).

### **1.7.2.2 UV-Sensitive Photoinitiators**

As reported above, photopolymerisation reactions can be either radical or cationic. Initiation takes place in the presence of light, and a photoinitiator or photoinitiator system is responsible for converting photolytic energy into reactive species (Lalevée *et al.*, 2012). A variety of commercially available UV-light sensitive photoinitiators have been used in 3D printing applications, particularly in the medical field (Bagheri and Jin, 2019).

A study carried out by Fantino and co-researchers (Fantino *et al.*, 2016) explored the use of two different photoinitiators, Irgacure 819 (BAPO) and Irgacure 1173 (DAROCUR) to initiate the photopolymerisation of poly(ethylene glycol) diacrylate (PEGDA) hydrogels in a DLP fabrication process to obtain polymer nanocomposites that were thermally treated to induce the generation of silver nanoparticles within the printed polymer matrix, providing electrical conductivity. Another study conducted by Chan and associates (Chan *et al.*, 2010) investigated the use of another commercially available photoinitiator known as Irgacure 2959; 2-hydroxy-4'-(2-hydroxyethoxy)-2-methylpropiophenone to photopolymerise PEGDA hydrogels via SLA 3D printing. In their research, mouse embryonic fibroblasts were seeded homogeneously within the 3D printed matrix of hydrogels and the material promoted cell proliferation, improved cell viability and spreading, suggesting high biocompatibility.

### **1.7.2.3 Visible Light-Sensitive Photoinitiators**

Visible light can overcome some of the limitations imposed by high-energy UV light exposure while also lowering the danger of eye injury. When compared to UV light, visible LEDs are more environmentally friendly, as they do not emit ozone and have a

minimal thermal effect with long lifetimes (Bagheri *et al.*, 2017). Furthermore, lights with longer wavelengths are less harmful to living organisms making them a preferable option for biomedical applications including the use in dentistry (Zhang and Xiao, 2018).

These benefits have led to the emergent use of visible light in 3D printing applications by incorporating visible light-sensitive initiators. A study by Liska and co-researchers (Liska, 2002) reported the use of a biological photoinitiator system incorporating camphorquinone (CQ) which is a commonly used photoinitiator, particularly in dental composite fillings alongside a tertiary amine; ethyl 4-dimethylaminobenzoate (DMAB) to initiate the photo-polymerisation under visible light irradiation. However, this combined initiator system has its own drawbacks such as releasing a toxic effect on the material, as well as its tendency for discoloration of the amine-based co-initiator.

The usage of dyes incorporating naphthalimide derivatives (1,8-naphthalimide derivatives possessing a methacrylate functional group) as light-sensitive photoinitiators was recently described in a study carried out by Xiao and colleagues (Zhang and Xiao, 2018). The study explored a variety of combinations of derivatives to induce cationic or radical polymerisation under visible light at 457 nm. They reported that the combinations they explored had higher versatility and ultimate better performance than a CQ/amine photoinitiator system.

Moreover, while photoinitiators with organic structures are widely used in light curing applications, organometallic photoinitiators have also been extensively employed in laboratory investigations. Strong visible light absorption, relatively long-lived excited states, and appropriate redox potentials are among the photochemical properties of



these metal complexes (Ohtsuki, Goto and Kaji, 2012). These compounds can operate as photo-redox catalysts (by either an oxidation or a reduction cycle) producing active species and driving photopolymerisation systems such as photo-induced atom transfer radical polymerization (ATRP), photo-induced RAFT, and other polymerisation systems (Bagheri and Jin, 2019).

#### **1.7.2.4 Enhancement of Photocurable Materials**

As previously stated, numerous photocurable formulations with diverse chemical and mechanical properties have been used in a 3D printing application. Although created technologies show significant potential in 3D printing, they are unable to meet all the final product's needs. As a result, more inventive studies are needed to tune the final properties of 3D printed materials in order to further extend and broaden the breadth of 3D printing applications. One potential area of further exploration is to improve the biocompatibility of the 3D printable, photocurable formulation.

3D bioprinting is a term that refers to processes for fabricating biocompatible materials, functional tissues, and organs in three dimensions with precise control over cell deposition (Kabb *et al.*, 2018). The advancement of 3D bioprinting has piqued interest in tissue engineering and regenerative medicine applications (O'bryan *et al.*, 2018). However, because to their low biocompatibility, transparency, elasticity, and other properties, current photocurable resins are generally restricted for biological applications. In the uncured state, commonly used methacrylate-based resins have high degrees of irritancy or even cytotoxicity. When the unreacted monomer/oligomer (as a result of low conversions of these resins) comes into direct contact with the human body, it can potentially cause health problems. The generation of methacrylic

acid as a result of possible hydrolytic breakdown of the methacrylate-based complex can lower the local pH and have an unfavourable effect on the physiological characteristics (Lebeau, Efromson and Lynch, 2020).

The biodegradation of polymeric materials is also a crucial factor in the field of tissue engineering which can be impacted by the choice of photoinitiator used to create the resin. Furthermore, only a small number of commercially available photoinitiators exhibit adequate biocompatibility and water solubility, suggesting the desire to create specialised biocompatible, biological resins with specific biological, mechanical and chemical properties. A study carried out by Kowalska and colleagues (Kowalska, Sokolowski and Bociong, 2021) explores the current commercial and alternative photoinitiator systems used in the field of dentistry. The study describes the effects that alternating photoinitiators have on the values of biomechanical properties including the hardness, degree of conversion and biocompatibility of the material in question. Their research compared a variety of initiators to the commonly used CQ, to find an alternative that compensates the disadvantages of CQ such as its yellow appearance and poor biocompatibility. They concluded that alternative photoinitiators such as novel acylphosphine oxide used alongside CQ were able to improve the aesthetic properties as well as the degree of conversion of a dental resin.

It has been established that the small, photoinitiator component of composite composition has a significant impact on the biomechanical and chemical properties of the materials used. Therefore, finding the ultimate 3D printable resin, which unites adequate mechanical qualities and aesthetic appearance of restoration, is an ever-increasing field of research.

### 1.7.3 3D Printing in Tissue Engineering

It is important to highlight the significant attention that 3D printing has garnered in the tissue engineering field, specifically the opportunities it presents in the craniofacial reconstruction sector, offering a personalised approach for patients to restore and replace critical size defects in this region. Many studies have been carried out to look at patient-specific scaffolds tailored to site-specific defects and if they maintain the mechanical properties that are needed upon implantation into the body. Suska and co-researchers (Suska *et al.*, 2016) studied EBM, to reconstruct a patient's mandibular defect. In this case study, EBM was used to construct an anatomically correct titanium mandible, which was then implanted into a patient who had undergone severe osteotomy (bone cutting) after a squamous cell cancer was removed. The implant was created by mirroring the bone's opposite mandible into the resected area. After a nine-month follow-up, the case study demonstrated to be highly beneficial in the creation of patient-specific solutions for mandibular reconstruction, with an excellent aesthetic result and increased patient satisfaction.

The use of biocompatible, suitable polymers such as PMMA and PEEK in combination with 3D printing has been of great interest for the development of personalised, patient specific maxillofacial implants (Jindal *et al.*, 2021). In a study carried out by Han and colleagues (Han *et al.*, 2019), PEEK and carbon fibre reinforced PEEK composites were fabricated by the process of FDM printing. Both the PEEK and the carbon fibre reinforced PEEK materials displayed acceptable biocompatibility qualities, indicating that they might be used for bone grafting in tissue engineering.

There is significant emergence of custom-made implants in craniofacial reconstruction to aid in the restoration and replacement of critical size defects. As of yet, the use of metals is favourable as it offers optimum mechanical strength, biocompatibility and availability. However, many commercially available materials have recently been developed which are not metal such as polymeric materials available at companies such as Sculpteo (Sculpteo, United Kingdom) that can be used to limit the drawbacks associated with metal implants such as metal corrosion, late onset implant failure and the lack of osteoconductive and osteoinductive properties (Bijukumar, McGeehan and Mathew, 2018).

Recent developments in AM show great promise in advancing treatments for restoring and repairing bone defects in the craniofacial region. However, significant research into finding the optimum material to use in 3D printing approaches is ongoing and can potentially be used in fabrication of custom-fit, patient-specific implants in facial reconstruction surgery.

### **1.8 Clinical Need for New Materials**

In the field of biomaterials, continual advances have been made to best fulfil the optimal selection criteria for maxillofacial implant functionality, biocompatibility, aesthetics, and durability. Among all the different materials discussed, there are still studies carried out to overcome their weaknesses and to come out with a material which can be labelled as the “ideal maxillofacial prosthetic material” (Sapru, Mohan and Roy, 1999).

While the materials presented have remarkable qualities, they also have defects, and as a result, they are unable to fully restore a maxillofacial abnormality to its previous state. A new material could help reduce the risk of bone graft risks such as insufficient supply of donor bone, rejection of the bone-graft, infections in the transplanted bone or donor site, difficulties in creating the exact shape required as well as pain and long-healing processes. Metal implants such as the ones discussed above can have complications such as metal toxicity, rejection of the implant, deterioration of the surrounding bone allowing the implant to become loose and multiple operations for children who need their implants replaced with larger sizes as they grow. All of these variables can lead to the need for more surgeries and, in turn, to psychological disorders, particularly in young patients or those with persistent deformity (Thrivikraman *et al.*, 2017).

While researching a variety of new biomaterials, the exemplar material should be biocompatible and chemically stable. Aesthetically, the colour, texture, form, and translucency should match the neighbouring skin as well as the component to be replaced.

### **1.9 Aims and Objectives**

In this thesis, we are aiming to synthesise a light-curable, degradable polymer and adapt it for 3D printing applications to prepare custom-fit facial implants for use in craniofacial reconstruction surgery. This project's purpose is to address the varying limitations that are associated with the current techniques and materials used in the industry. The polymeric system studied throughout, referred to as CSMA-2 should

prove cytocompatibility, be degradable, mechanically strong and easily adaptable for 3D printing purposes.

The overall objectives for this project are:

1. The synthesis, purification and characterisation of a degradable polymeric system and incorporation of 2 comparable photoinitiators to allow the system to be light-curable and mechanically stable.
2. The incorporation of a varying ratios of a calcium phosphate filler into the polymeric system which will facilitate surface apatite formation and eventually promote osseointegration.
3. To assess the mechanical and physical properties of CSMA-2 and its composites to ultimately achieve the goal of 3D printing the material.
4. To computationally design and format models ready for 3D printing to provide precise control over the shape and size of the scaffolds to address the limitations and drawbacks current techniques hold.
5. To biologically explore the materials cytocompatibility abilities as well as angiogenesis assessment.

## **Chapter 2 : Synthesis and 3D printing of a light-curable degradable polymeric system (CSMA-2)**

## 2.1 Introduction

As previously discussed in Chapter 1: Introduction and Literature Review, new techniques are constantly under review to overcome limitations and disadvantages of current approaches in restoring craniofacial defects. As reviewed, there are many events that can severely affect the cranium region leading to the need in cranioplasty. The current gold standard technique is the use of autografts which is when a graft of tissue is taken from the individual's own body. However, there are multiple drawbacks associated with autografts as well as the limitation of the defect's size and complexity which can further complicate the material choices. The advancement of alloplastic materials, including as polymers, ceramics, and metals, has resulted in advancements in cranioplasty and tissue engineering (Nikolova and Chavali, 2019). Biodegradable polymers offer the possibility of tailored mechanical properties to allow scaffolds to be built in the desired shape to facilitate the correct tissue growth. They have drawn significant attention in the field of tissue engineering over the last few decades (Song *et al.*, 2018) and continue to be of interest to researchers in the field particularly for use in cranio-maxillofacial reconstruction surgery.

The material of choice, along with the defect size and shape, are the determining factors in the successful restoration of the affected region (Kumar *et al.*, 2016). In the field of craniofacial reconstruction, the discovery of the ideal material for the correction of bone defects which addresses both aesthetic and functional complications is yet to be achieved. In the realm of bone tissue engineering, it's particularly crucial to emphasise the importance of isosorbide-based dimethacrylic monomers as biodegradable and light-curable polymers. The composite in question should consist of an inorganic filler phase and an organic matrix which is fabricated as a result of free



radical polymerisation of dimethacrylic monomers. Such systems are highly advantageous due to exhibition of lower polymerisation shrinkage, reduced monomer leaching and relatively high chemical resistance (Soares *et al.*, 2017).

Bioceramics made of calcium phosphate are commonly employed in the field of bone regeneration, especially in orthopaedics and dentistry. CaPs are the natural inorganic minerals found in human bones; they consist of calcium cations and phosphate anions. Incorporation of certain CaP fillers in bone substitutes have been extensively investigated over the last century due to their good osseointegration, osteoconduction and biocompatibility (Eliaz and Metoki, 2017). It has been said that combining CaP powders with scaffolds is advantageous as they can allow control of the porosity as well as provide stable properties to reduce cytotoxicity (Pina *et al.*, 2019).

The type of CaP incorporated into a scaffold can influence its porosity which can aid in improving the angiogenesis and revascularisation of the composite. In this thesis, hydroxyapatite (HA) has been used as it has osteoconductive properties and high biocompatibility as well as bone-binding capability which will encourage bone growth (Bruno *et al.*, 2020).

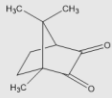
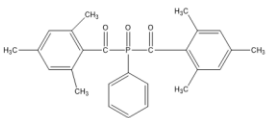
In this chapter, the synthesis of a light-curable polymeric system that has been under development for the purpose of 3D printing, custom-fit personalised scaffolds for use in craniofacial / maxillofacial surgery is explored. The material was previously investigated by Owji and co-researchers (Owji *et al.*, 2019), where the first variation of the polymer,(((3R,3aR,6S,6aR)-hexahydrofuro[3,2-b]furan-3,6-diyl)bis-(oxy))bis(ethane-2,1-diyl)bis((4-methyl-3-oxopent-4-en-1-yl)-carbamate) referred to as CSMA-1 was synthesised and characterised to be compared to

(((((((((((3R,3aR,6S,6aR)-hexahydrofuro[3,2-b]furan-3,6-diyl)bis(oxy))bis(ethane-2,1-diyl))bis- (oxy))bis(carbonyl))bis(azanediy))bis(methylene))bis(3,3,5-trimethylcyclohexane-5,1-diyl))bis(azanediy))bis(carbonyl))bis- (oxy))bis(ethane-2,1-diyl)bis(2-methylacrylate), referred to as CSMA-2.

As a starting material, bis(2-hydroxyethyl) isosorbide (BHIS) was used to make CSMA-2. The monomer has a methacrylate unit that is linked to isosorbide through a urethane linkage; the urethane coupling reaction between the isocyanate group and hydroxyl group allows synthesis of the final monomer. Potassium Carbonate ( $K_2CO_3$ ) is utilised in this reaction as a catalyst to speed up the process. It is easily removed prior to the final purification of CSMA-2 being achieved by column chromatography.

The addition of HA to CSMA-2 in varying ratios was investigated to find the optimum formulations for 3D printing. A range of 0-50 wt% HA was originally tested but could only be formulated by hand. The 3D printable composite polymer samples could reach a maximum of 10 wt% HA. Further to this, two photoinitiator systems were explored to find the best suited initiator for the composites (Table 2-1). Camphorquinone (CQ) and phenylbis(2,4,6-trimethylbenzoyl)phosphine oxide (BAPO) are both investigated within this study to decipher the optimum formulation for 3D printing of custom-fit facial implants.

Table 2-1: Description of the two photoinitiators used in the study, CQ and BAPO, with the appropriate nomenclature, abbreviation, chemical structure and molecular mass in g/mol.

| Abbreviation | Molecular structure   | Nomenclature  | Molecular mass (g/mol) |
|--------------|---|---|------------------------|
| <b>CQ</b>    |  | <b>Camphorquinone</b>                                     | <b>166.22</b>          |
| <b>BAPO</b>  |  | <b>Phenylbis (2,4,6-trimethylbenzoyl)-phosphine oxide</b> | <b>418.50</b>          |

As mentioned in Chapter 1, 3D printing technology has gotten a lot of attention in the last decade, especially in the medical field. Tissue and organ manufacturing, personalised implants and prostheses, and pharmaceutical research, including medication dosage forms, delivery, and discovery, are all examples of medical applications for 3D printing (Ventola, 2014). The use of 3D printing in medicine can provide many benefits such as the ability to design and create customised and personalised products, drugs and equipment as well as its cost-effectiveness and increased productivity (Schubert, Langveld and Donoso, 2014). Custom-made hearing aids, dentures, surgical models, orthopaedic implants, and prosthetic components are among the current medical applications of 3D printing (Wang *et al.*, 2017). Moreover, the exploration of 3D printing for use in tissue engineering to allow the fabrication of scaffolds that will be combined with bioactive materials and human cells to regenerate the tissue or organ is widely discussed in the field (Mabrouk, Beherei and Das, 2020). However, even with all the recent advancements in the field of 3D printing for tissue engineering, finding a suitable material for use remains the number one challenge.

For the purpose of craniofacial implants, the type of biomaterial employed in the implant's manufacturing determines its success. Ideally, an implant material should be inert, mechanically durable, and stable. Current materials previously discussed include metals, ceramics, polymers and composites. The use of all of these materials in facial implants carry potential drawbacks such as the risk of corrosion, being prone to infection, chance of rejection, laborious manufacturing methods, high-costs, difficult to mould and keeping the sterility (Tappa and Jammalamadaka, 2018).

Scaffold design in regenerative medicine is also considered a key element; direct printing produces 3D constructs with precise control over the exact size and complex internal structure of scaffolds. Subsequently, cell attachment and proliferation can be enhanced, and the mechanical strength of the construct can be tailored by controlling variables such as the porosity and addition of fillers (Turnbull *et al.*, 2018). The scaffold should serve to promote osteogenesis and angiogenesis as well providing mechanical support, allowing nutrient diffusion and cell infiltration through its pores (Bose, Roy and Bandyopadhyay, 2012).

Therefore, the current challenges in regeneration of bone defects can be addressed by exploiting 3D manufacturing approaches to ultimately overcome the issues associated with the current techniques.

The work in this chapter discusses 3D printing techniques using digital light processing, stereolithography, for the purpose of exploring the printability of CSMA-2 and its hydroxyapatite composites.

The vat polymerisation category of 3D printing includes both Digital Light Processing (DLP) and Stereolithography (SLA). An important difference between SLA and DLP is

the light source used to cure the material. DLP uses a digital light projector screen rather than direct UV light (Mukhtarkhanov, Perveen and Talamona, 2020). SLA is limited to the critical use of UV or visible light.

The process in DLP and SLA starts with a standard tessellation language (STL) file that is sliced on the provided software to allow the 3D model to be transformed into 2D slices that contain cross-section information. A layer-by-layer approach can be used to create the print based on these 2D slices. Firstly, the build platform is submerged in the tank and for DLP, a digital light projector screen is used to flash an image of each layer at once. In SLA, the UV or visible light laser beam traces the contours and solidifies the resin layer by layer (Huang, Qin and Wang, 2020). The build platform is lowered once the layer is complete in both systems, providing way for the following layer.

The photopolymer resin used in a DLP/ SLA system is comprised of a thermoset material that is light sensitive as well as a photoinitiator, and therefore, upon exposure to a certain wavelength of light, depending on the type of printer, chain polymerisation of the monomers takes place to generate a solid construct (Ligon *et al.*, 2017). The resolution and accuracy of prints are very important parameters when utilising 3D printing methods. When compared to other 3D printing techniques, DLP offers high printing accuracy at a low cost as well as having shorter build time compared to SLA. DLP allows precise control over the details of the surfaces as well as the flexibility of the print (Dabbagh *et al.*, 2021).

A recent emerging technology in the field is two-photon polymerisation 3D printing (TPP). It's a non-linear optical process in which two photons are absorbed

simultaneously in a photosensitive material, resulting in localised polymerisation. Afterwards, all non-polymerised material is washed away, revealing the structure. The ultimate material of the structures is not limited to photosensitive polymers, as later chemical processes can convert the basic structure into silicon or metals. To produce polymerisation, two-photon absorption employs a high-intensity, precisely focused infrared femtosecond laser beam (Mahmood and Popescu, 2021). Absorption occurs solely in the focus since it is proportional to the square of the intensity, resulting in high spatial resolution. The material polymerises solely in the ellipsoidal focus, referred to as a "voxel" or volume pixel, and the desired structure is written voxel-by-voxel by scanning the laser through the resist in all three dimensions. The presence of oxygen around the voxel helps to limit polymerisation to a certain extent, allowing for feature sizes of less than 100 nm. Furthermore, many polymers exhibit near-zero linear absorption in the near-infrared, allowing the laser to penetrate deep into the material and create otherwise inconceivable nanostructures (Bunea *et al.*, 2021)

In this chapter, a DLP technique was used for the purpose of 3D printing scaffolds to test for mechanical properties of CSMA-2 and its HA-incorporated composites as well as its degradation and cell-material interactions.

In summary the main aims and objectives of this chapter are as follows:

1. The synthesis of a light-curable degradable system in line with bone tissue engineering requirements, for restoring maxillofacial deficiencies.
2. The creation of composite-polymer specimens using two varying photoinitiators and varying ratios of hydroxyapatite fillers
3. The investigation of two photoinitiators for the purpose of DLP 3D printing of CSMA-2 along with its HA incorporated composites
4. The assessment of printing settings to optimise the technique to allow for easy and flexible printability of CSMA-2 and its composite-polymer specimens.
5. A comparison between the custom-designed STL files and the respective CT file to assess the accuracy and reliability of the DLP 3D printed scaffolds.

***The work in this chapter was published in the Journal of Biomedical Materials:***

*Shakouri, Taleen, Cha, Jae-Ryung, Owji, Nazanin et al. 'Comparative study of photoinitiators for the synthesis and 3D printing of a light-curable, degradable polymer for custom-fit hard tissue implants.' Biomedical Materials, vol. 16, issue 1, (2020), pp: 015007*

## 2.2 Materials and Methodology

### 2.2.1 Materials

Ethylene carbonate (1,3-dioxolan-2-one) (99%) was bought from Alfa Aesar (A15735-36) for the production of the starting monomer, BHIS (Haverhill, MA, USA). Scientific laboratory supplies (P5833-500) (Nottingham, UK) provided the potassium carbonate (99%) and Sigma-Aldrich provided the isosorbide (1,4:3,6-dianhydroD-sorbitol) (98%) (329207) (St Louis, MO, USA).

To continue the polymer synthesis to produce CSMA-2, the following chemicals were purchased from Sigma-Aldrich (St Louis, MO, USA) to continue the polymer synthesis to produce CSMA-2: isophorone diisocyanate (IPDI) (98%) (317 624), 2-hydroxyethyl methacrylate (HEMA) (97%) (128 635), triethylene glycol dimethacrylate (TEGDMA) (95%) (261548), dibutyltin dilaurate (99.8%) (322 415). For additional experimental synthesis, tert-butyl acrylate (98%) (327182) was also obtained from Sigma-Aldrich (St Louis, MO, USA).

For the purpose of purification, column chromatography was performed on the synthesised polymer. Merck (11511) (Darmstadt, Germany) provided silica gel beads (0.015–0.040 mm), while Sigma-Aldrich provided white quartz sand (274739). (St Louis, MO, USA). The photoinitiators camphorquinone (CQ) (97% ) (124893) and phenylbis(2,4,6-trimethylbenzoyl) phosphine oxide (BAPO) (97%) (511447) were acquired from Sigma-Aldrich (St Louis, MO, USA). to aid in photopolymerisation. 'CAPTAL R' hydroxyapatite (HA) with a Ca:P ratio of 1.67 and a high surface area of approximately 6–20 m<sup>2</sup>g<sup>-1</sup> was acquired from Plasma Biototal Limited (Buxton, UK) for



the addition of CaP fillers. Camphorquinone (CQ) and phenylbis(2,4,6-trimethylbenzoyl) phosphine oxide (BAPO) were the photoinitiators employed as an additive to CSMA-2 to aid in the DLP printing throughout the investigation (Sigma-Aldrich St Louis, MO, USA). The 3D printer used throughout the study is the 'Nobel Superfine' printer from (XYZ Printing, The Netherlands).

### 2.2.2 Synthesis of BHIS

The first attempt to synthesise Bis(2-hydroxyethyl) isosorbide (BHIS) involved using isosorbide and ethylene carbonate in the presence of a catalyst (potassium carbonate). In a 1000ml three-necked round bottom flask, a mixture of isosorbide (100 g, 684.27mmol) and ethylene carbonate (132.57 g, 1,505.45mmol) was degassed under dry nitrogen for 60 minutes. The flask was placed on a hot plate and heated to 70°C for 30 minutes while the contents were stirred. Potassium carbonate (208.06 g, 1,505.45 mmol) was added to the flask after the solid contents had completely melted and the mixture was left to react at 170°C for 48 hours. This method was previously explored by Owji *et al.* and Shakouri *et al.* (Owji *et al.*, 2019)(Shakouri *et al.*, 2020).

When adding the potassium carbonate, the reaction occurred very quickly, bubbling up and extruding via the vessels. This indicated that there was too much of the catalyst added therefore the amount had to be re-evaluated. After several re-evaluations of the components, the correct quantities were deciphered and used going forward (See Table 2-3).

Finally, BHIS was made by combining isosorbide (100 g, 684.3 mmol) with ethylene carbonate (132.57 g, 1505.5 mmol) in a 1000 ml three-necked round-bottom flask. The

flask was degassed with dry nitrogen for 60 minutes. The reaction mixture was then heated for 60 minutes on a hot plate at 70°C. The reaction liquid was heated to 170°C after the solid contents were entirely melted, and then potassium carbonate (3.0 g, 21.71 mmol) was added to the reaction mixture and left to react for 48 hours. To get high-purity BHIS, the synthesised BHIS was purified using silica column chromatography with a methanol/ethyl acetate (1/9) mobile phase and dried at 60°C for 24 hours under vacuum (figure 2-1 and 2-2).

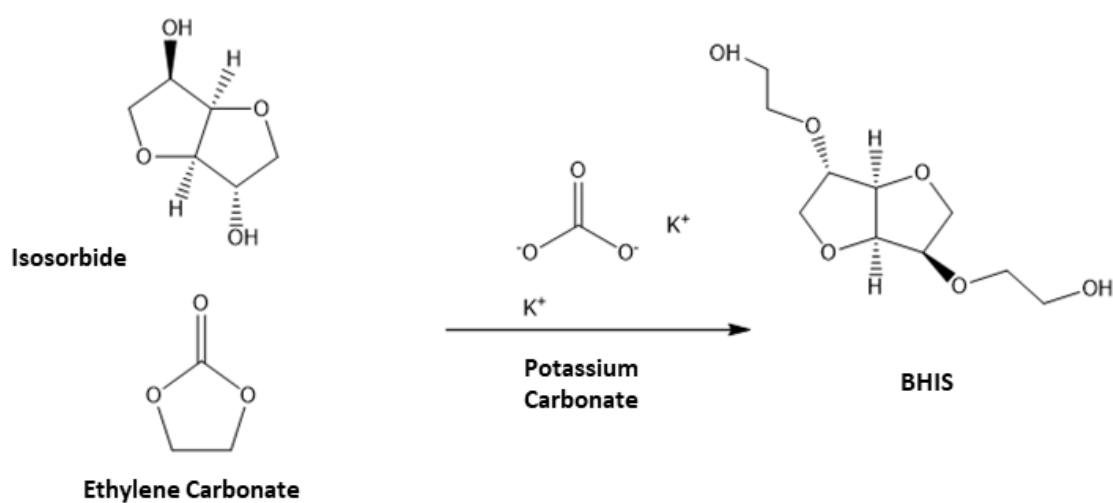
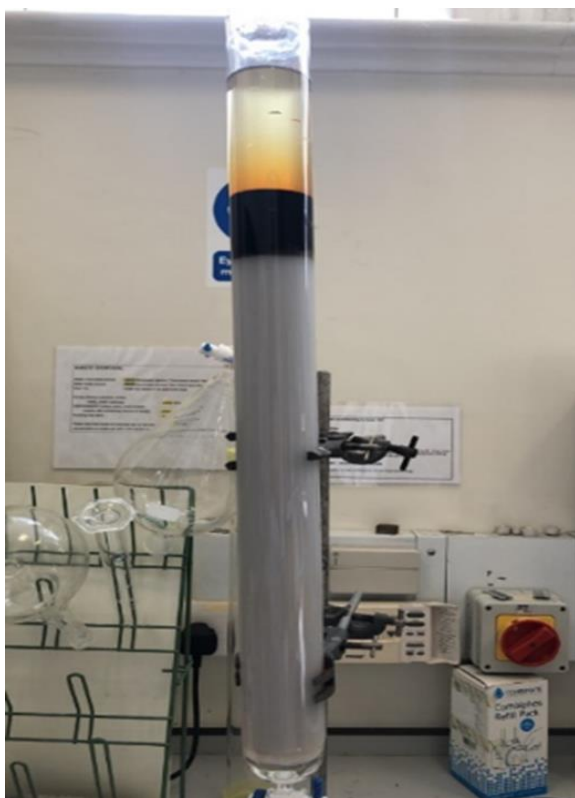


Figure 2-1: Chemical structures showing the production of bis(2-hydroxyethyl) isosorbide (BHIS).



*Figure 2-2: An image of the column set up for the final purification of the initial starting monomer, BHIS. Silica beads were used as a separation material and a mixture of methanol: ethyl acetate with a 1:9 ratio was used for the mobile phase. The column was then left to dry at 60°C for 24 hours under vacuum to obtain high-purity BHIS.*

### **2.2.3 Synthesis of CSMA-2**

In the presence of a diluent such as TEGDMA, a two-step reaction between the intermediate molecule, BHIS, and a three-fold excess of IPDI gave CSMA-2 (figure 2-3), which was followed by a reaction between the NCO-terminated monomer and 2-HEMA. BHIS (32.15 g, 79.37 mmol), IPDI (57.15 g, 257.07 mmol), TEGDMA (125 g, 436.56 mmol), and 5 drops (approximately 0.5 ml) of DBTDL were gradually added to a large amber glass beaker, which was then covered with aluminium foil to prevent light from entering. The reaction mixture was constantly stirred for 4 hours at 25°C. HEMA (71.42 g, 548.82 mmol) was added as a bonding agent to the resultant NCO-

terminated monomer in the reaction mixture, along with another 5 drops (approximately 0.5 ml) of DBTDL, due to its hydrophilic nature. The reaction mixture was agitated continuously for 12 hours at 25°C before being evaporated in a rotary evaporator resulting in the crude product which is a viscous colourless liquid.

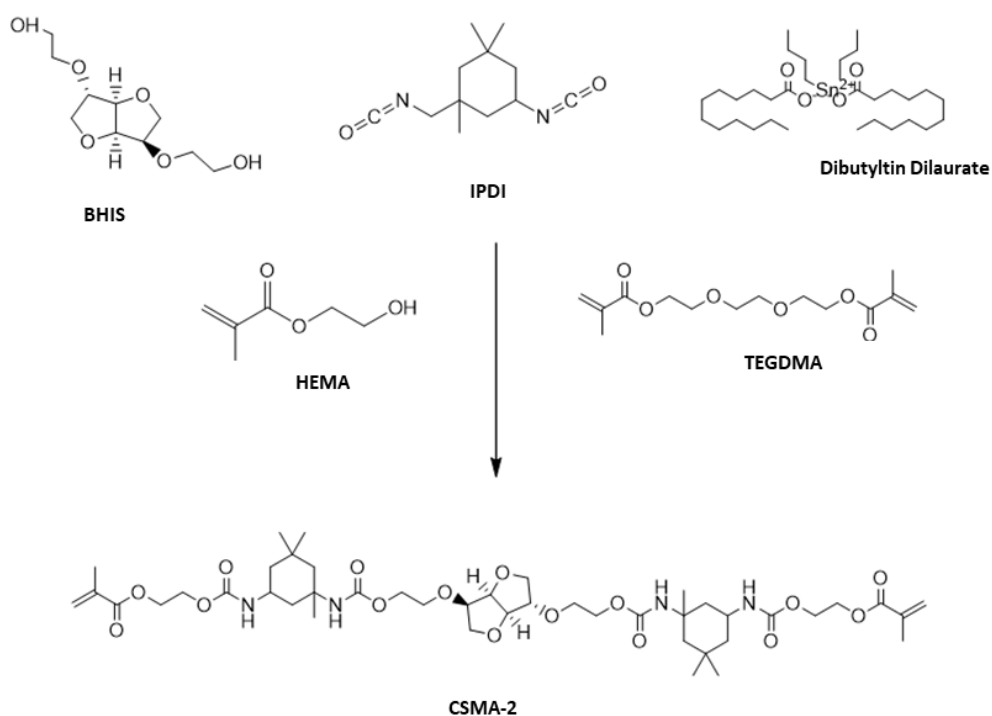


Figure 2-3: Preparation of (((((((((((((3R,3aR,6S,6aR)-hexahydrofuro[3,2-b]furan-3,6-diyl)bis(oxy))bis(ethane-2,1-diyl))bis-(oxy))bis(carbonyl))bis(azanediy))bis(methylene))bis(3,3,5-trimethylcyclohexane-5,1-diyl))bis(azanediy))bis(carbonyl))bis-(oxy))bis(ethane-2,1-diyl)bis(2-methylacrylate).

## **2.2.4 Photoinitiator systems**

To allow the synthesised monomers to photopolymerise, photoinitiators were investigated throughout the study. Camphorquinone (CQ) and phenylbis(2,4,6-trimethylbenzoyl) phosphine oxide (BAPO) (Table 2-1) were both used to prepare composite polymer pastes. To include the photoinitiator into the liquid phase system, 2 wt% of CQ or BAPO was accordingly added. 20 g of CSMA-2 was weighed into a brown glass jar and 2 wt% (0.4 g) of either CQ or BAPO were added and left to stir vigorously for 12 hours at room temperature to allow a thorough dispersion of the particles.

## **2.2.5 Material Characterisation**

### ***2.2.5.1 Nuclear magnetic resonance (NMR)***

In order to detect the chemical structure of the monomers, NMR was carried out on both BHIS and CSMA-2. The  $^1\text{H}$  NMR and  $^{13}\text{C}$  spectra were recorded using a JEOL NMR-ECA 600 spectrometer (600 MHz, Tokyo, Japan), and the solvent for both BHIS and CSMA-2 was deuterated chloroform ( $\text{CDCl}_3$ ). The 'delta NMR software; version 4.3.6' was used to calculate chemical shifts relative to tetramethylsilane ( $\delta$ , ppm).

The NMR sample preparation and analysis was carried out by myself for this study. However, the NMR was performed by a colleague, Dr Peter Haddow at the University of Hertfordshire School of Life and Medical Sciences.

### ***2.2.5.2 Fourier transform infrared spectroscopy (FTIR)***

The infrared spectrum of absorption or emission of a solid, liquid, or gas is obtained using the FTIR technique. FTIR allows users to analyse the infrared light that interacts

with materials at a molecular level. It works by measuring the wavelength and intensity of light absorption by the sample. The resulting signals correlate with vibration frequencies between the atomic bonds of the material (Bellisola and Sorio, 2012).

The degree of polymerisation, also referred to as the degree of monomer conversion is the successive linking of monomeric units in a macromolecule which depends on the kinetics of the reactants which is determined by their concentration and the rate of reaction (Moldovan *et al.*, 2019). The mechanical properties of a material such as a higher flexural strength, modulus, low shrinkage properties and better cytocompatibility have been said to correlate with higher degrees of polymerisation (Kangwankai *et al.*, 2017).

The rate of monomer conversion of the materials and appropriate composites in this study was determined by FTIR spectroscopy (Perkin Elmer series 2000 FTIR spectrometer, Seer Green, UK). To investigate the continuous change of the spectra, a drop of polymer premixed with 2 wt % CQ or 2 wt % BAPO was placed on the diamond of an attenuated total reflectance (ATR) (Golden Gate ATR, Specac Ltd., United Kingdom), and spectra were recorded for 1000 seconds after exposure to blue light. The resolution was set at  $4\text{ cm}^{-1}$  with the wavelength range of  $800\text{-}1800\text{ cm}^{-1}$ . A tiny aliquot of CSMA-2 combined with 2 wt% CQ/BAPO was put onto the diamond ATR to determine the optimum curing time. The temperature was set at  $37\text{ }^{\circ}\text{C}$  and Timebase software was used to record the observed changes. The absorbance profiles for the C–O stretch bond and the baseline were measured at roughly  $1320\text{ cm}^{-1} \pm 1$  (C–O stretch bond) and  $1335\text{ cm}^{-1} \pm 1$  (baseline). The following equation (2-1) was used to compute the rate of monomer conversion using these absorbance patterns.

$$C = 1 - \left[ \frac{A_f}{A_0} \right] \times 100$$

*Equation 2-1: Equation used to calculate the rate of monomer conversion; where C is the conversion, A<sub>0</sub> is the initial absorbance peak and A<sub>f</sub> is the final absorbance peak.*

## **2.2.6 Composite Preparation**

### **2.2.6.1 Manual Composite Preparation**

Initially, different amounts of HA filler were blended to make the composite polymer paste with CSMA-2 and 2 wt% CQ using a centrifugal planetary mixer (SpeedMixer, Hauschild Engineering, Hamm, Germany, DAC150.1 FVZ) at 1700RPM for 4 minutes. Polymer-composite discs with 1-50 wt% HA filler added were investigated for their mechanical properties and the ability to be used as a 3D printable resin as the presence of HA will inhibit light transmittance and therefore inhibit light-curing.

After mixing, the composite paste was spread into circlip discs of 10 mm in diameter which were placed on a thin acetate sheet and entirely filled. A new acetate sheet was placed on top of the sample discs and flattened with a glass block to ensure even distribution of the composite paste and parallel surfaces. The discs were then light cured with blue light emitting diode with a wavelength of 450-470nm for 40 seconds

on each side through the acetate sheet and then popped out of the circlip discs. Table 2-2 below shows the amounts of HA filler used in this study alongside the appropriate CSMA: HA ratios and volumes described.

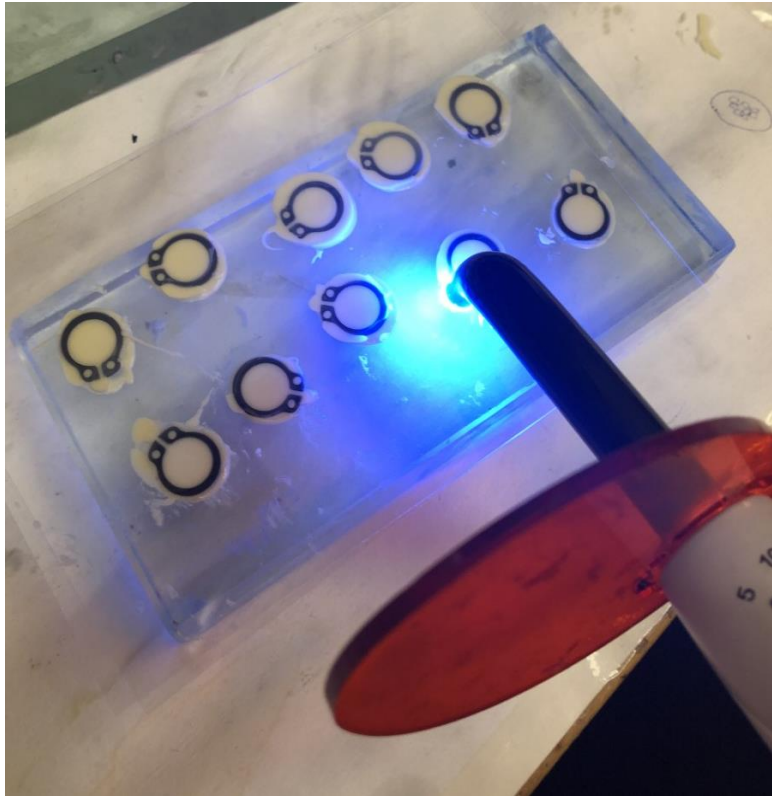


*Figure 2-4: An example of the manual method to produce composite-polymer discs by placing the polymer/ filler paste onto a metal circlip disc, layering it with an acetate sheet and light-curing with a 450-470nm blue light diode for 40 seconds each side*



Table 2-2: A table displaying the polymer to calcium phosphate filler wt % ratios for the composite polymer discs used in this study

| <u>CSMA-2 (wt%)</u> | <u>CSMA-2 (g)</u> | <u>Volume CSMA-2 (cm<sup>3</sup>)</u> | <u>Hydroxyapatite (wt%)</u> | <u>Hydroxyapatite (g)</u> | <u>Volume Hydroxyapatite (cm<sup>3</sup>)</u> | <u>Volume ratio HA:CSMA-2 (%)</u> |
|---------------------|-------------------|---------------------------------------|-----------------------------|---------------------------|---|-----------------------------------|
| 100                 | 10                | 8.47                                  | 0                           | 0.0                       | 0.00  | 0.00                              |
| 99                  | 9.9               | 8.39                                  | 1                           | 0.1                       | 0.03  | 0.36                              |
| 98                  | 9.8               | 8.30                                  | 2                           | 0.2                       | 0.06  | 1.08                              |
| 97                  | 9.7               | 8.22                                  | 3                           | 0.3                       | 0.09  | 1.09                              |
| 96                  | 9.6               | 8.14                                  | 4                           | 0.4                       | 0.13  | 1.59                              |
| 95                  | 9.5               | 8.10                                  | 5                           | 0.5                       | 0.16  | 1.97                              |
| 90                  | 9.0               | 7.63                                  | 10                          | 1.0                       | 0.32  | 4.19                              |
| 80                  | 8.0               | 6.78                                  | 20                          | 2.0                       | 0.63  | 9.29                              |
| 70                  | 7.0               | 5.93                                  | 30                          | 3.0                       | 0.95  | 16.02                             |
| 60                  | 6.0               | 5.08                                  | 40                          | 4.0                       | 1.27  | 25.00                             |
| 50                  | 5.0               | 4.24                                  | 50                          | 5.0                       | 1.58  | 37.26                             |
| 40                  | 4.0               | 3.39                                  | 60                          | 6.0                       | 1.90  | 56.05                             |
| 30                  | 3.0               | 2.54                                  | 70                          | 7.0                       | 2.22  | 87.40                             |

### **2.2.6.2 3D Printed Composite Preparation**

The composite-polymer discs made during this study were used for a variety of tests in order to find the optimum formulation for maxillofacial applications. 3D printing using the DLP technique was investigated to prepare the composite-polymer discs in less time with less chance of contamination or human error. It was soon discovered that the printer could only function with a maximum of 10 wt% HA as the viscosity of the polymeric system became higher and the printer could not produce detailed fine prints with a high viscosity. The mixtures of 0 wt%, 5 wt%, and 10 wt% inorganic phases: organic phase with either CQ or BAPO were loaded into the 3D printer (Nobel Superfine, XYZ Printing, The Netherlands), where discs with a diameter of 10 mm and a thickness of 1 mm were printed and photopolymerised at 450 nm based on the trial-and-error findings. Printability using CQ photoinitiator proved challenging due to having to use the printer on its maximum settings to allow for photopolymerisation to take place which would take an extensive amount of time as well as more material being required. Therefore, 3D printed samples were created using only 2 wt% of BAPO going forward.

To conduct testing using the dynamic mechanical analysis (DMA) method, 3D printing was used to construct composite polymer bars for mechanical testing. The same 0 wt%, 5 wt%, 10 wt% inorganic phases: organic phase combinations with either CQ or BAPO were produced and put into the 3D printer, where bars with dimensions of 20 mm x 5 mm x 1 mm were manufactured and photopolymerised at 450 nm.

### **2.2.7 Computer-Aided Design**

All printable constructs used in the study were designed using 'AutoCAD 2019' (Autodesk, USA). Once a model was created, it was exported to a Standard Tessellation Language file, also known as an STL file. The STL file is made up of several triangles, allowing the printer to understand the shape of the model in a simple, geometric way. Once converted into an STL file, the XYZ slicing software, 'XYZmaker Suite' was used to slice the file, essentially turning it into a G-code file which the 3D printer can make use of. The G-code is a series of commands that instructs the printer on what to do. The STL file is imported and checked for the same dimensions designed on AutoCAD. The file is then sliced into a G-code to prepare the printer settings.

### **2.2.8 Optimisation of Settings**

Once the STL file is set up on the printing software, the settings can be optimised according to the type of resin being used. The standard settings pre-set on the XYZ Nobel Superfine DLP printer can be seen below in figure 2-5. The base, intermediate and model set up explain the different parts of the print. The curing section contains the curing time, power intensity, power level and wait time. The curing time is critical when setting up a print as it is the amount of time that the light source will expose each layer during printing. The default for this printer is 19000 ms (19 seconds) but different printers have different defaults. The power intensity allows control of the power of the light source emitting onto the construct and the power level has three options to allow for customisation. The peeling section contains settings to control the speed and distance of the material polymerising and lifting off from the resin tank onto the build

platform. The platform ascending/descending refers to the speed at which the build plate is lifted from the resin tank between layers.

These settings were originally used to test the printing ability of CSMA-2 and its composites but were changed using a trial and error method to find the optimum settings for accurate printability.

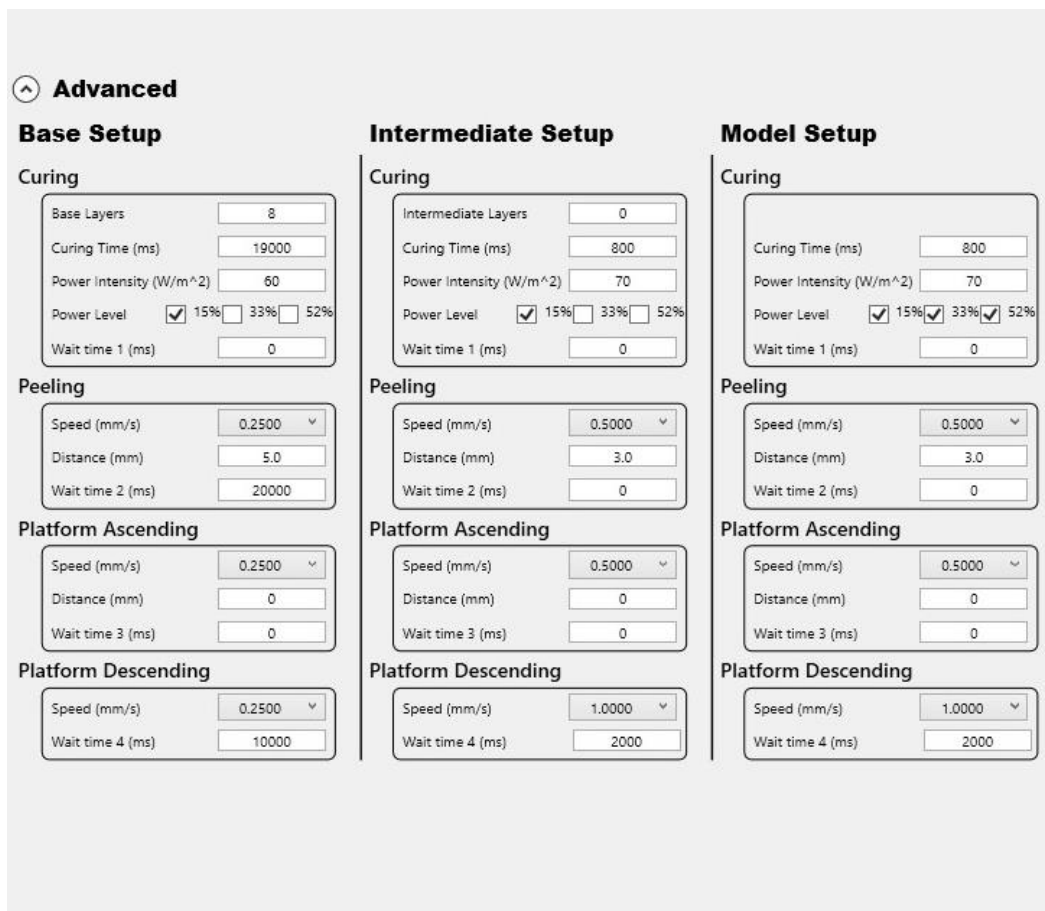


Figure 2-5: A screenshot image of the settings page from the standard options on the XYZ Nobel Superfine 3D printer. As seen, the curing settings include the curing time, power intensity and power level which are critical steps in the printing process. The peeling settings include the speed of which the construct is peeled off the platform and the distance it travels. The platform settings highlight the speed and distance of which the build platform ascends and descends when creating the construct layers.

When testing the CQ photoinitiator-incorporated composites, the curing time had to be set to the maximum on the software (65535 ms) with the power intensity at the maximum ( $100 \text{ W/m}^2$ ) and all three power levels selected. The platform ascending speed was set to 0.25 mm/s for the base set up and 0.5 mm/s for the intermediate and model set up. The platform descending speed at 0.25 m/s for the base set up and 1.0 mm/s for the intermediate and model set up. When incorporated HA fillers to the CQ photoinitiator CSMA-2 formulation, the printer was not able to produce any constructs.

When testing the BAPO photoinitiator-incorporated composites with no pores, the curing exposure time was set to 19000 ms, the power intensity at  $100 \text{ W/m}^2$  and the power level of 33 % was selected. For the intermediate and model set up sections, the curing time was set to 8300 ms and the power intensity also at  $100 \text{ W/m}^2$ . The platform ascending speed was set to 0.5 mm/s and the platform descending speed at 0.25 m/s for the base set up and 1.0 mm/s for the intermediate and model set up.

When exploring the incorporation of pores into the CSMA-2 scaffold, the settings had to be optimised to allow for porous infiltration of the material. The curing time for the base set up was set to 15000 ms, with it being 6000 ms for the intermediate and model set up. The power intensity was set to  $53 \text{ W/m}^2$  for all three modes and the power level was selected to be the minimum, at 15%. The peeling speed was set to 0.25 mm/s with a wait time of 30000 ms. The wait time is the time in between each layer peeling off from the resin tank onto the platform. The platform ascending speed was set to 0.25 mm/s and the descending speed set to 0.25 mm/s for the base set up, but then increased to 1.0 mm/s for the intermediate and model set up.

### **2.2.9 3D Printing**

Once the construct had been designed and imported into the software and the settings adjusted dependent on the material and the model type, the monomeric system containing well dispersed photoinitiator (CQ or BAPO) was placed into the resin tank of the printer. Figure 2-6 below shows (A) the XYZ Novel Superfine DLP printer, (B), the build platform and its moving axis and (C) the resin tank, or vat, where the liquid is filled into. The red cover for the printer seen in image A is critical and the print would not work without this being securely placed on top as it eliminates light.

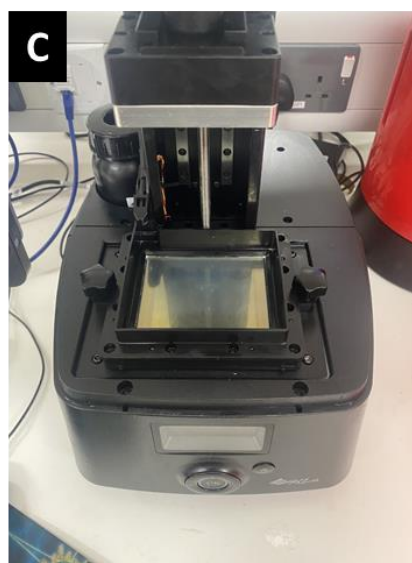
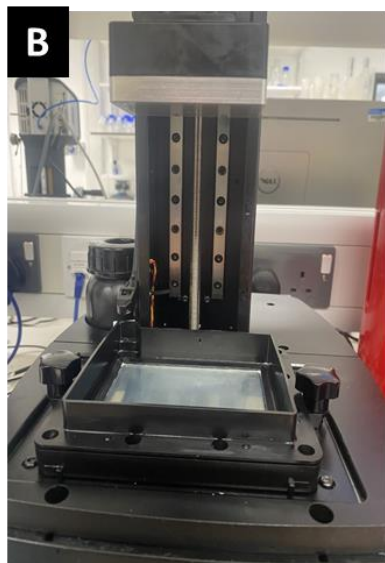


Figure 2-6: Images taken of the XYZ Nobel Superfine DLP 3D printer used in this study. Image (A) shows the printer itself with its red cover to eliminate light, (B) shows the build platform at the top of the moving axis and (C) shows the resin tank ready to be filled with the appropriate material.

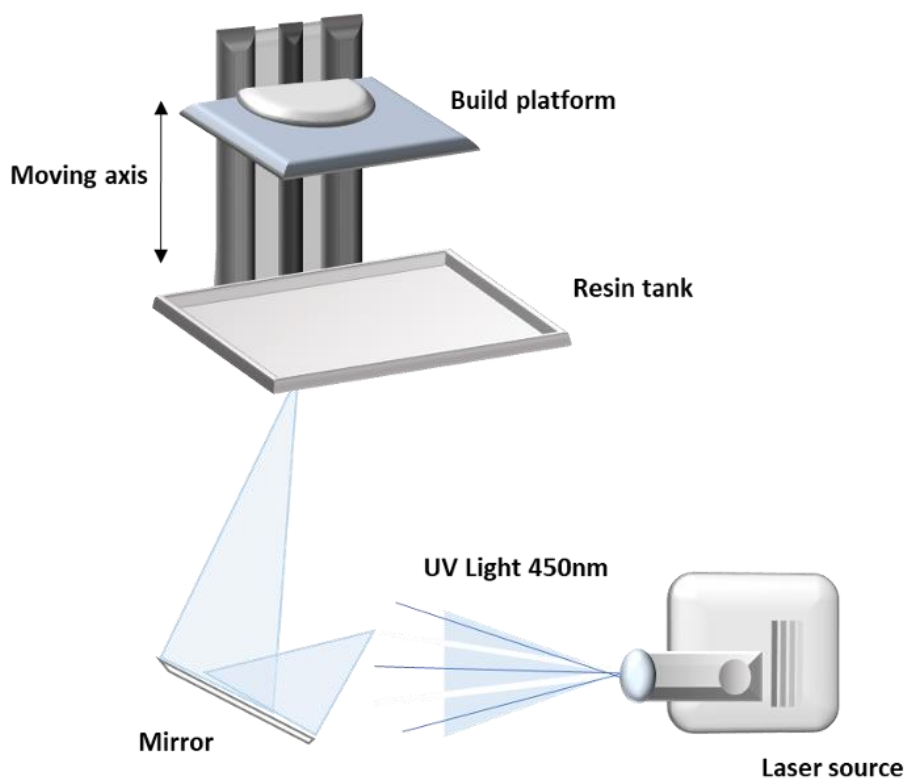


Figure 2-7: A schematic showing how the DLP 3D printer used in this study works beginning with the laser source emitting UV light at 450 nm which is transmitted via a mirrored projector screen onto the resin tank which is pre-filled with the required material. The build platform descends the moving axis, and the model is built layer by layer until it is complete, when the build platform will ascend back up to the top and allow the release of the model.

### 2.2.10 Post Curing

Following the successful digital light processing 3D print, the newly formed model is removed from the build platform and washed in 99.9% methanol (Sigma-Aldrich St Louis, MO, USA) to remove any remaining residue from the model. After 5 minutes of washing in methanol, to ensure an in-depth photopolymerisation, the model was placed into a UV chamber (XYZ Printing, The Netherlands) where post curing was facilitated for 5 minutes. The UV chamber seen below in figure 2-8 gives off a



wavelength of 375-405 nm emitted from a UV LED lamp allowing prints from various types of resins to be cured between 1-60 minutes.



*Figure 2-8: The XYZ Printing UV Chamber for the purpose of post curing the 3D printed models. Image (A) shows the chamber closed, with a solid red exterior to prevent any additional light emitting the chamber. Image (B) shows the chamber open, with the platform that the item is placed upon.*

### **2.2.11 Scanning Electron Microscopy (SEM)**

SEM images of 3D-printed specimens designed into a matrix of 0.50 mm X 1.00 mm cross-sectional dimensions were acquired (Philips XL30 field emission SEM, Amsterdam, Netherlands). 3 repeats of each specimen were analysed and SEM was utilised to visualise the specimen's surface and gather measurements to compare to the digital STL files in order to determine print accuracy.

All specimens were fixed in 3% glutaraldehyde (Agar Scientific, United Kingdom) in 0.1M cacodylate buffer (CAB) for 24 hours at 4°C. The samples were then mounted onto aluminium pin stubs, taking care with orientation, double-sided carbon tabs (Agar Scientific, United Kingdom). The samples are sputter coated with 95% gold and 5% palladium (Polaron E5000, Quorum Technology, United Kingdom) before being placed in the SEM where samples are examined in a ZEISS EVO MA10 (ZEISS, United Kingdom) operating at 10kV, spot size 300 for imaging.

### **2.2.12 Computed Tomography (CT)**

For the purpose of comparing the accuracy of the print to the original CAD design, MicroCT was used. AutoCAD was used to create a log pile structure that represents how cortical bone is constructed. 3 structures were created and assessed for the purpose of reproducibility. SkyScan 1172 was used to obtain CT scans of the printed build (Bruker, United Kingdom). The scan parameters were as follows: 0.5 mm aluminium filter, 100 mA current, 80 kV voltage, 666 ms exposure duration, 23.8 µm pixel size, rotation step 0.3°, frame averaging 6. NRecon software (Bruker, United Kingdom) was used to reconstruct the scans, and CTVox software was used to create 3D renderings (Bruker, United Kingdom). To guarantee that the faces of the cylinders from the build were orthogonal to the view direction, the dataset was re-oriented utilising DataViewer software (Bruker, United Kingdom) for numerical analysis. The reoriented dataset was then loaded into CTAn software (Bruker, UK), where binary data was created. Only the faces of the cylinders were visible in the slices selected at random through the dataset in both orthogonal directions. The area and diameter of each cylindrical cross-section were determined individually using 2D object analysis. Selecting four slices at random, two in each orthogonal direction. The area and area-

equivalent circle diameter of four random slices, two in each orthogonal direction, were employed for numerical analysis. This section of the work was also investigated and published in (Shakouri *et al.*, 2020).

The samples prepared for CT analysis were created by myself however, the running of the CT and analysis of the dataset were performed by a colleague at the University of Birmingham, Dr Thomas Robinson.

## **2.3 Results**

### **2.3.1 Polymer Synthesis**

#### **2.3.1.1 Variations of BHIS**

In the process of synthesising the starting monomer, BHIS, many variables were changed to ensure a stable reaction. Originally, following advice from researchers in our group at Dankook University, 208.06 g of potassium carbonate was suggested for use as the catalyst. However, when adding the potassium carbonate, the reaction occurred very quickly, bubbling up and extruding via the vessels. This indicated that the quantity of catalyst was too high and needed to be re-evaluated.

Table 2-3 below explains the changes carried out in the first part of the polymeric synthesis to formulate BHIS. The final product required a smaller amount of potassium carbonate than originally decided on in the protocol followed. This allowed the reaction to occur giving a viscous black liquid as the final product of BHIS which could then go on to be purified using the column chromatography filtration methods to give a clear viscous liquid.



Table 2-3: A table explaining the several steps taken in the production of the starting monomer, Bis(2-hydroxyethyl) isosorbide (BHIS) with all the varying quantities of catalyst used throughout the process along with their outcomes.

| Step | Variable   | Outcome  |
|------|--|--|
| 1    | Mixture of ethylene carbonate and isosorbide left to react for 2 hours instead of 1 hour | No change occurred   |
| 2    | Degassing under dry nitrogen carried out in vacuum oven instead of fume hood             | No change occurred   |
| 3    | Heated reaction up to 170°C after the addition of catalyst rather than before            | Catalyst took a longer time to mix in with reagents- no final change occurred        |
| 4    | Final product was left to cool for 12 hours post reaction                                | Product solidified inside the beaker   |
| 5    | Amount of K <sub>2</sub> CO <sub>3</sub> changed to 1.134g(8.205mmol)                    | Reaction occurred forming a light-yellow liquid – tested via FTIR to be solvent only |
| 6    | Amount of K <sub>2</sub> CO <sub>3</sub> changed to 3g (21.706mmol)                      | Product purified via column chromatography to give a clear viscous liquid (BHIS)     |

## **2.3.2 Material Characterisation**

### ***2.3.2.1 Nuclear Magnetic Resonance***

$^1\text{H}$  NMR and  $^{13}\text{C}$  NMR analysis confirmed the creation of the starting monomer precursor BHIS and the final monomer CSMA-2, both of which were manufactured from isosorbide as a starting material. The  $^1\text{H}$  NMR spectrum (figure 2-9) shows the confirmation of the synthesis of BHIS which is highlighted by the proton signal at 3.58~3.73 ppm, which represents the  $\text{H}_2\text{-C-C-H}_2$  protons and correspond to the ethylene groups in BHIS. (Figure 2-10) of BHIS highlights the integrals of the peaks. The area beneath an NMR resonance is proportional to the number of hydrogens represented by that resonance. Information on the relative number of chemically unique hydrogens can be found and analysed by combining the different NMR resonances. (Figure 2-11) displays the  $^{13}\text{C}$  NMR analysis of the monomer BHIS. The spectra depict ten visible carbon environments that correspond to the ten carbon environments found in the BHIS structure.

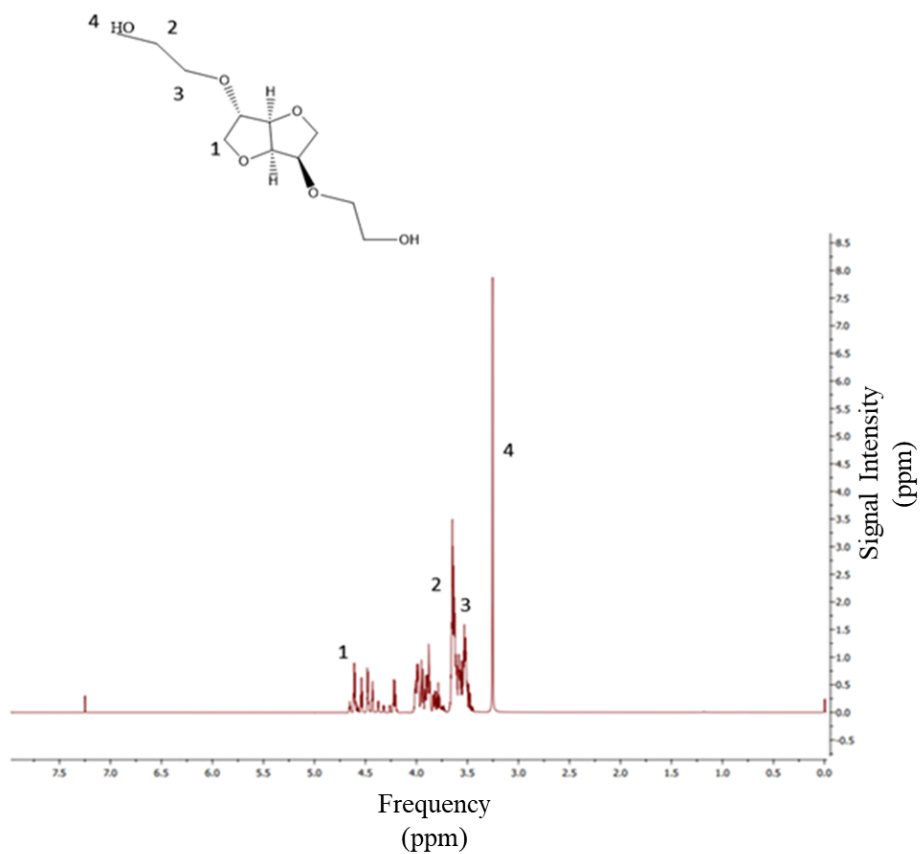


Figure 2-9: <sup>1</sup>H NMR spectra highlighting the chemical bond formation of BHIS. The synthesis is confirmed by the proton signal at 3.58~3.73 ppm, which represents the H<sub>2</sub>-C-C-H<sub>2</sub> protons and correspond to the ethylene group in BHIS. On the spectra 1= withdrawing electron density from O-, 2= Alkane, 3= Ethylene group and 4= Hydroxyl group.

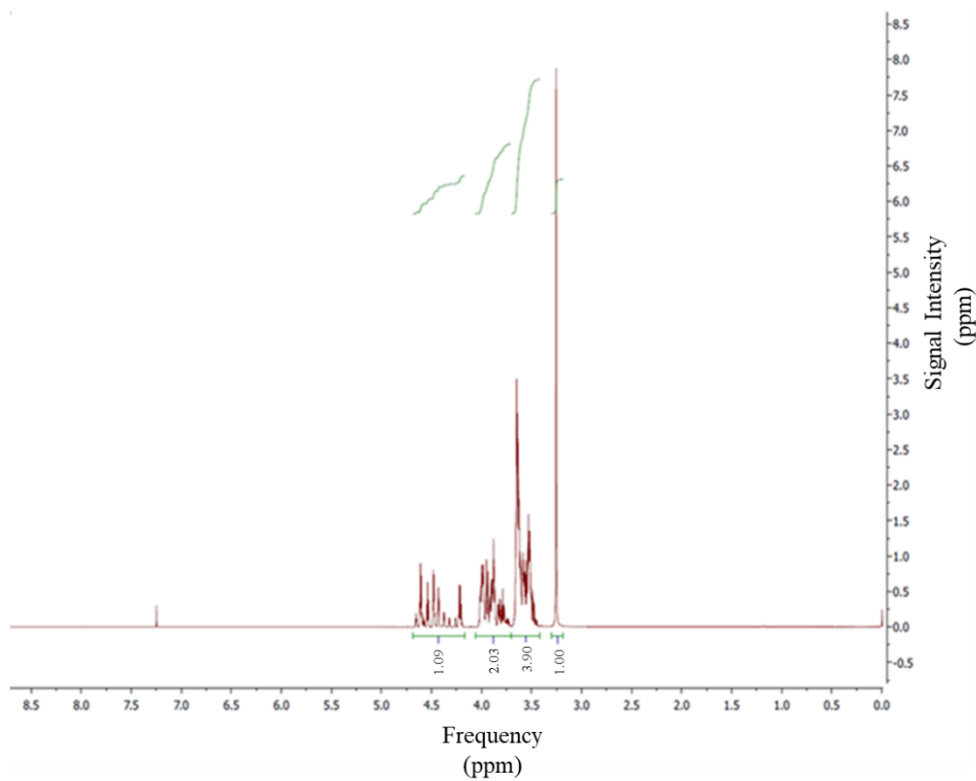


Figure 2-10: <sup>1</sup>H NMR spectra highlighting the chemical bond formation of BHIS with a focus on the integrals investigated throughout the spectra. The area under the NMR resonance is proportional to the number of hydrogens which that resonance represent.



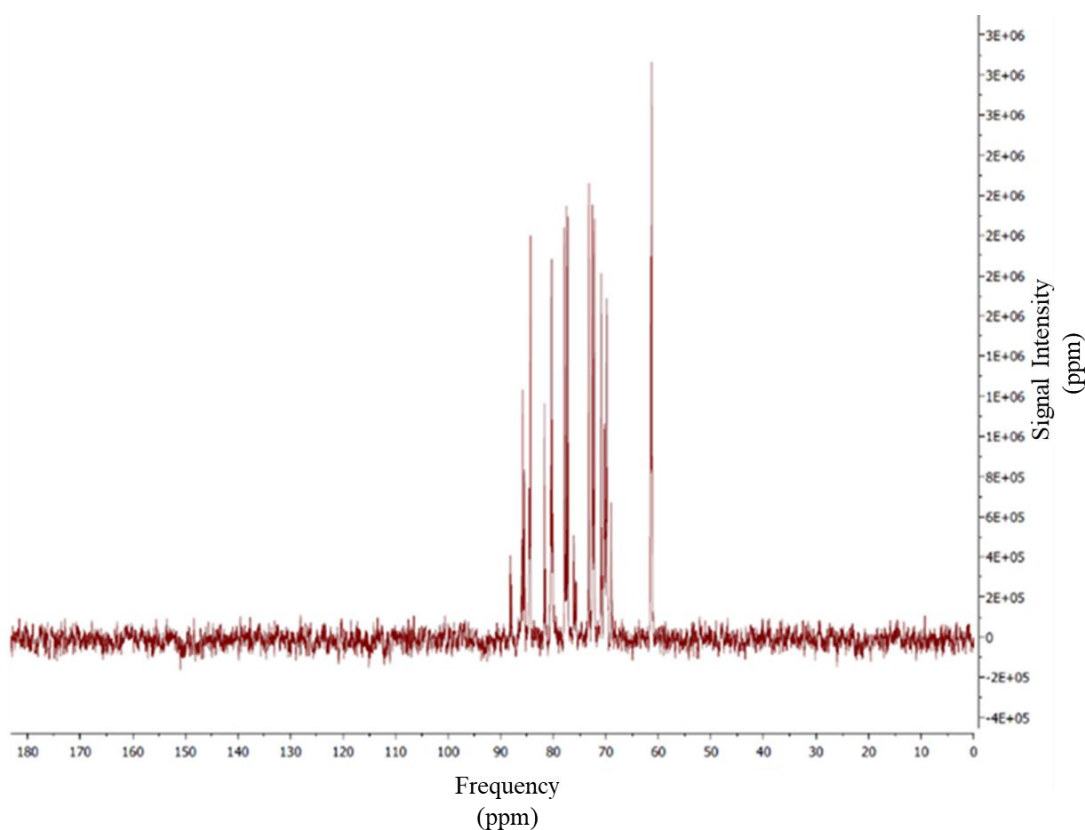


Figure 2-11:  $^{13}\text{C}$  NMR analysis of the monomer BHIS. The spectrum here shows 10 visible carbon environments which represent the 10 carbon environments seen in the structure of BHIS.

The  $^1\text{H}$  NMR and  $^{13}\text{C}$  NMR of CSMA-2 are represented in figures 2-12, 2-13 and 2-14 below. Figure 2-12 indicates that the protons of the methacryl group ( $\text{CH}_2=\text{C}-\text{CH}_3$ ) are represented by the three singlets present at 6.14, 5.59, and 1.96 ppm. The protons of the isophorone cycle correspond to the signals between 0.8 and 1.2 ppm. The protons of the urethane groups that link the methacrylate units to isosorbide, on the other hand, were not visible, possibly because they were obscured by other signals. These results are consistent with the  $^1\text{H}$  NMR spectra previously recorded by Owji and co-researchers (Owji *et al.*, 2019). The  $^{13}\text{C}$  NMR spectra shown in (figure 2-14) confirms the 19 visible carbon environments in the structure of CSMA-2.

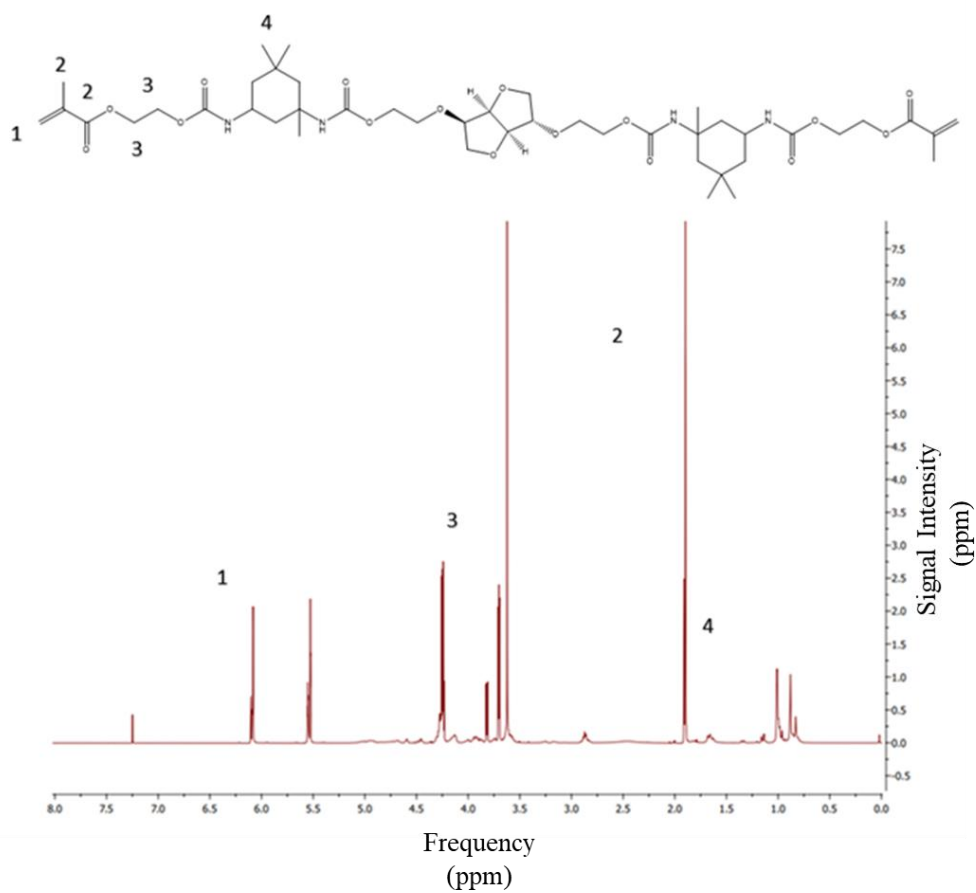


Figure 2-12:  $^1\text{H}$  NMR spectra highlighting the chemical bond formation of CSMA-2. The synthesis is confirmed by the three singlets present at 6.14, 5.59 and 1.96 ppm corresponding to the protons of the methacryl group ( $\text{CH}_2=\text{C}-\text{CH}_3$ ). The signals seen between 0.8 and 1.2 ppm correspond to the protons of the isophorone cycle. On the spectra 1= Alkene, 2=Methacrylate, 3= Ester bonds and 4=Isophorone cycle.

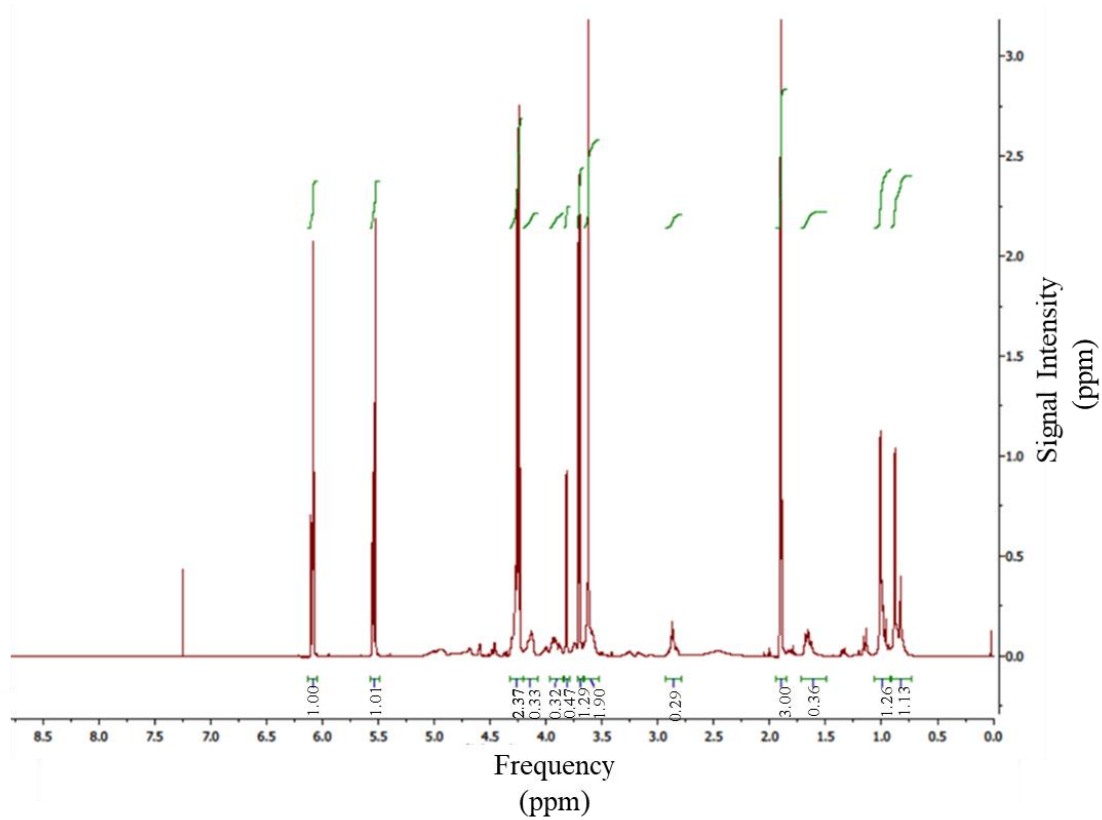


Figure 2-13:  $^1\text{H}$  NMR spectra highlighting the chemical bond formation of CSMA-2 with a focus on the integrals investigated throughout the spectra. The area under the NMR resonance is proportional to the number of hydrogens which that resonance represents.

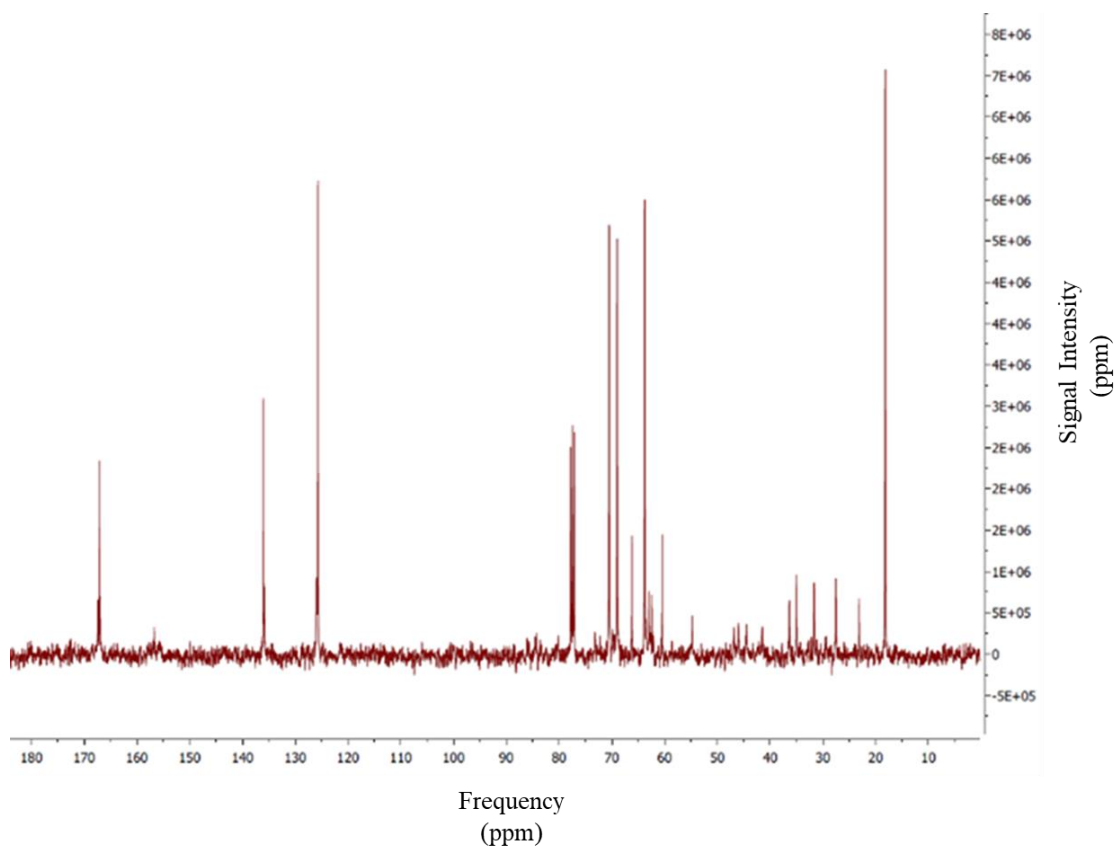


Figure 2-14:  $^{13}\text{C}$  NMR analysis of CSMA-2. The spectrum here shows 19 visible carbon environments which represent the 19 carbon environments seen in the structure of CSMA-2.

When used in NMR, integration refers to the number of hydrogens present at each signal. In a  $^1\text{H}$  NMR spectrum, the integrated intensity of a signal yields a ratio for the number of hydrogens that give rise to the signal, allowing the total number of hydrogens present in a sample to be calculated.

The area beneath an NMR resonance is proportional to the number of hydrogens represented by that resonance. Information on the relative number of chemically unique hydrogens can be found and analysed by combining the different NMR resonances.

### **2.3.2.2 Fourier-Transform Infrared Spectroscopy**

The monomer conversion rate during photopolymerisation of the liquid phase was determined using time-dependent FTIR spectra of CSMA-2 with two distinct photoinitiators. The level of conversion achieved during polymerisation has a direct impact on the physical and mechanical properties of photo-cured composites. The intensity of the methacrylate as it transforms from a monomer to a polymer is used to determine the degree of conversion (DC). A high DC may impact the polymer's durability and performance due to the presence of unreacted monomers, and an incomplete (or low) degree of polymerisation of any methacrylate monomer can affect biological properties, potentially leading to cytotoxic consequences. The calculation of the optimum curing time upon photo polymerisation in liquid phase was achieved through the analysis of monomer conversion rate of two different formulations, CSMA-2 + 2 wt% CQ photoinitiator and CSMA-2 + 2 wt% BAPO photoinitiator was carried out by the aid of Equation 2-1. In this equation, absorbance profiles were received at  $1320 \pm 1 \text{ cm}^{-1}$  (C–O stretch bond) and  $1335 \pm 2 \text{ cm}^{-1}$  was set as the baseline.

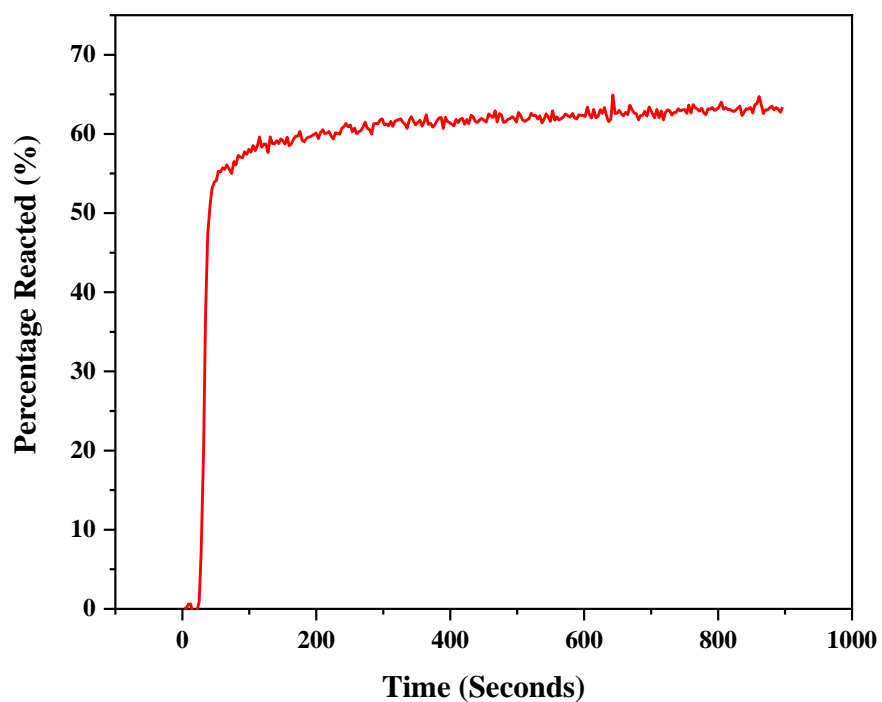


Figure 2-15: FTIR spectrum of CSMA-2 with 2% CQ photoinitiator showing the percentage of reacted monomers post curing; 65% of polymerisation was achieved in this formulation after exposure to blue light for 40 seconds. Absorbance profiles were received at  $1320 \pm 1 \text{ cm}^{-1}$  (C–O stretch bond) and  $1335 \pm 2 \text{ cm}^{-1}$  was set as the baseline.

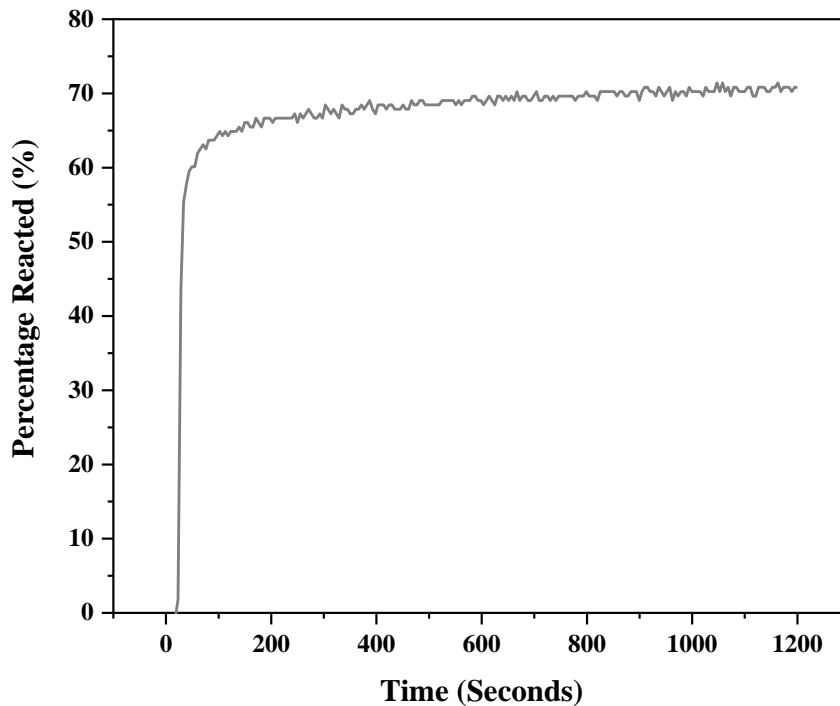


Figure 2-16: FTIR spectrum of CSMA-2 with 2% BAPO photoinitiator showing the percentage of reacted monomers post curing; 72% of polymerisation was achieved in this formulation after exposure to blue light for 40 seconds. Absorbance profiles were received at  $1320\text{ cm}^{-1}$  (C–O stretch bond) and  $1335 \pm 2\text{ cm}^{-1}$  was set as the baseline.

The conversion was calculated using the absorbance profiles, as shown in figures 2-15 and 2-16 and it was discovered that within the first 40 seconds of the spectra, 65% conversion of CSMA-2 was detected in the sample with CQ, and 72% conversion of CSMA-2 was observed in the sample with BAPO. These findings imply that a 40-second curing period is sufficient for further composite preparation. The monomer with BAPO initiator has a substantially higher degree of monomer conversion, implying that it would be a preferable alternative for use in the future to reduce time spent curing monomer systems. Figure 2-17 below shows how long it took for the reaction to start

occurring after the monomer was cured using a 450nm blue light diode. As per spectrum, it took approximately 4.65 seconds for the polymerisation to begin occurring.

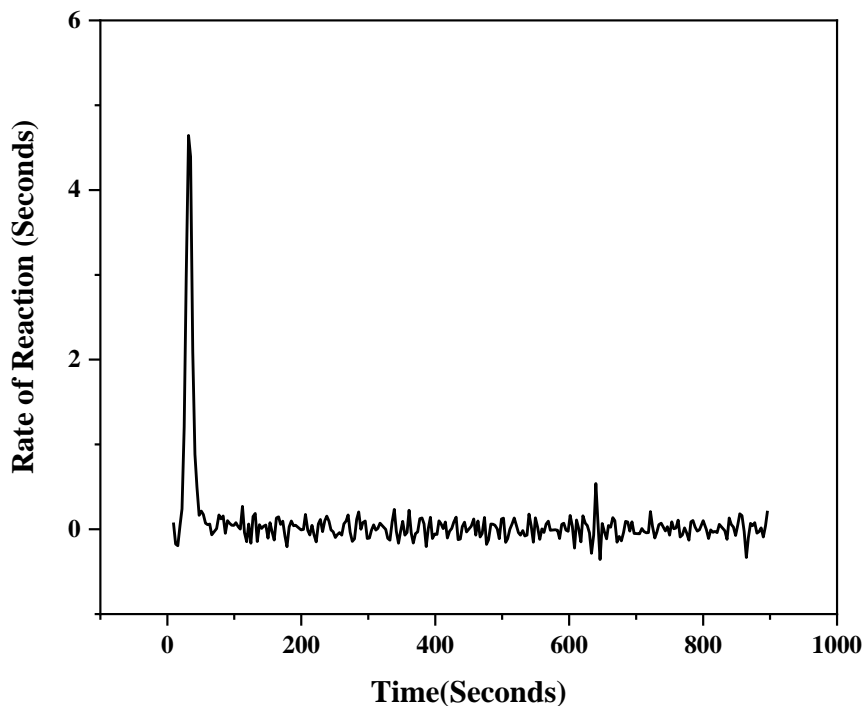


Figure 2-17: FTIR spectrum of CSMA-2 representing the rate of reaction to show the start time of the reaction (4.65 seconds)

### 2.3.3 3D Printed Constructs

Originally, following on from the manually prepared composite-polymer discs that were created in section 2.2.6 the discs used for the purpose of the assessing BAPO incorporated CSMA-2 composites for mechanical testing, degradation studies and *in vitro* studies were all 3D printed using the DLP technique. The standard, 10 mm in diameter and 1 mm thick discs designed via AutoCAD and 3D printed can be seen



below in figure 2-18. For the *ex-ovo* CAM assay, described in Chapter 4, section 4.2.5, porous 3D scaffolds were designed via AutoCAD and printed. The final porous scaffolds were designed to print at 6 mm in diameter and 3 mm thick with 0.5 mm pores. Figure 2-19 shows the porous scaffolds used for the purpose of the CAM with either 0, 5 or 10 wt% HA incorporated into the scaffold.

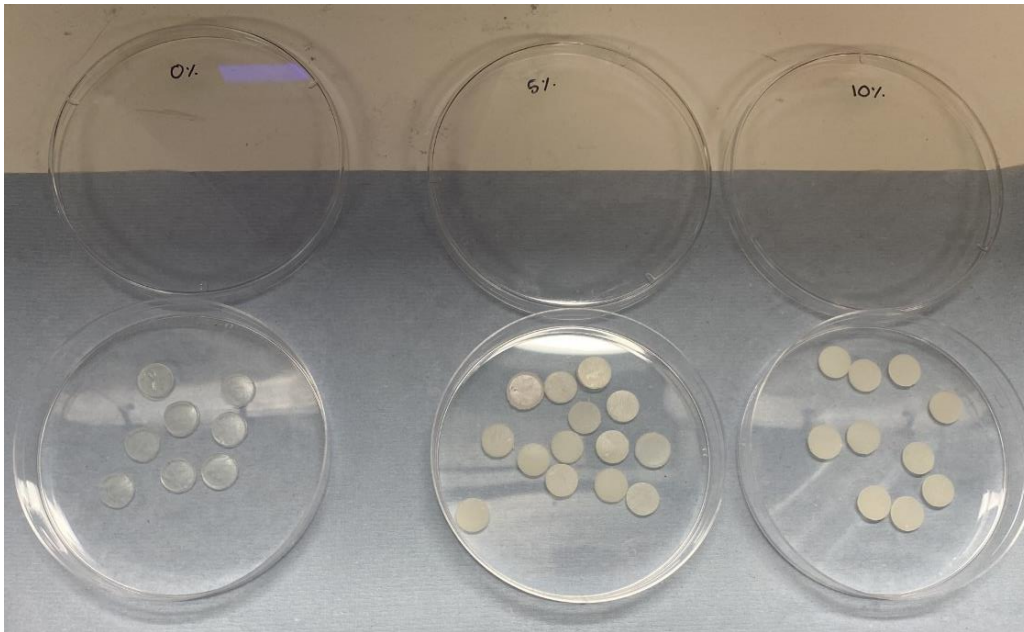


*Figure 2-18: 3D printed composite-polymer discs of 10 mm X 1 mm containing 0, 5 or 10 wt% hydroxyapatite, printed via the XYZ Nobel Superfine DLP printer and post cured via the methanol and UV curing chamber method.*

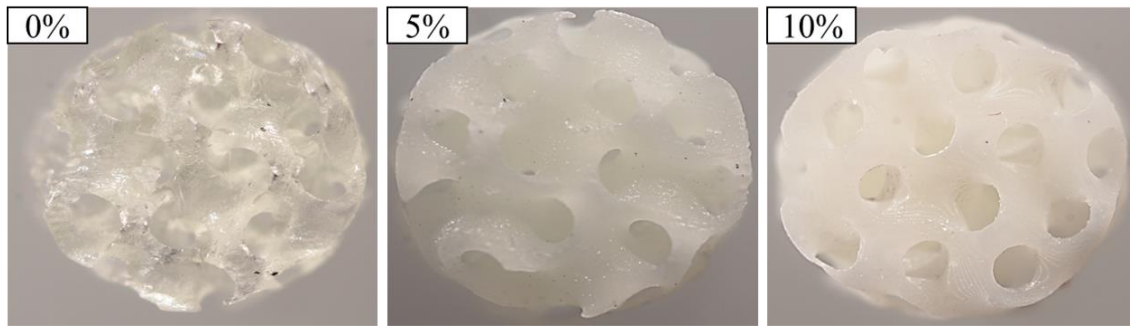


Figure 2-19: 3D printed porous scaffolds containing CSMA-2 + 2 wt% BAPO photoinitiator and either 0 wt% HA (left image) 5 wt% HA (middle image) and 10 wt% HA (right image). All scaffolds were designed using AutoCAD and are 6 mm in diameter and 3 mm thick with pores of 0.5 mm.

When exploring different designs on AutoCAD, a log-pile structure, symbolising how the cortical bone in the human body is built, and a trabecular bone structure were both designed and printed using CSMA-2. Figure 2-20 below shows (left-hand image) the cortical bone log-pile structure, and (right-hand image) the trabecular bone structure after printing via the DLP technique.

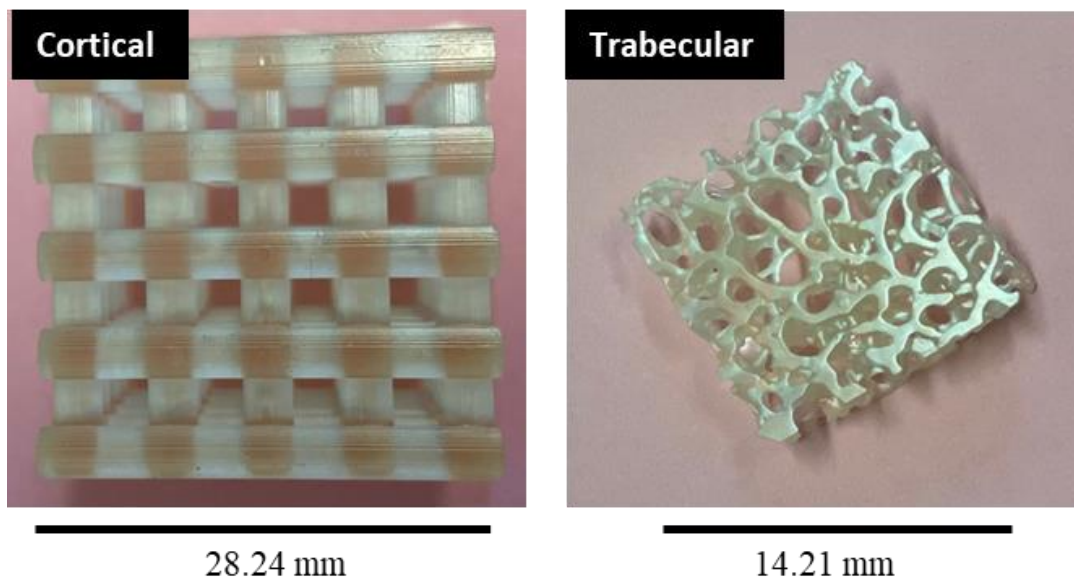


Figure 2-20: Images taken of the log-pile structure symbolising cortical bone, on the left and trabecular bone construct on the right. Both scaffolds were designed using AutoCAD and 3D printed using CSMA-2 with 2 wt% BAPO photoinitiator using the XYZ Nobel Superfine DLP Printer.

### 2.3.4 SEM Analysis

To determine the accuracy of the printing technique, SEM was used to observe constructs to allow for measurement between designed pores.

Figure 2-21 shows a comparison between the 3D printed matrix with cross-sectional dimensions of 0.50 mm X 1.00 mm between the matrixes.

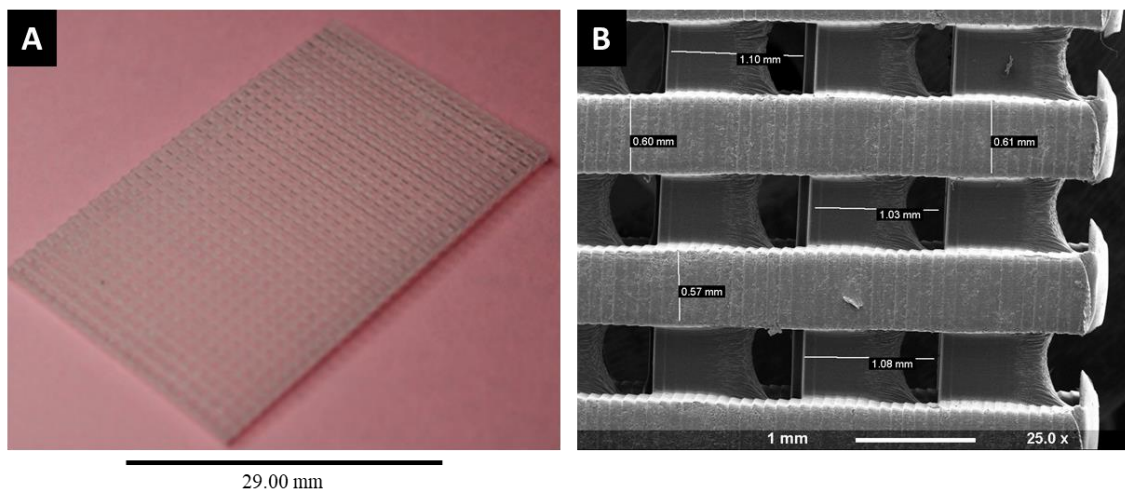


Figure 2-21: Image (A) shows a 3D printed matrix utilising CSMA-2 and 2% BAPO photoinitiator, followed by a matrix viewed via a SEM at 25 X magnification with highlighted dimensions (B).

The dimensions marked in figure 2-21B represent the cross-sectional measures between the matrixes. The cross-sectional dimensions of the original AutoCAD STL file were 0.50 mm x 1.00 mm. After printing and post curing, the SEM shows the dimensions as an average of 0.56 mm  $\pm$  0.10 mm x 0.91 mm  $\pm$  0.14 mm. This is significantly close to the original designed values, suggesting the accuracy of the printer and quality of the resin. The small difference in size could, however, be attributable to a balance between curing time, power intensity, and the amount of photoinitiator utilised.

### 2.3.5 CT Analysis

MicroCT analysis was utilised to evaluate the accuracy of the final product print to the original CAD design using the log-pile structure depicted in figure 2-21. The STL file was imported into the XYZmaker Suite software, and the model was printed with CSMA-2 and 2% BAPO photoinitiator. At the settings listed in section 2.2.8, printing the log structure took 3 hours 11 minutes. Following the completion of the printing, the model was post-cured to remove any leftover residues and firm all portions of the print.

As shown in figure 2-22, CT scans were reconstructed, and the dataset was reoriented so that the cylinders' faces were orthogonal to the view.

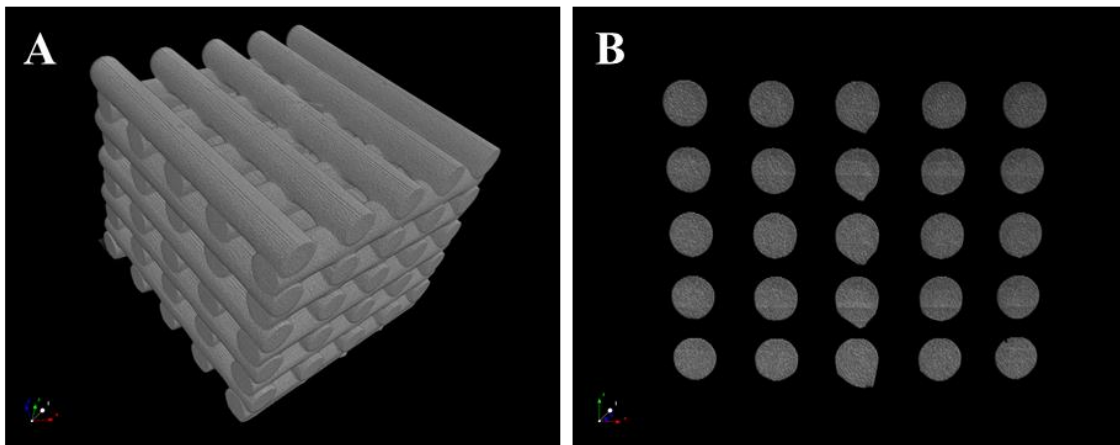


*Figure 2-22: Images of the log-pile structure reoriented using the Bruker MicroCT DataViewer programme to display the faces of the cylinders orthogonal to the perspective of direction. The sliced CAD image (A) displays the faces of the cylinders, whereas (B) shows the faces of the cylinders.*

To compute the area-equivalent circle diameter as well as the cross sectional area, an average of four random orthogonal slices depicting the cross sections of the cylinders were collected from both directions. Table 2-4 below highlights the numerical analysis from the CT scan, suggesting the accuracy of the print.

As seen in the table, the results were very consistent for all the faces of the cylinders and were not too different to the original dimensions from the STL file. The STL file had an area-equivalent circle diameter of  $3.46 \pm 0.20$  mm and a cross sectional area of  $37.96 \pm 4.32$  mm<sup>2</sup>. The average dimensions from the CT analysis were  $3.35 \pm 0.04$  mm and  $34.96 \pm 3.98$  mm<sup>2</sup> for both measurements respectively. The cylinder logs were kept uniform, it may be stated, throughout the printing and post-curing process as the 4 layers measured displayed very similar values ranging between 3.33- 3.36 mm for the area-equivalent circle diameter and 34.41- 35.50 mm<sup>2</sup> for the cross-sectional area.

Table 2-4: The results from the numerical CT scan analysis carried out on the log-pile structure highlighting the accuracy of the 3D printing. 4 orthogonal faces were chosen and measured for their area-equivalent circle diameter as well as their cross-sectional area to compare to the original STL file dimensions (last row).

| <b><u>Slice Number</u></b> | <b><u>Area-equivalent circle diameter (mm)</u></b> | <b><u>Cross sectional area (mm<sup>2</sup>)</u></b> |
|----------------------------|--|---|
| 1                          | 3.33 ± 0.02  | 34.90 ± 5.61  |
| 2                          | 3.34 ± 0.03  | 35.03 ± 0.66  |
| 3                          | 3.36 ± 0.04  | 34.41 ± 8.65  |
| 4                          | 3.36 ± 0.04  | 35.50 ± 1.01  |
| Average                    | 3.35 ± 0.04  | 34.96 ± 3.98  |
| STL Dimensions             | 3.46 ± 0.20  | 37.68 ± 4.32  |

## 2.4 Discussion

In this chapter, a light-curable, degradable polymeric system has been introduced with the potential to be 3D printed into custom-fit implants for use in craniofacial reconstruction surgery. Two types of photoinitiators were explored for their effect on the printability of the material to assess the best formulation to go forward within the study. The 3D printing settings were optimised and adjusted to ensure the accuracy of the constructs that were used for experimental exploration.

In this study, CSMA-2 was successfully synthesised from a reaction incorporating the starting monomer BHIS, in the presence of TEGDMA, HEMA and DBTDL. BHIS, was explored as the starting monomer in the reaction. The direct esterification of isosorbide was performed using potassium carbonate as the catalyst and ethylene carbonate as the water carrier for the reaction. Once the reaction took place after 48 hours, the crude product was filtered via column chromatography using (eluent: methanol/ethyl acetate = 1:9, v/v) to remove all excess solvents and reagents, producing BHIS. A similar material explored by Yu and colleagues (Yu *et al.*, 2019) where they used the same procedure to synthesise a novel bio-based monomer containing mono-acrylated isosorbide as their core scaffold. Isosorbide-based polymers are known to exhibit many excellent properties ranging from their optical clarity to their strong resistance to UV irradiation, heat, chemical degradation, impact, and abrasion (Saxon *et al.*, 2020). In the synthesis of CSMA-2, isosorbide provided core stability for the monomer to photopolymerise under UV light without having a negative impact on the structure of the polymer itself. Carrying out the CSMA-2 reaction in the presence of TEGDMA allowed an enhanced solubility of the final resin as well as a harder material, as TEGDMA acted as a diluent. HEMA was incorporated

in the final stage of synthesis. HEMA will lead the polymerised material to exhibit hydrophilic properties as well as promoting water uptake throughout the polymerisation process. Finally, the use of DBTDL was purely as a catalyst to improve the drying of curing systems, such as CSMA-2. DBTDL can also be used to aid the curing process of a variety of materials such as polyurethanes, silicone resins and silane modified polymers (Matveeva, Efremova and Baranets, 2018).

As discussed, CSMA-2 is modified with functional groups such as acrylates which undergo free-radical polymerisation in the presence of a photoinitiator and upon exposure to light (Chiulan *et al.*, 2021).

Light-curable polymers have a number of advantages, especially in biomedical applications, such as providing a minimally invasive approach, enhanced biological characteristics and the capacity to be crosslinked into dense networks in minutes (or less), giving potential for use in surgery (Di and Yoshihiro, 2014). UV radiation has been found to permeate the skin, allowing for photopolymerisation of injected polymers, which could be useful in plastic and reconstructive surgery, such as craniofacial reconstruction (Stalling, Akintoye and Nicoll, 2009).

Both CQ and BAPO are commercially used as photoinitiators with an amine system, generating primary radicals with light irradiation. The free electrons then attack the double bonds of resin monomers, such as CSMA-2, resulting in photopolymerisation. CQ absorbs very weakly at 468 nm, causing it to have a pale-yellow colour in appearance. On the other hand, BAPO absorbs at a lower 350-380 nm which explains its paler, more white appearance (Meereis *et al.*, 2014). The composite-polymer discs prepared by hand in this study contained 2 wt% CQ photoinitiator. CQ is a widely used



photoinitiator in biomedical applications and is by far the more popular choice in this field due to its well-established reputation and good clinical acceptance (Kamoun *et al.*, 2016). The initial composites were prepared with CQ and investigated for their properties however, it was found that the printability of CQ was not as efficient as BAPO. The 3D printed composite-polymer discs were prepared with 2 wt% BAPO and trialled through the printing process to find the optimum settings. BAPO also referred to commercially as IRGACURE 819, is used in a variety of formulations ranging from coatings on wood and metal, plastics and optical fibres as well as a variety of printing inks and resins (Zhang and Xiao, 2018). BAPO exhibits great curing performance at low concentrations and has very positive absorption properties which allow curing of more viscous materials at a faster rate.

To assess the rate of monomer conversion whilst photo polymerising, the degree of conversion of CSMA-2 was obtained with both initiator systems. Similarly, Galvão and colleagues (Galvão *et al.*, 2013), evaluated the DC of dental composites, finding that the composites tested had values ranging from 55 to 68%, which is the highest possible range for this type of material. The best results in this investigation are similar to the DC values observed for CSMA-2 which ranged between 65-72%. The BAPO photoinitiator formulation exhibited a higher degree of monomer conversion (72%) than the CQ system. This could be because the chemical structure contains more photo-crosslinking groups, allowing for a faster polymerisation time and hence more monomer polymerisation in the same amount of time.

In the fields of regenerative medicine and bone tissue engineering, 3D printing is a new technique that promises significant benefits by addressing present challenges in the development of patient-specific models (Tao *et al.*, 2019). Although the advance

in the field of additive manufacturing has been impactful, there are still quality-related challenges that exist, such as finding optimal materials that fit the specification required to provide a platform for the printable resin.

This chapter further focussed on the potential use of DLP 3D printing techniques in the fabrication of CSMA-2 based composites with the incorporation of two varying photoinitiators and up to 10 wt% HA fillers. This type of 3D printing provided fast light-curing upon photopolymerisation of the monomers. The accuracy of the printing was assessed via SEM imaging and CT analysis by taking various measurements of the final printed scaffold compared to the original CAD STL file. It can be said that using the optimised settings and a maximum of 10 wt% HA filler, CSMA-2 was accurately printed into solid discs, porous scaffolds, cortical bone log-pile structures and a variety of matrixes with different pore sizes.

Tao and associates (Tao *et al.*, 2019) studied applications of 3D printing for craniofacial tissue engineering using hydrogels combined with HA for the purpose of creating periodontal complex scaffolds. In their study, they analysed different types of 3D printing as well as a variety of materials such as polymers, ceramics and composites to find their optimum formulations. They concluded that a 3D printed hydrogel might help odontoblast cells survive in bone and cartilage, and that HA-modified ceramics can boost angiogenesis.

In order to improve the overall print quality, it is critical to achieve a balanced compromise between the amount of photoinitiator of use, cure time and cytotoxicity. A study carried out by Cheng and colleagues (Cheng and Chen, 2017), explored different concentrations of chitosan to add to PCL based resins for DLP 3D printable

scaffolds for tissue engineering applications. Their research looks at how chitosan affects structural wettability, cell adhesion, and cell proliferation. Chitosan is a naturally occurring polymer that is commonly utilised in biomedical materials; however, it has the drawback of having a poor mechanical strength. The findings suggested that chitosan can promote cell adherence and differentiation on the printing resin by tampering PCL's hydrophobic qualities. The work carried out in this thesis compares the effects of varying photoinitiators as well as varying ratios of CaP, HA fillers to the printable CSMA-2 resin.

Similarly, Hong and co-workers (Hong *et al.*, 2020) fabricated a glycidyl-methacrylate based scaffold which was mixed with silk fibroin for the aim of bone tissue engineering. DLP printing allowed the formation of the final Silk-GMA composite through layer by layer deposition of the polymer resin. Rapid printing of this scaffold resulted in good cell biocompatibility and low cytotoxicity which are advantageous in clinical applications.

Despite the abovementioned benefits of 3D printing, particularly DLP lithography, a substantial amount of work is currently dedicated to utilising this technique for printing hydrogel-based scaffolds. Even if the mechanical strength of such systems has improved significantly compared to typical hydrogels, the obtained values in non-load bearing regions are still much below the modulus of bone. Therefore, establishing a novel, mechanically strong and biocompatible synthetic polymer, such as CSMA-2, holds great promise in the field.

3D printing can potentially revolutionise custom-fit implants in the field of craniofacial reconstruction. It is important to mention that depending on the type of printing, cost

limitation can be a matter of concern for this method and clinical applications. Although considered a relatively low-cost manufacturing technique (Poomathi *et al.*, 2020) the price of the starting material, the software of use and the 3D printer device itself must all be considered, especially in larger-scale manufacturing systems. Moreover, the time taken to create the 3D printed models must be considered. The construct size and geometry from the original CAD file, as well as the printing resolution, power intensity and accuracy, are the factors that contribute to the required printing time (Shahrubudin *et al.*, 2020). The optimisable settings allow the user to generate a 3D prototype by facilitating layer-by-layer fabrication of the construct, which can take anywhere between 1 minute to 24 hours.

Furthermore, the aim of additive manufacturing in tissue engineering is the ability to create new tissue or organ scaffolds. Scaffolds are vital in this method because they act as a platform for cell adhesion and cell recruitment to infiltrate deep into the defective area. Thus, the patterning of cells and materials in a printed scaffold would need to be carefully engineered in order for it to give mechanical support and generate an environment similar to that of the organ's native extracellular matrix (ECM) (Wu and Hsu, 2015). Using additive printing techniques, the scaffold's size, geometry, and porosity may be controlled and customised, providing a platform for reproducibility and manipulation.

The previously mentioned challenges need to be addressed to bridge the gap between the current concepts to clinical applications. An approach to address such challenges would be to design materials in a way that ensures faster and more accurate

manufacturing as well as providing optimum biological properties without affecting the mechanical strength.

In this chapter, along with the synthesis of CSMA-2, DLP 3D printing was used for the potential formation of custom-fit implants for smaller defects in the craniofacial region. Using CSMA-2 as the resin for 3D printing has a promising future. The photoinitiators explored allowed optimisation for relatively fast printing and did not affect the mechanical properties or degradation time of the polymer, as confirmed in Chapter 3: Mechanical Properties and Degradation. Moreover, the non-cytotoxic nature of CSMA-2 as well as the ability to promote angiogenesis is confirmed in Chapter 4: Biological Exploration. Furthermore, regarding the printing resolution, a well-balanced system with a suitable compromise between the print time and the resolution can be designed. As seen in the CT analysis (see section **2.3.5**), the CSMA-2 printed construct displayed comparable values between the digital STL file and the final printed model. This confirms the ability of CSMA-2 to be used as a printing resin as it has a well-balanced dispersion of polymer to photoinitiator phases as well as providing good resolution and accurate print.

In summary, using additive manufacturing techniques to create custom-fit implants in the craniofacial region holds great promise. Such techniques can allow for the careful control of the defects distinctive contour while producing optimal printing resolution. This is a critical consideration when designing any biomaterial-based scaffold for tissue engineering since it promotes vascularisation and, eventually, the development of new tissue (Ma *et al.*, 2018). Furthermore, adopting a highly precise and accurate printed model can improve *in vivo* cell adhesion and proliferation which will ultimately

improve the aesthetic and functional outcomes of the bone defect restoration without the need for additional surgery (Aldaadaa, Owji and Knowles, 2018).

## **2.5 Conclusion**

To conclude, the studies carried out in this chapter were to explore the synthesis of an isosorbide-based light-curable, degradable polymeric system to assess its potential use in cranio-maxillofacial reconstruction. The incorporation of calcium phosphate fillers, particularly, hydroxyapatite, as well as the comparison between two different photoinitiator systems. The material was chemically characterised to confirm the synthesis and 3D printing techniques were introduced to explore the materials ability to act as a resin in a DLP type printing system. The printability of the formulations containing 2 wt% CQ or BAPO photoinitiator and 0, 5 and 10 wt% HA filler was investigated throughout the chapter to construct composite-polymer scaffolds for the purpose of assessing the materials mechanical properties as well as the rate of degradation and wettability which is discussed in detail in Chapter 3: Mechanical Properties and Degradation Studies. Further to this, the 3D printed scaffolds were used for the purpose of exploring the materials *in vitro* properties, using cell-culture experimental studies and *ex-ovo*, using the chorioallantoic membrane assay to determine their cytocompatibility and angiogenic response which is discussed in detail in Chapter 4: Biological Exploration.

# **Chapter 3 : Mechanical Properties and Degradation Studies**

### 3.1 Introduction

As previously discussed in Chapter 2: Synthesis and 3D printing of a light-curable degradable polymeric system, the material of choice for creating scaffolds for the purpose of restoring craniofacial defects is critical. An ideal implant material would be mechanically resilient and stable, inert, biocompatible, degrade gradually without being toxic and be easily malleable (Tappa and Jammalamadaka, 2018). Three-dimensional printed natural and synthetic biomaterials have emerged as gold standards for tissue engineering scaffolds in recent decades due to their role in hard tissue regeneration; yet the fundamental disadvantage of these scaffolds is their weak mechanical strength. When utilised in bone tissue engineering, implanted scaffolds are subjected to mechanical stresses such as compression, tension, torsion, and shearing. As a result, mechanical properties are crucial to their *in vivo* performance (Little, Bawolin and Chen, 2011). The structure required for replacement tissue must give appropriate mechanical strength and is thus a significant consideration when developing innovative materials since it must match the native tissues to be restored (Prasadh and Wong, 2018).

The materials studied in this project offer fundamental properties such as mechanical stiffness and good biocompatibility which can be altered and modified via the synthesis process as well as the addition of various amounts of CaP filler.

Young's modulus and tensile strength are key mechanical properties of bone, and a bone scaffold must mimic these mechanical properties to integrate with the bone architecture at a macroscopic level during the implantation stage, and to sustain these properties for regeneration later on (Tian and Chen, 2014). To improve mechanical



properties and promote osteoconductivity, many studies have been conducted where copolymers and bioceramics, such as CaPs have been incorporated into the original polymer (Bruno *et al.*, 2020). The strength, absorption and elasticity of the material in question should be in close association with the mechanical properties of the surrounding bone at the target site as well as retain its properties after implantation. Cortical bone has a strength that varies between 100 – 230 N/mm<sup>2</sup> and materials intended for scaffold use should be similar to this range to prevent the scaffold from failing after being transplanted into the body (Prasadh and Wong, 2018).

In this chapter, the mechanical properties and degradability of CSMA-2 and its composites containing 0-50 wt% HA were assessed alongside the effect of the two varying photoinitiators, CQ and BAPO on the mechanical properties. The mechanical bend strength, Young's modulus, wettability and hardness were explored in detail for formulations containing 0-50 wt% HA which was tested using manually prepared composite-polymer discs made using CQ photoinitiator. Once deciphering the maximum quantity of HA was able to be 3D printed, the formulations containing 0-10 wt% HA created with 2 wt% BAPO photoinitiator and 3D printed were further analysed for their comparative mechanical properties. Remineralisation of the composites was analysed to investigate the surface properties and the potential HA precipitation on the different ratios of CaP filler to CSMA-2. Finally, degradation studies were carried out over 6 months to understand the rate of degradation and the effect of the HA fillers on the degradation time.

As previously discussed in Chapter 1: Introduction and Literature Review, there are a variety of materials available for craniofacial bone regeneration implants. While the materials provided have some good properties, they also have defects, making them

incapable to restore a maxillofacial abnormality to its original state. There is a pressing need to investigate novel materials. A novel substance could assist to lower the likelihood of bone graft complications such as lack of donor bone, graft rejection and infections in the transplanted bone. The properties of an exemplar material should match the need to overcome these deficiencies whilst adapting to the appropriate mechanical, physical and biological properties.

Utilising hydroxyapatite in CSMA-2 composites for the purpose of this study has proven to be beneficial throughout. HA is one of the most important elements in bone and teeth. This bioactive ceramic is a potential biomaterial for bone regeneration due to its strong mechanical properties and favourable biocompatibility. HA possesses suitable osteoconductivity and biocompatibility since it is chemically and physically comparable to the mineral phase of real human bone. The HA particles are known to improve the scaffold's Young's modulus and tensile strength in most cases; however, this is dependent on the type of HA utilised (Corona-Gomez, Chen and Yang, 2016).

The mechanical properties of a material are critical in bone tissue engineering. In this chapter, various conditions have been adapted to assess the effect on the mechanical properties as well as the degradability of the material to find the optimum material formulation that displays potential advancement in this area.

In summary, the main aims and objectives of this chapter are as follows:

1. To assess the mechanical properties of CSMA-2 and its composites including up to 50 wt% hydroxyapatite fillers to find optimum formulations for the purpose of craniofacial implants.
2. Exploration of the effect of two varying photoinitiators on the mechanical properties of CSMA-2 and its composites.
3. Achieving biodegradability explored via degradation studies.

## **3.2 Materials and Methodology**

### **3.2.1 Materials**

The materials used in this chapter were previously discussed in Chapter 2: Synthesis and 3D printing of a light-curable degradable polymeric system (CSMA-2) and were either prepared by hand or 3D printing via DLP technology for the purpose of mechanical testing and degradation studies.

### **3.2.2 Mechanical testing**

#### ***3.2.2.1 Biaxial flexural testing***

Shimadzu Autograph AGS-X machinery (Shimadzu, Milton Keynes, United Kingdom) was used to perform a 3-point biaxial flexural test, which required applying a load via a 2 kN load cell at a displacement rate of 1 mm min<sup>-1</sup> in order to investigate and characterise the mechanical properties of the monomer alongside the composite-polymer discs. 10 samples were tested for the purpose of reproducibility. Origin Pro 2019 software was used to analyse the data. The biaxial flexural test was performed for ten specimens in each group until specimen failure. Prior to loading the specimens in the rig, callipers were used to measure the thickness (~1mm) and the diameter (~10mm) of each disc which was inputted into the system to calculate the equations needed for the test. The results of these tests allowed for the determination of the materials' flexural strength and Young's modulus. The flexural strength of a material, also known as bend strength, represents the material's maximum stress at the point of yield. The Young's modulus, also known as the modulus of elasticity, is a measurement of a material's stiffness that is determined using the formula shown below in equation 3-1

$$E = \frac{\sigma}{\epsilon}$$

*Equation 3-1: Equation showing how to calculate the Young's modulus where E represents the Young's modulus in pressure units,  $\sigma$  represents uniaxial stress, or uniaxial force per unit surface in pressure units and  $\epsilon$  represents the strain, or proportional deformation and is dimensionless.*

### **3.2.2.2 Dynamic Mechanical Analysis**

The three-point bend test via the DMA was used to determine the reproducibility of techniques, as well as the Young's modulus. The composite-polymer bars with nominal dimensions of 5 mm in width X 1 mm thick X 20 mm in length were bent at 1 mm<sup>-1</sup> on a 3-point bending rig until the instrument load limit of 18 N was reached. The modulus was calculated using the TA Instruments TRIOS programme to analyse the collected data. 10 samples were tested for the purpose of reproducibility. As the specimens did not reach a failure point, the bend strength could not be measured using the 3-point bending DMA method.

### **3.2.2.3 Hardness testing**

A Wallace Micro-hardness tester (Wallace Instruments, United Kingdom).was used to determine the hardness of the composite-polymer specimens. 10 samples were tested for the purpose of reproducibility. Micro hardness testing methods are to determine a material's hardness or its resistance to penetration. The Vickers pyramid number (HV), which is determined by the equation, is the unit of hardness supplied by the equation 3-2 below,

$$HV = \frac{F}{A}$$

*Equation 3-2: The Vickers pyramid number (HV) is an equation for determining the hardness of a material, where F is the force applied to the diamond in kg-force (kgf) and A is the surface area of the resulting indentation in square millimetres (mm<sup>2</sup>).*

To convert Vickers numbers (HV) into SI units, the force applied from kgf is converted to newtons and the area is converted from mm<sup>2</sup> to m<sup>2</sup> to give the results in Pascals as 1kgf/mm<sup>2</sup> – 9.80665x10<sup>6</sup> Pa.

#### **3.2.2.4 Water Contact Angle Measurement**

Water contact angle measurements were taken to determine the hydrophilic/hydrophobic nature of the composite-polymer samples and the influence of different CaP addition ratios into the composite. This was performed using a CAM 200 Optical Contact Angle Meter instrument (KSV Instruments, Finland) and the angles were obtained upon encounter of the specimen surface with the water droplet and were measured between the sample surface-water interface and the water-air interface. Hydrophilic samples have contact angles less than 80°, while hydrophobic samples have contact angles more than 90°.

### **3.2.3 Remineralisation Properties**

#### **3.2.3.1 X-Ray Diffraction**

To identify and investigate the precipitation of calcium phosphate crystals, X-ray diffraction (XRD) was used. The atomic and molecular structure of the specimen determines the scattering of the x-ray beam diffraction. The composite polymer discs including 0-50% HA with CQ photoinitiator and 0-10% HA with BAPO photoinitiator were placed in flat plate geometry on the instrument and XRD spectra were acquired with Ni filtered Cu Ka radiation using a Brüker D8 advance diffractometer (Bruker, Coventry, United Kingdom). Data were collected using a Lynx eye detector with an incident slit of 0.2 mm and step size of 0.019° over a 2θ range of 10–100°.

#### **3.2.3.2 Scanning Electron Microscopy**

SEM is a type of electron microscopy that creates images by scanning a material's surface with a focused beam of electrons (Raghavendra and Pullaiah, 2018). Signals are produced in correlation with composition of the specimen to give qualitative visualisation of the surface of the composite-polymer discs. All specimens were fixed in 3% glutaraldehyde (Agar Scientific, United Kingdom) in 0.1M cacodylate buffer (CAB) for 24 hours at 4°C. The samples were then mounted onto aluminium pin stubs, taking care with orientation, double-sided carbon tabs (Agar Scientific, United Kingdom). The samples are sputter coated with 95% gold and 5% palladium (Polaron E5000, Quorum Technology, United Kingdom) before being placed in the SEM where samples are examined in a ZEISS EVO MA10 (ZEISS, United Kingdom) operating at

10kV, spot size 300 for imaging to visualise the surface properties of the composite-polymer specimen discs.

### **3.2.4 Degradation Studies**

#### **3.2.4.1 pH Values**

Three discs from each variant (0, 5 and 10% HA) were immersed in 10 ml of Dulbecco's modified Eagle's medium (Gibco®, Life Technologies Ltd., Paisley, United Kingdom) and placed in a CO<sub>2</sub> incubator overnight to determine the acidity of the composite-polymer specimens. The pH of each disc was then measured by an Orion star A111 pH meter (Thermo Scientific, United Kingdom) which had been calibrated using standard solutions of pH 4 and 7. Measuring the acidity of the polymeric system provides an initial indication of the composites ability to act as a compatible resin.

#### **3.2.4.2 Percentage Mass Change**

To determine the degradation rate of the polymer itself as well as with 5 wt% and 10 wt% CaP incorporated, CSMA-2 plus the appropriate amount of HA were soaked in 10ml of PBS (pH 7.4 ± 0.1) and incubated at the physiological temperature of 37°C and a set incubated at 60°C for the duration of 6 months. The mass change of the composite-polymer discs were assessed at the following time intervals; day 1, 4, 7, 14, 28, 56, 84, 112, 140 and 168. 10 samples were tested for the purpose of reproducibility. At each of the given time points the discs were manually dried for 1 minute using laboratory provided blue paper and weighed using an analytical balance



accurate to 4 decimal places (OHAUS, US). For each time point until the final at day 168 (6 months), the discs were re-immersed in fresh PBS. The final weight measurement was recorded by transferring the specimens to a vacuum oven for two hours at 40°C before placing on the analytical balance and recording the weight.

The equation below was used to calculate the percentage mass change.

$$\% \text{ Mass Change} = \frac{\text{Final dry weight} - \text{Initial weight}}{\text{Initial weight}} \times 100$$

*Equation 3-3 : Equation showing how the percentage mass change was calculated for degradation studies.*

### **3.2.4.3 Biaxial Flexural Testing After Degradation**

Like the percentage mass change experiment described in section 3.2.4.2, composite-polymer discs with 0, 5 and 10 wt% of HA were incubated in 10ml of PBS at 37°C. Prior to incubation, 10 samples of each variation were tested on the Shimadzu as seen in section 3.2.2.1. Biaxial flexural testing was carried out to assess the samples bend strength and Young's modulus. 10 samples were tested for the purpose of reproducibility. After incubation for 1, 2, 3, 4, 5, and 6 months, the specimens were taken from the PBS and manually dried for 1 minute with blue paper towels before being measured and mechanically evaluated using the biaxial flexural method. Again, specimens were measured using callipers and found to be ~1mm thick and ~10mm in diameter. All sample variations had 10 repeats which were then tested, and the results

analysed using OriginPro 2019 software to determine the effect of degradation of the polymer on the mechanical properties.

### **3.2.5 Statistical Analysis**

In this chapter, all data were analysed using OriginPro 2020 (OriginPro, OriginLab Corporation, USA). The results are presented in mean  $\pm$  standard deviation. A one-way analysis of variance with Tukey's post hoc test was used throughout where  $p < 0.05$  was considered significant after being calculated at a 95% confidence interval.

## **3.3 Results**

### **3.3.1 Mechanical testing**

#### **3.3.1.1 *Biaxial Flexural Test***

A biaxial flexural test was used to assess the polymer and composite discs' flexural bend strength and Young's modulus values. The initial comparison was with the manually prepared composite-polymer discs of 2 wt% CQ and 0-50 wt% hydroxyapatite.

Figure 3-1 displays the bend strength results from the biaxial flexural test for the composite-polymer discs using 0-5 wt% HA. It can be seen that CSMA-2 with no added hydroxyapatite had the highest recorded bend strength value of 84.07 N/mm<sup>2</sup>. As the

amount of HA was increased from 1-5 wt%, the samples failed at lower values meaning lower loads were needed to fracture the material with higher amounts of CaP. The only statistically significantly different result was that of 5 wt% with a given value of 75.46 N/mm<sup>2</sup>.

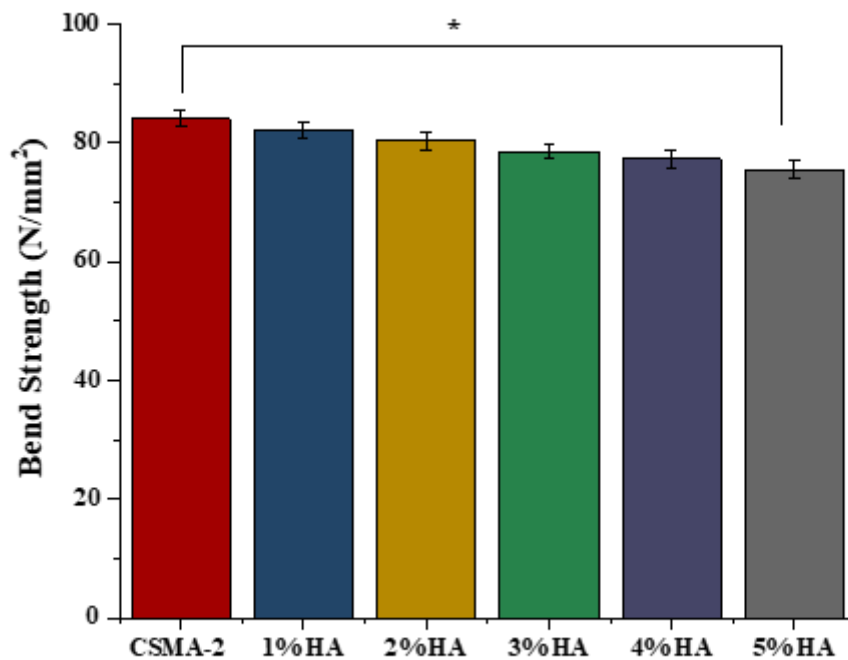


Figure 3-1: A graphical representation for the comparison of bend strength results from the biaxial flexural test done via the Shimadzu for composite-polymer discs with 2 wt% CQ and a range of 0-5 wt% HA. The highest recorded value was 84.07 N/mm<sup>2</sup> for CSMA-2 with 2 wt% CQ and no added HA. The lowest value recorded was 75.46 N/mm<sup>2</sup> for the 5 wt% HA composite polymer which was statistically significant with the result of the CSMA-2 polymer composite by itself. (\**p* < 0.05)

Composite polymer discs containing up to 50 wt% HA were also tested for the purpose of bend strength measurements. Figure 3-2 displays the bend strength results from the biaxial flexural test for the composite-polymer discs using 0-50 wt% HA. Similar to

the results shown in figure 3-1, CSMA-2 with no added HA had the highest recorded bend strength value of 84.07 N/mm<sup>2</sup>. As the amount of HA was increased from 10-50 wt%, the samples failed at lower values meaning lower loads were needed to fracture the material with higher amounts of CaP. The results for CSMA-2 alone were statistically significantly different to the results of the composite-polymer specimen containing 30 wt% at a value of 65.32 N/mm<sup>2</sup>, 40 wt% at a value of 63.50 N/mm<sup>2</sup> and finally the lowest value of 59.51 N/mm<sup>2</sup> for the composite sample containing 50 wt% HA.

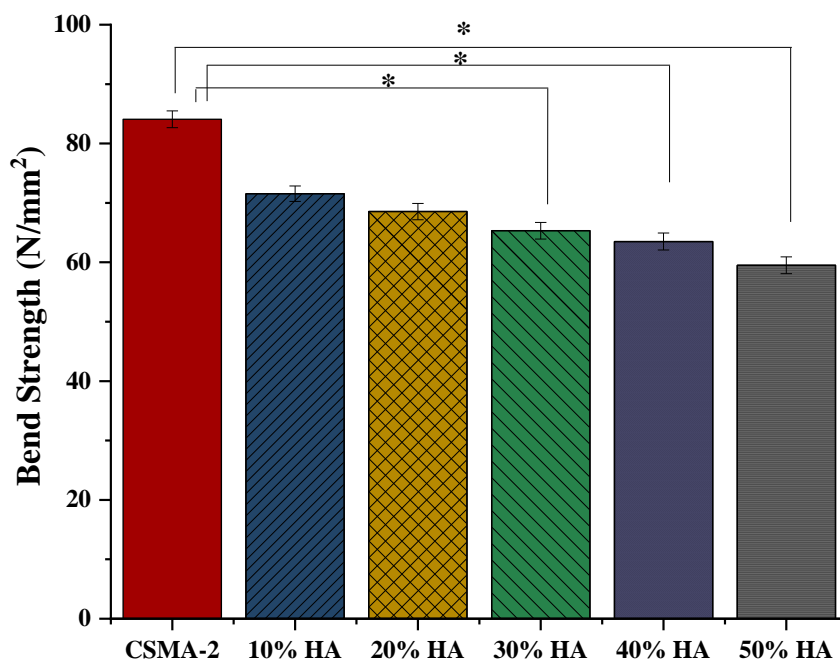


Figure 3-2: A graphical representation for the comparison of bend strength results from the biaxial flexural test done via the Shimadzu for composite-polymer discs with 2 wt% CQ and a range of 0-50 wt% HA. The highest recorded value was again, 84.07 N/mm<sup>2</sup> for CSMA-2 with 2 wt% CQ and no added HA. This was statistically significantly different to the value recorded for 30 wt% HA (65.31 N/mm<sup>2</sup>), 40 wt% (63.50 N/mm<sup>2</sup>) and the lowest value recorded which was 59.51 N/mm<sup>2</sup> for the 50 wt% HA composite polymer (\*p < 0.05).

The Young's modulus was tested via the same biaxial flexural method as the bend strength. Figure 3-3 below represents the modulus results from the biaxial flexural test done via the Shimadzu for the composite-polymer samples containing 2 wt% CQ photoinitiator and 0-5 wt% hydroxyapatite. The polymer itself, CSMA-2 has a Young's modulus value of 2.44 kN/mm<sup>2</sup> which is significantly stiffer than when HA is incorporated. The Young's modulus value for CSMA-2 is statistically significantly different at \*p<0.05 to the value for 3 wt% HA and the value for 5 wt% HA which is the lowest value at 1.96 kN/mm<sup>2</sup>.

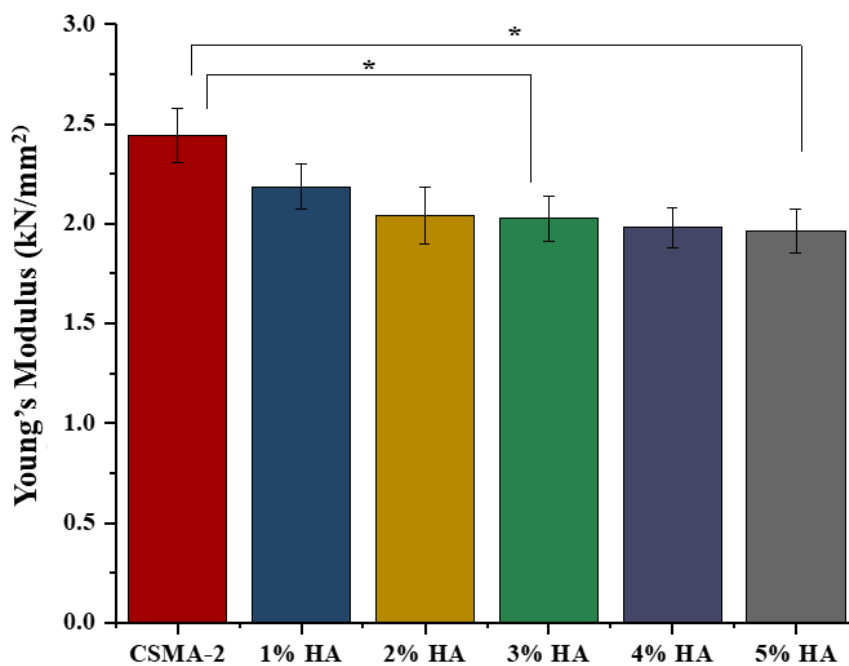


Figure 3-3: A graphical representation for the comparison of Young's Modulus results from the biaxial flexural test done via the Shimadzu for composite-polymer discs with 2 wt% CQ and a range of 0-5 wt% HA. The highest recorded value was 2.44 kN/mm<sup>2</sup> for CSMA-2 with 2 wt% CQ and no added HA. This was statistically significantly

*different to the lowest value recorded which was 1.96 kN/mm<sup>2</sup> for the 5 wt% HA composite polymers as well as the result for the 3 wt% HA composite-polymer sample which had a result of 2.02 kN/mm<sup>2</sup> (\*p < 0.05)*

Again, composite-polymer discs containing up to 50% Figure 3-4 displays the Young's modulus results from the biaxial flexural test for the composite-polymer discs using 0-50 wt% HA. Similar to the results shown in figure 3-3, CSMA-2 with no added HA had the highest recorded modulus value of 2.44 kN/mm<sup>2</sup>. It can be seen that the composites become less stiff as more HA is incorporated. Although there are small amounts of significant difference between the formulations, a slightly higher value was observed in the 50 wt% composite (1.89 kN/mm<sup>2</sup>) suggesting that the addition of a higher quantity of calcium phosphate caused an increase in the stiffness of the material.

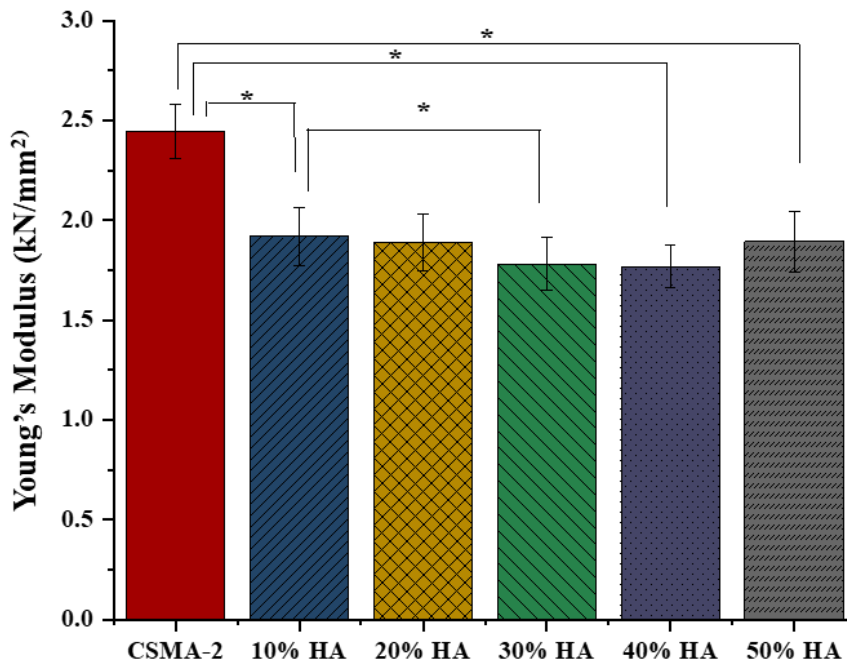


Figure 3-4: A graphical representation for the comparison of Young's Modulus results from the biaxial flexural test done via the Shimadzu for composite-polymer discs with 2 wt% CQ and a range of 0-50 wt% HA. The highest recorded value was 2.44 kN/mm<sup>2</sup> for CSMA-2 with 2 wt% CQ and no added HA. This was statistically significantly different to the lowest value recorded which was 1.76 kN/mm<sup>2</sup> for the 40 wt% HA composite polymers as well as the result for the 50 wt% HA composite-polymer sample which had a result of 1.89 kN/mm<sup>2</sup> (\* $p < 0.05$ ).

### 3.3.1.2 Hardness Testing

The Hardness of the polymer and the composite discs were investigated by running a Vickers Hardness test. The initial comparison was with the manually prepared composite-polymer discs of 2 wt% camphorquinone and 0-50 wt% hydroxyapatite.

Figure 3-5 below shows the Vickers Hardness results for the 0-10 wt% HA incorporated composite-polymer specimens. As seen, CSMA-2 by itself, represented by the 0 wt% column, has a VHN of 7.54 g/mm<sup>2</sup> which increases to 8.04 g/mm<sup>2</sup> at 5

wt% HA. The results show only a small significant difference as the quantity of HA increases.

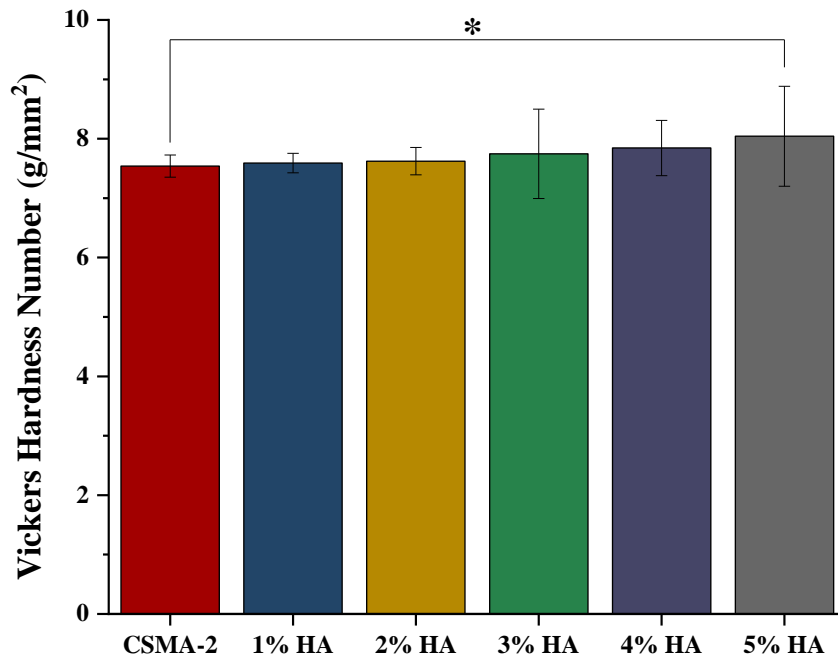


Figure 3-5: A graphical representation for the comparison of hardness results from the Vickers Hardness test done via the Wallace Micro-Hardness Tester for composite-polymer discs with 2 wt% CQ and a range of 0-5 wt% HA. The lowest recorded value was 7.54 g/mm<sup>2</sup> for CSMA-2 with 2 wt% CQ and no added HA. The highest value recorded was 8.04 g/mm<sup>2</sup> for the 5 wt% HA composite polymer which was statistically significant with the result of the CSMA-2 polymer composite by itself. (\* $p < 0.05$ )

Composite polymer discs containing up to 50 wt% HA were also tested for the purpose of hardness measurements. Figure 3-6 below displays the VHN results from the hardness test for the composite-polymer discs using 0-50 wt% HA. Similar to the results shown in figure 3-6, CSMA-2 with no added hydroxyapatite had the lowest recorded hardness value of 7.54 g/mm<sup>2</sup>. As the amount of HA was increased from 10-



50 wt%, the samples became harder. The results for CSMA-2 alone were statistically significantly different to the results of the composite-polymer specimen containing 40 wt% at a value of 14.28 g/mm<sup>2</sup> and 50 wt% HA at a value of 21.47 g/mm<sup>2</sup>.

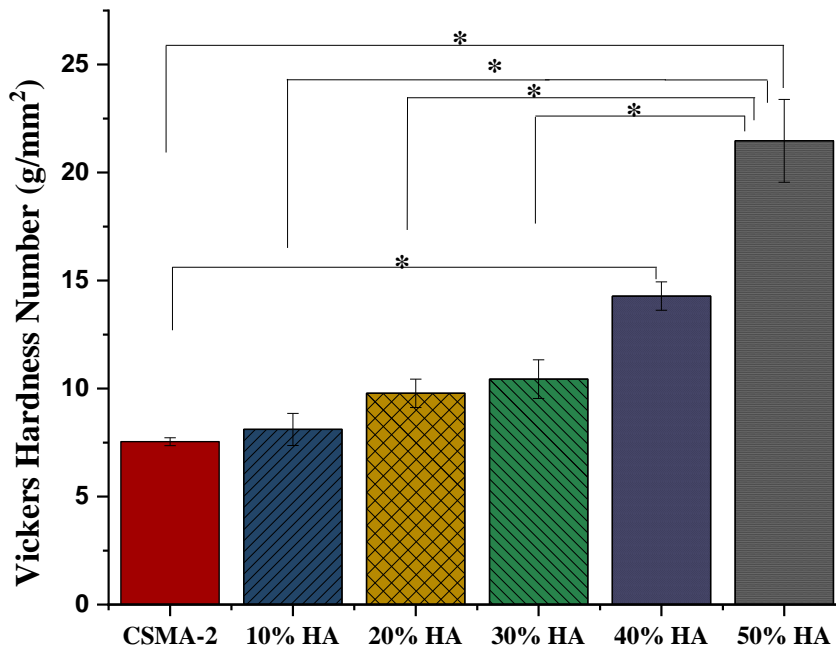


Figure 3-6: A graphical representation for the comparison of hardness results from the Vickers Hardness test done via the Wallace Micro-Hardness Tester for composite-polymer discs with 2 wt% CQ and a range of 0-50 wt% HA. The lowest recorded value was 7.54 g/mm<sup>2</sup> for CSMA-2 with 2 wt% CQ and no added HA. The highest value recorded was 21.47 g/mm<sup>2</sup> for the 50 wt% HA composite polymer which was statistically significant with the result of the CSMA-2 polymer composite by itself as well as the values for all the HA-incorporated composites 10-40 wt%. (\*p < 0.05)

### **3.3.1.3 Water Contact Angle**

Water contact angle measurements were analysed for CSMA-2 with no added CaP filler as well as 10-50 wt% HA incorporated composite polymer discs. The results (shown in figure 3-7 below) confirmed the hydrophilic nature of the monomer and the range of hydroxyapatite fillers. As expected, the addition of CaP fillers had a direct correlation with hydrophilicity of the composites; The 50 wt% HA formulations showed the most hydrophilic behaviour as it had a contact angle measurement of 42°. This was not significantly lower than the formulations of 10-40 wt% which had values between 54° and 46°. The CSMA-2 monomer with no added HA was the least hydrophilic out of the group with a contact angle measurement of 59° however, this was still well within the hydrophilic range as if a contact angle is smaller than 90°, the solid is considered hydrophilic (Fowkes, 1964).

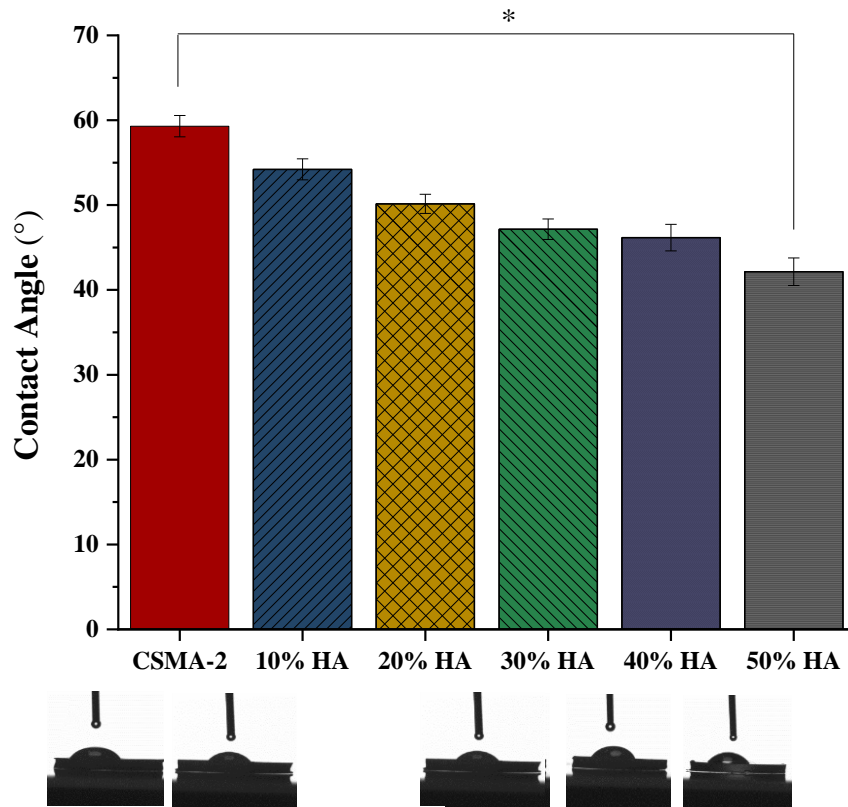


Figure 3-7: Water contact angle measurements investigating the hydrophilicity of the polymer with no added HA compared to HA incorporated composite discs: a direct correlation can be observed between hydrophilicity and addition of CaP fillers. The 50 wt% formulation showed the most hydrophilic behaviour (however not statistically significant,  $*P > 0.05$ , from the 10-40 wt% formulation) but statistically significantly different to CSMA-2 alone which had the highest contact angle measurement of  $59^\circ$  showing the least hydrophilic behaviour out of the composites but still exhibiting hydrophilicity as the angle is smaller than  $90^\circ$ . ( $*p < 0.05$ ).

### 3.3.2 Comparing CQ Vs. BAPO Mechanically

Mechanical testing was carried out for the purpose of comparing the results of these specimens with CQ and BAPO as the photoinitiator in question in order to decipher the optimum formulation for its intended purpose. The Bend strength, Young's Modulus,

Hardness and Hydrophilicity was tested again for the specimens with both types of photoinitiator.

### **3.3.2.1 Bend Strength and Young's Modulus**

The biaxial flexural test was performed via the Shimadzu as previously mentioned, for the composite-polymer samples containing 0-10 wt% HA and either 2 wt% CQ or 2 wt% BAPO photoinitiator.

Figure 3-8 below shows the results from the biaxial flexural test for the purpose of bend strength measurement for these specimens comparing the results between the CQ groups and BAPO groups with the addition of either 0, 5 or 10 wt% HA. As seen in the graph below, the bend strength values were higher in the BAPO formulations, ranging between 135.49-98.57 N/mm<sup>2</sup>, than those of CQ, which ranged between 84.07-71.55 N/mm<sup>2</sup>. The results for both formulations decreased significantly with higher amounts of HA, suggesting a less stiff material being formed.

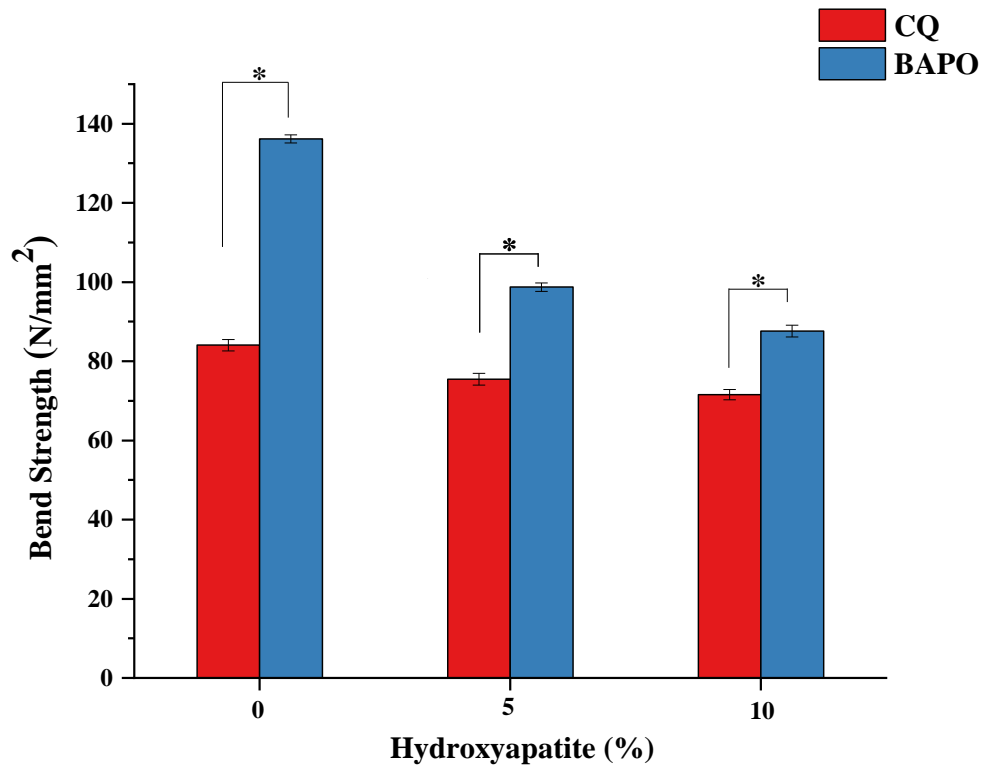


Figure 3-8: A graphical representation for the comparison of flexural strength results from the biaxial flexural test done via the Shimadzu for composite-polymer discs with 2 wt% CQ (red) and a range of 0-10 wt% HA vs. composite-polymer discs with 2 wt% BAPO (blue) and a range of 0-10 wt% HA. The highest recorded value was 135.49 N/mm<sup>2</sup> for CSMA-2 with 2 wt% BAPO and no added HA. All CQ values were significantly lower than their respective BAPO incorporated values (\*p < 0.05).

The Young's Modulus was also evaluated for the purpose of comparing the CQ formulations against BAPO formulations with 0-10 wt% HA incorporated. For the purpose of repeatability, the Young's modulus values of the 0-10 wt% HA samples with 2 wt% BAPO photoinitiator were also determined using the three-point bend test via the DMA. Figure 3-9 below shows the graphical representation for these results highlighting that BAPO (shown in blue) had a significant impact on the elasticity of the composites with modulus values ranging between 1.96-1.71kN/mm<sup>2</sup> which

significantly compares to the CQ values (shown in red) which range between 2.44-1.66 kN/mm<sup>2</sup>. As well as BAPO having an effect, the higher amounts of HA also lowered the Young's Modulus values, leading to a more elastic material. The DMA tested modulus did not show any significant difference with modulus values of 1.855 kN/mm<sup>2</sup> for CSMA-2 with no added HA, 1.75 kN/mm<sup>2</sup> for 5 wt% and 1.68 kN/mm<sup>2</sup> for the 10 wt% HA formulation. The trend is also consistent with the results from the biaxial flexural test method in the sense that as the HA amount increases, the modulus decreases, leading to a more elastic material.

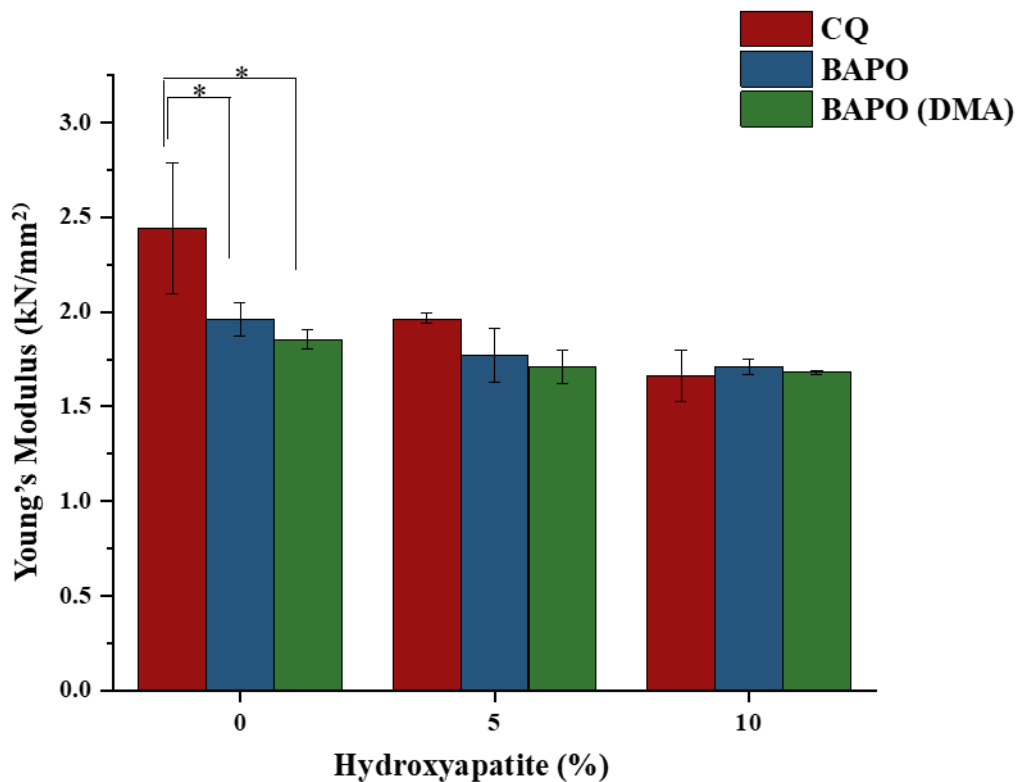


Figure 3-9: A graphical representation for the comparison of Young's Modulus results from the biaxial flexural test done via the Shimadzu for composite-polymer discs with 2 wt% CQ (red) and a range of 0-10 wt% HA vs. composite-polymer discs with 2 wt% BAPO (blue) and a range of 0-10 wt% HA as well as comparing the Young's modulus results from the DMA test. The highest recorded value was 2.44 kN/mm<sup>2</sup> for CSMA-2 with 2 wt% CQ

and no added HA. This was statistically significantly different to the respective values with BAPO and the BAPO formulations carried out via DMA (\* $p < 0.05$ ).

### **3.3.2.2 Hardness Testing**

The hardness of the composite-polymer discs containing 0-10 wt% HA with either 2 wt% CQ or 2 wt% BAPO were evaluated and compared using the Vickers Hardness method as previously carried out.

The hardness measurements for CSMA-2 and composite discs containing 0%–10% HA (figure 3-10) reveal that as the amount of HA increases, so does the amount of CQ and BAPO integrated therein, implying that the material gets harder. As seen, CSMA-2 by itself, represented by the 0 wt% columns, has a VHN of 7.54 g/mm<sup>2</sup> for the CQ value and 8.21 g/mm<sup>2</sup> for the BAPO value which increases with the higher amounts of HA. The results for the CQ formulations had lower VHN values than the BAPO formulations as the CQ ranged from 7.54-8.09 g/mm<sup>2</sup> which were all statistically significantly different at  $p^* < 0.05$  to the BAPO formulations ranging from 8.21-9.79 g/mm<sup>2</sup>.

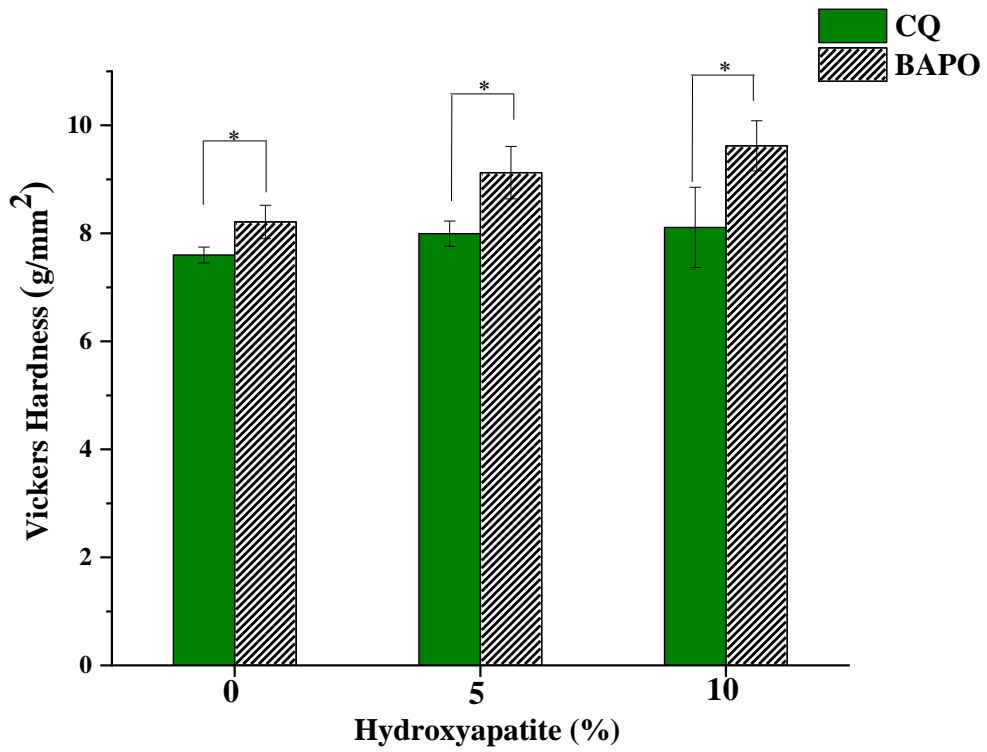


Figure 3-10: A graphical representation for the comparison of hardness results from the Vickers Hardness test done via the Wallace Micro-Hardness Tester for composite-polymer discs with 2 wt% CQ (green) and a range of 0-10 wt% HA vs. composite-polymer discs with 2 wt% BAPO (white) and a range of 0-10 wt% HA. The CQ values ranged from 7.54-8.09 g/mm<sup>2</sup> for CSMA-2 which compare to the BAPO values which ranged from 8.21-9.79 g/mm<sup>2</sup>. All CQ incorporated formulations had significantly lower hardness values than their respective BAPO incorporated formulations (\**p* < 0.05).



### **3.3.2.3 Water Contact Angle**

The hydrophilicity of the composite-polymer discs containing 0-10 wt% HA with either wt% CQ or 2 wt% BAPO were evaluated and compared using the water contact angle measurement method as previously carried out.

The contact angle measurements for CSMA-2 and composite discs containing 0%–10% CaP (figure 3-11) show that the CQ and BAPO included formulations decrease as the quantity of HA increases, implying that the material becomes more hydrophilic as the amount of HA increases. As seen, CSMA-2 by itself, represented by the 0 wt% columns, has a contact angle measurement of 59° for the CQ value and 54° for the BAPO value which was statistically significant and which decreases with the higher amounts of HA. The difference between the CQ and BAPO formulations for the water contact angle measurements were not statistically significantly different at  $p^* < 0.05$  for the 5 and 10 wt% HA formulations but did have slight differences in the range of values. The results for the CQ formulations had slightly higher WCA values than the BAPO formulations as the CQ ranged from 55°-59 and the BAPO formulations which ranged between 54°-55°. The results confirmed the hydrophilic nature of the monomer and the range of hydroxyapatite fillers. As expected, the addition of CaP fillers had a direct correlation with hydrophilicity of the composites.

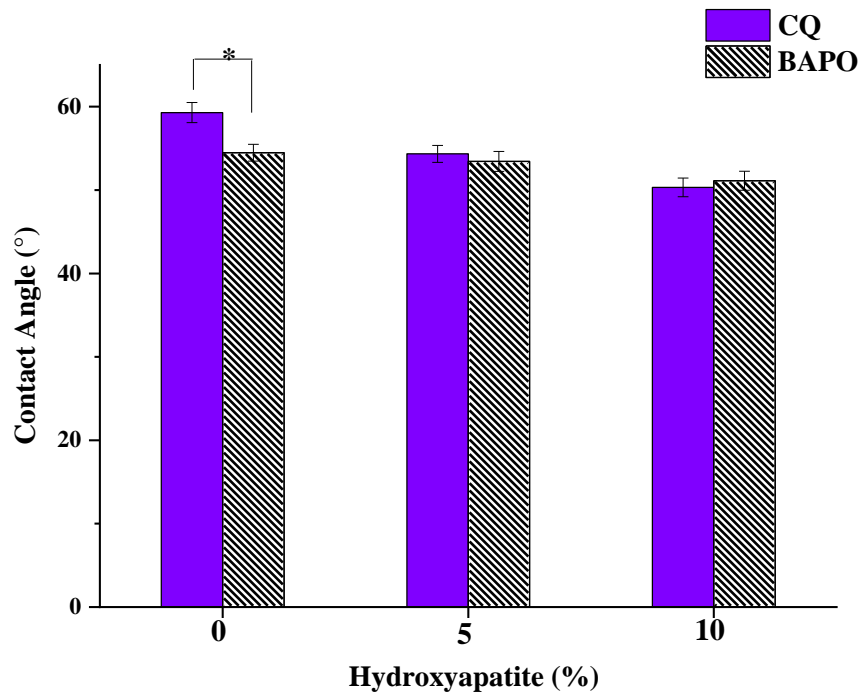


Figure 3-11: A graphical representation for the comparison of the contact angle measurements for the purpose of investigating the hydrophilicity of the composite-polymer discs with 2 wt% CQ (purple) and a range of 0-10 wt% HA vs. composite-polymer discs with 2 wt% BAPO (white) and a range of 0-10 wt% HA. The CQ values range from 54°-59° which compare to the BAPO values which ranges from 54°- 55°. A direct correlation can be observed between the hydrophilicity and the addition of CaP fillers. (\* $p < 0.05$ )

### 3.3.3 Remineralisation Properties

#### 3.3.3.1 Scanning Electron Microscopy

In order to investigate surface remineralisation and potential hydroxyapatite precipitation of the different ratios of CaP filler to CSMA-2, scanning electron microscopy was used. The SEM images, shown in Figure 3-12 present a series of images of CaP deposition on the surface of the composite-polymer discs. CSMA-2 by itself with no added hydroxyapatite, shows a smooth layer with no clumps or material

bubbles. A slight scratch seems to be present which could be from handling of the sample. More HA particles were visible on the surface of the composite-polymer discs as the amount of HA grew from 10 to 50 wt% resulting in a continuous layer of merged crystals. These images justify the results for the mechanical properties as they suggest each specimen had a good distribution of calcium phosphate and the polymer was well immersed in it.

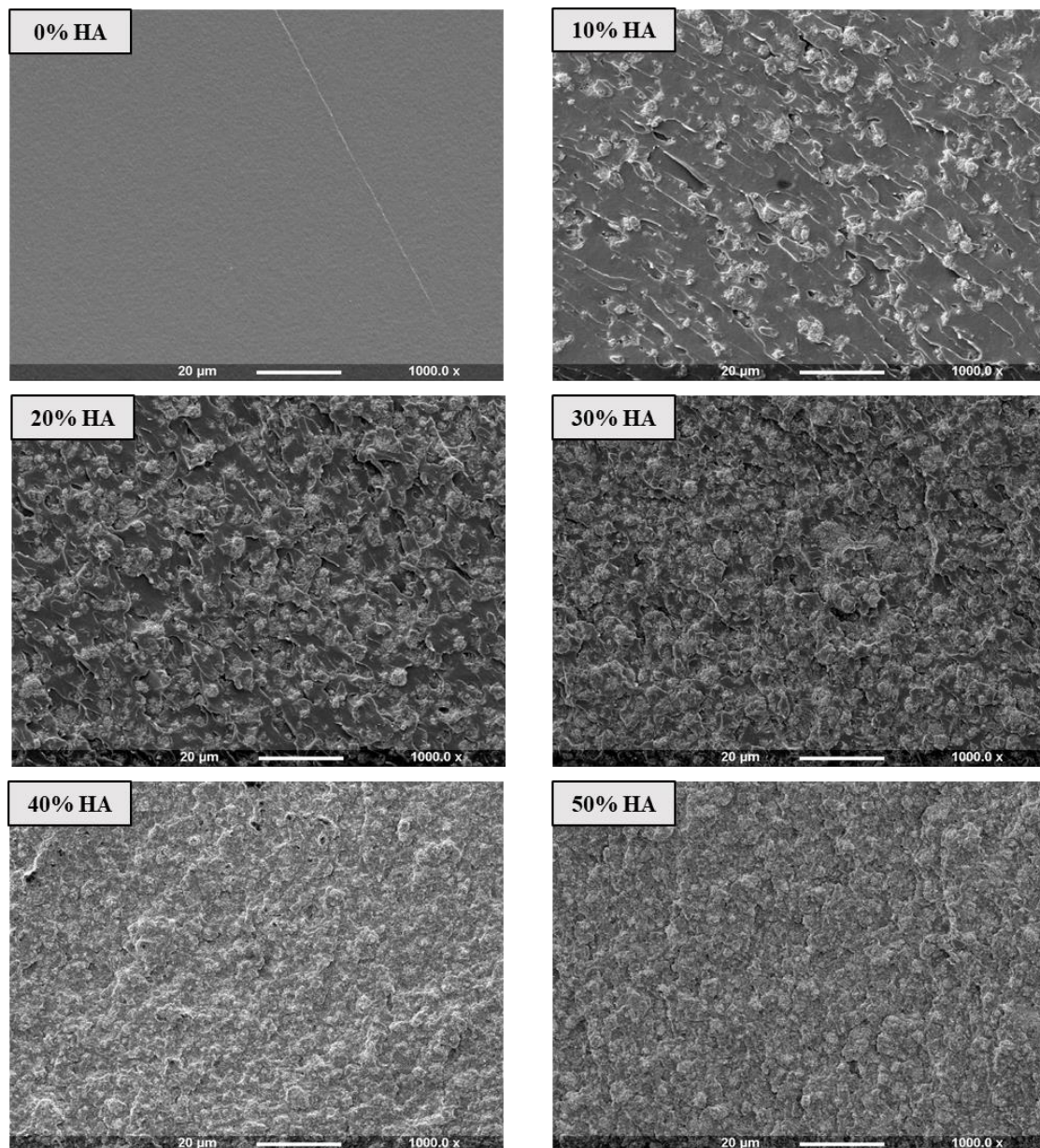


Figure 3-12: SEM images highlighting the surface remineralisation of 0-50 wt% HA incorporated composite-polymer discs. Deposition of HA particles can be clearly observed on the surface of the discs as the quantity increased. The first image, CSMA-2 alone with no added HA, showed a clear surface with no particles attached. By 50 wt% HA, there was a significantly greater amount of HA particles dispersed on the surface of the discs which are shown to be a continuous layer of merged crystals.

### **3.3.3.2 X-Ray Diffraction**

Subsequently, the presence of CaP precipitates observed via SEM microscopy was confirmed through XRD analysis. XRD analysis is a non-destructive test method for examining crystalline materials' structure. This diffraction technique precisely examines the formation of precipitates inside the CaP incorporated samples. The composite-polymer discs made manually by hand, using 2 wt% CQ photoinitiator were analysed using XRD to assess the mineralisation of HA. As seen in figure 3-13, the samples containing 10-50 wt% HA have a significant HA diffraction peak in comparison to the polymer by itself (represented in black).

Figure 3-14 displays the XRD analysis for the 3D printed composite-polymer samples prepared with 2 wt% BAPO photoinitiator along with 0-10 w% HA. Similar results can be seen here, where the HA diffraction peak is observed in the 5 and 10 wt% samples and not in the polymer by itself. It can be said that the photoinitiator did not have an impact on the XRD results as neither CQ nor BAPO have a crystalline structure.

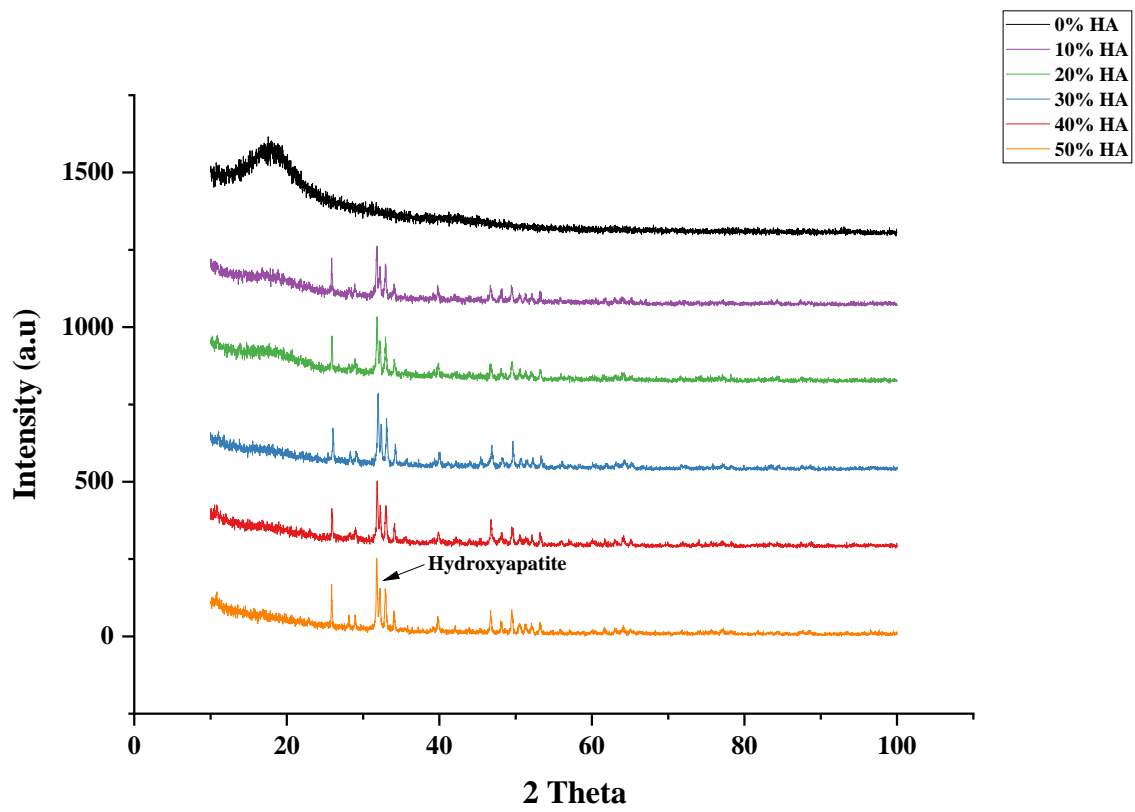


Figure 3-13: X-Ray Diffraction analysis of calcium phosphate precipitation in the 0-50 wt% HA with 2 wt% CQ composite-polymer specimens. Hydroxyapatite diffraction peaks began to be observed in the 10 wt% HA specimens (purple) then increased in size as the quantity of HA increased up to 50 wt% HA (orange).

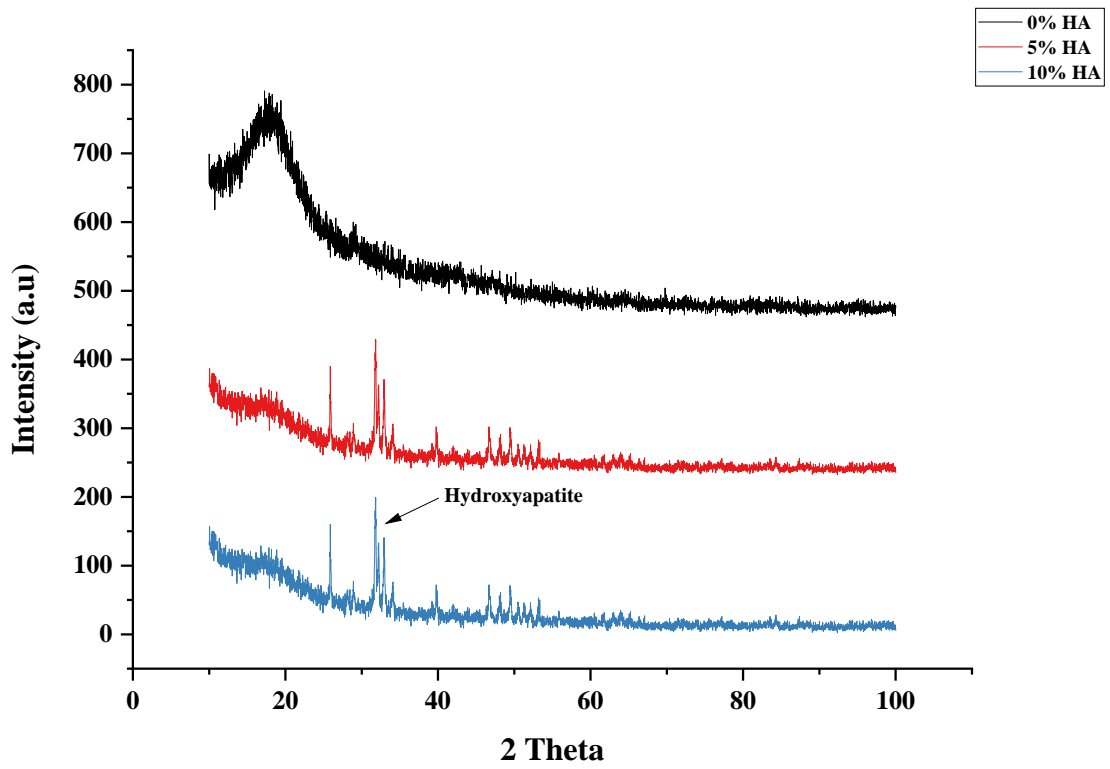


Figure 3-14: X-Ray Diffraction analysis of calcium phosphate precipitation in the 0-10 wt% HA with 2 wt% BAPO composite-polymer specimens. Hydroxyapatite diffraction peaks began to be observed in the 5 wt% HA specimens (red) and the 10 wt% HA specimens (blue).

### 3.3.4 Degradation Studies

#### 3.3.4.1 pH Values

The acidity of CSMA-2 and the composite-polymer discs was investigated by immersing the specimens into a neutral culture media solution as shown in figure 3-15. All samples gave rise to a slightly acidic solution post incubation with pH values ranging from 6-7.4. It can be seen that the addition of HA increases the pH level, but no significant difference was observed between the polymer and the HA incorporated formulations (\*p < 0.05).

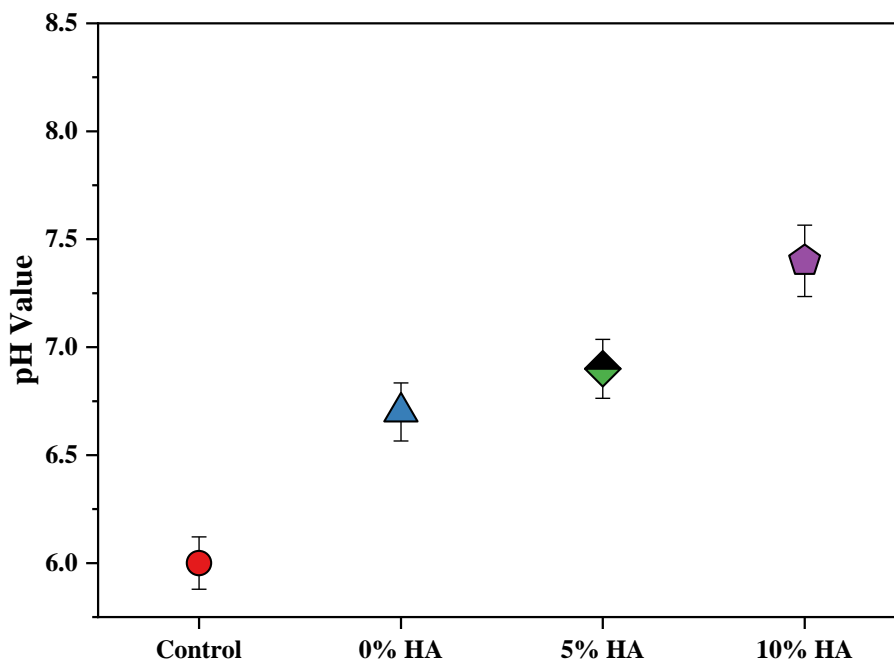


Figure 3-15: pH values of a glass control disc in comparison with CSMA-2 with 2 wt% BAPO photoinitiator, 5 wt% HA and 10 wt% HA incorporated composite discs post 24-hour immersion in a neutral culture media. All samples showed acidic behaviour with the values ranging from 6-7.4. The 10 wt% HA formulations exhibited the highest pH at 7.4, however all the groups remained in the acidic-basic range. (\*p<0.05)



#### **3.3.4.2 Percentage Mass Change**

The cumulative percentage mass change was investigated across a 6-month incubation period. The degradation was tested at a standard physiological temperature of 37°C as well as an accelerated temperature of 60°C for comparison. Equation 3-3 allowed calculation of the rate of degradation with respect to the initial dry weight. 3D-printed composite discs containing CSMA-2 with 2 wt% BAPO photoinitiator and 0-10 wt% HA incorporated formulations exhibited a relatively slow degradation behaviour, where the highest mass loss percentage was seen in the 10 wt% composite-polymer disc with a total of 8% drop in weight over the incubation period. S, in this case the maximum degradation of the polymer alone was 6%, whilst the HA incorporated specimens gave a 10% percentage mass loss.

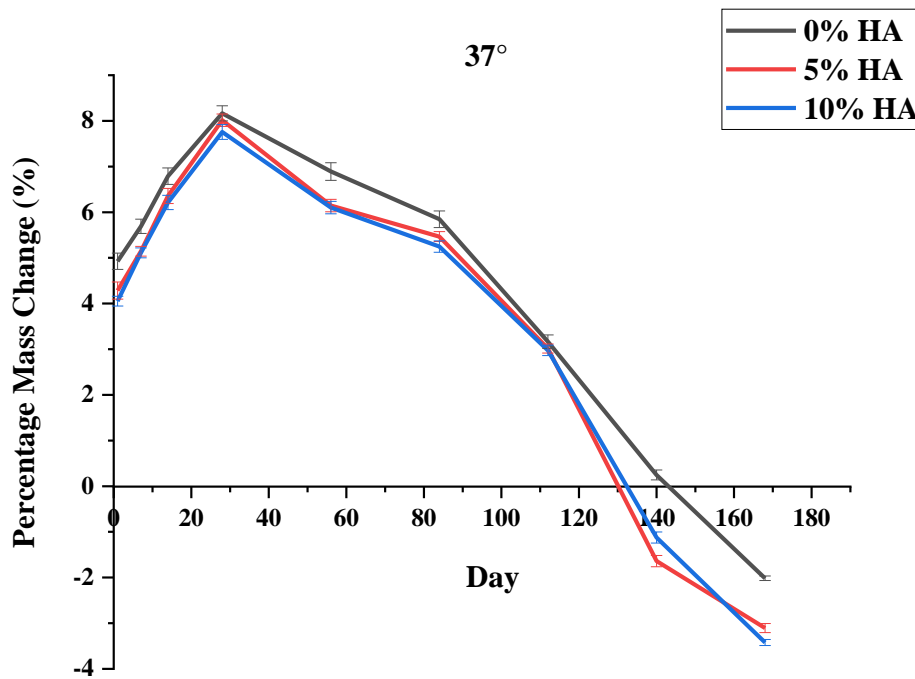


Figure 3-16: Representation of the cumulative percentage mass change across a 6-month incubation period at the set physiological temperature 37°C. Equation 2-4 allowed calculation of the rate of degradation with respect to the initial dry weight percentage mass change of CSMA-2 compared to the CaP incorporated composite discs in phosphate buffered saline: the highest rate of mass change is observed in the 10 wt% CaP discs with a 8% drop in weight (blue), while the lowest value was exhibited by the CSMA-2 polymer by itself which had a 6% drop in weight over the 6-month period (black).

At an accelerated temperature of 60°C, the degradation rate was slightly faster as expected. Similarly, to the 37°C experiment, the specimens were immersed in PBS for the duration of 6 months. As seen, the formulation containing 10 wt% HA had the highest drop in weight over the 6-month incubation period at 10%, however, this was not significantly different to the percentage mass change of the CSMA-2 composite-disc with no added HA which had a percentage mass change drop of 9.1% and the 5

wt% incorporated specimen which had a drop of 9.2%. These results suggest that with an accelerated temperature control the degradation of CSMA-2 and its composites occurs at a faster rate as the percentage mass change increased as when compared to the standard 37°C.

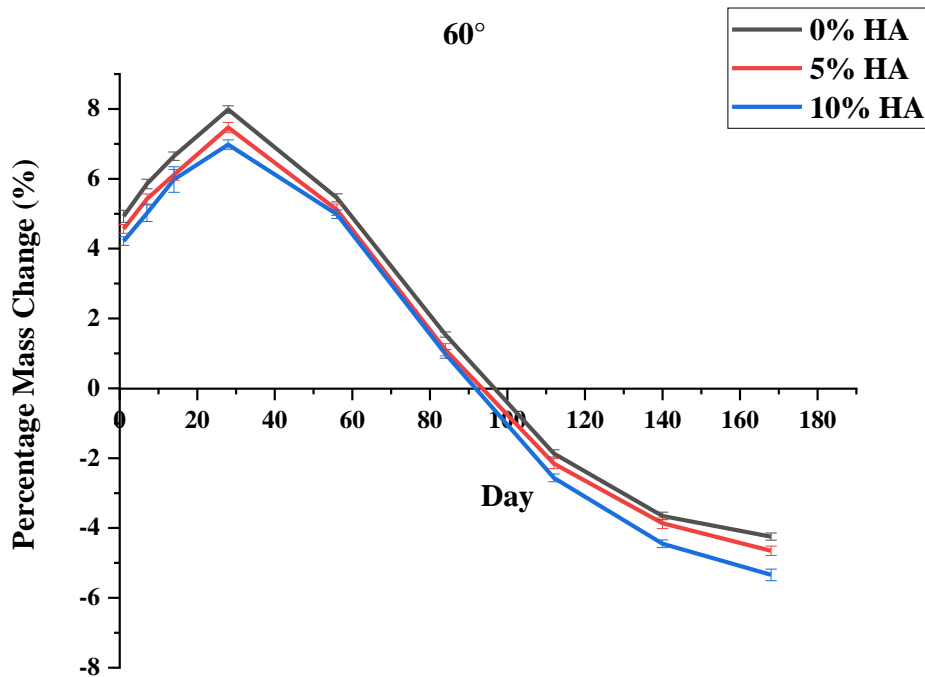


Figure 3-17: Representation of the cumulative percentage mass change across a 6-month incubation period at a set temperature of 60°C. Equation 2-4 allowed calculation of the rate of degradation with respect to the initial dry weight percentage mass change of CSMA-2 compared to the CaP incorporated composite discs in phosphate buffered saline: the highest rate of mass change is observed in the 10 wt% CaP discs with a 10 % drop in weight (blue), while the lowest value was exhibited by the CSMA-2 polymer by itself which had a 9% drop in weight over the 6-month period (black).

### **3.3.4.3 Mechanical Testing Post Degradation**

To further explore the degradation properties of the composite-polymer formulations of 0, 5 and 10 wt% HA were tested mechanically after a set period incubation in 10ml of PBS at 37°C. After the set time point of 0-6 months, the sample was dried and tested via the biaxial flexural method for the purpose of bend strength and Young's modulus evaluation. Figure 3-18 below represents the results for the bend strength measurements of the samples after each incubation time point. It can be seen that CSMA-2 with no added hydroxyapatite after 1 month of incubation time in PBS had the highest recorded bend strength value of 137.54 N/mm<sup>2</sup>. After 6 months of incubation at 37°C in PBS, the CSMA-2 specimen with no added HA had a significantly lower bend strength value of 88.21 N/mm<sup>2</sup>. The values for the 5 wt% HA and 10 wt% HA incorporated composite-polymer discs followed a similar trend where their bend strength value increased slightly in the first 2 months, due to water absorption and retention, then significantly dropped in value between 3-6 months. The 5 wt% HA formulations ranged between 107 N/mm<sup>2</sup> – 64.56 N/mm<sup>2</sup> whilst the 10 wt% HA formulations ranged between 104.54 N/mm<sup>2</sup> – 57.21 N/mm<sup>2</sup>. The samples failed at lower values as the amount of HA was increased from 0-10 wt%, implying that lower loads were required to fracture the material with increasing quantities of CaP.

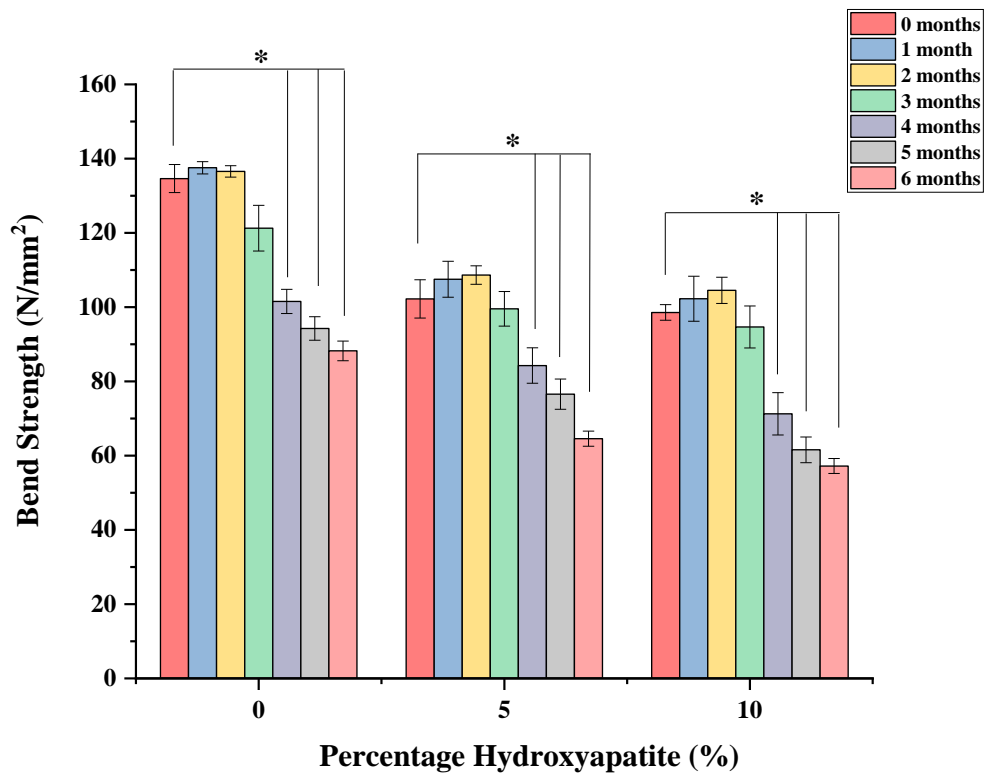


Figure 3-18: A graphical representation for the comparison of bend strength results from the biaxial flexural test done via the Shimadzu for composite-polymer discs with 2 wt% BAPO and a range of 0-5 wt% HA across 6 months of incubation time to assess the degradation properties. The highest recorded value was 137.54 N/mm<sup>2</sup> for CSMA-2 with 2 wt% BAPO and no added HA after 1 month of incubation in PBS. The lowest recorded value for CSMA-2 with no added HA was at the 6-month time point giving a bend strength value of 88.21 N/mm<sup>2</sup>. The lowest value recorded throughout the experiment was 57.21N/mm<sup>2</sup> for the 10 wt% HA composite polymer after 6 months of incubation in PBS. The results for the 4,5 and 6-month time points were statistically significantly different compared to the results from 0-3 months incubation for all 3 formulations. (\*p < 0.05)

The Young's Modulus was also evaluated for the purpose of exploring the degradation properties of the composite-polymer formulations of 0, 5 and 10 wt% HA. Figure 3-19 below represents the results for the Young's modulus measurements of the samples after each incubation time point. It can be seen that CSMA-2 with no added hydroxyapatite after 1 month of incubation time in PBS had the highest recorded

modulus value of 2.62 kN/mm<sup>2</sup>. As well as BAPO having an effect, the higher amounts of hydroxyapatite also lowered the Young's Modulus values, leading to a more elastic material. After 6 months of incubation at 37°C in PBS, the CSMA-2 specimen with no added HA had a significantly lower Young's modulus value of 1.20 kN/mm<sup>2</sup>. The values for the 5 wt% HA and 10 wt% HA incorporated composite-polymer discs followed a similar trend where their Young's Modulus values increased slightly in the first 2 months, due to water absorption and retention, then significantly dropped in value between 3-6 months. The 5 wt% HA formulations ranged between 2.11 kN/mm<sup>2</sup> – 1.01 kN/mm<sup>2</sup> whilst the 10 wt% HA formulation ranged between 1.99 kN/mm<sup>2</sup> – 0.94 kN/mm<sup>2</sup>. As the amount of HA was increased from 0-10 wt%, the samples had significantly lower modulus values, suggesting that the addition of a higher quantity of calcium phosphate caused a decrease in the stiffness of the material. As clearly visible in this experiment, the Young's modulus is significantly impacted over a prolonged period of incubation time in PBS as the values for all formulations are statistically significantly different between the measurement taken before immersion in PBS and after 4 months of incubation time leading to a more elastic composite.

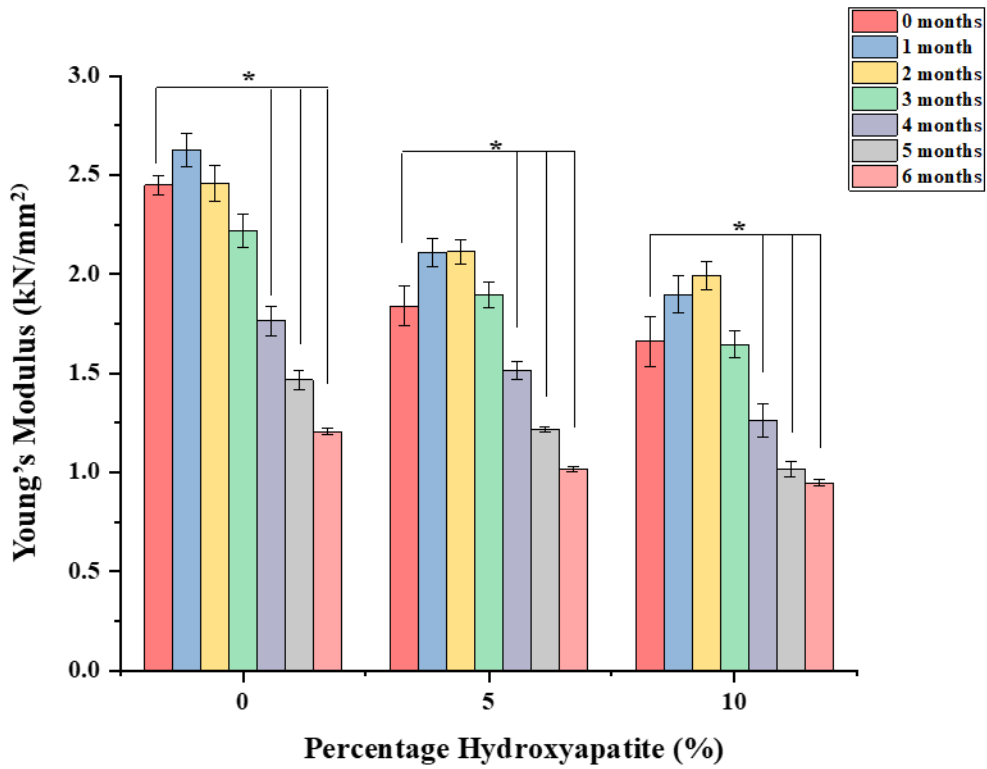


Figure 3-19: A graphical representation for the comparison of Young's modulus results from the biaxial flexural test done via the Shimadzu for composite-polymer discs with 2 wt% BAPO and a range of 0-5 wt% HA across 6 months of incubation time to assess the degradation properties. The highest recorded value was 2.62 kN/mm<sup>2</sup> for CSMA-2 with 2 wt% BAPO and no added HA after 1 month of incubation in PBS. The lowest recorded value for CSMA-2 with no added HA was at the 6-month time point giving a modulus value of 1.20 kN/mm<sup>2</sup>. The lowest value recorded throughout the experiment was 0.944 kN/mm<sup>2</sup> for the 10 wt% HA composite polymer after 6 months of incubation in PBS. The results for the 4,5 and 6-month time points were statistically significantly different compared to the results from 0-3 months incubation for all 3 formulations. (\*p < 0.05)

### 3.4 Discussion

In this chapter, a light-curable, degradable and 3D printable polymeric system has been explored for its mechanical and physical properties, highlighting the effects of the addition of hydroxyapatite fillers in a variety of ratios. Two types of photoinitiators were explored for their effect on the mechanical properties to assess the best formation to go forward within the study.

Matching the mechanical strength of the synthetic material to the native tissue is one of the most critical things to consider when building a biomaterial-based scaffold to prevent the possibility of material extrusion and infection (Koons, Diba and Mikos, 2020). Many scaffolds' biostability is determined by variables such as strength, flexibility, and absorption. To induce rapid tissue regeneration in the surrounding area, a polymer-based scaffold should have mechanical properties and degradation rates with the bioactive surface (Nair and Laurencin, 2007). The scaffold must be able to endure and conduct the loads and stresses that the new promoting tissue will be subjected to in order to be used successfully in tissue engineering applications. Due to this, it is essential to evaluate the elastic modulus and flexural strength accordingly (Dhandayuthapani *et al.*, 2011).

The mechanical properties of cortical and trabecular bone are important to compare to the results in this study. Significant research involves the measurement of Young's modulus as well as mechanical strength for both cortical and trabecular bone. A study carried out by Gerhardt and colleagues (Gerhardt and Boccaccini, 2010) investigated the comparison of mechanical properties of human bone against a commercially available bioglass and found that the compressive strength of these columnar



bioactive glass scaffolds is >1.5 times higher than the highest strength reported for trabecular bone. In comparison with CSMA-2, table 3-1 below highlights the comparison of tensile strength and Young's modulus against CSMA-2 with 0-10 wt% HA.

Table 3-1: Comparison of mechanical strength and Young's modulus values for trabecular and cortical bone compared to CSMA-2

| Material Property                        | Trabecular Bone | Cortical Bone | Reference  | CSMA-2       |
|--|-----------------|---------------|--|--------------|
| Mechanical Strength (N/mm <sup>2</sup> ) | 0.1-20          | 100-230       | Rezwan <i>et al.</i> , 2006<br>Gerhardt <i>et al.</i> , 2010 | 84.07-135.49 |
| Young's Modulus (KN/mm <sup>2</sup> )    | 0.05-0.5        | 7-30          | Kellet <i>et al.</i> , 2001<br>Lefevre <i>et al.</i> , 2019  | 1.96-2.4     |

The mismatched stiffness of current commercially available implant materials such as PMMA and PEEK has led to complications for patients. Stress shielding, which correlates to a decrease in bone mass density and implant loosening, is one of the key concerns (Sas *et al.*, 2019). Furthermore, increasing local stress concentrations at the implant site might result in detachment, extrusion, and infection risk. In the synthesis of CSMA-2, the addition of ethylene glycol groups to isosorbide delivered optimal mechanical stiffness. CSMA-2 however, displayed a significantly lower Young's modulus compared to the literature values for modulus of similar bone cement such as PMMA. In a study by Abdallah (Abdallah, 2016), the Young's modulus of PMMA with no added substitutes was 4.45 kN/mm<sup>2</sup> which compares with CSMA-2 with a

modulus value of 1.96-2.4 kN/mm<sup>2</sup> with BAPO and CQ initiators respectively. This considerable change could be related to the increased degree of crosslinking in the material, which causes the structure to become less elastic with time. As CSMA-2 is highly viscous, it has a higher resistance to flow, which might affect powder particle dispersion, resulting in a stiffer composite with a higher Young's Modulus. As seen throughout the study, the addition of hydroxyapatite filler has an impact on Young's modulus causing it to decrease slightly with higher amounts of HA. A study by Aldabib and colleagues (Aldabib and Ishak, 2020) investigated the effect of hydroxyapatite filler concentration on mechanical properties of PMMA denture bases and found a significant improvement in the modulus of PMMA with incorporated HA as the quantity of HA was increased. HA could resist the stress and limit the movement of the cross-linked molecular chain in a polymeric system such as PMMA or CSMA-2 for instance when a load is applied on the composite.

The mechanical strength is also crucial when exploring a biomaterial for tissue engineering purposes. The mechanical strength of cortical bone in humans ranges between 100-230 N/mm<sup>2</sup>. The values witnessed from the studies in this chapter revealed CSMA-2 to have varying mechanical strength properties of 84.07 N/mm<sup>2</sup> when prepared with CQ photoinitiator and 135.49 N/mm<sup>2</sup> when prepared with BAPO photoinitiator suggesting that the type of photoinitiator did have a significant effect on the mechanical properties of the material.

A study by Zhao and fellow researchers (Zhao and Liang, 2017) developed a new combined scaffold with chitosan and hydroxyapatite for bone tissue engineering that has improved mechanical properties. They employed 3D printing to manufacture two moulds, one with pores and the other without, to build a biomimetic comby scaffold

that increased the material's mechanical strength. The compressive strength and reactions of preosteoblast cells were studied on the scaffolds. The strength and modulus values of the high-porosity scaffold were comparable to those of cancellous bone.

Similarly, the mechanical properties of CSMA-2 and composite discs, such as hardness determination, are directly proportional to the filler content, with the addition of HA increasing the overall hardness of the material (Yunus Basha, Sampath and Doble, 2015). In a study by Musib and colleagues (Musib *et al.*, 2012), the hardness of PMMA bone cement was compared to that of CSMA-2 with 10% HA incorporated, and the results showed that PMMA had similar hardness qualities to CSMA-2 with 10% HA incorporated.

However, it can be said that a higher resistance to flow is exhibited as a function of shear rate which inevitably impacts the flow and dispersion of the CaP fillers, leading to an increase in Young's Modulus and Biaxial Flexural strength measurements if the filler content exceeded a certain amount. For example, the Young's Modulus value began to increase accordingly when reaching 50 wt% HA filler as a more viscous polymeric phase will only permit a limited amount of CaP powder through without triggering agglomeration and poor filler dispersion (Ryabenkova *et al.*, 2017). Due to these findings, as well as the suitability for 3D printing, the 10 wt% HA incorporated specimen was established as the optimum formulation within the ranges investigated.

The biocompatibility of a polymeric based scaffold can be determined by its wettability, often expressed by the water contact angle. The hydrophilic nature of biomaterials can encourage *in vitro* and *in vivo* proliferation on the surface of the material which is

dependent on the powder dispersion, amount and type of filler of choice and the surface properties (Xueyong Deng *et al.*, 2021). In this study, CSMA-2 and its composites were assessed to determine the materials' wettability. All composite specimens exhibited a hydrophilic behaviour. As expected, the addition of CaP fillers had a direct correlation with the hydrophilicity of the composites; The 50 wt% HA formulations showed the most hydrophilic behaviour as it had a contact angle measurement of 42°. This was not significantly lower than the formulations of 10-40 wt% which had values between 54° and 46°. When comparing the two photoinitiator types, CQ and BAPO, the water contact angle measurements followed the same pattern. For both groups of formulations, CSMA-2 displayed hydrophilic behaviour which became more hydrophilic with added HA fillers. These results essentially reflect on optimum adhesion between the CaP particles and the liquid phase. CaP particles, like hydroxyapatite, tend to demonstrate a link with surface energy, where any filler incorporation at higher quantities increases the surface energy (Wang *et al.*, 2018). Carrier and co-researchers (Carrier and Bonn, 2015) investigated the effect of the sample surface area and roughness of the material and its impact on hydrophilicity. In the study they concluded that if a sample characteristic is rough, a hydrophobic substrate will be much more hydrophobic than the identical smooth substrate, and vice versa. The difference between the contract angle and roughness of a solid is represented by Wenzel's equation (equation 3-4).

$$\cos\Theta_m = r\cos\Theta_Y$$

*Equation 3-4: Wenzel's equation stating the relationship between surface roughness and wettability where  $\Theta_m$  is the measured contact angle,  $\Theta_Y$  is Young's contact angle and  $r$  is the roughness ratio.*

As well as hydrophilicity, the pH of a polymer-based scaffold is also critical for determining biocompatibility. CSMA-2 and its HA-incorporated samples gave rise to an acidic-basic solution post-incubation in neutral culture media with pH values ranging from 6-7.4 suggesting that the biocompatibility of the system is not affected by the addition of HA fillers. The recorded literature pH value for standard hydroxyapatite in aqueous solution is between 6.6-7.2 (Christoffersen, Christoffersen and Kjaergaard, 1978) which reflects on the results obtained when assessing the pH in this study.

Hydroxyapatite, in higher quantities is known to promote remineralisation, making HA an important factor in encouraging osteogenesis in new tissue formation (Hughes *et al.*, 2018). The remineralisation of HA was assessed using SEM for this study. The distribution of HA particles agglomerated across the surface of the polymer disc and can be seen to be evenly distributed throughout the formulations.

Achieving biodegradability was one of the main objectives of this chapter. Biodegradable polymers have revolutionised the applications of biomaterials for tissue engineering implants (Dhandayuthapani *et al.*, 2011). The degradation rate is an important variable when designing polymeric scaffolds for the purpose of clinical applications as the rate of new tissue formation must match the rate of degradation in proportion (Chen, Zhou and Li, 2011). A biodegradable scaffold degrades over time, eventually being replaced by newly produced tissue from attached cells. In this study, we anticipate the degradation of the polymeric system to be replaced by new bone tissue growth in the region where the material is implanted. The degradation that occurs as a result of scaffold disassembly results in material dissolution or resorption

through the scaffold's bulk or surface degradation (Middleton and Tipton, 2000). Scaffolds that degrade in bulk frequently tear down the internal structure of the scaffold, lowering the molecular mass of the material. On the other hand, materials that undergo surface degradation have a constant degradation rate, providing longer mechanical stability for the surrounding tissue to regenerate (Woodruff and Hutmacher, 2010). The rate of degradation of a polymeric scaffold is determined by the chemical structure, hydrophilicity, presence of hydrolytically unstable bonds, crystalline/amorphous morphology, and overall molecular weight of the polymer (Dhandayuthapani *et al.*, 2011). A study carried out by Ye *et al.* (Ye *et al.*, 1997) explored the *in vitro* degradation of PCL and PLA scaffolds to explore the influence of composition, temperature and morphology on the degradation rate. It was found that the controllable degradation should match the rate of tissue growth *in vitro* and *in vivo* for biodegradable materials.

CSMA-2 and its composite polymer specimens displayed a relatively slow degradation, with the highest mass loss observed in the 10 wt% HA formulations with a total of 8% drop in weight over the incubation period. Using accelerated temperature controls, the degradation rate was slightly faster with the highest mass loss observed in the 10 wt% HA formulations with a total of 10% drop in weight over the 6-month incubation period. These properties can be beneficial in a dynamic *in vivo* environment as slow degradation can prevent the sudden pH changes that are usually expected, as well as potentially offering long-term mechanical stability (Chen and Liu, 2016). A study by Huang and co-workers (Jinhui Huang *et al.*, 2019) investigated the differences in bone repair between three polymer-based scaffolds of varying degradability. The study resulted that PLGA scaffolds incorporated with nano-HA had

the fastest degradation rate, potentially leading to the loss of scaffold structural integrity therefore a reduction of bone volume when implanted *in vivo*. Furthermore, it was found that the polymer-based scaffold containing nano-HA and PCL had the slowest degradation rate and maintained its structural integrity throughout suggesting that it was the model to use as a scaffold that can keep its structural integrity until the completion of bone reconstruction around it is more ideal for the repair of bone deformities.

As discussed in Chapter 1: Literature Review, PLGA is a well-known degradable polymer, however, its fast degradation has limited its use in clinical settings over the recent years. Therefore, CSMA-2 may address one of the major drawbacks associated with the currently reviewed synthetic degradable polymer scaffolds (Elmowafy, Tiboni and Soliman, 2019). The amount of CaP filler addition is also an important variable in determining several properties of the polymeric-based composites such as the modification of degradability. The *in vivo* degradation of CaP materials is dependent on the physicochemical and cellular mechanisms and processes (Yuan *et al.*, 2010). As seen in the degradation studies, the higher amounts of HA filler added to CSMA-2 lead to a slightly faster degradation time. Initial degradation of the composite-polymer specimens (Habraken *et al.*, 2016) was achieved through the hydrolysis of the filler phase. Hydroxyapatite fillers are relatively hydrophilic at a content of 2 wt% or more thus explaining the difference in mass loss throughout the experiment. Furthermore, the degradation of HA leaves behind holes and pits in specimens such as CSMA-2 composites, which can affect the degradation of CSMA-2 as the surface area of the specimen will be increased. However, it is important to mention that although HA is

advantageous in systems like CSMA-2, finding the right balance of polymer: filler ratio is critical to prevent rapid degradation (Sheikh *et al.*, 2015).

### **3.5 Conclusion**

To conclude, the studies carried out in this chapter were to assess the mechanical and physical properties of an isosorbide-based light-curable, degradable polymeric system for its potential use in craniofacial bone regeneration. The effect of the addition of varying ratios of hydroxyapatite, as well as the use of two different photoinitiators on the mechanical and physical properties, were also investigated throughout this chapter in the hope to find the ultimate formulations for use *in vitro* and *in vivo*.

The formulations containing over 10 wt% HA were not used after this chapter of work due to them not being compatible with the 3D printing method of choice. Therefore, the formulations using 0, 5 and 10 wt% HA were used to explore the *in vitro* properties in Chapter 4: Biological Exploration. The results from this work also suggested that the formulation containing 2 wt% BAPO photoinitiator with 10 wt% hydroxyapatite, created via the DLP 3D printing technique holds promising advances in addressing the current drawbacks associated with commercial materials, particularly in restoring cranial defects. Its results have been consistently positive throughout this chapter of the study, highlighting the positive impact HA can have on mechanical properties as well as the rate of degradation and wettability properties.



## **Chapter 4 : Biological Exploration**

## 4.1 Introduction

As previously discussed in Chapter 1: Introduction and Literature Review as well as in Chapter 2: Synthesis and 3D printing of a light-curable, degradable polymeric system (CSMA-2), bone grafts and alloplastic materials are the current treatment options for restoring bone. Autograft bone grafts, in which bone or tissue is transferred from one location on a patient's body to another, are currently the gold standard treatment for providing osteoinductive and osteoconductive qualities (Kohli *et al.*, 2021). However, as previously discussed in this study, these types of grafts have a significant risk of complications such as the increased risk of infection and rejection at the site of the implant. As a result, numerous attempts have been made to create bone implants with better biological qualities. An exemplar material should possess excellent biocompatibility and promote angiogenesis. Biocompatibility is the ability of a material to function with an appropriate host response in a specific application. When a live organism is exposed to a biomaterial, it has a natural predisposition to respond. Many interconnected local and systemic interactions can occur at the biomaterial-biological system interface. Therefore, biocompatibility is difficult to define as it includes all the responses of the biological system to the biomaterial. In general, a biocompatible material will not be rejected when introduced to a living organism and will not produce a toxic or immunological response when exposed to the body or bodily fluids (Song *et al.*, 2018).

Angiogenesis is a process that involves the differentiation of endothelial cells that line the inside walls of blood vessels to produce new blood vessels. The success of tissue healing, such as bone rebuilding, depends on enabling angiogenesis. A suitable material should allow vascularisation to recruit cells and populate them to further

encourage the creation of tissue matrix chemicals for optimal tissue regeneration. A material intended for use in tissue engineering should promote angiogenic events to ultimately lead to the formation of re-vascularised tissue. A study by Lee and co-workers (Lee *et al.*, 2021) investigates the angiogenesis strategies based on materials to repair and regenerate damaged tissues such as bone. The study explores a variety of materials tailoring the physio-chemical properties as well as mechanical properties throughout. They concluded that scaffolds with 3D open-pore architectures are the most often employed biomaterials for tissue healing. This is because the pore area is quickly filled with cells, causing vascularisation to aid the repair process.

Since biocompatibility and angiogenesis are key for successful bone regeneration (Noori *et al.*, 2017), the addition of an osteogenic component to the scaffold was investigated, in this case, hydroxyapatite (HA) to promote vascularisation as well as help the material in its biocompatibility towards cells. Hydroxyapatite is a complex calcium phosphate with a chemical composition similar to that of bone material and promotes good biocompatibility, osteoconductivity and osteoinductive properties (Deligianni *et al.*, 2000).

The work carried out in this chapter explores the biological properties of CSMA-2 along with its composite-polymer specimens formulated with 0-10 wt% hydroxyapatite filler for the purpose of cytocompatibility testing to determine the ultimate custom-fit scaffold for use in cranio-maxillofacial surgery. The material, previously synthesised and characterised in Chapters 2 and 3, was prepared for the purpose of *in vitro* cell culture and *Ex-Ovo* Chick Chorioallantoic Membrane Assays experimentation. MG-63 cells, a line derived from human osteosarcoma cancer cells, and mesenchymal stem cells

(MSCs) derived from adipose tissue (human adipose-derived stem cells) (hADSCs), were explored for the purpose of cell proliferation and metabolic activity.

hADSCs possess the ability to readily expand *in vitro* and can undergo osteogenic, adipogenic, chondrogenic and myogenic differentiation (Gir *et al.*, 2012). The differentiation process toward osteoblasts is regulated by a number of genes. In this study, using hADSCs, osteogenic differentiation was assessed to understand the effect of the materials on bone-related gene expression. All of the osteoblast marker genes, Runt-related transcription factor 2 (RUNX2), Collagen type 1 (COL1A1), Osteopontin (OPN), and Osteocalcin (OCN), appear to be expressed during the developmental sequence of osteoblast differentiation. They are known to play an important role in regulating cell differentiation, mineralisation and bone matrix formation (Sun *et al.*, 2008).

Finally, the composite-polymer specimens were also investigated for their angiogenic response using an *ex-ovo* Chick Chorioallantoic Membrane Assay. These investigations will provide details on the ideal formulation in an *in vitro* environment.

In summary, the main aims and objectives of this chapter are as follows:

1. The assessment of MG-63 Osteosarcoma cells on both manually prepared composite-polymer discs using CQ photoinitiator and up to 10 wt% HA filler and 3D printed composite-polymer discs using BAPO photoinitiator and up to 10 wt% HA fillers.
2. The investigation of human-adipose derived stem cells on 3D printed composite-polymer specimens to evaluate the cytocompatibility of the scaffolds.
3. A comparison between the use of standard hADSCs media and osteogenic supplemented media to assess the differentiation of the cells via the composite-polymer scaffolds.
4. A differentiation study using real-time PCR techniques to assess gene expression of specific bone markers via the composite-polymer scaffolds.
5. Exploring the angiogenic response of the composite-polymer scaffolds using the *ex-ovo* Chorioallantoic Membrane Assay.

## **4.2 Materials and Methodology**

### **4.2.1 Materials**

The materials used in this chapter were the previously discussed CSMA-2 composite-polymer discs with dimensions of 10 mm in diameter and 1 mm thick as well as the porous scaffolds with dimensions of 6 mm in diameter and 3 mm thick with 0.5 mm pores. The materials used for the comparison of metabolic activity using MG-63 cells between two photoinitiators were CQ and BAPO. The CQ discs were prepared in the manual method as per Chapter 2 section **2.2.6.1** and the BAPO discs were 3D printed. All the 3D printed materials incorporated 2 wt% BAPO photoinitiator and either 0, 5 or 10 wt% hydroxyapatite filler and were printed using the XYZ Nobel Superfine DLP Printer (XYZ Printing, The Netherlands) as previously described in Chapter 2 section **2.2.9**.

### **4.2.2 Cell Culture**

#### **4.2.2.1 MG-63 Osteosarcoma Cell Line**

To assess the efficacy and biological activity of the composite-polymer discs, MG-63 human osteosarcoma cell line passage number 10 (European Collection of Authenticated Cell Cultures, United Kingdom) was grown in T-45 polystyrene flasks in Dulbecco's modified Eagle's media with 10% foetal bovine serum (Gibco, Life Technologies Ltd., United Kingdom) (FBS) (Sigma-Aldrich St Louis, MO, USA), 1% of L-Glutamine (Sigma-Aldrich St Louis, MO, USA), and 0.1% of penicillin/streptomycin

(P/S) (Sigma-Aldrich St Louis, MO, USA). The cells in the media were cultured at 37°C with 5% CO<sub>2</sub> and used once they had attained about 80% confluency. To continue culture, the cell culture media was replaced every two days.

MG-63 *in vitro* work was published previously in: Shakouri, T., Cha, J.-R., Owji, N., Haddow, P., Robinson, T. E., Patel, K. D., García-Gareta, E., Kim, H.-W. and Knowles, J. C. (2020). 'Comparative study of photoinitiators for the synthesis and 3D printing of a light-curable, degradable polymer for custom-fit hard tissue implants'. *Biomedical Materials*, 16 (1), p. 015007. doi: 10.1088/1748-605X/aba6d2.

#### **4.2.2.2 Human Adipose Derived Stem Cells**

To further explore the biological activity of the composite-polymer discs, human adipose-derived stem cells (hADSCs) passage 0 (Lonza, United Kingdom) were cultured in T-45 polystyrene flasks in MesenPRO RS Media (ThermoFisher, United Kingdom) with 2% MesenPRO RS growth supplement (ThermoFisher, United Kingdom) and 0.1% of penicillin/streptomycin (P/S) (Sigma-Aldrich St Louis, MO, USA). The cells in the media were cultured at 37°C with 5% CO<sub>2</sub> and used once they had attained about 80% confluency. To continue culture, the cell culture media was replaced every two days.

### **4.2.3 Cell Metabolic Activity**

#### **4.2.3.1 MG-63 Osteosarcoma Cell Line**

A resazurin-based alamarBlue assay was performed to assess the cytocompatibility of the composite-polymer specimens by measuring the level of cells metabolic activity at different time points. Once confluent, the cells were passaged by using trypsin-EDTA (Invitrogen, Paisley, United Kingdom). The composite-polymer discs investigated included the 0, 5 and 10 wt% HA composites containing wither 2 wt% CQ or 2 wt% BAPO photoinitiator to assess if there were any significant differences between the two initiators. The CQ based discs were prepared by hand (see chapter 2, section 2.2.6.1) and the discs containing BAPO were prepared via SLA 3D printing (see chapter 2, section 2.2.6.2). The control for this experiment was the tissue culture plastic (TCP). All discs were sterilised for 30 minutes on each side under UV light (254 nm) before being inserted in 24-well tissue culture plates (Thermo Fisher Scientific, Loughborough, United Kingdom). 1 ml of MG-63 cell suspension ( $1 \times 10^4$ ) was added to each well and incubated at 37 °C, 5% CO<sub>2</sub>. To determine cell metabolic activity at day 1, 4 and 7 of culture, 100 µl of alamarBlue dye (alamarBlue agent, ThermoFisher, United Kingdom) was added to each well and incubated for a further 3-hour period. See figure 4-1 for a representation of the protocol. Before adding alamarBlue, the samples were placed into new 48 well plates to avoid any contribution



from the cells that had attached to the previous well plate.

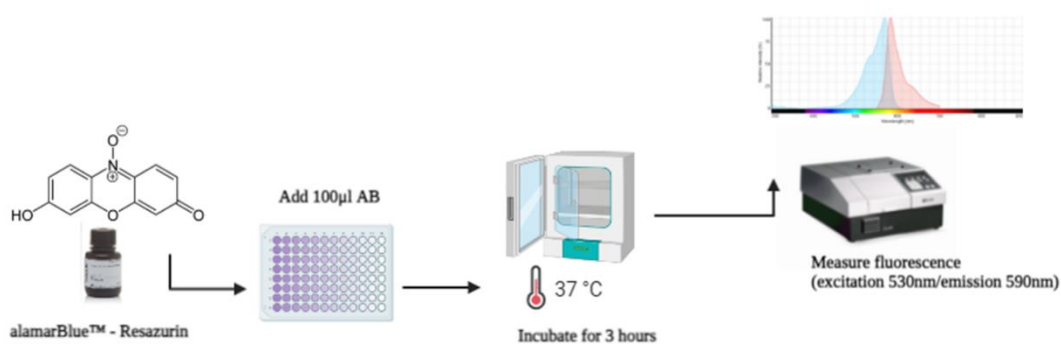


Figure 4-1: Diagram representing the process for the metabolic activity alamarBlue assay. Interpreted from the alamarBlue assay user guide provided by ThermoFisher Scientific. The diagram was created using BioRender.com

#### 4.2.3.2 Human Adipose Derived Stem Cells

To further investigate the *in vitro* properties of the composite-polymer materials, hADSCs were explored. The composite-polymer discs investigated included the 0, 5 and 10 wt% HA composites containing 2 wt% BAPO photoinitiator to assess the effect of the varying amounts of hydroxyapatite on the stem cells. All discs were sterilised for 30 minutes on each side under UV light (254 nm) before being inserted in 24-well tissue culture plates. 1 ml of human adipose derived stem cell suspension ( $3 \times 10^4$ ) was added to each well and incubated at 37 °C, 5% CO<sub>2</sub>. To determine cell metabolic activity, 100 µl of alamarBlue dye was added to each well at day 1, 4 and 7 of culture and incubated for a further 3-hour period.

#### **4.2.3.3 Osteogenic Differentiation**

In order to further understand the cytocompatibility of the polymer discs and the effect of filler addition on osteogenic differentiation, a final cell culture experiment took place with the hADSCs at passage 2. The cells were cultured comparing hADSCs in regular media (MesenPRO RS Media) against the hADSCs in osteogenic supplemented media (hMSC Osteogenic Differentiation Media with SingleQuoats supplements) containing 20ml of mesenchymal cell growth supplement (MCGS), 4ml of L-Glutamine, 2ml of P/S, 2ml of  $\beta$ -glycerol-phosphate, 1ml of Ascorbic acid and 1ml of dexamethasone were added to the media. Like the previous cultures, the composite-polymer discs investigated included the 0, 5 and 10 wt% HA composites containing 2 wt% BAPO photoinitiator to assess the effect of the varying amounts of hydroxyapatite on osteogenic differentiation. All discs were sterilised for 30 minutes on each side under UV light (254 nm) before being placed in 24-well tissue culture plates. 1 ml of human adipose derived stem cell suspension ( $3 \times 10^4$ ) was added to each well and the relevant media added then incubated at 37 °C, 5% CO<sub>2</sub>. To determine cell metabolic activity and compare the different conditions, 100  $\mu$ l of alamarBlue dye was added to each well at day 1, 7, 14, 21 and 28 of culture and incubated for a further 3-hour period.

#### **4.2.3.4 Fluorescence Measurements**

A BioTek FLx800 microplate reader was used to detect fluorescence in all three cell culture experiments (excitation wavelength 530 nm, emission wavelength 590 nm) (BioTek, USA). Finally, the fluorescence intensity ratio of the reduced alamar blue was

compared with the coverslip control (Thermanox plastic coverslips, ThermoFisher, United Kingdom) to evaluate the relative cell viability.

#### **4.2.4 Phalloidin and DAPI Staining**

Cells were cultivated on 3D-printed surfaces, and cell morphology was monitored using fluorescence microscopy throughout the length of the experiment (as mentioned above). The samples were removed from the culture material and transferred to new well plates as the time points were achieved, where they were gently washed three times with PBS before being fixed with 4.0% paraformaldehyde (Sigma-Aldrich, St Louis, MO, USA) for 10 minutes at room temperature. After fixation, samples were rinsed three times in PBS before being penetrated for 10 minutes with 0.1% TritonX-100 (Sigma-Aldrich, St Louis, MO, USA) in PBS. The samples were then incubated with phalloidin-iFlour 488 (Abcam, United Kingdom) for 30 minutes at room temperature. After the phalloidin was removed, the samples were washed three times with PBS to eliminate any leftover residue. Finally, to facilitate nuclear visualisation, the cell nuclei were stained with 4',6-diamino-2-phenylindole (DAPI) (Abcam, United Kingdom) by covering the samples for 10 minutes at room temperature. After a final wash with PBS, the samples were photographed using a Leica DMIRB fluorescent microscope (Leica Microsystems United Kingdom) and a QImaging QICam Mono camera (Media Cybernetics United Kingdom). QCapture software (Media Cybernetics United Kingdom) was used to take the photos, and ImageJ was used to analyse them (ImageJ, National Institutes of Health, USA).

## 4.2.5 Real-Time Polymerase Chain Reaction

For the purpose of exploring the osteogenic differentiation and gene expression of the hADSCs, Real-Time Polymerase Chain Reaction (qPCR) was performed. The details below highlight the steps taken to reach the final gene expression analysis for the markers of interest.

### 4.2.5.1 RNA Isolation

Under sterile and RNA-free environmental conditions, RNA was isolated by the TRIzol® (Invitrogen, Paisley, United Kingdom) method on days 7, 14, 21 and 28 of culture throughout the hADSC experiment investigating the osteogenic differentiation as mentioned in section 4.2.3.2. The TRIzol® protocol involves a series of steps highlighted in figure 4-2.

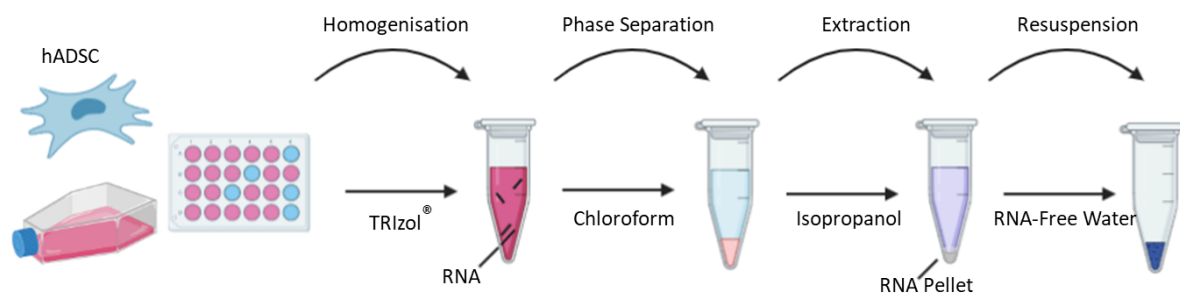


Figure 4-2: Diagram highlighting the steps involved in RNA isolation via the conventional TRIzol® method.

The protocol was interpreted from the TRIzol® user guide provided by ThermoFisher Scientific. The diagram was created using BioRender.commet

As seen in the diagram, the starting step is to homogenise the cells with the addition of the TRIzol® reagent which is the brand name for guanidinium thiocyanate. 0.75ml of the reagent is added to the cultured samples in the well-plate and homogenised for

a prolonged period to ensure all cells have detached from the surface of the material. The homogenised solution was transferred into a 1.5ml RNA-free Eppendorf microcentrifuge tube (ThermoFisher, United Kingdom) and incubated at room temperature for 5 minutes. 0.2ml of molecular grade 99.8% Chloroform (Sigma-Aldrich, St Louis, MO, USA) was added to each Eppendorf tube and then centrifuged using a Biofuge Fresco Centrifuge (Heraeus, Germany) at 13000 RPM for 15 minutes to allow for phase separation. From the centrifuged Eppendorf's, the aqueous phase (top layer) was removed at a 45° angle to avoid disruption of the organic phase.

Once the aqueous phase has been carefully removed it is added to a 0.5ml RNA-free microcentrifuge tube (ThermoFisher, United Kingdom) ready for the extraction phase which involves the addition of 0.5ml of molecular grade 99.5% Isopropanol (Fisher Scientific, United Kingdom). The Eppendorf was then placed on an IKA MS 3 Basic Vortex Mixer (Fisher Scientific, United Kingdom) to mix the components before incubating at room temperature for 10 minutes. Centrifugation was then carried out at 12000 RPM for 10 minutes prior to the supernatant being discarded. To further isolate the RNA, 1ml of a 75% dilution of 99% extra pure ethanol (Fisher Scientific, United Kingdom) was added, shaken and then centrifuged for 5 minutes at 7500 RPM. The ethanol was then removed carefully, ensuring not to disrupt the RNA pellet seen at the bottom of the Eppendorf. The tube was left to air-dry for 15 minutes to ensure removal of any excess ethanol. Finally, the RNA was re-suspended in 50µl of RNase-free water (Sigma-Aldrich, St Louis, MO, USA) and placed on a heat block for 10 minutes at 55°C. The yield of RNA was quantified by spectrophotometry (Spectronic Camspec Ltd., United Kingdom).

#### **4.2.5.2 cDNA Synthesis**

Complementary DNA (cDNA) is a DNA copy of a messenger RNA molecule produced by reverse transcriptase. For this study, cDNA synthesis was carried out using QuantiNova Reverse Transcription Kit (Qiagen, Germany). The components of the kit are highlighted in table 4-1 below. The kit includes integrated genomic DNA (gDNA) removal mix as well as an additional internal control. gDNA contamination in RNA samples is effectively eliminated by the gDNA Removal Mix which is crucial for accurate gene expression results and the internal control RNA can be used to test successful reverse transcription and amplification.

Table 4-1: Table representing the components of the QuantiNova Reverse Transcription Kit used for the synthesis of cDNA. The protocol was interpreted from Qiagen's procedural guide.

| <b>Component</b>      | <b>Benefits</b>                                    |
|-----------------------|--|
| gDNA Removal Mix      | Detection of RNA only in real-time PCR             |
| Internal Control RNA  | Verification of successful RT-PCR performance      |
| Reverse Transcriptase | Use of a wide range of RNA amounts (10 pg-5µg RNA) |
| RT Buffer System      | Read-through of difficult templates                |
| RT Primer Mix         | cDNA synthesis from all regions of transcripts     |

The whole procedure of cDNA synthesis is set up on ice to minimise the risk of RNA degradation. The gDNA removal reaction is prepared by mixing 2 µl of gDNA removal mix, 1 µl of internal control RNA, 5 µg of template RNA (from previous steps) and 6 µl of RNase-free water to make up the reaction volume of 15 µl. All the above components were mixed in a 0.2 ml PCR microcentrifuge tube (Fisher Scientific, United Kingdom) and incubated for 2 minutes at 45°C then placed immediately on ice.

The Reverse-transcription master mix was then prepared on ice by mixing 1 µl of the reverse transcription enzyme, 4µl of the reverse transcription mix and 15 µl of the template RNA (entire gDNA elimination reaction) from the previous step to make up a total reaction volume of 20 µl.

Using a PTC-100 Programmable Thermal Controller (MJ Research, Inc. Canada) the gDNA elimination and reverse-transcription temperature protocol was followed.

Table 4-2 below highlights the steps taken throughout the cycle.

Table 4-2: Reverse-transcription thermal cycle protocol followed.

| <b>Step</b>              | <b>Time</b> | <b>Temperature</b> |
|--------------------------|-------------|--------------------|
| Annealing                | 3 minutes   | 25°C               |
| Reverse-transcription    | 10 minutes  | 45°C               |
| Inactivation of reaction | 5 minutes   | 85°C               |

The reverse-transcription reactions were then placed in the -20°C freezer where they were stored until real-time PCR was carried out.

#### **4.2.5.3 qPCR Workflow**

Power Sybr Green PCR master mix (ThermoFisher, United Kingdom) and pre-prepared primers (Taqman Gene Expression Assay) (ThermoFisher, United Kingdom) (Table 4-3) were used to perform real-time polymerase chain reaction (qPCR) for the analysis of differentiation pathways of hADSCs. Beta-2-microglobulin (B2M), glyceraldehyde 3-phosphate dehydrogenase (GAPDH) and peptidylprolyl isomerase A (PPIA) were used as reference genes until the first time point, where expression of B2M and PPIA was not seen so GAPDH was used to go forward with in the experiment. The primers of interest for this study were Runt-related transcription factor 2 (RUNX2), Collagen, type 1 (COL1A1), Osteocalcin (OCN) and Osteopontin (OPN / SPP1).



Table 4-3: Table representing the forward and reverse primer sequences used for qPCR highlighting the species acquired from and the annealing temperature for each gene.

| Gene                   | Forward Primer          | Reverse Primer          | Species | Annealing Temperature (°C) |
|------------------------|-------------------------|-------------------------|---------|----------------------------|
| GAPDH (Reference Gene) | GTCTCCTCTGACTTCAACAGCG  | ACCACCCTGTTGCTGTAGCCAA  | Human   | 56.5                       |
| RUNX2                  | CCCAGTATGAGAGTAGGTGTCC  | GGGTAAGACTGGTCATAGGACC  | Human   | 55                         |
| COL1A1                 | GATTCCTGGACCTAAAGGTGC   | AGCCTCTCCATCTTTGCCAGCA  | Human   | 57                         |
| OCN                    | CGCTACCTGTATCAATGGCTGG  | CTCCTGAAAGCCGATGTGGTCA  | Human   | 64                         |
| OPN (SPP1)             | CGAGGTGATAGTGTGGTTTATGG | GCACCATTCAACTCCTCGCTTTC | Human   | 60                         |

To prepare the reaction mix and the well-plate ready for qPCR, all the TaqMan Gene Expression Assays mentioned above were thawed on ice along with the cDNA samples and the Sybr Green Master Mix. According to the protocol provided by Applied Biosystems and Thermo Fisher, triplicates of each reaction should be performed for the purpose of reproducibility.

Table 4-4 below shows the components of the PCR reaction mix and their required volumes for a 20 µl reaction.

Table 4-4: Table highlighting the quantity required of each component for the qPCR reaction.

| PCR Reaction Mix Component       | Volume Per 20 µl Single Reaction |
|----------------------------------|----------------------------------|
| 20X TaqMan Gene Expression Assay | 1.0                              |
| 2X Sybr Green Master Mix         | 10.0                             |
| cDNA Template                    | 4.0                              |
| RNAse-free Water                 | 5.0                              |

The 20  $\mu$ l of PCR reaction mix was transferred to a 96-well reaction plate (ThermoFisher, United Kingdom) and sealed with an appropriate cover slip. The plate was centrifuged for 20 seconds before being loaded into the instrument. The instrument used was the Applied Biosystems 7300 Real-Time PCR System.

The qPCR reaction was run for a total of 40 cycles with it at 95°C for 15 seconds and 60°C for 1 minute. Analysis was performed by viewing the amplification plots for the entire plate, setting the baseline and threshold values and using the comparative cycle threshold ( $C_T$ ) values.

#### **4.2.5.3 qPCR Analysis**

Absolute and relative quantification are the two approaches to presenting quantitative gene expression. To provide the data of the gene of interest relative to an internal control gene, relative gene expression was used in this study. To eliminate any sources of variation in RNA concentration and cDNA between samples, a normalisation procedure is required. These equations have been described in detail by Livak and colleagues (Livak and Schmittgen, 2001), and will be discussed briefly below. All  $C_t$  values were exported from the qPCR machine and transferred to an Excel spreadsheet, where the relative gene expression value was calculated using the delta  $C_t$  method ( $\Delta\Delta C_t$ ) with GAPDH as the reference gene and TCP expression as the control.

The data was normalised to ensure high precision for both the target and reference genes. The gene of interest is the target gene, while the housekeeping gene is the

reference gene. All of them were tested in triplicates, yielding several Ct values that were added together to create an average Ct value for both genes.

To normalise the average Ct of the target gene in relation to the average Ct of the reference gene, equation 4-1 was used.

$$\Delta Ct = \text{Average target Ct} - \text{Average reference Ct}$$

*Equation 4-1: Normalisation step to calculate the  $\Delta Ct$ .*

The control sample group used throughout the experiment, in this case the cells seeded on tissue culture plastic, are selected as the calibrator sample. This allows the calculation of  $\Delta\Delta Ct$  for each sample. The calibrator sample was also calibrated against itself to produce a value of zero in order to generate a value of 1 which will be set as the baseline for the relative gene expression comparison.

$$\Delta\Delta Ct = \Delta Ct \text{ target} - \Delta Ct \text{ calibrator}$$

*Equation 4-2: Calibration step to set a value for the baseline*

Finally, a fold change was calculated using the obtained gene expression values of the samples that were higher or lower than the baseline (set to 1) represented by the final equation  $2^{-\Delta\Delta Ct}$  (equation 4-1).

$$\text{Relative quantification} = 2^{-\Delta\Delta Ct}$$

*Equation 4-3: Showing the final form of the  $2^{-\Delta\Delta Ct}$  equation, the derivation of which has been reported previously by Livak and colleagues (Livak and Schmittgen, 2001).*

Expanding relative quantification to its full form gives the equation:

$$2^{-\Delta\Delta Ct} = \frac{[(CT \text{ gene of interest} - CT \text{ internal control})_{\text{sample A}}]}{[(CT \text{ gene of interest} - CT \text{ internal control})_{\text{sample B}}]}$$

Equation 4-4: Expanded relative quantification where the equation may be used to compare the gene expression in two different samples (sample A and sample B); each sample is related to an internal control gene.

All qPCR reactions were performed in triplicate and each of the gene signals were normalised to the GAPDH signal detected simultaneously on the same plate. The data were presented as the mean fold change (relative expression) ( $\pm$  SD) compared with that of control cells cultured on TCP in either standard or osteogenic media in the absence of any material additions.

#### 4.2.6 Angiogenesis Assessment

For the purpose of evaluating the biocompatibility and angiogenic response to the polymer (CSMA-2) along with its composites containing either 5 wt% HA or 10 wt% HA, an *ex-ovo* (embryo cultured outside of the eggshell) Chick Chorioallantoic Membrane (CAM) Assay was used. The glass-cling film set-up method followed for this procedure was previously explored by Kohli and co-researchers (Kohli *et al.*, 2020). The use of chick embryos in this study did not require ethical permission, according to Institutional Animal Care and Use Committee (IACUC) guidelines, which specify that a chick embryo would not experience pain before the 14th day of its gestation cycle, therefore it can be used for experiments. Fertilised pathogen-free eggs were procured from a licenced local farm in Middlesex (United Kingdom) and incubated for three days at 38°C with 40-45% humidity in an egg incubator with automatic rotation. The eggs were cracked onto a glass-cling film set up on embryonic day 3 (ED 3). Observing the unbroken egg yolk and the beating heart of the chick

embryo, as shown in figure 4-3 below, confirms a successful embryo transfer into the set-up. 500  $\mu$ l of antimicrobial solution was pipetted onto the albumen to prevent contamination from the eggshells. To give time for growth, the successful embryo glasses were covered with a Petri dish and placed in the incubator at 38°C and 80-90% humidity for another 6 days until ED 9.

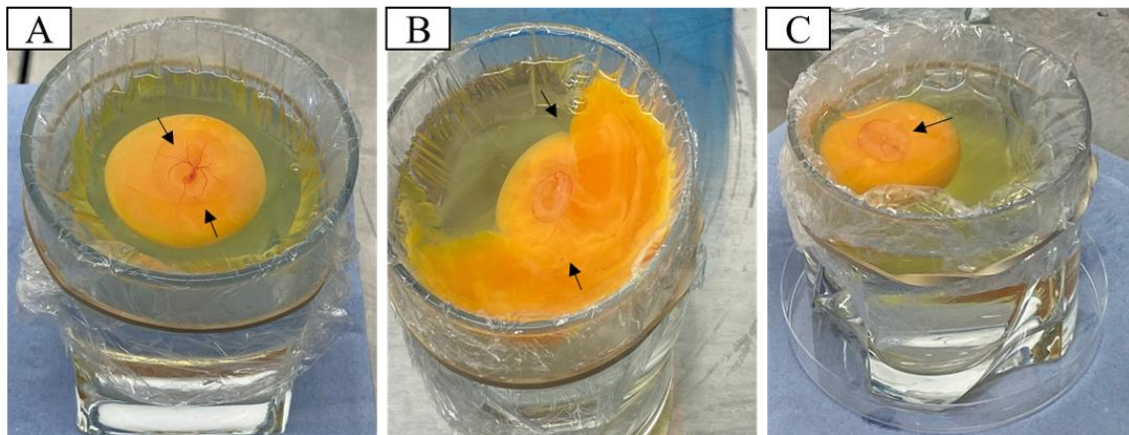


*Figure 4-3: Observation of (A) successful embryo transfer with an intact egg yolk and live embryo on embryonic development day 3. (B) An unsuccessful embryo transfer with a live embryo. (C) Successful embryo transfer with an intact egg yolk but a dead embryo as the heart is not beating.*

On ED 9, all the scaffolds and control samples were implanted on the developing CAM to allow infiltration of blood vessels. All samples were sterilised by dipping in ethanol. The positive control was filter paper discs soaked in 10 ng/ml of vascular endothelial growth factor (VEGF) solution and the negative control was filter paper discs soaked in PBS. CSMA-2 composite-polymer porous scaffolds, 6 mm in diameter and 3 mm thick with 0.5 mm pores were designed via AutoCAD (Autodesk, United Kingdom) and 3D printed using the XYZ Nobel Superfine SLA Printer (XYZ Printing, The

Netherlands) (See Chapter 2, section 2.2.9 for details). After placement of the scaffolds (figure 4-4) the ex-ovo cultures were incubated for a further 3 days until ED 12.

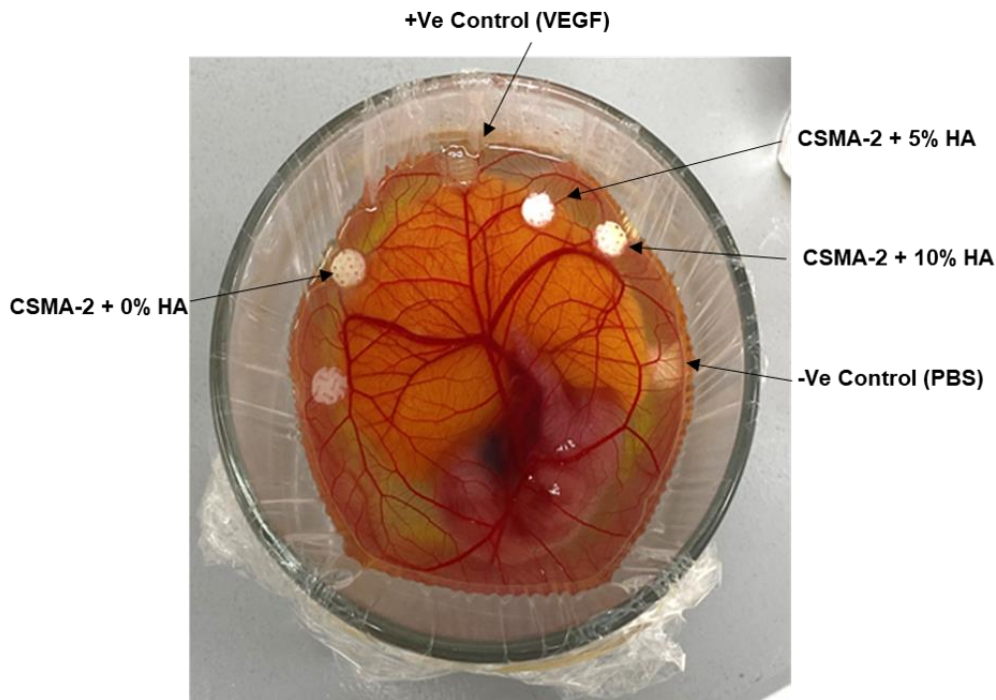


Figure 4-4: An image taken from above the ex-ovo culture on embryonic development day 9 showing the implantation of CSMA-2 composite-polymer porous scaffolds that were prepared via SLA 3D printing along with the positive and negative controls which were all sterilised using ethanol before implantation on the CAM.

#### 4.2.6.1 CAM Assay Analysis

At the end of the testing period, on embryonic development day 12, the cultured embryos were euthanised as per UK Home Office regulations by freezing at  $-20^{\circ}\text{C}$  for 15 minutes before being fixed in 5 ml of 4% paraformaldehyde for another 15 minutes to avoid any bleeding of the CAM after excision. The scaffolds were dissected with a small amount ( $\sim 5$  mm) of the CAM excised along with the scaffold.

Digital images were taken using a Canon EOS 1300D camera (Canon UK Ltd, Uxbridge, United Kingdom) with a Nikon (Nikon UK, Kingston Upon Thames, United Kingdom) macro lens (AF Micro Nikkor 55 mm). The samples were inverted to observe the infiltrating blood vessels from underneath.

The images taken were analysed further using ImageJ software. The images were first converted into grey scale images, followed by binary images to allow the vascular density area to be calculated via the programme's area fraction function. Bifurcation points were also counted in each image using ImageJ's counter function which digitally selects the number of branching points seen in the image of each scaffold.

#### **4.2.7 Statistical Analysis**

In this chapter, all data were analysed using OriginPro 2020 (OriginPro, OriginLab Corporation, USA). All experiments have three repeats ( $n = 3$ ). The results are presented in mean  $\pm$  standard deviation. A one-way analysis of variance with Tukey's post hoc test was used throughout where  $p < 0.05$  was considered significant after being calculated at a 95% confidence interval.

### **4.3 Results**

#### **4.3.1 Cytocompatibility Studies**

##### **4.3.1.1 MG-63 Metabolic Activity**

In order to investigate the cytocompatibility of CSMA-2 and the effect of the two photoinitiators, CQ and BAPO, the metabolic activity and proliferation of MG-63 osteosarcoma cells were initially assessed. Additionally, incorporation of various filler percentages (0, 5 and 10 wt% hydroxyapatite) into the composite and its effect on the

metabolic activity of the cells was evaluated. Figure 4-5 shows the findings of the alamarBlue assay, which provided a quantitative evaluation of cell metabolism.

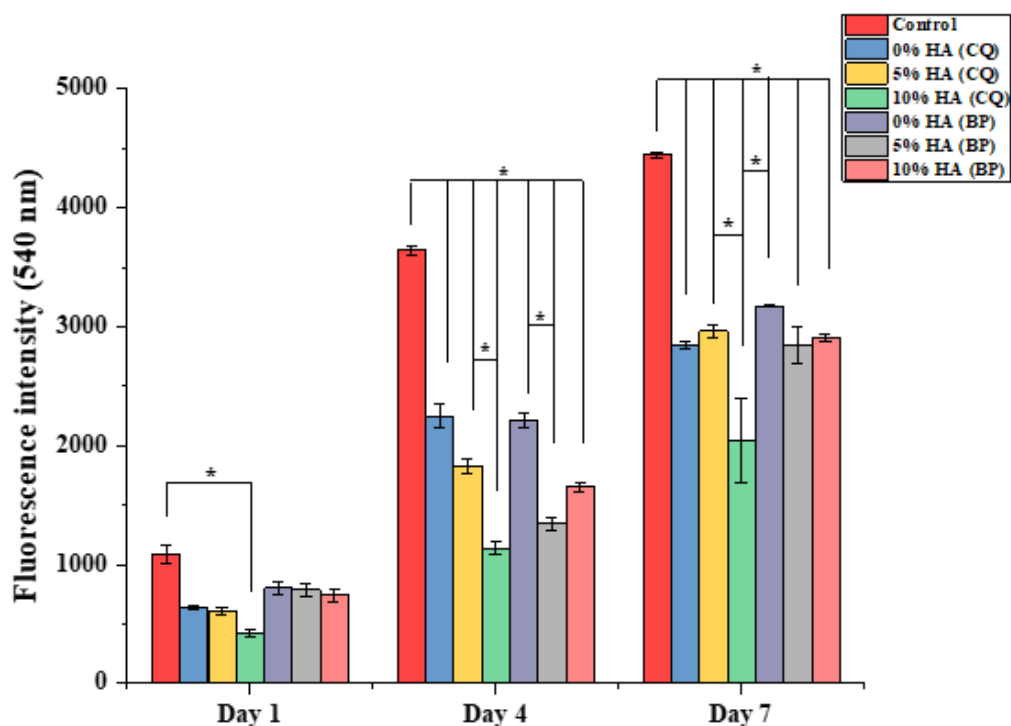


Figure 4-5: Metabolic activity of MG-63 cells on 0, 5 and 10 wt% HA incorporated composite discs with either CQ or BAPO (BP) photoinitiator at 1, 4 and 7 days post incubation. The values are compared to cells grown on tissue culture plastic (TCP) control in this experiment. As seen in the graph, the discs containing BAPO (BP) initiator have higher fluorescence intensity values, suggesting a higher metabolic activity on those samples. The control is significantly different to all the samples in the day 4 and 7 cultured experiment at ( $*p < 0.05$ ).

Figure 4-5 demonstrates that both the CQ and BAPO groups had an increase in metabolic activity throughout the study, albeit at a substantially lower pace than the control group, which exhibited fluorescence intensity measurement findings ranging from 1084 to 4442. The control group for this experiment was seeding cells on tissue culture plastic (TCP) which offers a good platform for cells to proliferate on due to its



pre-treated hydrophilic surface. The addition of HA had an effect on cell metabolic activity as well, albeit it is unclear whether this was a good or negative effect based on the results of this experiment. The results also suggest an increase in metabolic activity rate for the BAPO photoinitiator prepared specimens as they were all consistently higher than the CQ formulations. These results suggested that the focus of the rest of the study should be on the BAPO incorporated CSMA-2 specimens with an investigation into the effects of up to 10 wt% HA.

#### **4.3.1.2 MG-63 Fluorescence Microscopy**

For the purpose of investigating the MG-63 cells morphology and attachment, DAPI and phalloidin staining were used. DAPI highlights the nucleus and phalloidin highlights cytoskeleton of the cell which can be seen in blue and green respectively in figures 4-6, 4-7 and 4-8. The staining allowed the analysis of cell interaction with the surface of the polymer in comparison with the control samples. The images at day 1 (figure 4-6) confirm that the cells adhered and spread well on the surface and of the composite-polymer discs in a similar pattern as the control samples which were seeded on TCP. The same pattern can also be observed for the day 4 results (figure 4-7) and by day 7 (figure 4-8) the surface was completely covered in cells on all the formulations. It can be seen in figure 4-6 that the results from the CQ groups (B, D and F) are harder to visualise as the discs became slightly concave after curing under the UV for a prolonged period. This could also suggest that the 3D printed discs gave better uniformity as they did not change in structure over time, even when exposed to the same amount of UV as the CQ, manually prepared specimens. The composite-

polymer made with 2 wt% BAPO and 10 wt% HA (represented by image G) seemed to exhibit the highest quantity of cells present at all-time points with little difference to the control sample.

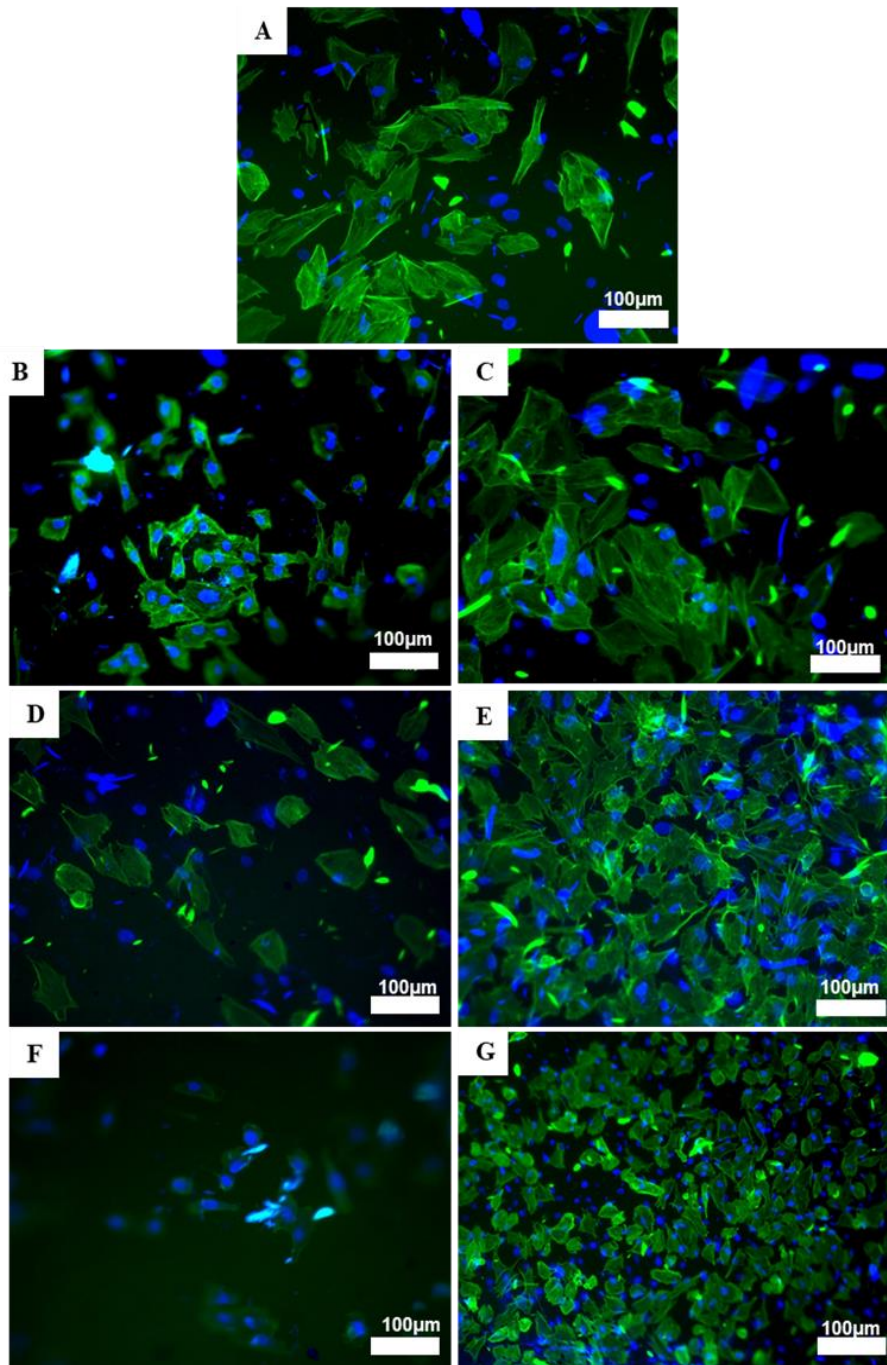


Figure 4-6: Fluorescence imaging results for DAY 1 using DAPI and phalloidin (blue and green respectively) to assess the proliferation and morphology of MG-63 osteosarcoma cells on the surface of the tissue culture plastic control (A) compared to CSMA-2 prepared with 2 wt% CQ photoinitiator (B), CSMA-2 with 2 wt% BAPO photoinitiator (C), CSMA-2 with 2 wt% CQ and 5 wt% HA (D), CSMA-2 with 2 wt% CQ and 10 wt% HA (E) and CSMA-2 with 2 wt% BAPO and 10 wt% HA (G). Scale Bar = 100µm

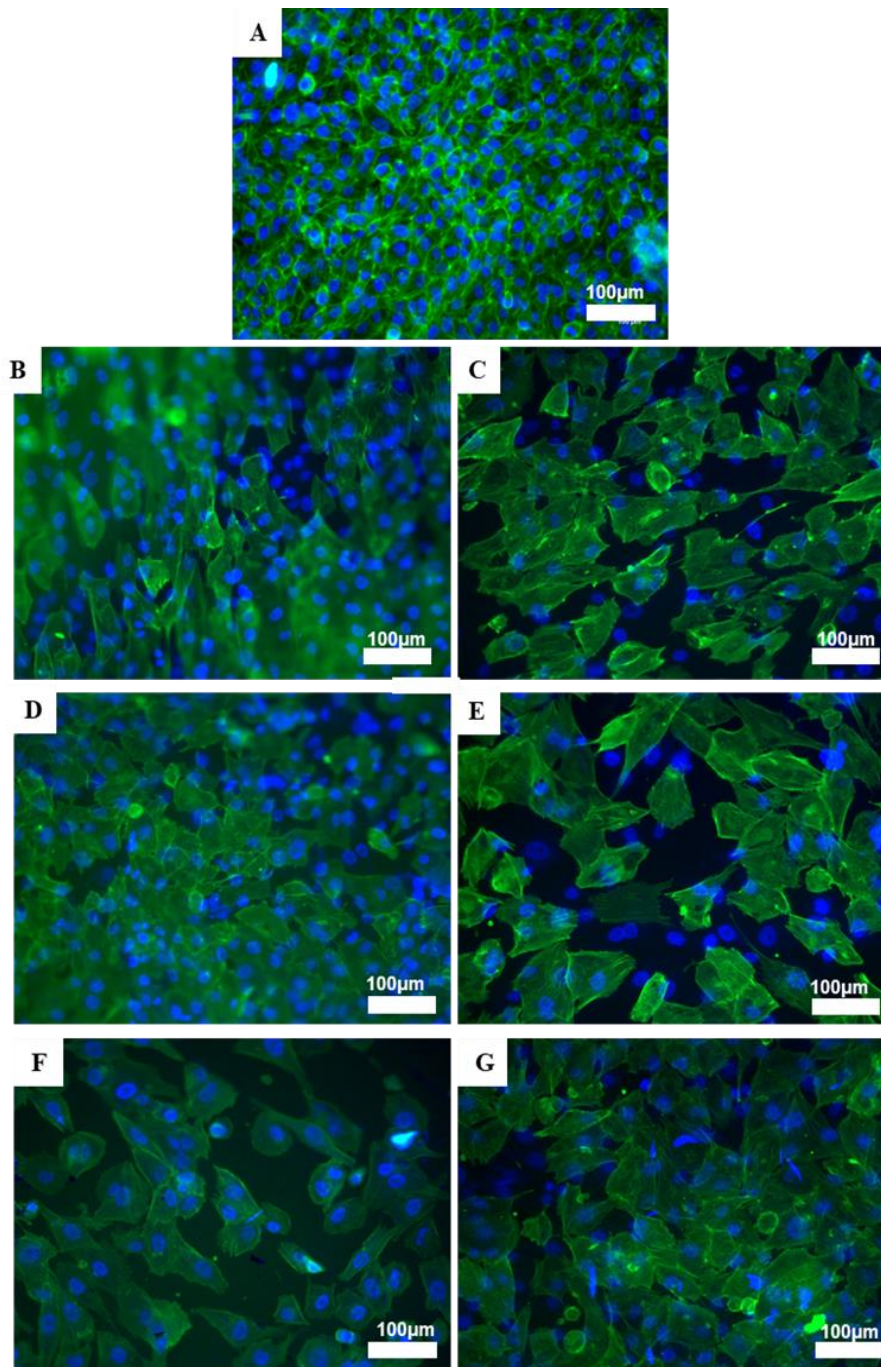


Figure 4-7: Fluorescence imaging results for DAY 4 using DAPI and phalloidin (blue and green respectively) to assess the proliferation and morphology of MG-63 osteosarcoma cells on the surface of the tissue culture plastic control (A) compared to CSMA-2 prepared with 2 wt% CQ photoinitiator (B), CSMA-2 with 2 wt% BAPO photoinitiator (C), CSMA-2 with 2 wt% CQ and 5 wt% HA (D), CSMA-2 with 2 wt% CQ and 10 wt% HA (E) and CSMA-2 with 2 wt% BAPO and 10 wt% HA (G). Scale Bar = 100µm

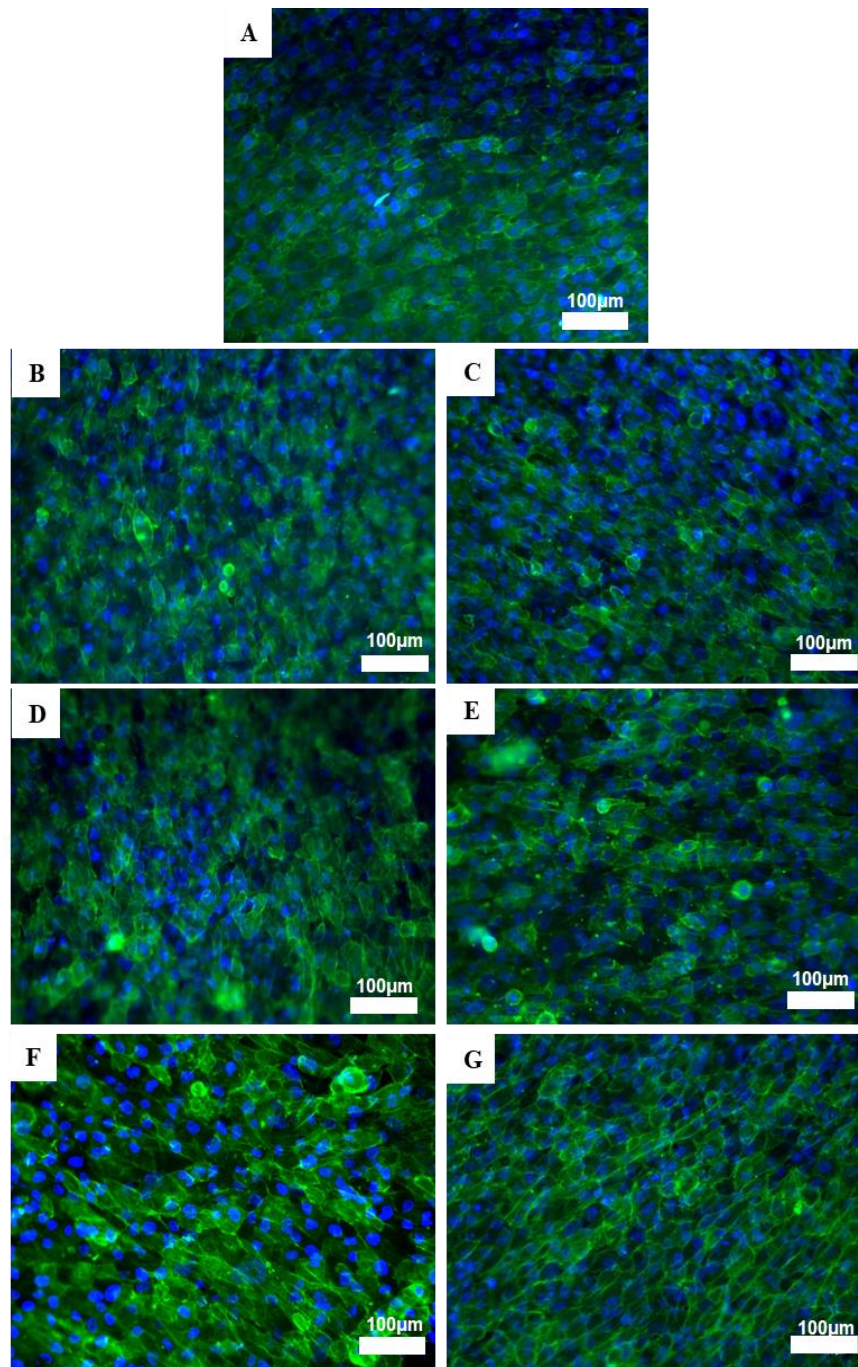


Figure 4-8: Fluorescence imaging results for DAY 7 using DAPI and phalloidin (blue and green respectively) to assess the proliferation and morphology of MG-63 osteosarcoma cells on the surface of the tissue culture plastic control (A) compared to CSMA-2 prepared with 2 wt% CQ photoinitiator (B), CSMA-2 with 2 wt% BAPO photoinitiator (C), CSMA-2 with 2 wt% CQ and 5 wt% HA (D), CSMA-2 with 2 wt% CQ and 10 wt% HA (E) and CSMA-2 with 2 wt% BAPO and 10 wt% HA (G). Scale Bar = 100µm

#### **4.3.1.3 hADSC Metabolic Activity**

The cytocompatibility of CSMA-2 and its composites was further analysed by using Human Adipose Derived Stem Cells. Based on the previous MG-63 experiment in section 4.3.1.1, the BAPO photoinitiator gave better results for the metabolic activity compared to the CQ samples. As a result of this, the formulations carried forward for further *in vitro* investigation were all 3D printed into 10 mm x 1 mm discs using 2 wt% BAPO as the photoinitiator. The control sample used in this study was a glass cover slip of the same dimensions and the formulations chosen for use were 0, 5 and 10 wt% HA incorporated composite-polymer discs. Figure 4-9 shows the findings of the alamarBlue assay, which provided a quantitative evaluation of cell metabolism in hADSCs.

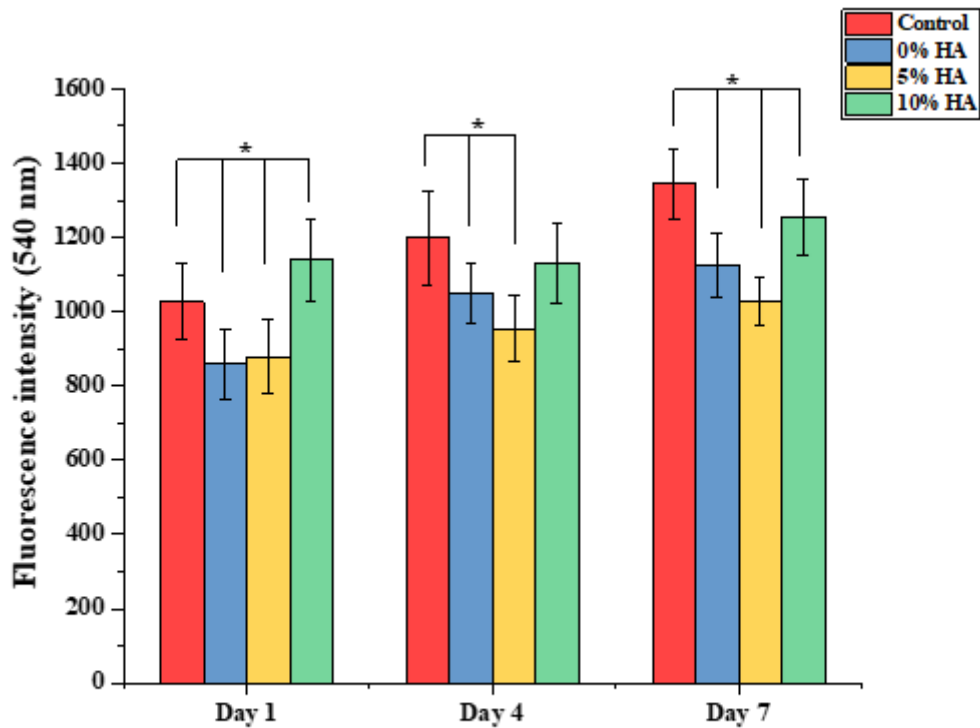


Figure 4-9: Metabolic activity of hADSCs on 0, 5 and 10 wt% HA incorporated composite discs with BAPO photoinitiator at 1, 4 and 7 days post incubation. The values are compared to cells grown on the surface of a control glass. As seen in the graph, the discs containing 10 wt% HA have significantly higher fluorescence intensity values when comparing them to the 0 and 5 wt% HA samples, suggesting a higher metabolic activity for that formulation. The control is significantly higher than the other formulations for all of the time points except for day 4 where the control and 10 wt% HA formulations are not significantly different. (\* $p < 0.05$ ).

The results from figure 4-9 show that the effect of higher quantities of HA have a positive impact on the metabolic activity of hADSCs. All 3 groups continued to show an increase in metabolic activity throughout the study time points but remained significantly lower than the control group, apart from the 10 wt% HA formulations. CSMA-2 by itself, with no added HA (blue) promoted good cell growth and proliferation with a fluorescence intensity measurement ranging between 858-1125 throughout, but

the results were consistently significantly lower than the 10 wt% HA incorporated formulation which ranged between 1138-1255.

#### **4.3.1.4 hADSC Fluorescence Microscopy**

For the purpose of investigating the hADSCs morphology and attachment, DAPI and phalloidin staining were used. DAPI highlights the nucleus and phalloidin highlights cytoskeleton of the cell which can be seen in blue and green respectively in figures 4-10, 4-11 and 4-12. The images at day 1 (figure 4-10) confirm the attachment and proliferation of the cells on the surface of the composite-polymer discs in a similar pattern as the control samples, represented by image (A) in the figures, which were seeded on glass cover slips. As seen in the figures, the hADSCs adhered and spread well on the scaffolds, as seen by their change from a rounded shape on day 1 (figure 4-10 B, C and D) to a flattened and elongated spread morphology by day 4 and day 7. It can be seen in all the timepoints that the 10 wt% formulation (represented by image D) has the highest quantity of cells attached to the surface, closely comparing to the control group.



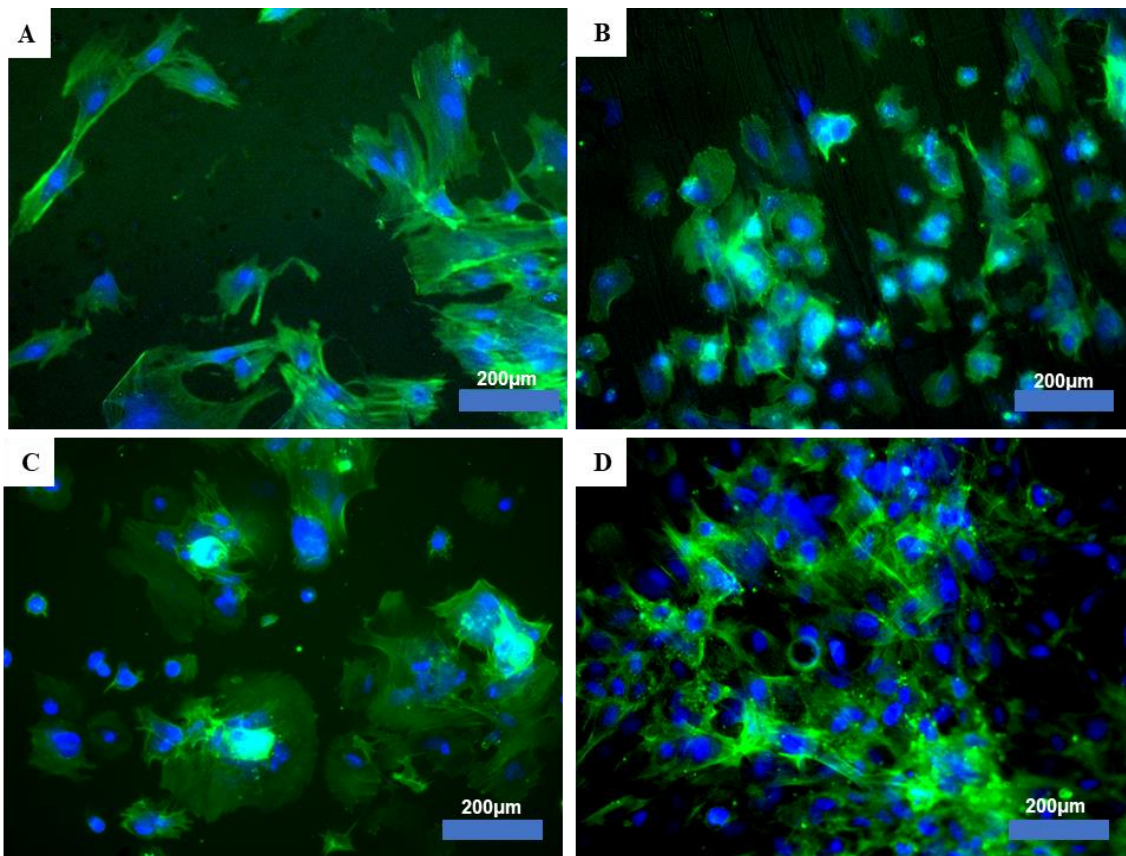


Figure 4-10: Fluorescence imaging results for DAY 1 using DAPI and phalloidin (blue and green respectively) to assess the proliferation and morphology of hADSCs on the surface of a control glass coverslip (A) compared to CSMA-2 prepared with 2 wt% BAPO photoinitiator and no added HA (B), CSMA-2 with 2 wt% BAPO and 5 wt% HA (C) and CSMA-2 with 2 wt% BAPO and 10 wt% HA (D). Scale Bar = 200µm

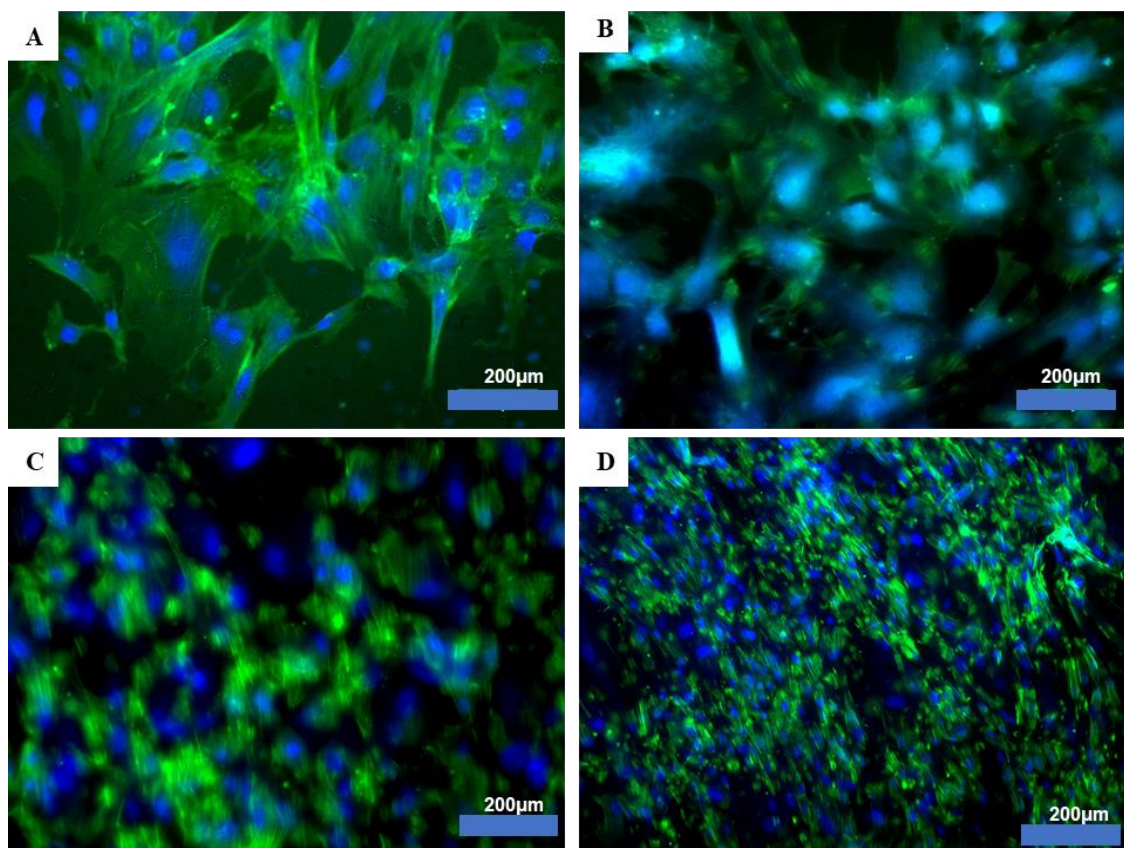


Figure 4-11: Fluorescence imaging results for DAY 4 using DAPI and phalloidin (blue and green respectively) to assess the proliferation and morphology of hADSCs on the surface of a control glass coverslip (A) compared to CSMA-2 prepared with 2 wt% BAPO photoinitiator and no added HA (B), CSMA-2 with 2 wt% BAPO and 5 wt% HA (C) and CSMA-2 with 2 wt% BAPO and 10 wt% HA (D). Scale Bar = 200 $\mu$ m

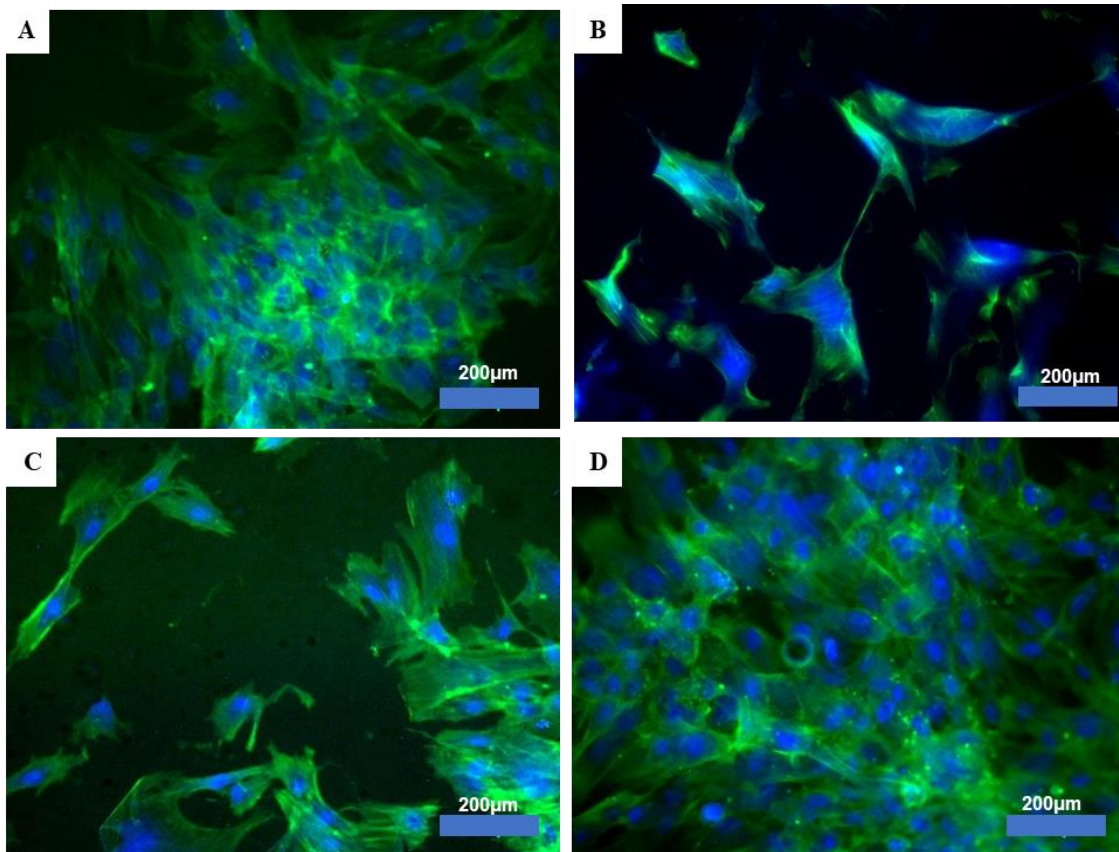


Figure 4-12: Fluorescence imaging results for DAY 7 using DAPI and phalloidin (blue and green respectively) to assess the proliferation and morphology of hADSCs on the surface of a control glass coverslip (A) compared to CSMA-2 prepared with 2 wt% BAPO photoinitiator and no added HA (B), CSMA-2 with 2 wt% BAPO and 5 wt% HA (C) and CSMA-2 with 2 wt% BAPO and 10 wt% HA (D). Scale Bar = 200µm

### 4.3.2 Osteogenic Differentiation

#### 4.3.2.1 Metabolic Activity

In order to assess the osteogenic differentiation of hADSCs on CSMA-2 and its composite-polymer specimens the metabolic activity and proliferation of the cells grown in either standard MesenPRO RS Media (SM) or the cells grown in osteogenic

supplemented media (OM) were assessed alongside the incorporation of various filler percentages (0, 5 and 10 wt% HA) into the composite. The alamarBlue assay gave a quantitative measurement of cell metabolic activity and the results can be seen in figure 4-13 below.

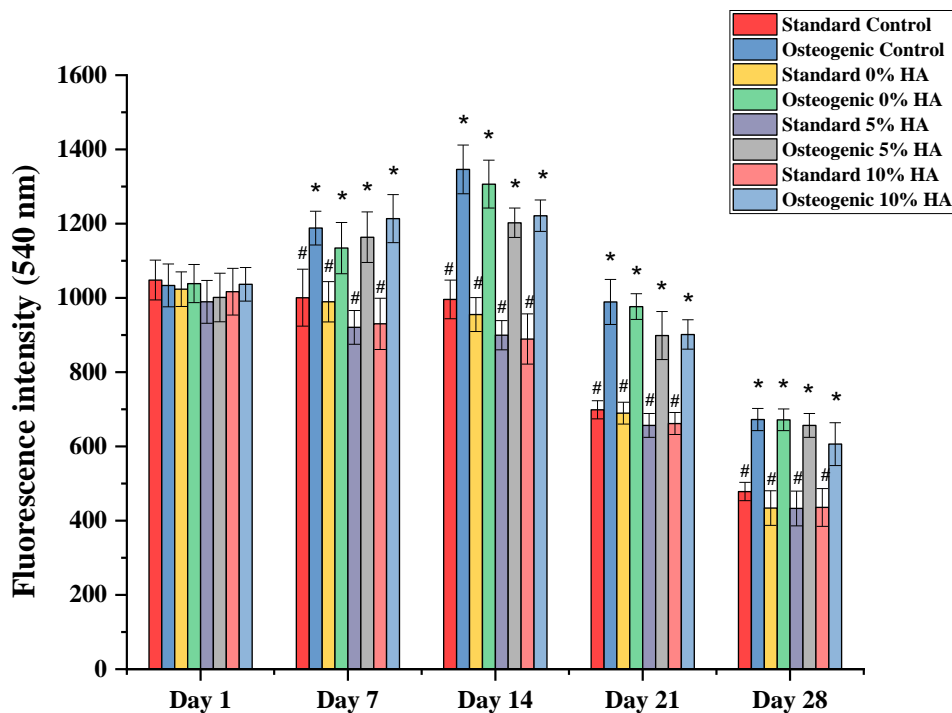


Figure 4-13: Metabolic activity of hADSCs cultured in either SM or OM on 0, 5 and 10 wt% HA incorporated composite discs with BAPO photoinitiator at 1, 7, 14, 21 and 29 days post incubation. The values are compared to cells grown on the surface of a control glass disc. As seen in the graph, after 7 days of culture, the cells grown in OM had a higher metabolic activity and this trend remained the same throughout. The SM groups were compared statistically to the OM groups where all the timepoints from day 7 onwards showed significant differences. The highest metabolic activity was seen in the OM-0% HA group, although this was not significantly different to the OM control or the 5 and 10 wt% HA formulations, suggesting promotion of cell metabolic activity throughout. Data are presented as Mean  $\pm$  SD, n=3. (\*p < 0.05) where \* represents significant difference to the SM control sample and # represents significant difference to the OM control sample.

The results from figure 4-13 show that the osteogenic media used to culture the hADSCs had a bigger impact on the cell metabolic activity than the standard media used. Consistently from day 7- day 28, the metabolic activity results were higher for all the formulations in OM. The standard control displayed fluorescence intensity measurements ranging between 478-1048, the lowest being day 28 again, and the highest being day 1. This significantly compares to the osteogenic-supplemented media results as the OM control samples displayed fluorescence intensity measurements ranging between 672-1346, the lowest being at the end of the experiment (day 28) and the highest being at day 14.

When comparing the polymer and its composite formulations, the OM cultured CSMA-2 with no added HA (highlighted in the green) showed the closest results to the OM control with measurements ranging between 671-1306 which is significantly higher than its standard media culture (highlighted in the yellow) which ranged from 434-1023. The HA incorporated formulations also followed a similar trend where the osteogenic media group displayed higher metabolic activity than the standard media.

By day 21, the rate of metabolic activity took a negative toll, where the quantity reduced quite drastically. This could be due to the stress that the cells were under, given it was such a lengthy experiment, or that the cells had grown in such a way that there was no space left for more proliferation to occur.

#### ***4.3.2.2 Fluorescence Microscopy***

Like the previous experiments, for the purpose of investigating the hADSCs morphology and attachment, DAPI and phalloidin staining were used. DAPI highlights

the nucleus and phalloidin highlights cytoskeleton of the cell which can be seen in blue and green respectively in figures 4-14, 4-15, 4-16 and 4-17.

The images were taken for the day 7, 14, 21 and 28 timepoints. The day 1 results did not stain in the expected way therefore fluorescent images could not be captured to show the attachment after day 1. In all the figures below, the left hand side images represent the cell culture that took place in standard media, and the right hand side images represent the cell culture that took place in osteogenic-supplemented media. Figure 4-14, highlighting day 7s results, confirms the attachment and proliferation of the cells on the surface of the composite-polymer discs in a similar pattern as the control samples. It can be seen clearly the difference in morphology of the hADSCs in the two different media states. The standard media cells have an elongated morphology, showing their attachment to one another. The osteogenic media cells show a more rounded morphology, especially during the early time points as they are differentiated over time. The figures show that the hADSCs adhered and spread well on the scaffolds in comparison to the control samples that were seeded on glass cover slips. The day 14 (figure 4-15) and the day 21 (figure 4-16) show a significantly higher number of cells attached to the surface with their cytoskeleton and nucleus clearly highlighted. The cells cultured in osteogenic-supplemented media can be seen to differentiate into potential osteoblasts throughout the study, however they can also be differentiating into other types of cells such as chondrocytes, myocytes or adipocytes which explains the variations in morphology seen in the figures below.

### Standard Media

### Osteogenic-Supplemented Media

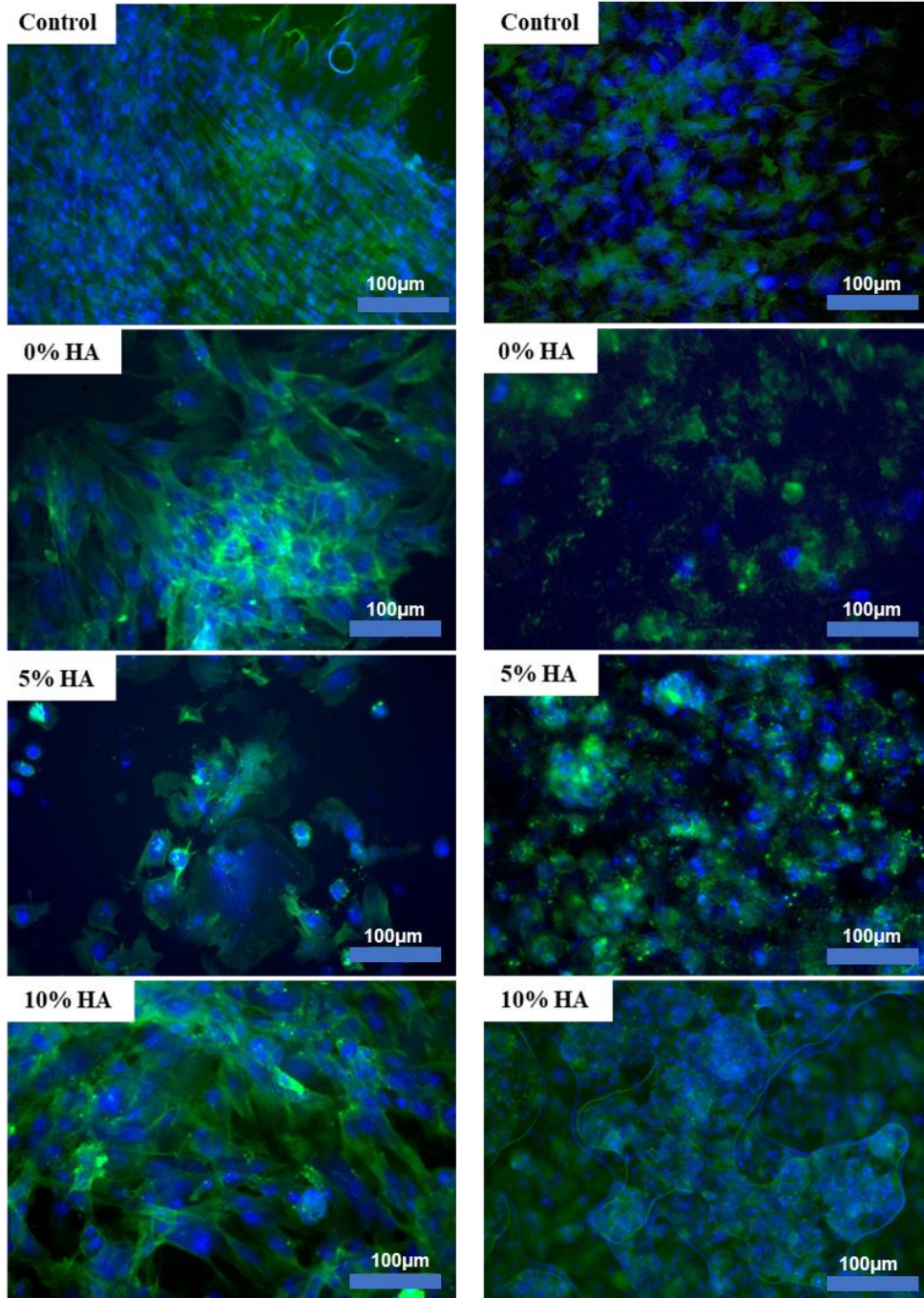


Figure 4-14: Fluorescence imaging results for DAY 7 using DAPI and phalloidin (blue and green respectively) to assess the proliferation and morphology of hADSCs on the surface of the composite-polymer specimens prepared in either standard media or osteogenic supplemented media. The left hand side images are the results for the standard media, and they're compared to the right hand side images which are the osteogenic supplemented specimens. Scale Bar= 100µm.

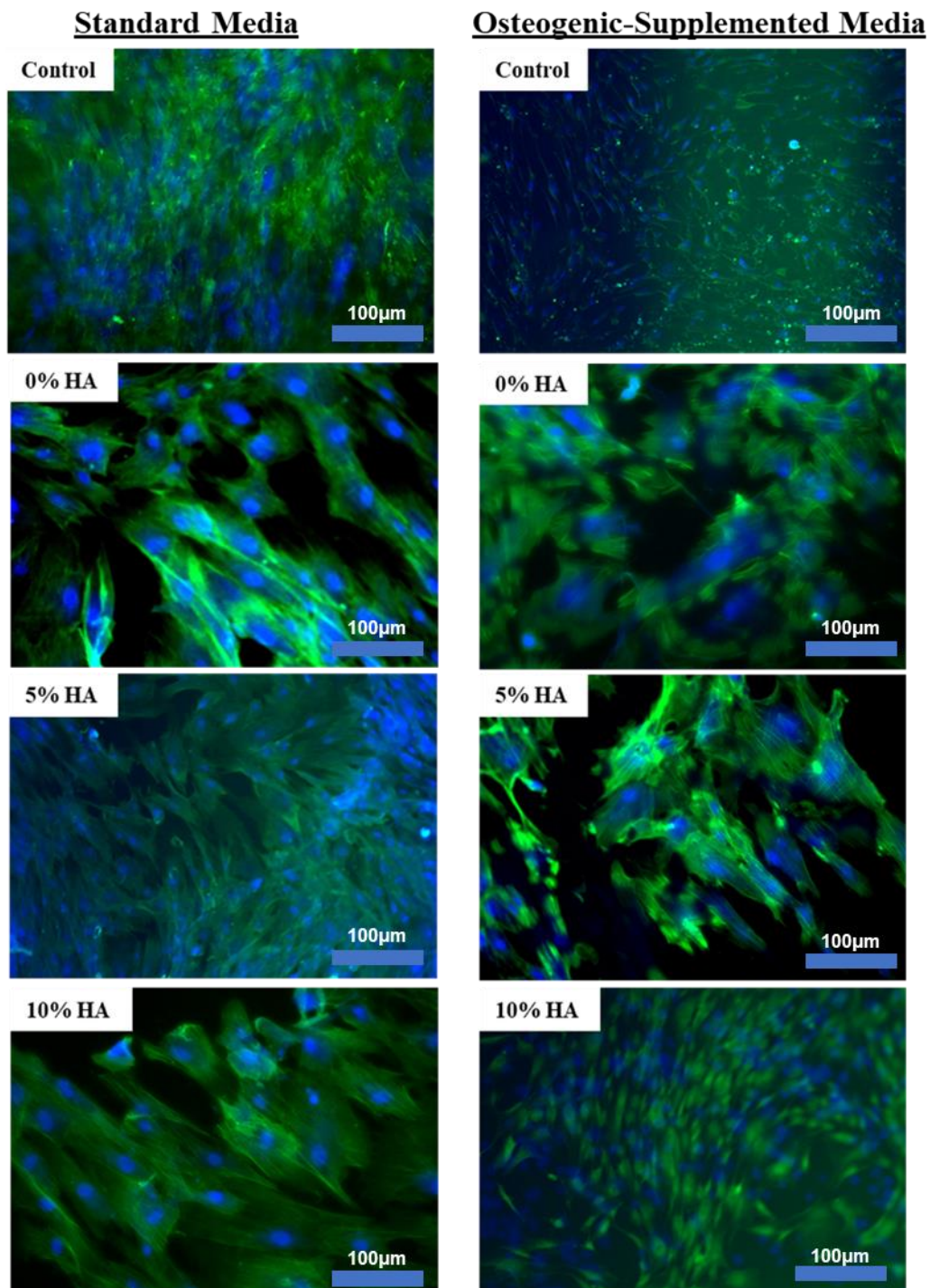
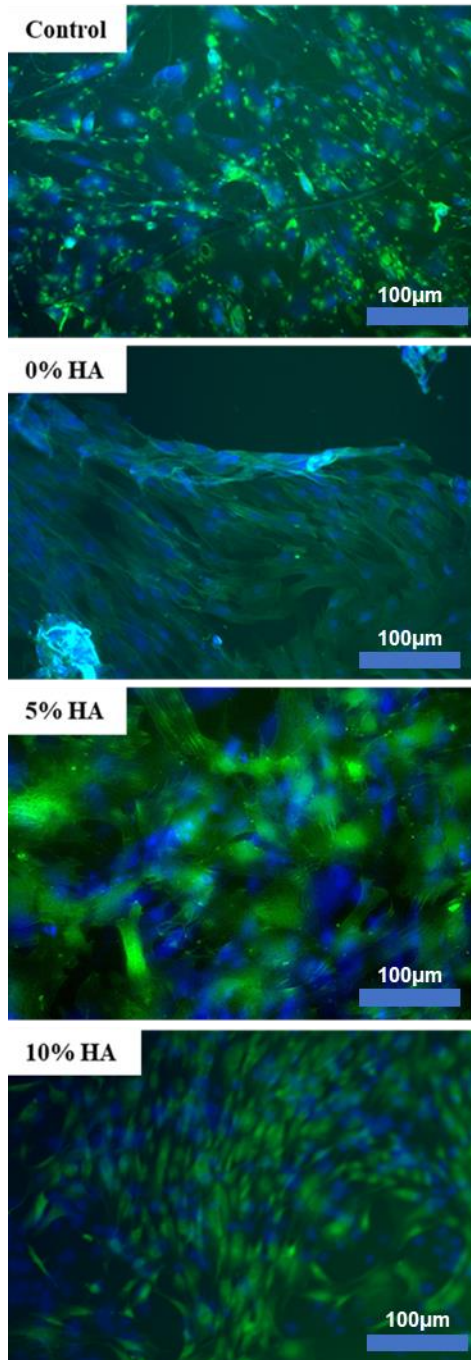


Figure 4-15: Fluorescence imaging results for DAY 14 using DAPI and phalloidin (blue and green respectively) to assess the proliferation and morphology of hADSCs on the surface of the composite-polymer specimens prepared in either standard media or osteogenic supplemented media. The left hand side images are the results for the standard media, and they're compared to the right hand side images which are the osteogenic supplemented specimens. Scale Bar= 100µm.



### Standard Media



### Osteogenic-Supplemented Media

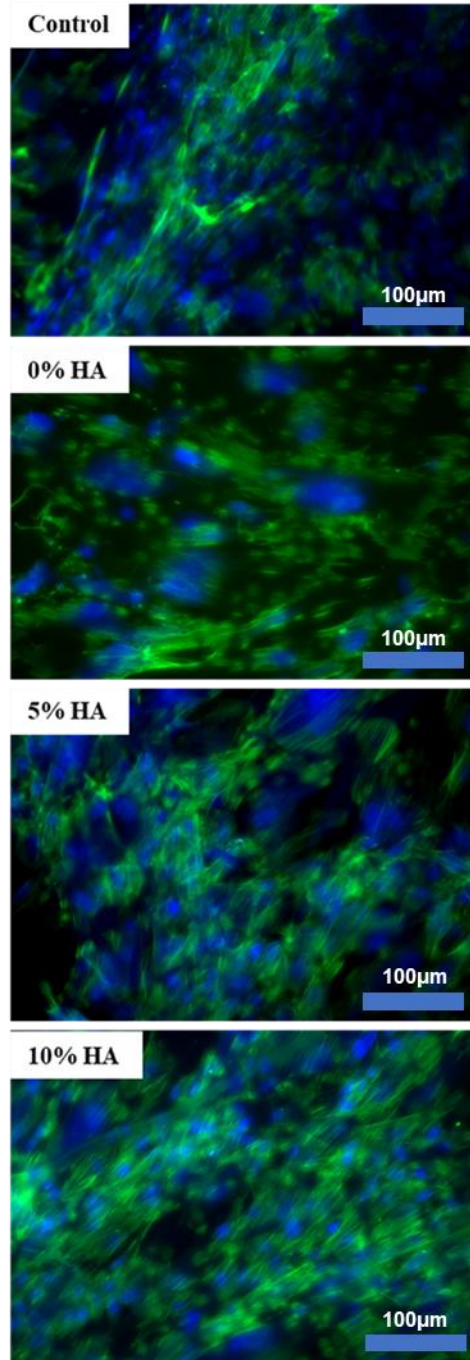


Figure 4-16: Fluorescence imaging results for DAY 21 using DAPI and phalloidin (blue and green respectively) to assess the proliferation and morphology of hADSCs on the surface of the composite-polymer specimens prepared in either standard media or osteogenic supplemented media. The left hand side images are the results for the standard media, and they're compared to the right hand side images which are the osteogenic supplemented specimens. Scale Bar= 100µm.

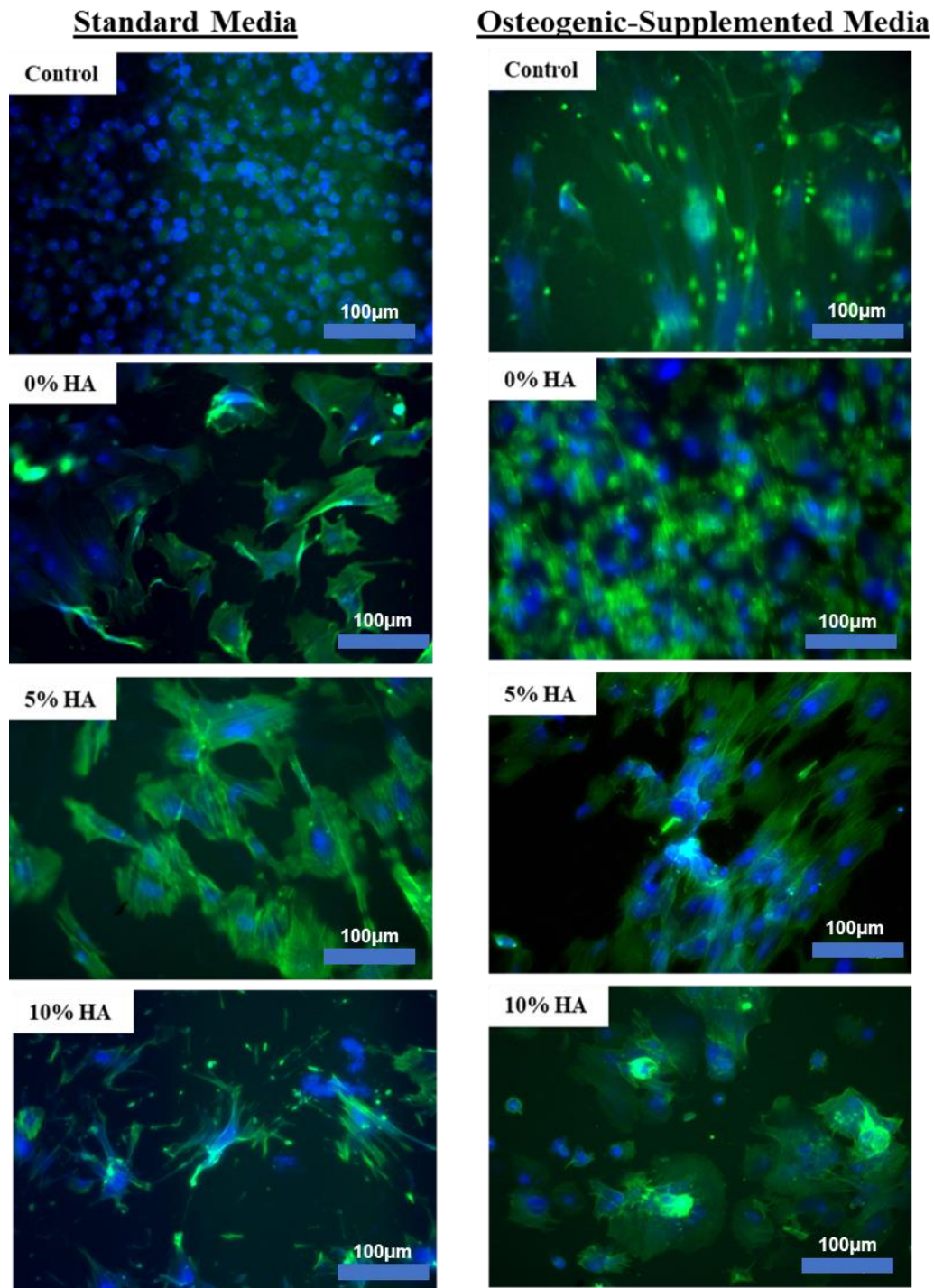


Figure 4-17: Fluorescence imaging results for DAY 28 using DAPI and phalloidin (blue and green respectively) to assess the proliferation and morphology of hADSCs on the surface of the composite-polymer specimens prepared in either standard media or osteogenic supplemented media. The left hand side images are the results for the standard media, and they're compared to the right hand side images which are the osteogenic supplemented specimens. Scale Bar= 100µm.

### 4.3.3 Differentiation Studies (qPCR)

Osteogenic gene expression was assessed by qPCR by investigating the expression of RUNX2, COL1A1, OPN and OCN on hADSCs cultured on CSMA-2 and 0, 5 or 10 wt% HA composite-polymer specimens prepared in either standard or osteogenic-supplemented media. The gene expression was normalised using the  $\Delta\Delta C_t$  method, using GAPDH as the reference gene and assessing the expression on TCP as the control. The results were presented as an amplification plot which gave an absolute cycle threshold ( $C_t$ ) value. These results were further analysed to find the relative gene expression fold change. Figures 4-18-4-21 are the pooled data from the three technical repeats per experimental condition. Each figure highlights the relative gene expression for that specific gene throughout the varying conditions and time points of the experiment. As seen below, the results are only explored for days 7, 14 and 21, this being due to a low, or non-existent gene expression on days 1 and 28 of the experiment. As confirmed by the metabolic activity results in section 4.3.2.1, figure 4-13, the cell viability was compromised by day 28, showing a significant decrease in the metabolic activity with both OM and SM formulations. Thus, the gene expression was not investigated past day 21.

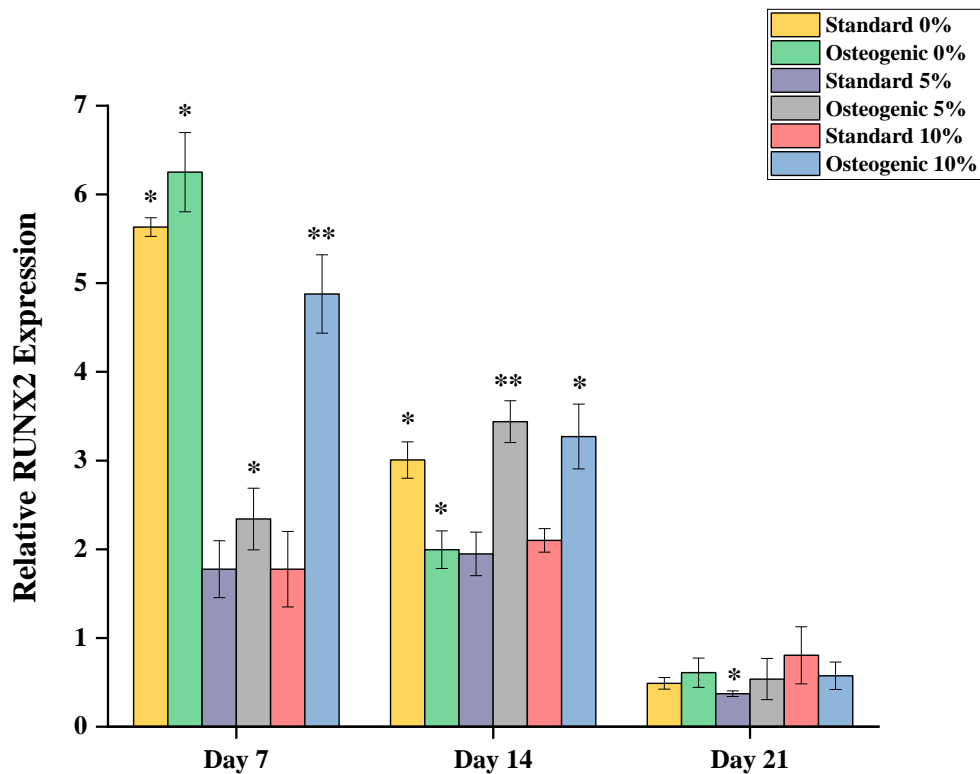


Figure 4-18: Runt-related transcription factor 2 (RUNX2) gene expression quantification by qPCR of hADSCs grown on 3D printed CSMA-2 discs with either 0, 5 or 10 wt% HA incorporated at day 7, 14 and 21. The gene expression was normalised against the housekeeping gene, GAPDH expression and using the expression on TCP as a baseline control. A high upregulation of RUNX2 expression occurred on all specimens at day 7 which reduced by day 21 as RUNX2 is an early marker. The osteogenic samples had a better upregulation throughout, with the 0 wt% HA and 10 wt% HA showing the highest expression of RUNX2 when compared to the control. Data are shown as Mean  $\pm$  SD, n=3. (\*p < 0.05) (\*\*p < 0.01)

Looking at the expression of RUNX2 in figure 4-18 allowed an investigation of osteogenic gene expression on the hADSCs seeded on the composite-polymer discs. The differences in gene expression were mainly noticed at day 7 and day 14 timepoints. The polymer by itself with no added HA, represented by the yellow and

green bars shows the highest upregulation of RUNX2 expression. The 10 wt% HA incorporated formulation also showed an advanced expression of the gene, particularly at the earlier timepoints. RUNX2 is the first transcription factor required for determination of osteoblast lineage so explains why it is upregulated at earlier points in the experiment. When comparing the RUNX2 expression between the standard and osteogenic media treated hADSCs, it is apparent that the osteogenic-supplemented media provides a better platform for the upregulation of gene expression as the relative expression was significantly higher when normalised against the reference gene, and in comparison, with the baseline control. The low induction of RUNX2 expression on day 21 is due to the transcription factor typically being upregulated at the onset of osteogenic differentiation (Komori, 2010)

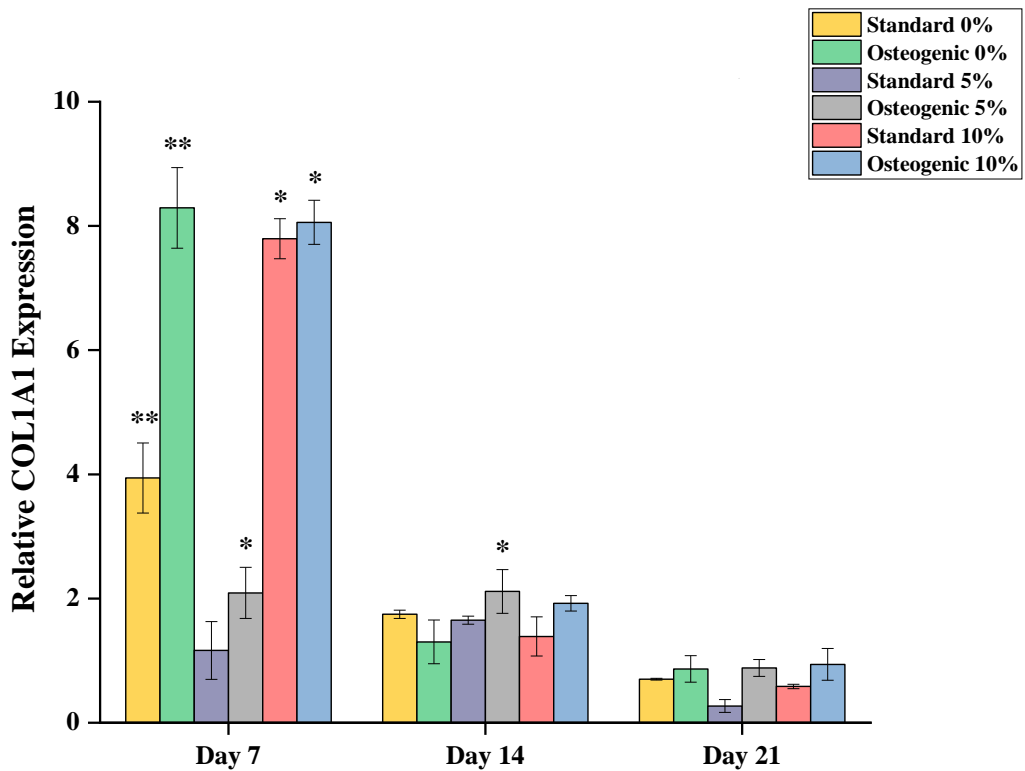


Figure 4-19: Collagen type 1 (COL1A1) gene expression quantification by qPCR of hADSCs grown on 3D printed CSMA-2 discs with either 0, 5 or 10 wt% HA incorporated at day 7, 14 and 21. The gene expression was normalised against the housekeeping gene, GAPDH expression and using the expression on TCP as a baseline control. The early timepoints displayed an upregulation of COL1A1 expression as it is an early marker of osteoblast. Downregulation of COL1A1 expression occurred by day 21. The osteogenic formulations gave a significantly higher level of expression in comparison to the standard media formulations and in comparison, to the control. Data are shown as Mean  $\pm$  SD, n=3. (\*p < 0.05) (\*\*p<0.01)

Figure 4-19 displays the relative gene expression of COL1A1 on the hADSCs seeded on the CSMA-2 and its composites in either standard, or osteogenic media. Like RUNX2, the differences in gene expression were mainly noticed at day 7 and day 14 timepoints. Both markers reached a maximum expression at day 7, decreased to a lower expression, but still very well upregulated at day 14, to completely decreasing

at day 21. The polymer by itself with no added HA treated in osteogenic media showed a much higher expression of COL1A1 compared to the same sample treated in standard media. Furthermore, the 10 wt% HA formulations represented by the red and blue bars show a high upregulation of COL1A1 expression, suggesting the addition of HA is promoting a positive effect on expression of the genes on the cell-seeded sample

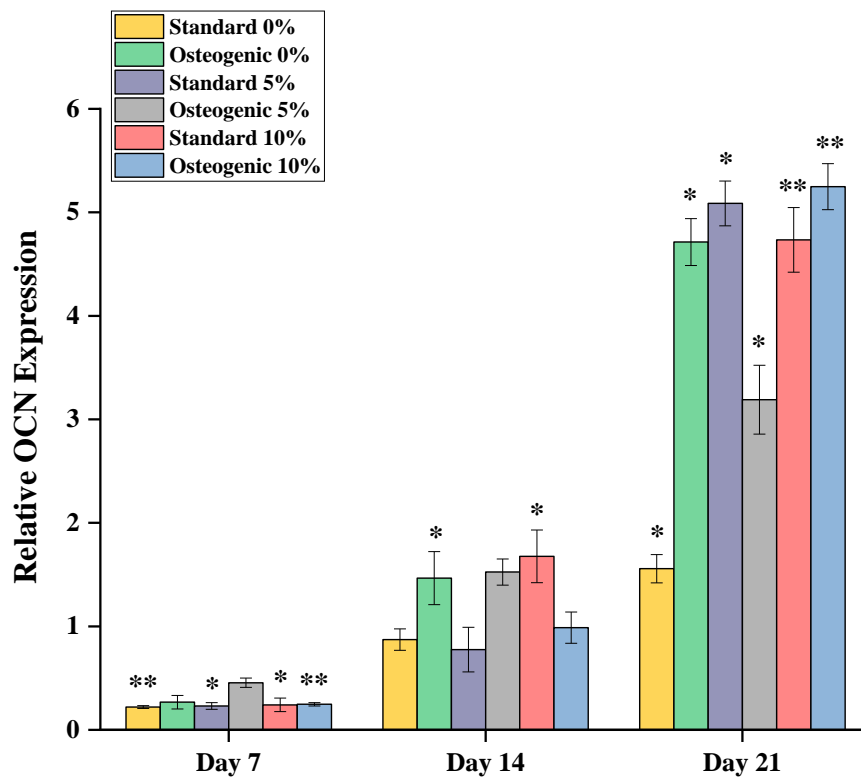


Figure 4-20: Osteocalcin (OCN) expression quantification by qPCR of hADSCs grown on 3D printed CSMA-2 discs with either 0, 5 or 10 wt% HA incorporated at day 7, 14 and 21. The gene expression was normalised against the housekeeping gene, GAPDH expression and using the expression on TCP as a baseline control. Day 7 did not display much expression as the later timepoints as OCN is a late onset marker. Day 14s results display an upregulation in gene expression, particularly for the osteogenic formulations which compared significantly with the control. A high upregulation of OCN expression occurred on all specimens at day 21 however, the standard 0 wt% formulation was significantly lower than the remainder of the group. The osteogenic samples had a better upregulation throughout, with the 10 wt% HA showing the highest expression of OCN. Data are shown as Mean  $\pm$  SD, n=3. (\*p < 0.05) (\*\*p<0.01)

As seen in figure 4-20 above, the relative gene expression of OCN on the hADSCs seeded on the CSMA-2 and its composites in either standard, or osteogenic media. Unlike RUNX2 and COL1A1, the differences in gene expression were mainly noticed at day 14 and 21 timepoints. OCN is a small conserved non-collagenous extracellular matrix protein which is found in the bone and is expressed during late osteoblast differentiation. This explains why the results for day 21 were significantly upregulated when compared to the earlier timepoints, as well as the control. Once again, the use of hydroxyapatite gave a slightly better platform to promote OCN gene expression as seen in the graph in the 5 and 10 wt% HA formulations. For the polymer by itself, the sample with no added HA that was treated in osteogenic media showed a much higher expression of OCN compared to the same sample treated in standard media.



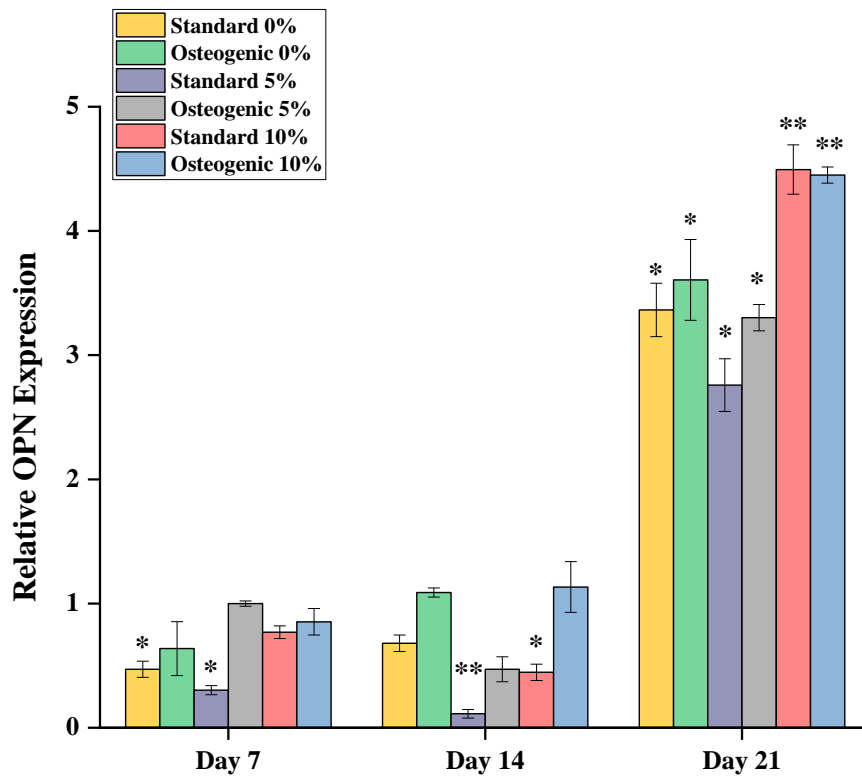


Figure 4-21: Osteopontin (OPN) expression quantification by qPCR of hADSCs grown on 3D printed CSMA-2 discs with either 0, 5 or 10 wt% HA incorporated at day 7, 14 and 21. The gene expression was normalised against the housekeeping gene, GAPDH expression and using the expression on TCP as a baseline control. Day 7 and day 14 showed a small gene expression but not a high amount of expression as the later timepoints as OPN is a late onset marker. A high upregulation of OPN expression occurred on all specimens at day 21 with the highest expression being seen in the 10 wt% formulations which significantly compare to the remaining groups. The 5 wt% formulation was not as consistent as other genes explored but still had significant expression of OPN throughout. Data are shown as Mean  $\pm$  SD, n=3. (\* $p < 0.05$ ) (\*\* $p < 0.01$ )

Figure 4-21 highlights the relative gene expression of OPN on the hADSCs seeded on the CSMA-2 and its composites in either standard, or osteogenic media. Like OCN, the differences in gene expression were mainly noticed later in the experiment, at the day 21 timepoint. Osteopontin is a bone sialoprotein involved in osteoclast attachment

to the bone matrix and is expressed during late osteogenic differentiation which confirms the results. The addition of HA to the polymer made a significant impact towards the upregulation of OPN gene expression as seen by the 10 wt% HA specimen results displaying the highest relative gene expression. The osteogenic supplemented media promoted upregulation of OPN against the formulations when compared to the standard media.

#### 4.3.4 Angiogenic Response (CAM)

An *Ex-Ovo* chicken chorioallantoic membrane (CAM) assay was used to test the angiogenic potential of CSMA-2 and its composites including 5 and 10 wt% hydroxyapatite. The 3D printed scaffolds and the control samples were excised from the CAM on embryonic development day 12 where vasculature was studied for each formulation. The positive control sample which was filter paper soaked in VEGF showed a good level of vascularisation when compared to the negative control which was soaked in PBS. The two control samples can be seen in figure 4-22 below and the three CSMA-2 composite-polymer scaffolds that were 3D printed and used for CAM assay can be seen in figure 4-23. Vascularisation was noticed in all conditions tested. The first images (a) represent the original image taken of the scaffold after inversion. The newly formed blood vessels are shown clearly in red, and differences were observed in the vascular infiltration of the different composites as indicated by the growth of the vessels. Images (b) represent the grey-scale images that were prepared on Microsoft PowerPoint for the purpose of analysis on ImageJ and images (c) represent the binary image of the scaffold on ImageJ which allows for a more detailed comparison of the vascular area with new blood vessels shown in black.

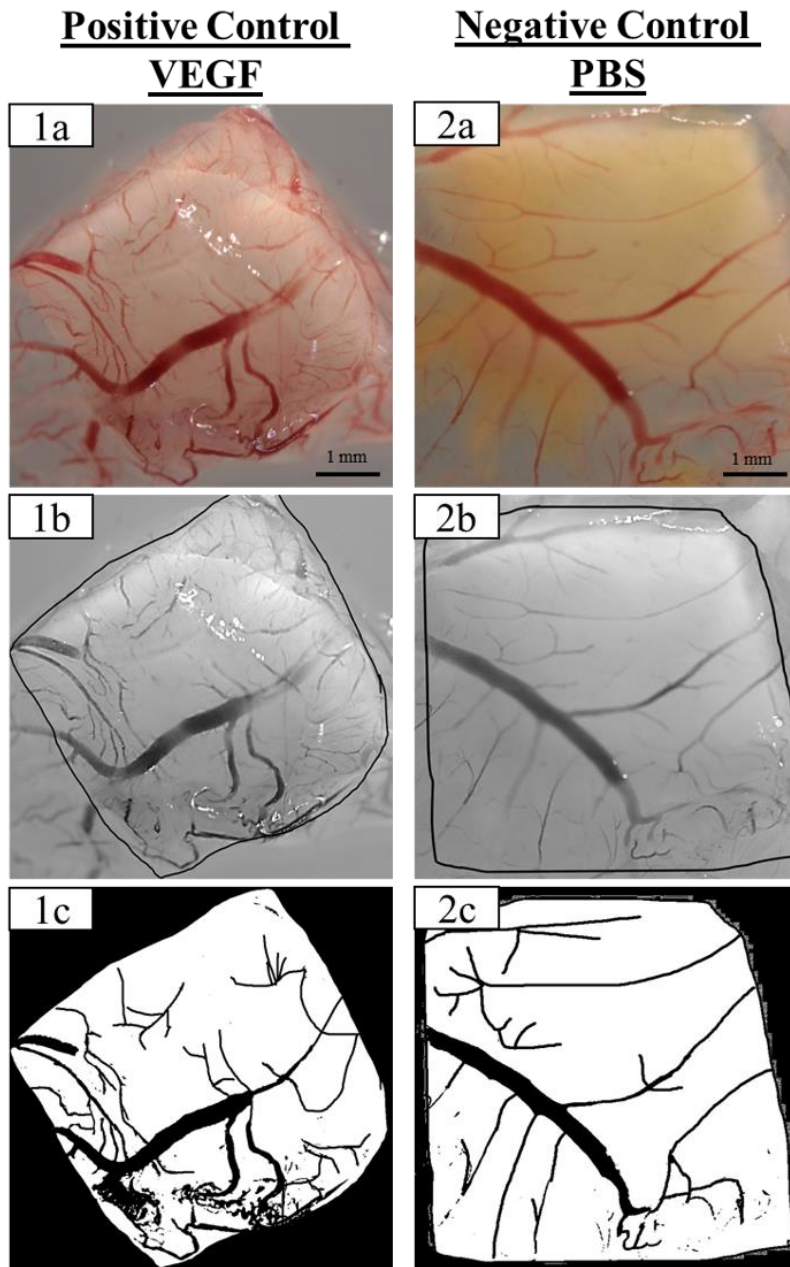


Figure 4-22: The results from the control groups for the CAM assay. The left hand side represents the positive control sample, filter paper soaked in VEGF and the right hand side images represent the negative control sample, filter paper soaked in PBS. Images taken of the control sample, (b) grey-scale prepared image for analysis and (c) binary image. Scale bar = 1 mm.

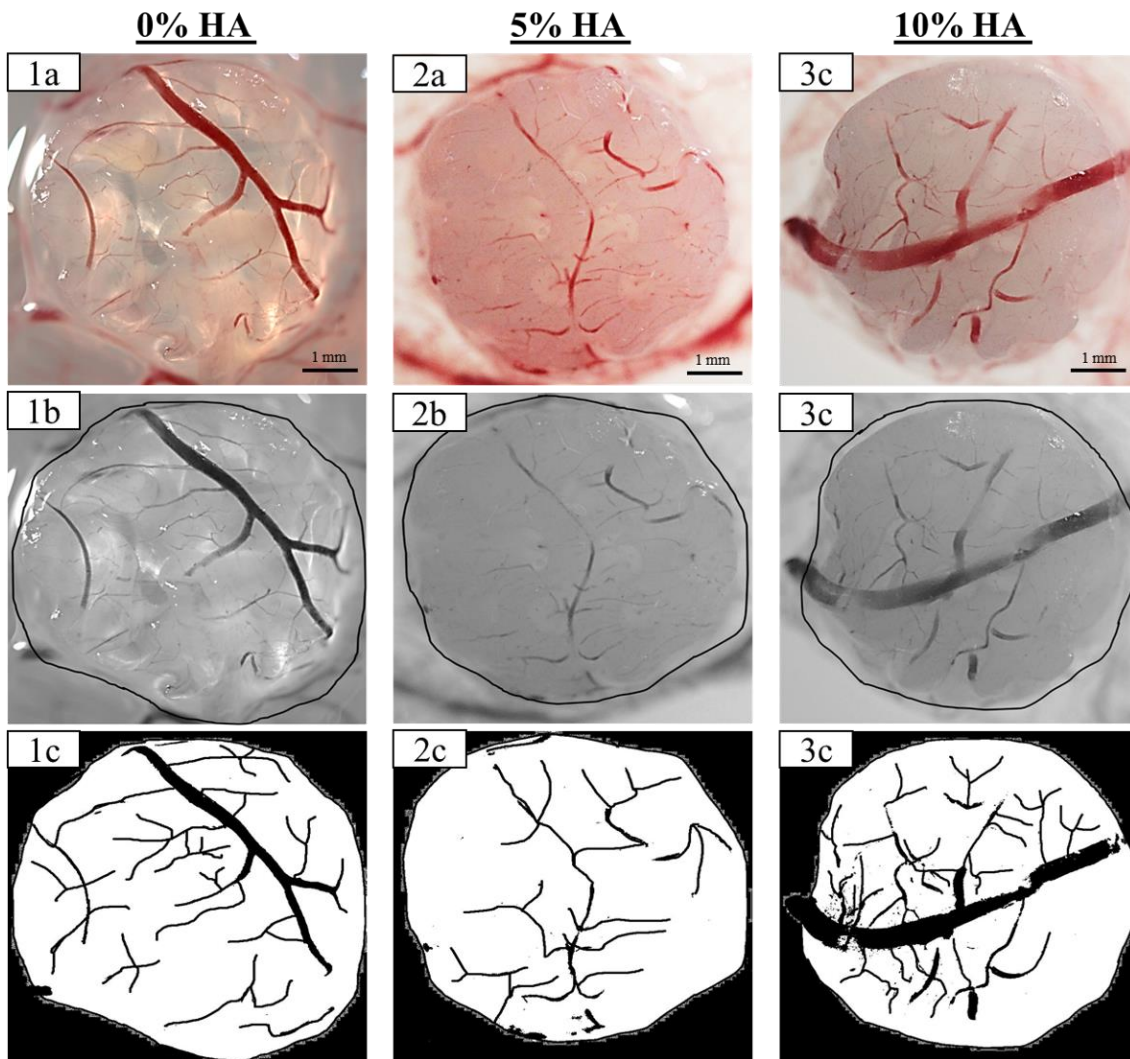


Figure 4-23: The results from the CAM assay assessing angiogenesis on CSMA-2 with 0, 5 or 10 wt% HA composite scaffolds. The left-hand side images represent the results for 0% HA, CSMA-2 by itself. The middle set of images represent the results for 5 wt% HA and the right-hand side images represent the results for 10 wt% HA samples. Images (a) show the first standard image of the excised sample that was tested. The differences were observed in the vascular infiltration of the different composites as indicated by the growth of blood vessels seen in red (Scale bar = 1 mm). Images (b) show the grey-scale prepared image on Microsoft PowerPoint to allow for ImageJ analysis and images (c) show the binary images on ImageJ which allow a detailed edge of the scaffold to be identified and newly formed blood vessels shown in black.

As seen in figure 4-23, blood vessels were observed in all the composite-polymer scaffolds in varying extents depending on the composition of the material. The CSMA-2 scaffold represented by the 0% HA images show a high level of vascularisation as

demonstrated by the formation of new blood vessels which can be seen in red. There is a significant large vessel with several capillaries branching from it, suggesting CSMA-2 promotes angiogenesis. The 5 wt% HA scaffolds did not show as many blood vessels infiltrated within the material when compared to the polymer by itself. This could be due to the HA particles not being evenly distributed or the clarity of the pores. The 10 wt% HA formulation showed significant vascularisation with a thick red line highlighting the infiltration of a blood vessel through the pores of the material with several new capillaries branching from it.

#### **4.3.4.1 Vascular Area**

The number of newly formed vessels was comparable between the control groups and the 3 experimental conditions: CSMA-2 with 0, 5 and 10 wt% HA. The vascular area was calculated for each formulation and represented below in figure 4-24 as a graph comparing the vascularisation of the controls against the composite-polymer scaffolds. The positive control sample had a vascular area of 19.43% which significantly compared to the negative control sample which had a vascular area of 9.35%. The composite-polymer scaffold with the highest percentage of vascularisation throughout was the 10 wt% HA formulations with an average vascular area of 13.31%. CSMA-2 by itself gave a vascular area average of 11.95% and the 5 wt% HA formulations had the lowest vascularisation at 8.79%. These results suggest that CSMA-2 prepared with 10 wt% HA has the best potential to promote vascularisation which could be due to the addition of the HA filler being well dispersed within the scaffold as well as the material itself having significant pores where the vessels are running through. These

results are consistent with the images seen above in figure 4-23 as the 10 wt% HA formulation display major vessels and numerous capillaries.

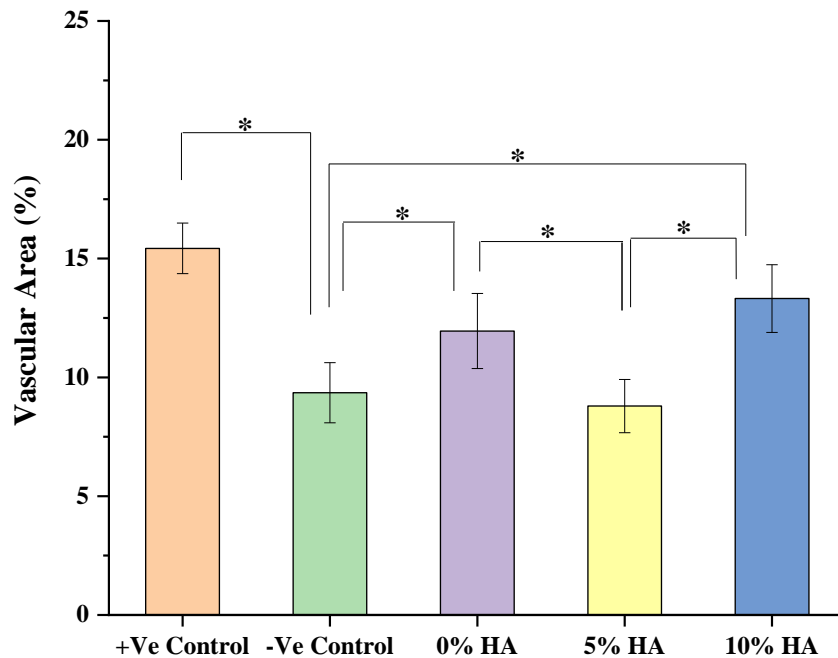


Figure 4-24: Graphical representation of the vascular density for the control samples and each composite-polymer material scaffold calculated after the CAM assay. The positive control had the highest vascular area at 15.15%. However, this was not significantly different to the results for 0 and 10 wt% HA which had vascular area results of 11.95 % and 13.32 % respectively. The negative control gave a vascular area of 9.35 % which is significantly different to all the formulations, apart from the 5 wt% group. The 5 wt% HA composites had a lower vascular density with only 8.79 % which compared significantly with the 0 and 10 wt% groups as confirmed by the digital images. Data are presented as Mean  $\pm$  SD, n=3. (\*p < 0.05)

#### 4.3.4.2 Bifurcation Points

Bifurcation points (BF), also known as branching points, were counted for each formulation. Like the results for the percentage vascular area, CSMA-2 with 10 wt% HA formulations displayed the highest number of bifurcation points. As seen in figure

4-254 on average, 40 points were seen in the 10 wt% HA formulations, which was significantly higher than the other groups. The positive control sample had an average of 27 BF points which is similar and not significantly different to the CSMA-2 scaffold with no added HA which had an average of 28 BF points. Once again, the 5 wt% HA formulations had the lowest results, displaying only an average of 22 BF points. These results suggest that the highest level of vascularisation took place in the 10 wt% HA scaffolds. The 5 wt% group may be displaying less vascularisation and branching due to the HA particles not being dispersed properly prior to 3D printing of the scaffolds. The 10 wt% HA scaffolds had the clearest pores, which allow the new capillaries to bifurcate more freely than in the other scaffolds where the pores may not be as clear to flow through. However, all three experimental groups obtained significantly higher bifurcation point numbers than the negative control sample, prepared in PBS which had an average of 18 BF points.



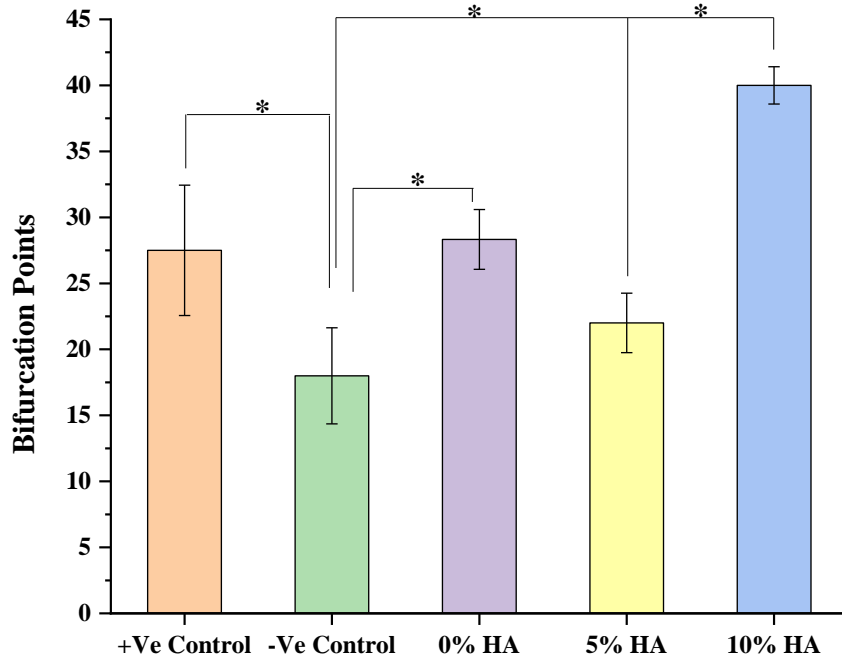


Figure 4-25: Graphical representation of the bifurcation points for the control samples and each composite-polymer material scaffold calculated after the CAM assay. The 10 wt% HA composite had the highest number of BF points at 40 which compared significantly to the 5 wt% HA formulations at 22 BF. All groups were significantly higher than the negative control group which only displayed 18 BF points. All Data are presented as Mean  $\pm$  SD, n=3. (\*p < 0.05)

#### 4.4 Discussion

In this chapter, the biological properties of CSMA-2 along with its composite-polymer specimens formulated with 0-10 wt% hydroxyapatite filler to determine the ultimate custom-fit scaffold for use in cranio-maxillofacial surgery were explored. The addition of HA to the polymeric system was investigated via cytocompatibility, differentiation and angiogenic assessments. Two different cell lines, MG-63 osteosarcoma human cells and human adipose-derived stem cells were explored in this chapter as well as the osteogenic differentiation of the cells seeded on the polymer utilising relative gene expression of specific bone markers and the materials ability to promote angiogenesis.

With respect to cell culture, both metabolic activity and visual investigation of the cell morphological changes were assessed; initially, MG-63 cells were seeded on the surface of CSMA-2 discs, prepared with either CQ or BAPO photoinitiator, by hand or 3D printing respectively. Two ratios of CSMA-2: HA were explored, 95:5 and 90:10, which established the ideal formulations. The 3D printed, BAPO photoinitiator-prepared composites containing either 0, 5 or 10 wt% HA were used going forward. Subsequently, hADSCs were used to investigate the impact of HA filler addition on the proliferation of stem cells.

Materials that are commonly used for implants such as PMMA have been seen to be relatively cytocompatible, however the majority of commercially available materials have had to incorporate other extracellular membrane components to improve mechanical properties as well as compatibility to cells. A study carried out by Jiang and co-workers (Jiang *et al.*, 2015) investigated the improvement of PMMA implants

by incorporating mineralised collagen. Their cell adhesion and proliferation results were significantly improved on the modified materials, as well as beneficial results for good osteointegration formation between the bone implant and the host bone tissue.

As mentioned previously, calcium phosphates can significantly influence various biochemical properties of composite systems in bone tissue engineering (Jeong *et al.*, 2019). A study by Ku and colleagues (Ku *et al.*, 2019) explored the effects on the biological activity of poly(methyl methacrylate) (PMMA) when incorporating hydroxyapatite. The PMMA polymer was adapted to incorporate ethylene glycol and poly ( $\epsilon$ -caprolactone) (PCL) to improve affinity between the polymer and ceramic particles. Along with some mechanical properties improving with the addition of HA particles, the 20 wt% PCL-grafted ethylene glycol-HAP formulation promoted pre-osteoblast metabolic activity *in vitro* and showed the best osteogenic activity between the composites when tested *in vivo*.

In a similar study, Ma and collaborators (Ma and Guo, 2019) assessed the role of HA incorporation in a polyetheretherketone (PEEK) composite to evaluate the bioactivity of the composite, cell attachment and proliferation of cells. It was found that the HA incorporated PEEK composites promoted higher cell growth and attachment on the material surface than when seeded on the PEEK polymer alone. Using microscopy, it was seen that the cells on the HA/PEEK composite exhibited a higher spreading efficiency on the material surface compared to those on the pure PEEK. Alkaline phosphatase activity (ALP) was also assessed for the purpose of bone-implant interfacial osseointegration and their results revealed that the cells on the HA/PEEK composite demonstrated higher ALP activity, suggesting the material is supporting osteoblast growth and osteogenic differentiation.

Throughout this chapter, the metabolic activity of CSMA-2 and its composites of 5 and 10 wt% HA filler was intensely examined to find the most biocompatible formulation when assessing MG-63 and hADSC cells. The most optimum formulation for the MG-63 study was the 0% HA (BP) sample which is the polymer by itself with no added HA, prepared via 3D printing with 2 wt% BAPO photoinitiator. The BAPO formulated discs provided a higher metabolic activity with the MG-63 cells than the CQ formulated discs and were therefore chosen to explore further throughout the study. This change could be due to the composition of the photoinitiator itself, for example, the extra cross-linking group in BAPO, or the uniformity that was achieved throughout the 3D printing process for the BAPO samples (Shakouri *et al.*, 2020).

Adipose-derived stem cells were used throughout this thesis due to their ability to maintain self-renewal properties and enhanced multi-differentiation potential. Through the production of a number of paracrine factors and extracellular vesicles, ADSCs can allow the healing of damaged organs and tissues. Many studies have reviewed the use of ADSCs in research against bone marrow-derived mesenchymal stem cells (BM-MSCs) to find the optimum usage. A study carried out by Kunze and fellow researchers (Kunze *et al.*, 2020) explores the advantages of ADSCs over BM-MSCs, for example, having the ability to obtain higher yields of ADSCs from subcutaneous regions through minimally invasive, and painless, procedures. Furthermore, ADSCs can maintain their phenotype in culture for longer periods of time and have a higher proliferation ability, leading to more suitability for potential allogenic transplantation (Zhang *et al.*, 2020). As previously mentioned, ADSCs can differentiate into adipocytes, osteoblasts, chondrocytes, neurocytes, and hepatocytes from the three development germ layers (endoderm, mesoderm and ectoderm). Due to all of these advantages, ADSCs are an

attractive source for use in regenerative medicine and tissue engineering research (Dai *et al.*, 2016). Therefore, hADSCs were chosen to examine the cytocompatibility of the material as well as the osteogenic differentiation.

Further assessments of cytocompatibility of the BAPO incorporated CSMA-2 discs with either 0, 5 or 10 wt% HA filler was carried out where hADSCs were selected as the cell type of choice. All 3 formulations continued to proliferate throughout the study time points of days 1, 4 and 7 but remained significantly lower than the control group, apart from the 10 wt% HA formulations where the metabolic activity increased significantly. This can be explained by exploring hydroxyapatite's presence in the formulation. Hydroxyapatite incorporation has traditionally been shown to enhance cytocompatibility of scaffolds as a result of its osteoconductive nature (Polo-Corrales, Latorre-Esteves and Ramirez-Vick, 2014) but it is important to consider the importance of achieving uniformity of dispersion between the liquid and powder phases. This is critical when related to cell metabolic activity and the overall cytocompatibility of the materials. In the hADSC experiment in this study, the 5 wt% HA incorporated composite-polymer specimens did not achieve the same level of metabolic activity as the 10 wt% HA formulation which could be due to the quantity of HA not being quite enough to make a positive impact, or the mixing process of the HA with CSMA-2 not being as evenly distributed as with the 10 wt% group. There is also the possibility that during the 3D printing, SLA process the composites containing 5 wt% HA did not photopolymerise evenly, causing more HA particles to be dispersed on one side of the disc.

Osteogenic differentiation of human adipose-derived stem cells is functionally defined by their capacity to self-renew and their ability to differentiate into multiple cell types

including osteoblasts (Zhou *et al.*, 2021). In this study, the osteogenic potential of human mesenchymal stem cells (MSCs) isolated from adipose tissue (hADSCs) has been evaluated *in vitro* in combination with CSMA-2 scaffolds and hydroxyapatite-incorporated composites. In order to assess the osteogenic differentiation of hADSCs on the materials, the metabolic activity and proliferation of the cells grown in either standard MesenPRO RS Media (SM) or the cells grown in osteogenic supplemented media (OM) were assessed. As seen by the metabolic activity results (see section 4.3.2.1), the OM provided a non-harmful enhancement to cell growth. Quite often, growth factors are incorporated to improve the cytocompatibility of polymeric systems. Bone Morphogenic Proteins (BMPs) and Vascular Endothelial Growth Factors (VEGF) have exhibited successful results in enhancing osteogenesis as well as vascularisation in bone regeneration (Aryal *et al.*, 2014). A review by García-Gareta and fellow researchers (García-Gareta, Coathup and Blunn, 2015) discussed the osteoinduction of bone grafting materials in depth. It was noted that BMPs are transforming growth factors that tend to play a major role in stimulating bone growth. VEGF was also discussed in its role to promote angiogenesis. Therefore, both growth factors can be included in a scaffold to significantly improve tissue formation. However, it has been widely studied that delivery of growth factors can be a complex procedure, as well as time-consuming, expensive and limitations when achieving optimum mechanical properties (Fernandez de Grado *et al.*, 2018).

A study carried out by Tirkkonen and collaborators (Tirkkonen *et al.*, 2013) explored the benefits of osteogenic media for hADSCs in comparison with common growth factors. The study revealed that osteogenic differentiation was detected solely with OM and the addition of growth factors such as bone morphogenetic proteins (BMP-2

and BMP-7) and VEGF did not enhance the osteogenic differentiation of hADSC more than just the standard media used. In this chapter, similar results were found, where there was higher metabolic activity when the hADSCs were cultured in OM, compared to SM. Consistently from day 7- day 28, the metabolic activity results were higher for all the formulations in OM. The results for CSMA-2 by itself, with no added HA, were significantly higher than the standard control and all the SM cultured formulations. Throughout this study, it has been demonstrated that the varying amounts of calcium phosphates can also affect the potential of osteogenic differentiation. The addition of HA to the composites made a positive impact on the metabolic activity, where the 5 and 10 wt% HA groups gave high metabolic activity readings, significantly different to the same groups in standard media. Another study carried out by Calabrese and co-workers (Calabrese *et al.*, 2016) explored the osteogenic differentiation *in vitro* of hADSCs on collagen-hydroxyapatite scaffolds. They explored the difference in osteogenic response using standard media vs. osteogenic media and concluded that the osteogenic media demonstrated more osteoinductive features of the scaffold to support the potential of hADSCs inducing the formation of new bone tissue. To further understand the potential of osteogenic media, a study carried out by Nishimura and associates (Nishimura *et al.*, 2015) explored the effect of osteogenic differentiation media on the proliferation of hADSCs. They found that by culturing the cells in OM, the cell metabolic activity was significantly promoted in both their static and dynamic cultivation for 14 days of their experiment. This can be explained as the OM induces the stem cells to differentiate to preosteoblast-like cells, which can expand faster than undifferentiated stem cells (Katayama *et al.*, 2012). Furthermore, the supplements

added to the osteogenic media promotes cell division and proliferation as they themselves have mitogenic properties (Jaiswal *et al.*, 1997).

One way to determine the ability of the cells to differentiate into osteoblasts is through gene expression exploration, quantitatively measured through real-time polymerase chain reaction (qPCR). To perform qPCR, an internal control gene is selected to be used as the reference gene which is quantified along with the target gene (Kuang *et al.*, 2018). The most common housekeeping gene, GAPDH was used as the reference gene after exploring B2M and PPIA did not give any amplification whereas GAPDH provided a stable reference gene. This also correlated to a study undertaken by Panina and colleagues (Panina *et al.*, 2018), which compared 12 common housekeeping genes for their stability and reliability and observed that GAPDH outperformed the 12 other selected genes for stability on the mRNA level.

Upregulation of osteoblastic differentiation markers, RUNX2, COL1A1, OCN and OPN was observed throughout the experiment, particularly for the cells cultured in the osteogenic media.

RUNX2 is a protein that is detected first in preosteoblast, and then upregulated in immature osteoblasts, but downregulated in mature osteoblasts. RUNX2 is the first transcription factor required for determining the osteoblast lineage, therefore triggers the expression of major bone matrix genes during the early stages of osteoblast differentiation (Komori, 2010). In this study, RUNX2 was upregulated at the early time points (day 7 and 14) and downregulated later (day 21). When comparing the RUNX2 expression between the standard and osteogenic media treated hADSCs, it is apparent that the OM provides a better platform for the upregulation of gene



expression as the relative gene expression was significantly higher when normalised against the reference gene, GAPDH, and in comparison, with the baseline control. The low induction of RUNX2 expression on day 21 is due to the transcription factor typically being upregulated at the onset of osteogenic differentiation.

COL1A1 is the most abundant protein in all vertebrates. It assembles into fibres that form the structural matrix of bone (Ricard-Blum, 2011). COL1A1 is known to be an early marker of osteogenic cells which explains why the upregulation of COL1A1 in this study occurred mainly at day 7 and day 14 time points (Kaneto *et al.*, 2016). Like RUNX2, the COL1A1 reached a maximum expression at day 7, decreased to a lower expression, but still very well upregulated at day 14, to completely decreasing at day 21. CSMA-2 with no added HA treated in OM displayed a much higher expression of COL1A1 compared to the SM treated cells. Following the same pattern as with RUNX2, the addition of HA promoted a positive effect on the upregulation of gene expression on the cells treated with OM. A study by Kannan and collaborators (Kannan, Ghosh and Dhara, 2020) investigated the osteogenic differentiation potential of MSCs treated in different basal media. They found that COL1A1 had a varying expression for the cells grown in the different media options, but the osteogenic differentiation media promoted the up-regulation of COL1A1 when exploring its activity.

Osteocalcin, the most abundant non-collagenous protein expressed in bone, is solely expressed and secreted by osteoblasts (Moser and van der Eerden, 2019). OCN on the hADSCs seeded on CSMA-2 and its composites in either SM or OM was investigated in this study. It was found that, unlike RUNX2 and COL1A1, the differences in gene expression were mainly noticed at day 14 and 21 time points. OCN

is known to be expressed during late osteoblast differentiation (Ikegame, Ejiri and Okamura, 2019). This explains why the results for day 21 were significantly upregulated when compared to the earlier time points, as well as the control. Once again, the addition of HA gave a better platform to promote OCN gene expression. Again, for all groups of the composite-polymer specimens, those treated in OM showed a much higher expression of OCN compared to the same sample group treated in SM.

Finally, Osteopontin, also known as bone sialoprotein I, is involved in osteoclast attachment to the mineralised bone matrix (Kruger *et al.*, 2014). OPN is a late-onset marker, which is expressed mainly at the initiation phase of mineralisation. A similar study to ours carried out by Rozila and associates (Rozila *et al.*, 2016) explored the quantitative gene expression of OPN on hADSCs seeded on electrospun 3D poly[(R)-3-hydroxybutyric acid] (PHB) scaffolds with incorporated bovine-derived hydroxyapatite (BHA). It was concluded that the OPN expression was increasingly upregulated throughout the study within the hADSCs seeded on the PHB-BHA scaffold group suggesting that the stable co-culture system has a strong impact on exerting the osteogenic differentiation ability. In this study, like OCN, the differences in gene expression of OPN on hADSCs seeded on the composite-polymer specimens were mainly noticed later in the experiment, at the day 21 timepoint. Following the same pattern as previous genes, the addition of HA to the polymer made a significant impact on the upregulation of OPN gene expression. Notably, the osteogenic supplemented media promoted upregulation of OPN against the formulations when compared to the standard media.

Reaching the end of the experiment, towards day 28, there was no upregulation of gene expression determined due to the materials not supporting the cells to proliferate for 28 days. This is confirmed by the sudden decrease of metabolic activity that can be seen in Figures 3-16. There is a possibility that the expression of the genes was also not induced by the hADSCs later in the experiment as the mRNA expression returned to the baseline level after the condensation and aggregation process during the first week of induction. Hamid and co-workers (Hamid *et al.*, 2012) also discussed this in their study of chondrogenic genes during induction of cartilage differentiation. They explain how the continuous culture of the cells in the chondrogenic induction media did not promote further ECM production to increase the size of cell aggregates suggesting that one week of their experiment was sufficient for the cartilage regeneration.

The final aim of this chapter was to explore the angiogenic response of the composite-polymer scaffolds using the *ex-ovo* Chorioallantoic Membrane Assay. The *ex-ovo* method chosen for use in this study provides full uninhibited access to the embryo. Many researchers prefer the windowing method to study chick development as it is simpler to perform and has positive survival rates to late-stage development, however, it has limitations such as the ability to view the entire embryo and obtaining good visibility to see inside the egg (El-Ghali *et al.*, 2010). To overcome such limitations, the *ex-ovo* CAM assay method is discussed in detail by Cloney and co-workers (Cloney and Franz-Odenaal, 2015), in a study describing the advantages of having full uninhibited access to the embryo. They explain the ability of the whole embryo being observed under high magnification microscopy to allow for easy viewing and manipulation of embryos without the limitations on access at the late stage of the

development. The *ex-ovo* technique utilised in this study uses a simple glass-cling film set-up that can be easily replicated by others, easily demonstrated in teaching scenarios and minimising any trauma to the chick embryo. A further advantage to using this *ex-ovo* method is the ability to compare multiple samples in one CAM at the same time, providing reliability and reproducibility but also decreasing the number of eggs needed for the experiment which in turn reduces cost and time consumption. Finally, in this *ex-ovo* method, the chicken embryo can fully develop in the same way it would in an *in ovo* method. Schomann and co-workers (Schomann *et al.*, 2013) explored both methodologies to find out the optimum survival rate for chicken embryos cultivated in both systems. In their study, they concluded that the *ex-ovo* system, similar to the one used for the purpose of this thesis, allows survival of chicken embryos for up to embryonic day 15, showing normal growth in regard to its weight and size, as well as the cartilage, bone and nerves developing in the intended way.

In a CAM assay, blood vessels penetrate from the edges of the scaffold towards the centre of the scaffold, leading to vascularisation. This represents the vascularisation that would occur in an *in vivo* environment upon implantation of the scaffold (Marshall, Kanczler and Oreffo, 2020). A study by Kohli and colleagues (Kohli *et al.*, 2020) discuss in depth further advantages of this *ex-ovo* method by assessing its suitability for screening biomaterials. The study investigates angiogenic properties such as the vascular density, the number of bifurcation points and presence of blood vessels within the materials tested. The vascular density, or area, is a quantitative measurement to calculate the percentage of newly formed blood vessels infiltrating the scaffold (Kohli *et al.*, 2021). The bifurcation points, or branching points, are points on the scaffold that the infiltrated blood vessel branches out to a new capillary. Both measures were

investigated for the newly formed blood vessels infiltrating the CSMA-2 composite-polymer scaffolds in this study.

The results from the CAM assay conducted on the CSMA-2 composite scaffolds demonstrated good blood vessel formation. The varying ratios of HA added to the polymer did lead to a varying angiogenic response as the formulation with 10 wt% HA gave the highest level of vascularisation demonstrated by the formation of new blood vessels in the microscopy images as well as the highest percentage of the vascular area and the highest number of branching points.

Porosity and pore size of the scaffolds also play a vital role in determining mechanical properties as well as angiogenic properties. The porosity of a scaffold is determined by the volume, size, shape, orientation, and connectivity of its pores. Cell growth, homogenous cell distribution and vascularisation are all possible using porous scaffolds. Although greater porosity and pore size of scaffold materials have various advantages, it compromises the scaffolds compressive strength, resulting in a decrease in the mechanical strength and properties (Karageorgiou and Kaplan, 2005). Usual porosity ranges from 50-90% with pore sizes ranging from 150  $\mu\text{m}$  to 600  $\mu\text{m}$ . Various studies have previously suggested that the architecture of the pores in a biomaterial plays an important role in its revascularisation *in vivo* (Mehdizadeh *et al.*, 2015). A study reported by Feng and fellow researchers (Feng *et al.*, 2011) investigated the role of pore size on tissue ingrowth and neovascularisation in porous bioceramics and found that the amount of vascularisation is proportional to the size of the pore, therefore suggesting that a pore size smaller than 400  $\mu\text{m}$  limits the growth of new blood vessels. Furthermore, according to Di Luca and co-workers (Luca *et al.*, 2016), increasing the porosity of the scaffold increases the regeneration of the bone.

The extracellular matrix (ECM) mineralisation and differentiation of hADSCs both increase when the pore size is altered.

The CSMA-2 composite-polymer scaffolds designed, and 3D printed for this CAM assay were 6 mm in diameter and 3 mm thick with 0.5 mm pores which is a good size to promote new blood vessel infiltration. The control group samples were filter paper dipped in VEGF (positive control) and PBS (negative control) and all the scaffolds were grafted well within the CAM, suggesting that the materials were well-tolerated by the embryo (Kohli *et al.*, 2021). It is suggestive from the results of the CAM assay that the blood vessel infiltration is dependent on the porosity of the scaffold as well as the composition of the material. The filter sample soaked in VEGF that was used as the positive control did not show significantly higher vascular density compared to the CSMA-2+HA based scaffolds suggesting the importance of porosity, and the pore size, for critical bone formation. In a study conducted by Boller and colleagues (Boller *et al.*, 2015), it is highlighted that increasing the VEGF concentration above 10 ng/ml does not result in increased angiogenesis which suggests that using VEGF for our positive control in this CAM study did not have any biased impact.

Blood vessels were observed in all the composite-polymer scaffolds to varying extents depending on the composition of the material. The CSMA-2 scaffold shows a high level of vascularisation and there is a significant large vessel with several capillaries branching from it, suggesting CSMA-2 promotes angiogenesis. The 5 wt% HA scaffolds did not show as many blood vessels infiltrated within the material when compared to the polymer by itself. This could be due to the HA particles not being evenly distributed or the clarity of the pores. The 10 wt% HA formulation showed significant vascularisation with newly formed blood vessels infiltrating the pores of the

scaffold and several capillaries branching from it. The branching points are indicative of the vessel sprouting phase, where pre-existing blood supply leads to vascular sprouting that then develops into mature blood vessels (Kohli *et al.*, 2020). The CSMA-2 with 10 wt% HA formulation showed increased bifurcation points, suggesting an increase in vessel sprouting potential which could be due to the HA deposited into the material, giving a platform for angiogenesis to occur. CaPs such as HA are known to induce pro-angiogenic factors and therefore are a good addition to promote angiogenesis in biomaterials (Saberianpour *et al.*, 2018). Furthermore, as discussed in Chapter 2; section 2.3.6: Degradation studies, the 10 wt% HA formulations had the highest rate of degradation under standard (37°C) and accelerated (60°C) conditions. This could suggest that the increased quantity of HA had increased vessel branching potential due to the degradation of the CaP ions. The faster dissolution process makes calcium ions more readily available, which are known to promote angiogenesis (Kohli *et al.*, 2021). The 5 wt% HA displayed significantly lower branching points than the polymer by itself and the 10 wt% HA group. This group may be displaying less vascularisation and branching due to the HA particles not being dispersed properly before 3D printing of the scaffolds. The 10 wt% HA scaffolds had the clearest pores, which allow the new capillaries to bifurcate more freely than in the other scaffolds where the pores may not be as clear to flow through. However, all three experimental groups obtained significantly higher bifurcation point numbers than the negative control sample, prepared in PBS.

## 4.5 Conclusion

To conclude, the studies carried out in this chapter were to explore the biological properties including the cytocompatibility, osteogenic differentiation and angiogenic response of an isosorbide-based light-curable, degradable polymeric system and assess its potential use in craniofacial reconstruction. The biological impact from the addition of hydroxyapatite filler to the polymer was evaluated in-depth with the assessment of metabolic activity, osteogenic differentiation studies, osteogenic gene expression and angiogenesis development.

MG-63 and hADSCs were explored for their ability to proliferate and promote cell growth on the surface of CSMA-2:HA composite-polymer discs. To further investigate the materials cytocompatibility, a comparative experiment was carried out to explore the effect of treating hADSCs in osteogenic-supplemented media vs. standard media. The real-time PCR technique was used for the purpose of differentiation studies to assess gene expression of RUNX2, COL1A1, OCN and OPN bone markers. Finally, the angiogenic response of the composite-polymer scaffolds was investigated using the *ex-ovo* CAM assay model.

The formulation of CSMA-2 with 10 wt% HA demonstrated promising results throughout the chapter and can address the current drawbacks associated with current commercial materials when looking into craniofacial bone regeneration. The positive results highlight the importance of HA and the positive impact the addition of such calcium phosphates can have on the proliferation of cells as well as the promotion of angiogenesis.



## **Chapter 5 : General Discussion and Conclusion**

## 5.1 Discussion

The overall aim of this thesis was to explore an isosorbide-based, light-curable, degradable polymeric system for the purpose of 3D printing custom-fit implants for patients requiring facial reconstruction surgery affecting their head and neck region. The material, referred to throughout the study as CSMA-2, was synthesised and chemically characterised in Chapter 2 to explore its printability using a DLP, stereolithographic technique to allow photopolymerisation to take place. Chapter 3 investigated the mechanical and physical properties of the polymer alongside a comparison of the effect of varying ratios of hydroxyapatite, as well as the effect of two different photoinitiators to ultimately find the optimum formulation going forward. A thorough biological exploration took place in Chapter 4, where two cell lines, MG-63 and hADSC's were assessed for their compatibility with the composite-polymer scaffolds. This was advanced by the assessment of osteogenic differentiation as well as gene expression through the materials. Finally, an intensive angiogenesis assessment was investigated to understand the capabilities of the material to promote vascularisation.

For the ultimate goal of achieving osteogenesis, bone tissue engineering in craniofacial reconstruction is most effective when it can mimic and interact with the surrounding native environment. As explored in Chapter 1, various issues and limitations are inhibiting the use of current techniques and technologies in craniofacial reconstruction, mainly due to insufficient biochemical stability, poor mechanical properties, lack of durability and degradability. For years, researchers have been trying to overcome limitations such as these by developing novel materials that would potentially be better-suited candidates for use in surgery. However, a balance between

the physiochemical characteristics and biocompatibility is required to bridge the gap between research and clinical applications.

In this study, CSMA-2, a highly advantageous light-curable polymer was explored in depth. Previous work done by our group, (Owji *et al.*, 2019) confirmed the polymers exhibition of low polymerisation shrinkage, reduced monomer leaching and improved biological cytocompatibility. The exploration of the monomer's ability to rapidly photopolymerise offers advantages, particularly when exploring a minimally invasive surgical approach. Two photoinitiators, CQ and BAPO were investigated throughout the study for their photopolymerisation properties as well as the toxic effect they may have in a biological environment. The formulations created with CQ initiator were only made by the manual method which involved the monomer liquid (or paste when incorporated with HA) being poured into 10 mm circlip discs and cured with a hand-held blue light-emitting diode for 40 seconds on each side. The composites with CQ were attempted to be 3D printed, however, the settings had to be set to maximum for the power intensity, curing time and power level to allow the material to photopolymerise. When incorporated HA fillers to the CQ photoinitiator CSMA-2 formulation, the printer was not able to produce any constructs therefore the CQ composite-polymer specimens were all prepared by hand to allow for physiochemical and mechanical testing. BAPO on the other hand, allowed a uniform 3D printed structure to be printed whilst incorporating up to 10 wt% HA with the CSMA-2 formulation. When exploring the differences between CQ and BAPO, BAPO proved to be the more suitable initiator to use as it gave a better rate of reaction time, suggesting less time was needed for BAPO incorporated monomers to polymerise. This allowed for the 3D printing of CSMA-2 composite polymer specimens to be prepared using the

DLP method. When assessing the effect of the varying photoinitiators mechanically, BAPO gave better results in particular with the bend strength of the material which gave a value of 135.49 N/mm<sup>2</sup> significantly comparing to the bend strength of the polymer incorporating CQ which gave a value of 84.07 N/mm<sup>2</sup>. Further to this, the hardness, modulus and wettability of BAPO-incorporated polymers were superior to the results from the CQ-incorporated polymers. Moreover, when assessing the cytocompatibility of CSMA-2 composite-polymers with either CQ or BAPO using MG-63 osteosarcoma cells, the metabolic activity for the BAPO incorporated polymers proved to be slightly more positive than the CQ. Therefore, moving forward with the studies, the 3D printed BAPO-incorporated CSMA-2 composite polymer specimens were used for further *in vitro* assessments.

Hydroxyapatite, a calcium phosphate similar to the human hard tissues, was added into the CSMA-2 composites for further characterisation. The modulus values of CSMA-2 and HA composites were examined as matching the mechanical properties of synthetic materials to the native tissue is a crucial principle in creating biomaterial-based scaffolds. Originally, up to 50 wt% HA formulations were investigated mechanically to understand the effect of higher additions of calcium phosphates on the polymeric system. The results up to 5 wt% HA showed little significant difference for the modulus, bend strength, hardness and wettability however, when increasing the quantity up to 50 wt% HA, the modulus significantly decreased, the bend strength slightly decreased and the contact angle became smaller, proving a more hydrophilic material. Following on from this, when assessing printability, the 1: 10 liquid to powder phase formulation was the maximum the 3D printer could handle as it still flowed freely. Therefore, with the mechanical and physiochemical properties and the printability, the

10 wt% HA formulation was established to be the optimum formulation as a result of suitable mixing between the liquid and powder phase. Achieving biodegradability was also a critical objective in this thesis. CSMA-2 and its composite polymer specimens displayed a relatively slow degradation, with the highest mass loss observed in the 10 wt% HA formulations over the 6-month incubation period. These characteristics can be advantageous in a dynamic *in vivo* environment since slow degradation can minimise abrupt pH shifts, as well as potentially providing long-term mechanical stability (Brooks and Alper, 2021).

For the purpose of reproducibility and reliability, the formulations tested for further investigation of *in vitro* and *ex vivo* were the 0, 5 and 10 wt% HA incorporated CSMA-2 polymer composites.

Following cultivation of MG-63 cells on the surface of CSMA-2 and CSMA-2 + 5 or 10 wt% HA discs prepared with either CQ or BAPO photoinitiator and compared to the cells seeded on tissue culture plastic, a difference in metabolic activity was detected. Both CQ and BAPO groups continued to grow throughout the study, but the BAPO group had consistently higher metabolic activity than the CQ. This observation was consistent and in parallel with the quantitative cell metabolic activity findings; hence, the cytocompatibility of the materials was confirmed, particularly improved by the BAPO incorporated specimens. These results suggested that the focus of the rest of the study should be on the BAPO incorporated CSMA-2 specimens with an investigation into the effects of up to 10 wt% HA.

Preliminary cytocompatibility characterisation was followed by a more extensive investigation of the effects of the composite-polymer specimens on hADSCs, a

clinically relevant source for tissue engineering applications. The 3 formulations, 0, 5 and 10 wt% HA incorporated BAPO prepared CSMA-2 discs, continued to show significant metabolic activity throughout the study time points but mainly remained significantly lower than the control group, with an exception for the 10 wt% HA formulations where the metabolic activity increased significantly compared to the control. The results can be confirmed by understanding the effect of HA which is known to have osteoconductive properties which in turn enhance cytocompatibility of scaffolds. The results for the 5 and 10 wt% HA formulations compare significantly suggesting better metabolic activity for the 10 wt% HA group. This could be due to the quantity of HA not being quite enough to make a positive impact, or the mixing process of the HA with CSMA-2 not being as evenly distributed to achieve uniformity, which is a critical factor when related to cell proliferation and biocompatibility (Ghassemi *et al.*, 2018).

The exploration of hADSCs cultivated on CSMA-2 composite-polymer discs was expanded to include the comparison of cell metabolic activity when cultured using standard media or osteogenic-supplemented media. Osteogenic differentiation promotes the differentiation of osteogenic cells to develop into osteoblasts, which are responsible for new bone formation (Rutkovskiy, Stenslkken and Vaage, 2016). Mesenchymal stem cells (MSCs), which are present in multiple tissues such as bone marrow and fat tissue, can give rise to osteoblasts, chondrocytes, myoblasts and adipocyte lineages (Canalis, 2008). The follow-up differentiation is governed by transcriptional regulators, for osteoblasts this is RUNX2. The activation of RUNX2 allows the cells to be defined as preosteoblast, as they undergo a 3-stage differentiation. RUNX2 directs stem cells including hADSCs, to differentiate into

osteoblasts and inhibits other differentiation pathways, especially adipocyte differentiation (Komori, 2010). As previously discussed, to achieve optimal differentiation efficiency, cell-material interactions are explored. Many efforts have been undertaken to specifically mimic tissue-specific *in vivo* environments by modifying numerous material properties (Han *et al.*, 2020).

The osteogenic media in this experiment provided a non-harmful environment to enhance cell growth, without the addition of external growth factors. There was significantly higher metabolic activity when the hADSCs were cultured in osteogenic media, compared to standard media consistently throughout the 28-day experiment. Throughout this hADSC study, it has been demonstrated that the varying amounts of calcium phosphates can also affect the potential of osteogenic differentiation. The addition of HA to the composites made a positive impact on the metabolic activity, where the 5 and 10 wt% HA groups gave high metabolic activity readings, significantly different to the same groups in standard media.

The osteogenic potential was further explored quantitatively by real-time PCR. Osteogenic gene expression was assessed by qPCR by investigating the expression of RUNX2, COL1A1, OPN and OCN on hADSCs cultured on CSMA-2 and 0, 5 or 10 wt% HA composite-polymer discs prepared in either standard or osteogenic-supplemented media. The results for this experiment suggested that there was an upregulation of osteogenic genes being expressed through the hADSCs cultivated on the composite-polymer specimens. The results for the osteogenic supplemented media prepared specimens showed consistent upregulation after induction by hADSCs on the material, compared to the standard media. These findings indicate that the osteogenic media could increase the expression of osteogenic genes in

hADSCs when seeded on CSMA-2 and its composites, and stimulate their osteogenesis and therefore lead to a cellular resource for bone regeneration (Park, Bae and Park, 2015).

Angiogenesis, the formation of new blood vessels, was investigated on CSMA-2 along with its composites containing 5 and 10 wt% HA. The chorioallantoic membrane (CAM) assay is an affordable and simple screening method for the assessment of angiogenic characteristics and the materials potential to be used in the field of tissue engineering (Merckx *et al.*, 2020). There are two main types of CAM assays that researchers use, one is the *in ovo* technique, incorporating the material inside the eggshell, and the other is the *ex-ovo* technique where the entire egg content can be grown in a recipient (Nowak-Sliwinska, Segura and Iruela-Arispe, 2014). For this study, the *ex-ovo* CAM technique was used. The formation of new blood vessels was observed in all the composite-polymer scaffolds to varying extents depending on the composition of the material. The CSMA-2 scaffold showed a high level of vascularisation as well as the group containing 10 wt% HA which demonstrated the closest angiogenic response as the positive control sample. The CAM results were quantitatively analysed by calculating the percentage of vascular density as well as investigating the number of branching points. Throughout the CAM study, the 10 wt% HA formulation was significantly closest to the positive control, which was treated in VEGF, suggesting the addition of HA to the polymer promoted a higher level of vascularisation. The presence of pores in the scaffolds promoted the formation of new blood vessels just as explained by Karageorgiou and associates (Karageorgiou and Kaplan, 2005) in their study assessing the porosity of 3D biomaterials on osteogenesis. They concluded that the porosity and pore size of a scaffold plays a critical role in bone formation *in vitro* and



*in vivo* (Karageorgiou and Kaplan, 2005). Their study also suggested that when exploring cell-material interactions *in vitro*, lower porosity stimulates osteogenesis by suppressing cell proliferation and forcing cell aggregation. However, when an *in vivo* environment is implemented, higher porosity and a larger pore size result in greater bone ingrowth. Therefore, the results from the CAM assay in this study are positive in suggesting potential bone regeneration when materials will be implanted *in vivo*.

Throughout this thesis the potential use of 3D printing techniques in the fabrication of bone tissue engineering scaffolds was explored. Although the incorporation of CaP particles was found to be considerably challenging, small variations in the manufacturing process and optimisation of settings can allow the printing of the polymeric system to allow it to be applicable in restoring cranial defects by allowing the production of customised implants. The DLP 3D printing technique was assessed and chosen to be the printing technique of choice for this study due to its photopolymerisation properties as well as the relatively low cost, and speedy printing time. This technology allowed for quick printing at a high resolution, allowing for the correct creation of complicated constructions while maintaining exact control over the defects unique contour (Ghaffar, Corker and Fan, 2018). The utilisation of a high-resolution printing technique can considerably enhance cell attachment and proliferation in a dynamic *in vivo* environment (Augustine *et al.*, 2021) which will ultimately improve the aesthetic and functional outcomes in the replacement of bone defects without the need for additional surgery, limiting the trauma caused to patients. Finally, it is important to emphasise the advantages of the fabrication of CSMA-2 as a polymeric system for use as a printable resin. The synthesis route taken allowed for a clean, reliable and accurate polymerisation to take place. The precursors used to

prepare the starting monomer, BHIS, include isosorbide, ethylene carbonate and potassium carbonate. Isosorbide is an affordable, greener compound that is used in a variety of medical applications, in particular in the synthesis of biodegradable scaffolds for tissue repair and regeneration. Ethylene carbonate is used in a variety of applications including being used as a plasticiser in polymers and potassium carbonate is used as a mild base catalyst in the reaction. All of these components are sourced easily, as well as being cost-effective and do not cause a release of any toxic side products when reacting together to form BHIS. The synthesised BHIS was filtered using the classic column chromatography method incorporating silica gel beads and an ethyl acetate and methanol solvent phase which eliminated any unnecessary toxins and solvents that did not react. Whilst this method was effective to achieve a relatively high yield of BHIS, it is time consuming, irreproducible and difficult to pack a good column. This can be substituted by an automated flash chromatography device. These devices are used in industrial scale polymer synthesis to purify products in an automated and more accurate manner by using pre-packed flash columns and a fully automated instrument to isolate target molecules from synthetic reactions (Compton *et al.*, 2020).

To complete the synthesis of CSMA-2, TEGDMA, a monomer widely used in the composition of composite resins in dentistry, and HEMA, a colourless viscous liquid that forms a variety of polymers, were both incorporated. Again, the components are easily and affordably sourced and are safe to use in a small scale laboratory synthesis. The benefits mentioned in regard to the pre-cursors, led to a successful fabrication of an isosorbide based, light-curable, degradable polymeric system with no side products

being formed throughout the synthesis, and a positive contribution to 3D printable resins.

## 5.2 Future Work

The main areas that require further investigation if future work was to be carried out related to this study would be as follows:

1. Further work to assess the osteogenic differentiation of stem cells seeded on CSMA-2 and its composites by using staining techniques to qualitatively visualise the upregulation of gene expression. Further expanding the gene expression work into protein expression by carrying out gel electrophoresis to confirm these findings from the qPCR.
2. Potential investigation of different CaP fillers to further improve the physiochemical and mechanical properties of CSMA-2 to ultimately achieve the aim of creating custom-fit facial implants for use in craniofacial reconstruction surgery.
3. Optimisation of printing settings to incorporate higher quantities of calcium phosphate powders into the CSMA-2 formulations to allow suitable printability using the DLP 3D printing system.
4. Enhance the porosity of the material by designing larger scaffolds, with greater porosity to potentially enable further angiogenesis as well as promote further cell growth.
5. Potential investigation into other extracellular membrane components such as collagen to incorporate into the scaffold for further compatibility assessment.
6. Investigating the *in vivo* properties of CSMA-2 and its appropriate composite-polymer formulations by implanting scaffolds into a cranial defect of rats to evaluate the materials ability to promote healthy bone formation when translated into clinical trials in humans.

### 5.3 Conclusion

In conclusion, the experimental findings presented in this thesis reveal the successful fabrication of a light-curable, degradable polymeric system that offers mechanical strength, flexibility, printability and non-cytotoxicity which can be beneficial to fit the specific needs for a biomaterial to restore cranio-maxillofacial defects. With the incorporation of a suitable photoinitiator, as well as the support from a calcium phosphate powder phase filler, when compared to current polymeric systems that have been widely reviewed in tissue engineering, this material holds significant promising features.

The positive outcomes observed *in vitro* and *ex vivo* in this study suggest a clinical potential of the tissue-engineered approach developed as part of this work and future experiments need to be designed to prove the efficacy of the polymeric system *in vivo*. These studies will be aimed at characterising this material in an animal model to translate the current manufacturing process to a clinical setting to achieve successful osteogenesis.

Finally, the utilisation of 3D printing technology allows for the fabrication of customised-fitted implants which can address the aesthetic concerns linked with the already available commercial materials used in this field. Furthermore, the rapid photopolymerisation of CSMA-2 via DLP 3D printing offers promising results in terms of reducing surgery time and the number of surgeries required for a patient, pushing CSMA-2 as a viable biomaterial alternative in craniofacial bone regeneration.

## Bibliography

Abdallah, R. M. (2016). 'Evaluation of polymethyl methacrylate resin mechanical properties with incorporated halloysite nanotubes'. *Journal of Advanced Prosthodontics*. Korean Academy of Prosthodontic, 8 (3), pp. 167–171. doi: 10.4047/jap.2016.8.3.167.

Abdo Filho, R. C. C., Oliveira, T. M., Lourenço Neto, N., Gurgel, C. and Abdo, R. C. C. (2011). 'Reconstruction of bony facial contour deficiencies with polymethylmethacrylate implants: Case report'. *Journal of Applied Oral Science*. Bauru School of Dentistry, University of Sao Paulo, 19 (4), pp. 426–430. doi: 10.1590/S1678-77572011000400021.

Ahmed, Y. A., Tatarczuch, L., Pagel, C. N., Davies, H. M. S., Mirams, M. and Mackie, E. J. (2007). 'Physiological death of hypertrophic chondrocytes'. *Osteoarthritis and Cartilage*. W.B. Saunders, 15 (5), pp. 575–586. doi: 10.1016/j.joca.2006.10.016.

Akter, F. and Ibanez, J. (2016). 'Bone and Cartilage Tissue Engineering'. in *Tissue Engineering Made Easy*. Elsevier Inc., pp. 77–97. doi: 10.1016/B978-0-12-805361-4.00008-4.

Aldaadaa, A., Owji, N. and Knowles, J. (2018). 'Three-dimensional Printing in Maxillofacial Surgery: Hype versus Reality'. *Journal of Tissue Engineering*. SAGE Publications Ltd, 9. doi: 10.1177/2041731418770909.

Aldabib, J. M. and Ishak, Z. A. M. (2020). 'Effect of hydroxyapatite filler concentration on mechanical properties of poly (methyl methacrylate) denture base'. *SN Applied*

*Sciences 2020 2:4*. Springer, 2 (4), pp. 1–14. doi: 10.1007/S42452-020-2546-1.

AlGhamdi, A. S., Shibly, O. and Ciancio, S. G. (2010). 'Osseous grafting part II: xenografts and alloplasts for periodontal regeneration--a literature review.' *Journal of the International Academy of Periodontology*, pp. 39–44. Available at: <https://europepmc.org/article/med/20465030> (Accessed: 10 November 2020).

Alghamdi, H. S. (2018). 'Methods to improve osseointegration of dental implants in low quality (type-IV) bone: An overview'. *Journal of Functional Biomaterials*. MDPI AG. doi: 10.3390/jfb9010007.

Anderson, J. M. and Shive, M. S. (1997). 'Biodegradation and biocompatibility of PLA and PLGA microspheres'. *Advanced Drug Delivery Reviews*. Elsevier Sci B.V., pp. 5–24. doi: 10.1016/S0169-409X(97)00048-3.

Apratim, A., Eachempati, P., Salian, K. K. K., Singh, V., Chhabra, S. and Shah, S. (2015). 'Zirconia in dental implantology: A review'. *Journal of International Society of Preventive & Community Dentistry*. Wolters Kluwer -- Medknow Publications, 5 (3), p. 147. doi: 10.4103/2231-0762.158014.

Aryal, R., Chen, X., Fang, C. and Hu, Y. (2014). 'Bone Morphogenetic Protein- 2 and Vascular Endothelial Growth Factor in Bone Tissue Regeneration: New Insight and Perspectives'. *Orthopaedic Surgery*. Wiley-Blackwell, 6 (3), p. 171. doi: 10.1111/OS.12112.

Askari, M., Naniz, M. A., Kouhi, M., Saberi, A., Zolfagharian, A. and Bodaghi, M. (2021). 'Recent progress in extrusion 3D bioprinting of hydrogel biomaterials for tissue regeneration: a comprehensive review with focus on advanced fabrication techniques'. *Biomaterials Science*. The Royal Society of Chemistry, 9 (3), pp. 535–

573. doi: 10.1039/D0BM00973C.

Augustine, R., Kalva, S. N., Ahmad, R., Zahid, A. A., Hasan, S., Nayeem, A., McClements, L. and Hasan, A. (2021). '3D Bioprinted cancer models: Revolutionizing personalized cancer therapy'. *Translational Oncology*. Elsevier, 14 (4), p. 101015. doi: 10.1016/J.TRANON.2021.101015.

Bagheri, A., Arandiyani, H., Adnan, N. N. M., Boyer, C. and Lim, M. (2017). 'Controlled Direct Growth of Polymer Shell on Upconversion Nanoparticle Surface via Visible Light Regulated Polymerization'. *Macromolecules*. American Chemical Society, 50 (18), pp. 7137–7147. doi: 10.1021/ACS.MACROMOL.7B01405.

Bagheri, A. and Jin, J. (2019). 'Photopolymerization in 3D Printing'. *ACS Applied Polymer Materials*. American Chemical Society, 1 (4), pp. 593–611. doi: 10.1021/ACSAPM.8B00165.

Baino, F., Novajra, G. and Vitale-Brovarone, C. (2015). 'Bioceramics and scaffolds: A winning combination for tissue engineering'. *Frontiers in Bioengineering and Biotechnology*. Frontiers Media S.A. doi: 10.3389/fbioe.2015.00202.

Barfeie, A., Wilson, J. and Rees, J. (2015). 'Implant surface characteristics and their effect on osseointegration'. *British Dental Journal*. Nature Publishing Group. doi: 10.1038/sj.bdj.2015.171.

Bellisola, G. and Sorio, C. (2012). 'Infrared spectroscopy and microscopy in cancer research and diagnosis'. *American Journal of Cancer Research*. E-Century Publishing Corporation, pp. 1–21. Available at: [www.ajcr.us](http://www.ajcr.us) (Accessed: 3 March 2021).



Best, S. M., Porter, A. E., Thian, E. S. and Huang, J. (2008). 'Bioceramics: Past, present and for the future'. *Journal of the European Ceramic Society*. Elsevier, 28 (7), pp. 1319–1327. doi: 10.1016/j.jeurceramsoc.2007.12.001.

Bhatt, R. A. and Rozental, T. D. (2012). 'Bone Graft Substitutes'. *Hand Clinics*. Elsevier, pp. 457–468. doi: 10.1016/j.hcl.2012.08.001.

Bijukumar, D. R., McGeehan, C. and Mathew, M. T. (2018). 'Regenerative Medicine Strategies in Biomedical Implants'. *Current Osteoporosis Reports*. Current Medicine Group LLC 1, pp. 236–245. doi: 10.1007/s11914-018-0441-0.

Bladen, J. C., Norris, J. H. and Malhotra, R. (2012). 'Indications and outcomes for revision of gold weight implants in upper eyelid loading.' *The British journal of ophthalmology*. BMJ Publishing Group Ltd, 96 (4), pp. 485–9. doi: 10.1136/bjophthalmol-2011-300732.

Blair, H. C., Larrouture, Q. C., Li, Y., Lin, H., Beer-Stoltz, D., Liu, L., Tuan, R. S., Robinson, L. J., Schlesinger, P. H. and Nelson, D. J. (2017). 'Osteoblast differentiation and bone matrix formation in vivo and in vitro'. *Tissue Engineering - Part B: Reviews*. Mary Ann Liebert Inc., pp. 268–280. doi: 10.1089/ten.teb.2016.0454.

Boddapati, A., Rahane, S. B., Slopek, R. P., Breedveld, V., Henderson, C. L. and Grover, M. A. (2011). 'Gel time prediction of multifunctional acrylates using a kinetics model'. *Polymer*. Elsevier Ltd, 52 (3), pp. 866–873. doi: 10.1016/J.POLYMER.2010.12.024.

Boller, C., Prado, M. R., Toledo, M., Garbelini, M., OrtolaniMachado, C., Nakashima, T. and Zibetti, R. (2015). 'The Anti-angiogenic Effect of Chamomila recutita Aqueous

Extract Determined Using a Modified Chicken Chorioallantoic Membrane ex ovo assay'. *International Journal of Current Microbiology and Applied Sciences*, 4 (8), pp. 231–243.

Borkotoky, S. S., Dhar, P. and Katiyar, V. (2018). 'Biodegradable poly (lactic acid)/Cellulose nanocrystals (CNCs) composite microcellular foam: Effect of nanofillers on foam cellular morphology, thermal and wettability behavior'. *International Journal of Biological Macromolecules*. Elsevier B.V., 106, pp. 433–446. doi: 10.1016/j.ijbiomac.2017.08.036.

Bose, S., Roy, M. and Bandyopadhyay, A. (2012). 'Recent advances in bone tissue engineering scaffolds'. *Trends in biotechnology*. Trends Biotechnol, 30 (10), pp. 546–554. doi: 10.1016/J.TIBTECH.2012.07.005.

Bottini, M., Mebarek, S., Anderson, K. L., Strzelecka-Kiliszek, A., Bozycki, L., Simão, A. M. S., Bolean, M., Ciancaglini, P., Pikula, J. B., Pikula, S., Magne, D., Volkmann, N., Hanein, D., Millán, J. L. and Buchet, R. (2018). 'Matrix vesicles from chondrocytes and osteoblasts: their biogenesis, properties, functions and biomimetic models'. *Biochimica et biophysica acta*. NIH Public Access, 1862 (3), p. 532. doi: 10.1016/J.BBAGEN.2017.11.005.

Boyle, W. J., Simonet, W. S. and Lacey, D. L. (2003). 'Osteoclast differentiation and activation'. *Nature*. Nature, pp. 337–342. doi: 10.1038/nature01658.

Branemark, P. I. (1983). 'Osseointegration and its experimental background'. *The Journal of Prosthetic Dentistry*. doi: 10.1016/S0022-3913(83)80101-2.

Breeland, G. and Menezes, R. G. (2019). *Embryology, Bone Ossification*. StatPearls. StatPearls Publishing. Available at: <http://www.ncbi.nlm.nih.gov/pubmed/30969540>

(Accessed: 9 October 2020).

Breeland, G., Sinkler, M. A. and Menezes, R. G. (2021). 'Embryology, Bone Ossification'. *StatPearls*. StatPearls Publishing. Available at:

<https://www.ncbi.nlm.nih.gov/books/NBK539718/> (Accessed: 9 August 2021).

Brooks, S. M. and Alper, H. S. (2021). 'Applications, challenges, and needs for employing synthetic biology beyond the lab'. *Nature Communications* 2021 12:1.

Nature Publishing Group, 12 (1), pp. 1–16. doi: 10.1038/s41467-021-21740-0.

Bruno, Z., Angelo, N., Riccardo, S., Nicola, Z., Stefano, P., Camillo, P., Federico, N. and Carlotta, M. (2020). 'Custom-made hydroxyapatite cranioplasty: Radiological and histological evidence of bone-biomaterial osteointegration in five patients'.

*Asian Journal of Neurosurgery*. Medknow, 15 (1), p. 198. doi: 10.4103/ajns.ajns\_208\_19.

Buchanan, E. P. and Hyman, C. H. (2013). 'LeFort i osteotomy'. *Seminars in Plastic Surgery*. Thieme Medical Publishers, 27 (3), pp. 149–154. doi: 10.1055/s-0033-

1357112.

Bunea, A.-I., del Castillo Iniesta, N., Droumpali, A., Wetzel, A. E., Engay, E. and Taboryski, R. (2021). 'Micro 3D Printing by Two-Photon Polymerization:

Configurations and Parameters for the Nanoscribe System'. *Micro*, 1 (2), pp. 164–180. doi: 10.3390/micro1020013.

Buser, D., Sennerby, L. and De Bruyn, H. (2017). 'Modern implant dentistry based on osseointegration: 50 years of progress, current trends and open questions'.

*Periodontology 2000*. Blackwell Munksgaard, pp. 7–21. doi: 10.1111/prd.12185.

Calabrese, G., Giuffrida, Raffaella, Fabbi, C., Figallo, E., Furno, D. Lo, Gulino, R.,

Colarossi, C., Fullone, F., Giuffrida, Rosario, Parenti, R., Memeo, L. and Forte, S. (2016). 'Collagen-Hydroxyapatite Scaffolds Induce Human Adipose Derived Stem Cells Osteogenic Differentiation In Vitro'. *PLOS ONE*. Public Library of Science, 11 (3), p. e0151181. doi: 10.1371/JOURNAL.PONE.0151181.

Campana, V., Milano, G., Pagano, E., Barba, M., Cicione, C., Salonna, G., Lattanzi, W. and Logroscino, G. (2014). 'Bone substitutes in orthopaedic surgery: from basic science to clinical practice'. *Journal of Materials Science: Materials in Medicine*. Kluwer Academic Publishers, 25 (10), pp. 2445–2461. doi: 10.1007/s10856-014-5240-2.

Canalis, E. (2008). 'Notch signaling in osteoblasts'. *Science signaling*. Sci Signal, 1 (17). doi: 10.1126/STKE.117PE17.

Carlino, P., Pepe, V., Pollice, G. and Grassi, F. R. (2008). 'Immediate transmucosal implant placement in fresh maxillary and mandibular molar extraction sockets: description of technique and preliminary results.' *Minerva stomatologica*, 57 (10), pp. 471–83. Available at: <http://www.ncbi.nlm.nih.gov/pubmed/19078889> (Accessed: 13 May 2019).

Carnicer-Lombarte, A., Chen, S. T., Malliaras, G. G. and Barone, D. G. (2021). 'Foreign Body Reaction to Implanted Biomaterials and Its Impact in Nerve Neuroprosthetics'. *Frontiers in Bioengineering and Biotechnology*, 9 (April), pp. 1–22. doi: 10.3389/fbioe.2021.622524.

Carrier, O. and Bonn, D. (2015). 'Contact Angles and the Surface Free Energy of Solids'. *Droplet Wetting and Evaporation*. Academic Press, pp. 15–23. doi: 10.1016/B978-0-12-800722-8.00002-3.

Chan, Zorlutuna, P., Jeong, J., Kong, H. and Bashir, R. (2010). 'Three-dimensional photopatterning of hydrogels using stereolithography for long-term cell encapsulation'. *Lab on a chip*. Lab Chip, 10 (16), pp. 2062–2070. doi: 10.1039/C004285D.

Chatani, S., Kloxin, C. J. and Bowman, C. N. (2014). 'The power of light in polymer science: photochemical processes to manipulate polymer formation, structure, and properties'. *Polymer Chemistry*. The Royal Society of Chemistry, 5 (7), pp. 2187–2201. doi: 10.1039/C3PY01334K.

Chen, F. M. and Liu, X. (2016). 'Advancing biomaterials of human origin for tissue engineering'. *Progress in Polymer Science*. Elsevier Ltd, pp. 86–168. doi: 10.1016/j.progpolymsci.2015.02.004.

Chen, Y., Zhou, S. and Li, Q. (2011). 'Mathematical modeling of degradation for bulk-erosive polymers: Applications in tissue engineering scaffolds and drug delivery systems'. *Acta Biomaterialia*. Elsevier, 7 (3), pp. 1140–1149. doi: 10.1016/J.ACTBIO.2010.09.038.

Cheng, Y. L. and Chen, F. (2017). 'Preparation and characterization of photocured poly ( $\epsilon$ -caprolactone) diacrylate/poly (ethylene glycol) diacrylate/chitosan for photopolymerization-type 3D printing tissue engineering scaffold application'. *Materials Science and Engineering: C*. Elsevier, 81, pp. 66–73. doi: 10.1016/J.MSEC.2017.07.025.

Chiulan, I., Heggset, E. B., Voicu, Ș. I. and Chinga-Carrasco, G. (2021). 'Photopolymerization of Bio-Based Polymers in a Biomedical Engineering Perspective'. *Biomacromolecules*. American Chemical Society, 22 (5), pp. 1795–

1814. doi: 10.1021/ACS.BIOMAC.0C01745.

Christoffersen, J., Christoffersen, M. R. and Kjaergaard, N. (1978). 'The kinetics of dissolution of calcium hydroxyapatite in water at constant pH'. *Journal of Crystal Growth*. North-Holland, 43 (4), pp. 501–511. doi: 10.1016/0022-0248(78)90350-0.

Clarke, B. (2008). 'Normal Bone Anatomy and Physiology The Skeleton'. *Clin J Am Soc Nephrol*, 3, pp. 131–139. doi: 10.2215/CJN.04151206.

Cloney, K. and Franz-Odenaal, T. A. (2015). 'Optimized Ex-ovo Culturing of Chick Embryos to Advanced Stages of Development'. *Journal of Visualized Experiments : JoVE*. MyJoVE Corporation, 95 (95), p. 52129. doi: 10.3791/52129.

Colasante, C., Sanford, Z., Garfein, E. and Tepper, O. (2016). 'Current Trends in 3D Printing, Bioprosthesis, and Tissue Engineering in Plastic and Reconstructive Surgery'. *Current Surgery Reports 2016 4:2*. Springer, 4 (2), pp. 1–14. doi: 10.1007/S40137-016-0127-4.

Comesaña, R., Lusquiños, F., Val, J. del, Malot, T., López-Álvarez, M., Riveiro, A., Quintero, F., Boutinguiza, M., Aubry, P., Carlos, A. De and Pou, J. (2011). 'Calcium phosphate grafts produced by rapid prototyping based on laser cladding'. *Journal of the European Ceramic Society*, 1–2 (31), pp. 29–41. doi: 10.1016/J.JEURCERAMSOC.2010.08.011.

Compton, D. L., Appell, M., Kenar, J. A. and Evans, K. O. (2020). 'Enzymatic Synthesis and Flash Chromatography Separation of 1,3-Diferuloyl-sn-Glycerol and 1-Feruloyl-sn-Glycerol'. *Methods and Protocols 2020, Vol. 3, Page 8*. Multidisciplinary Digital Publishing Institute, 3 (1), p. 8. doi: 10.3390/MPS3010008.

Corona-Gomez, J., Chen, X. and Yang, Q. (2016). 'Effect of Nanoparticle Incorporation and Surface Coating on Mechanical Properties of Bone Scaffolds: A Brief Review'. *Journal of Functional Biomaterials* 2016, Vol. 7, Page 18. Multidisciplinary Digital Publishing Institute, 7 (3), p. 18. doi: 10.3390/JFB7030018.

Crockett, J. C., Mellis, D. J., Scott, D. I. and Helfrich, M. H. (2011). 'New knowledge on critical osteoclast formation and activation pathways from study of rare genetic diseases of osteoclasts: Focus on the RANK/RANKL axis'. *Osteoporosis International*. Springer, pp. 1–20. doi: 10.1007/s00198-010-1272-8.

Dabbagh, S. R., Sarabi, M. R., Rahbarghazi, R., Sokullu, E., Yetisen, A. K. and Tasoglu, S. (2021). '3D-printed microneedles in biomedical applications'. *iScience*. Elsevier, 24 (1), p. 102012. doi: 10.1016/J.ISCI.2020.102012.

Dai, R., Wang, Z., Samanipour, R., Koo, K. I. and Kim, K. (2016). 'Adipose-Derived Stem Cells for Tissue Engineering and Regenerative Medicine Applications'. *Stem Cells International*. Hindawi Limited, 2016. doi: 10.1155/2016/6737345.

Dallas, S. L., Prideaux, M. and Bonewald, L. F. (2013). 'The Osteocyte: An Endocrine Cell. .. and More'. doi: 10.1210/er.2012-1026.

Deligianni, D. D., Katsala, N. D., Koutsoukos, P. G. and Missirlis, Y. F. (2000). 'Effect of surface roughness of hydroxyapatite on human bone marrow cell adhesion, proliferation, differentiation and detachment strength'. *Biomaterials*. Elsevier, 22 (1), pp. 87–96. doi: 10.1016/S0142-9612(00)00174-5.

Dennis, S. C., Berkland, C. J., Bonewald, L. F. and Detamore, M. S. (2015). 'Endochondral Ossification for Enhancing Bone Regeneration: Converging Native Extracellular Matrix Biomaterials and Developmental Engineering in Vivo'. *Tissue*

*Engineering - Part B: Reviews*. Mary Ann Liebert Inc., pp. 247–266. doi:

10.1089/ten.teb.2014.0419.

Dhandayuthapani, B., Yoshida, Y., Maekawa, T. and Kumar, D. S. (2011). 'Polymeric scaffolds in tissue engineering application: A review'. *International Journal of Polymer Science*. Hindawi Publishing Corporation. doi: 10.1155/2011/290602.

Di, Z. and Yoshihiro, I. (2014). 'SCIENCE CHINA Chemistry Visible light-curable polymers for biomedical applications', 57, pp. 510–521. doi: 10.1007/s11426-014-5069-z.

Doblaré, M., García, J. M. and Gómez, M. J. (2004). 'Modelling bone tissue fracture and healing: A review'. *Engineering Fracture Mechanics*. Elsevier BV, pp. 1809–1840. doi: 10.1016/j.engfracmech.2003.08.003.

Dorozhkin, S. V. (2009). 'Calcium orthophosphates in nature, biology and medicine'. *Materials*. Multidisciplinary Digital Publishing Institute (MDPI), pp. 399–498. doi: 10.3390/ma2020399.

Dorozhkin, S. V. (2012). 'Calcium orthophosphates and human beings: a historical perspective from the 1770s until 1940.' *Biomatter*. Taylor & Francis, pp. 53–70. doi: 10.4161/biom.21340.

Duan, B. and Wang, M. (2011). 'Title Selective laser sintering and its application in biomedical engineering'. *MRS BULLETIN • VOLUME*, 36. doi: 10.1557/mrs.2011.270.

Dumas, B. M., Nava, A., Law, H. Z., Smartt, J., Derderian, C., Seaward, J. R., Kane, A. A. and Hallac, R. R. (2019). 'Three-dimensional printing for craniofacial surgery: A



single institution's 5-year experience'. *Cleft Palate-Craniofacial Journal*. SAGE Publications Ltd, 56 (6), pp. 729–734. doi: 10.1177/1055665618798292.

Dym, H. and Pierse, J. (2011). 'Advanced techniques in bone grafting procedures'. *Dental Clinics of North America*. Dent Clin North Am, pp. 453–460. doi: 10.1016/j.cden.2011.02.003.

Eibel, A., Fast, D. E. and Gescheidt, G. (2018). 'Choosing the ideal photoinitiator for free radical photopolymerizations: predictions based on simulations using established data'. *Polymer Chemistry*. The Royal Society of Chemistry, 9 (41), pp. 5107–5115. doi: 10.1039/C8PY01195H.

El-Ghali, N., Rabadi, M., Ezin, M. and Bellard, M. E. de. (2010). 'New Methods for Chicken Embryo Manipulations'. *Microscopy research and technique*. NIH Public Access, 73 (1), p. 58. doi: 10.1002/JEMT.20753.

Eliaz, N. and Metoki, N. (2017). 'Calcium phosphate bioceramics: A review of their history, structure, properties, coating technologies and biomedical applications'. *Materials*. MDPI AG, 10 (4). doi: 10.3390/ma10040334.

Elmowafy, E. M., Tiboni, M. and Soliman, M. E. (2019). 'Biocompatibility, biodegradation and biomedical applications of poly(lactic acid)/poly(lactic-co-glycolic acid) micro and nanoparticles'. *Journal of Pharmaceutical Investigation 2019 49:4*. Springer, 49 (4), pp. 347–380. doi: 10.1007/S40005-019-00439-X.

Emons, J., Chagin, A. S., Hultenby, K., Zhivotovsky, B., Wit, J. M., Karperien, M. and Sävendahl, L. (2009). 'Epiphyseal fusion in the human growth plate does not involve classical apoptosis'. *Pediatric Research*. Nature Publishing Group, 66 (6), pp. 654–659. doi: 10.1203/PDR.0b013e3181beaa8c.

Family, R., Solati-Hashjin, M., Nik, S. N. and Nemati, A. (2012). 'Surface modification for titanium implants by hydroxyapatite nanocomposite'. *Caspian Journal of Internal Medicine*. Babol University of Medical Sciences, 3 (3), pp. 460–465. Available at: [/pmc/articles/PMC3755845/?report=abstract](https://pubmed.ncbi.nlm.nih.gov/3755845/) (Accessed: 18 January 2021).

Fantino, E., Chiappone, A., Calignano, F., Fontana, M., Pirri, F. and Roppolo, I. (2016). 'In Situ Thermal Generation of Silver Nanoparticles in 3D Printed Polymeric Structures'. *Materials (Basel, Switzerland)*. *Materials (Basel)*, 9 (7). doi: 10.3390/MA9070589.

Feng, B., Jinkang, Z., Zhen, W., Jianxi, L., Jiang, C., Jian, L., Guolin, M. and Xin, D. (2011). 'The effect of pore size on tissue ingrowth and neovascularization in porous bioceramics of controlled architecture in vivo'. *Biomedical Materials*. IOP Publishing, 6 (1), p. 015007. doi: 10.1088/1748-6041/6/1/015007.

Feng, X. and McDonald, J. M. (2011). 'Disorders of bone remodeling'. *Annual Review of Pathology: Mechanisms of Disease*. NIH Public Access, 6, pp. 121–145. doi: 10.1146/annurev-pathol-011110-130203.

Fernandes da Silva, A. L., Borba, A. M., Simão, N. R., Pedro, F. L. M., Borges, A. H. and Miloro, M. (2014). 'Customized Polymethyl Methacrylate Implants for the Reconstruction of Craniofacial Osseous Defects'. *Case Reports in Surgery*. Hindawi Limited, 2014, pp. 1–8. doi: 10.1155/2014/358569.

Fernandes, H. R., Gaddam, A., Rebelo, A., Brazete, D., Stan, G. E. and Ferreira, J. M. F. (2018). 'Bioactive Glasses and Glass-Ceramics for Healthcare Applications in Bone Regeneration and Tissue Engineering'. *Materials*. Multidisciplinary Digital Publishing Institute (MDPI), 11 (12). doi: 10.3390/MA11122530.

Fernandes, J. S., Gentile, P., Pires, R. A., Reis, R. L. and Hatton, P. V. (2017). 'Multifunctional bioactive glass and glass-ceramic biomaterials with antibacterial properties for repair and regeneration of bone tissue'. *Acta Biomaterialia*. Acta Materialia Inc, pp. 2–11. doi: 10.1016/j.actbio.2017.06.046.

Fernandez de Grado, G., Keller, L., Idoux-Gillet, Y., Wagner, Q., Musset, A. M., Benkirane-Jessel, N., Bornert, F. and Offner, D. (2018). 'Bone substitutes: a review of their characteristics, clinical use, and perspectives for large bone defects management'. *Journal of Tissue Engineering*. SAGE Publications Ltd. doi: 10.1177/2041731418776819.

Fillingham, Y. and Jacobs, J. (2016). 'Bone grafts and their substitutes'. *The Bone & Joint Journal*. British Editorial Society of Bone & Joint Surgery, 98-B (1\_Supple\_A), pp. 6–9. doi: 10.1302/0301-620x.98b.36350.

Florencio-Silva, R., Rodrigues Da, G., Sasso, S., Sasso-Cerri, E., Simões, M. J. and Cerri, P. S. (2015). 'Biology of Bone Tissue: Structure, Function, and Factors That Influence Bone Cells'. doi: 10.1155/2015/421746.

Foster, K. A., Shin, S. S., Prabhu, B., Fredrickson, A. and Sekula, R. F. (2016). 'Calcium Phosphate Cement Cranioplasty Decreases the Rate of Cerebrospinal Fluid Leak and Wound Infection Compared with Titanium Mesh Cranioplasty: Retrospective Study of 672 Patients'. *World Neurosurgery*. Elsevier Inc., 95, pp. 414–418. doi: 10.1016/j.wneu.2016.02.071.

Fouassier, J. P., Allonas, X., Lalevée, J. and Dietlin, C. (2010). 'Photoinitiators for Free Radical Polymerization Reactions'. *Photochemistry and Photophysics of Polymer Materials*. John Wiley & Sons, Ltd, pp. 351–419. doi:

10.1002/9780470594179.CH10.

Fowkes, F. M. (1964). *Contact Angle, Wettability, and Adhesion*. Edited by F. M. Fowkes. WASHINGTON, D.C.: AMERICAN CHEMICAL SOCIETY (Advances in Chemistry). doi: 10.1021/ba-1964-0043.

De Fusco, C., Messina, A., Monda, V., Viggiano, E., Moscatelli, F., Valenzano, A., Esposito, T., Chieffi, S., Cibelli, G., Monda, M. and Messina, G. (2017). 'Osteopontin: Relation between Adipose Tissue and Bone Homeostasis'. *Stem Cells International*. Hindawi Publishing Corporation. doi: 10.1155/2017/4045238.

Galvão, M. R., Caldas, S. G. F. R., Bagnato, V. S., Rastelli, A. N. de S. and de Andrade, M. F. (2013). 'Evaluation of degree of conversion and hardness of dental composites photoactivated with different light guide tips'. *European Journal of Dentistry*. Dental Investigations Society, 7 (1), pp. 86–93.

Gan, X., Fei, G., Wang, J., Wang, Z., Lavorgna, M. and Xia, H. (2020). 'Powder quality and electrical conductivity of selective laser sintered polymer composite components'. *Structure and Properties of Additive Manufactured Polymer Components*. Woodhead Publishing, pp. 149–185. doi: 10.1016/B978-0-12-819535-2.00006-5.

Ganster, B., Fischer, U. K., Moszner, N. and Liska, R. (2008). 'New Photocleavable Structures, 4'. *Macromolecular Rapid Communications*. John Wiley & Sons, Ltd, 29 (1), pp. 57–62. doi: 10.1002/MARC.200700620.

Garagiola, U., Grigolato, R., Soldo, R., Bacchini, M., Bassi, G., Roncucci, R. and De Nardi, S. (2016). 'Computer-aided design/computer-aided manufacturing of hydroxyapatite scaffolds for bone reconstruction in jawbone atrophy: a systematic

review and case report'. *Maxillofacial Plastic and Reconstructive Surgery*. Springer Science and Business Media LLC, 38 (1), pp. 1–9. doi: 10.1186/s40902-015-0048-7.

García-Gareta, E., Coathup, M. J. and Blunn, G. W. (2015). 'Osteoinduction of bone grafting materials for bone repair and regeneration'. *Bone*. Elsevier Inc., pp. 112–121. doi: 10.1016/j.bone.2015.07.007.

Garzón-Alvarado, D. A., González, A. and Gutiérrez, M. L. (2013). 'Growth of the flat bones of the membranous neurocranium: A computational model'. *Computer Methods and Programs in Biomedicine*. Elsevier, 112 (3), pp. 655–664. doi: 10.1016/j.cmpb.2013.07.027.

Gauvin, R., Chen, Y., Lee, J., Soman, P., Zorlutuna, P., Nichol, J., Bae, H., Chen, S. and Khademhosseini, A. (2012). 'Microfabrication of complex porous tissue engineering scaffolds using 3D projection stereolithography'. *Biomaterials*. Biomaterials, 33 (15), pp. 3824–3834. doi: 10.1016/J.BIOMATERIALS.2012.01.048.

Gentile, P., Chiono, V., Carmagnola, I. and Hatton, P. V. (2014). 'An overview of poly(lactic-co-glycolic) Acid (PLGA)-based biomaterials for bone tissue engineering'. *International Journal of Molecular Sciences*. Molecular Diversity Preservation International, pp. 3640–3659. doi: 10.3390/ijms15033640.

Gerhardt, L. C. and Boccaccini, A. R. (2010). 'Bioactive glass and glass-ceramic scaffolds for bone tissue engineering'. *Materials*, 3 (7), pp. 3867–3910. doi: 10.3390/ma3073867.

Ghaffar, S. H., Corker, J. and Fan, M. (2018). 'Additive manufacturing technology and its implementation in construction as an eco-innovative solution'. *Automation in Construction*. Elsevier, 93, pp. 1–11. doi: 10.1016/J.AUTCON.2018.05.005.

Ghassemi, T., Shahroodi, A., Ebrahimzadeh, M. H., Mousavian, A., Movaffagh, J. and Moradi, A. (2018). 'Current Concepts in Scaffolding for Bone Tissue Engineering'. *Archives of Bone and Joint Surgery*. Mashhad University of Medical Sciences, 6 (2), p. 90. Available at: /pmc/articles/PMC5867363/ (Accessed: 9 August 2021).

Giannoudis, P. V., Dinopoulos, H. and Tsiridis, E. (2005). 'Bone substitutes: an update.' *Injury*. Injury. doi: 10.1016/j.injury.2005.07.029.

Gilardino, M. S., Chen, E. and Bartlett, S. P. (2009). 'Choice of internal rigid fixation materials in the treatment of facial fractures.' *Craniofacial trauma & reconstruction*. Thieme Medical Publishers, 2 (1), pp. 49–60. doi: 10.1055/s-0029-1202591.

Gir, P., Oni, G., Brown, S. A., Mojallal, A. and Rohrich, R. J. (2012). 'Human adipose stem cells: Current clinical applications'. *Plastic and Reconstructive Surgery*, 129 (6), pp. 1277–1290. doi: 10.1097/PRS.0B013E31824ECAE6.

Goldberg, V. M. and Akhavan, S. (2005). 'Biology of bone grafts'. in *Bone Regeneration and Repair: Biology and Clinical Applications*. Humana Press, pp. 57–65. doi: 10.1385/1-59259-863-3:057.

Gou, L., Yang, W., Qiao, X., Ye, L., Yan, K., Li, L. and Li, C. (2018). 'Marginal or segmental mandibulectomy: treatment modality selection for oral cancer: a systematic review and meta-analysis'. *International Journal of Oral and Maxillofacial Surgery*. Churchill Livingstone, pp. 1–10. doi: 10.1016/j.ijom.2017.07.019.

Gou, M., Qu, X., Zhu, W., Xiang, M., Yang, J., Zhang, K., Wei, Y. and Chen, S. (2014). 'Bio-inspired detoxification using 3D-printed hydrogel nanocomposites'.

*Nature Communications*. Nature Publishing Group, 5. doi: 10.1038/NCOMMS4774.

Gougoutas, A. J., Bastidas, N., Bartlett, S. P. and Jackson, O. (2015). 'The use of computer-aided design/manufacturing (CAD/CAM) technology to aid in the reconstruction of congenitally deficient pediatric mandibles: A case series'. *International Journal of Pediatric Otorhinolaryngology*. Elsevier Ireland Ltd, 79 (12), pp. 2332–2342. doi: 10.1016/j.ijporl.2015.10.038.

Grémare, A., Guduric, V., Bareille, R., Heroguez, V., Latour, S., L'heureux, N., Fricain, J.-C., Catros, S. and Le Nihouannen, D. (2018). 'Characterization of printed PLA scaffolds for bone tissue engineering'. *Journal of Biomedical Materials Research Part A*. John Wiley and Sons Inc., 106 (4), pp. 887–894. doi: 10.1002/jbm.a.36289.

Gross, T. P., Jinnah, R. H., Clarke, H. J. and Cox, Q. G. N. (1991). 'The biology of bone grafting'. *Orthopedics*, pp. 563–568. doi: 10.3928/0147-7447-19910501-11.

Gu, Q., Hao, J., Lu, Y. J., Wang, L., Wallace, G. G. and Zhou, Q. (2015). 'Three-dimensional bio-printing'. *Science China Life Sciences*. Science in China Press, 58 (5), pp. 411–419. doi: 10.1007/s11427-015-4850-3.

Habraken, W., Habibovic, P., Epple, M. and Böhner, M. (2016). 'Calcium phosphates in biomedical applications: materials for the future?' *Materials Today*. Elsevier, 19 (2), pp. 69–87. doi: 10.1016/J.MATTOD.2015.10.008.

Hadjidakis, D. J. and Androulakis, I. I. (2006). 'Bone remodeling'. in *Annals of the New York Academy of Sciences*. Blackwell Publishing Inc., pp. 385–396. doi: 10.1196/annals.1365.035.

Hamid, A. A., Idrus, R. B. H., Saim, A. Bin, Sathappan, S. and Chua, K.-H. (2012). 'Characterization of human adipose-derived stem cells and expression of chondrogenic genes during induction of cartilage differentiation'. *Clinics. Hospital das Clinicas da Faculdade de Medicina da Universidade de Sao Paulo*, 67 (2), p. 99. doi: 10.6061/CLINICS/2012(02)03.

Han, S.-B., Kim, J.-K., Lee, G. and Kim, D.-H. (2020). 'Mechanical Properties of Materials for Stem Cell Differentiation'. *Advanced Biosystems*. John Wiley & Sons, Ltd, 4 (11), p. 2000247. doi: 10.1002/ADBI.202000247.

Han, X., Yang, D., Yang, C., Spintzyk, S., Scheideler, L., Li, P., Li, D., Geis-Gerstorfer, J. and Rupp, F. (2019). 'Carbon Fiber Reinforced PEEK Composites Based on 3D-Printing Technology for Orthopedic and Dental Applications'. *Journal of Clinical Medicine*, 8 (2), p. 240. doi: 10.3390/jcm8020240.

Harrell, C. R., Djonov, V., Fellabaum, C. and Volarevic, V. (2018). 'Risks of using sterilization by gamma radiation: The other side of the coin'. *International Journal of Medical Sciences*, 15 (3), pp. 274–279. doi: 10.7150/ijms.22644.

Hart, N. H., Nimphius, S., Rantalainen, T., Ireland, A., Siafarikas, A. and Newton, R. U. (2017). 'Mechanical basis of bone strength: influence of bone material, bone structure and muscle action'. *Journal of Musculoskeletal & Neuronal Interactions*. International Society of Musculoskeletal and Neuronal Interactions (ISMNI), 17 (3), p. 114. Available at: /pmc/articles/PMC5601257/ (Accessed: 9 August 2021).

Hench, L. L. (2006). 'The story of Bioglass®'. in *Journal of Materials Science: Materials in Medicine*. J Mater Sci Mater Med, pp. 967–978. doi: 10.1007/s10856-006-0432-z.



Hench, L. L. and Wilson, J. (1993). *An Introduction to Bioceramics. An Introduction to Bioceramics*. WORLD SCIENTIFIC. doi: 10.1142/2028.

Hong, H., Seo, Y., Kim, D., LEE, J., Lee, Y., Lee, H., Ajiteru, O., Sultan, M., Lee, O., Kim, S. and Park, C. (2020). 'Digital light processing 3D printed silk fibroin hydrogel for cartilage tissue engineering'. *Biomaterials*. Biomaterials, 232. doi: 10.1016/J.BIOMATERIALS.2019.119679.

Huang, H., Jiang, C., Feng, Z. Z. and Jiang, X. (2014). 'Comparing the process of creeping substitution between allograft bone and local bone grafting in lumbar interbody fusion'. *European Spine Journal*. Springer Verlag, 23 (10), pp. 2068–2074. doi: 10.1007/s00586-014-3388-6.

Huang, J., Qin, Q. and Wang, J. (2020). 'A Review of Stereolithography: Processes and Systems'. *Processes 2020, Vol. 8, Page 1138*. Multidisciplinary Digital Publishing Institute, 8 (9), p. 1138. doi: 10.3390/PR8091138.

Hughes, E. A., Parkes, A., Williams, R. L., Jenkins, M. J. and Grover, L. M. (2018). 'Formulation of a covalently bonded hydroxyapatite and poly(ether ether ketone) composite': <https://doi.org/10.1177/2041731418815570>. SAGE Publications Sage UK: London, England, 9. doi: 10.1177/2041731418815570.

Hull, C. W. and Arcadia, C. (1984). 'Apparatus for production of three-dimensional objects by stereolithography'.

Hunter, G. K. and Goldberg, H. A. (1994). 'Modulation of crystal formation by bone phosphoproteins: Role of glutamic acid-rich sequences in the nucleation of hydroxyapatite by bone sialoprotein'. *Biochemical Journal*. Portland Press Ltd, 302 (1), pp. 175–179. doi: 10.1042/bj3020175.

Hutchison, I. L., Ridout, F., Cheung, S. M. Y., Shah, N., Hardee, P., Surwald, C., Thiruchelvam, J., Cheng, L., Mellor, T. K., Brennan, P. A., Baldwin, A. J., Shaw, R. J., Halfpenny, W., Danford, M., Whitley, S., Smith, G., Bailey, M. W., Woodward, B., Patel, M., McManners, J., Chan, C.-H., Burns, A., Praveen, P., Camilleri, A. C., Avery, C., Putnam, G., Jones, K., Webster, K., Smith, W. P., Edge, C., Mcvicar, I., Grew, N., Hislop, S., Kalavrezos, N., Martin, I. C. and Hackshaw, A. (2019).

‘ARTICLE Nationwide randomised trial evaluating elective neck dissection for early stage oral cancer (SEND study) with meta-analysis and concurrent real-world cohort’. *British Journal of Cancer*, p. 121. doi: 10.1038/s41416-019-0587-2.

Ikegame, M., Ejiri, S. and Okamura, H. (2019). ‘Expression of Non-collagenous Bone Matrix Proteins in Osteoblasts Stimulated by Mechanical Stretching in the Cranial Suture of Neonatal Mice’. *Journal of Histochemistry and Cytochemistry*. Histochemical Society, 67 (2), p. 107. doi: 10.1369/0022155418793588.

Inoue, S., Otsuka, H., Takito, J. and Nakamura, M. (2018). ‘Decisive differences in the bone repair processes of the metaphysis and diaphysis in young mice’. *Bone Reports*. Elsevier Inc, 8, pp. 1–8. doi: 10.1016/j.bonr.2017.11.003.

Jaiswal, N., Haynesworth, S. E., Caplan, A. I. and Bruder, S. P. (1997). ‘Osteogenic Differentiation of Purified, Culture-Expanded Human Mesenchymal Stem Cells In Vitro’. *Journal of Cellular Biochemistry*, 64 (2), pp. 295–312. doi: 10.1002/(SICI)1097-4644(199702)64:2.

Jayaswal, Gaurav P, Dange, S. P., Khalikar, A. N., Jayaswal, G P, Dange, • S P and Khalikar, • A N. (2010). ‘Bioceramic in Dental Implants: A Review’. *Journal of Indian Prosthodontic Society*, 10, pp. 8–12. doi: 10.1007/s13191-010-0002-4.

Jayesh, R. S. and Dhinakarsamy, V. (2015). 'Osseointegration'. *Journal of Pharmacy and Bioallied Sciences*. Medknow Publications, pp. S226–S229. doi: 10.4103/0975-7406.155917.

Jeong, J., Kim, J. H., Shim, J. H., Hwang, N. S. and Heo, C. Y. (2019). 'Bioactive calcium phosphate materials and applications in bone regeneration'. *Biomaterials Research*. BioMed Central Ltd., pp. 1–11. doi: 10.1186/s40824-018-0149-3.

Jiang, H. J., Xu, J., Qiu, Z. Y., Ma, X. L., Zhang, Z. Q., Tan, X. X., Cui, Y. and Cui, F. Z. (2015). 'Mechanical properties and cytocompatibility improvement of vertebroplasty PMMA bone cements by incorporating mineralized collagen'. *Materials*, 8 (5), pp. 2616–2634. doi: 10.3390/ma8052616.

Jindal, S., Manzoor, F., Haslam, N. and Mancuso, E. (2021). '3D printed composite materials for craniofacial implants: current concepts, challenges and future directions'. *International Journal of Advanced Manufacturing Technology*. Springer Science and Business Media Deutschland GmbH, pp. 635–653. doi: 10.1007/s00170-020-06397-1.

Jinhui Huang, Xue Xia, Qin Zou, Jingqi Ma, Shue Jin, Jidong Li, Yi Zuo and Yubao Li. (2019). 'The long-term behaviors and differences in bone reconstruction of three polymer-based scaffolds with different degradability'. *Journal of Materials Chemistry B*. Royal Society of Chemistry, 7 (48), pp. 7690–7703. doi: 10.1039/C9TB02072A.

Johansson, P., Jimbo, R., Naito, Y., Kjellin, P., Currie, F. and Wennerberg, A. (2016). 'Polyether ether ketone implants achieve increased bone fusion when coated with nano-sized hydroxyapatite: A histomorphometric study in rabbit bone'.

- International Journal of Nanomedicine*. Dove Medical Press Ltd., 11, pp. 1435–1442.  
doi: 10.2147/IJN.S100424.
- Jones, J. R. (2013). 'Review of bioactive glass: From Hench to hybrids'. *Acta Biomaterialia*. Elsevier, pp. 4457–4486. doi: 10.1016/j.actbio.2012.08.023.
- Jose, A., Nagori, S. A., Agarwal, B., Bhutia, O. and Roychoudhury, A. (2016). 'Management of maxillofacial trauma in emergency: An update of challenges and controversies'. *Journal of Emergencies, Trauma, and Shock*. Wolters Kluwer -- Medknow Publications, 9 (2), p. 73. doi: 10.4103/0974-2700.179456.
- Kabb, C., O'Bryan, C., Deng, C., Angelini, T. and Sumerlin, B. (2018). 'Photoreversible Covalent Hydrogels for Soft-Matter Additive Manufacturing'. *ACS applied materials & interfaces*. ACS Appl Mater Interfaces, 10 (19), pp. 16793–16801. doi: 10.1021/ACSAMI.8B02441.
- Kamoun, E. A., Winkel, A., Eisenburger, M. and Menzel, H. (2016). 'Carboxylated camphorquinone as visible-light photoinitiator for biomedical application: Synthesis, characterization, and application'. *Arabian Journal of Chemistry*. Elsevier, 9 (5), pp. 745–754. doi: 10.1016/J.ARABJC.2014.03.008.
- Kaneto, C. M., Lima, P. S. P., Zanette, D. L., Oliveira, T. Y. K., de Assis Pereira, F., Lorenzi, J. C. C., dos Santos, J. L., Prata, K. L., Neto, J. M. P., de Paula, F. J. A. and Silva, W. A. (2016). 'Osteoblastic differentiation of bone marrow mesenchymal stromal cells in Bruck Syndrome'. *BMC Medical Genetics* 2016 17:1. BioMed Central, 17 (1), pp. 1–9. doi: 10.1186/S12881-016-0301-7.
- Kangwankai, K., Sani, S., Panpisut, P., Xia, W., Ashley, P., Petridis, H. and Young, A. M. (2017). 'Monomer conversion, dimensional stability, strength, modulus, surface

apatite precipitation and wear of novel, reactive calcium phosphate and polylysine-containing dental composites'. *PLoS ONE*. Public Library of Science, 12 (11). doi: 10.1371/journal.pone.0187757.

Kannan, S., Ghosh, J. and Dhara, S. K. (2020). 'Osteogenic differentiation potential and marker gene expression of different porcine bone marrow mesenchymal stem cell subpopulations selected in different basal media'. *bioRxiv*. Cold Spring Harbor Laboratory, p. 2020.04.27.063230. doi: 10.1101/2020.04.27.063230.

Karageorgiou, V. and Kaplan, D. (2005). 'Porosity of 3D biomaterial scaffolds and osteogenesis'. *Biomaterials*. Biomaterials, 26 (27), pp. 5474–5491. doi: 10.1016/J.BIOMATERIALS.2005.02.002.

Karaplis, A. C. (2002). 'Embryonic Development of Bone and the Molecular Regulation of Intramembranous and Endochondral Bone Formation'. in *Principles of Bone Biology*. Elsevier, pp. 33–IV. doi: 10.1016/b978-012098652-1.50105-0.

Kashani, H. and Rasmusson, L. (2016). 'Osteotomies in Orthognathic Surgery'. A *Textbook of Advanced Oral and Maxillofacial Surgery Volume 3*. IntechOpen. doi: 10.5772/63345.

Katayama, A., Arano, T., Sato, T., Ikada, Y. and Yoshinari, M. (2012). 'Radial-Flow Bioreactor Enables Uniform Proliferation of Human Mesenchymal Stem Cells Throughout a Three-Dimensional Scaffold'. <https://home.liebertpub.com/tec>. Mary Ann Liebert, Inc. 140 Huguenot Street, 3rd Floor New Rochelle, NY 10801 USA , 19 (2), pp. 109–116. doi: 10.1089/TEN.TEC.2011.0722.

Kattimani, V. S., Kondaka, S. and Lingamaneni, K. P. (2016). 'Hydroxyapatite—Past, Present, and Future in Bone Regeneration'. *Bone and Tissue Regeneration Insights*.

SAGE Publications, 7, p. BTRI.S36138. doi: 10.4137/btri.s36138.

Khan, S. N., Cammisa, F. P. J., Sandhu, H. S., Diwan, A. D., Dirardi, F. P. and Lane, J. M. (2005). *The Biology of Bone Grafting : JAAOS - Journal of the American Academy of Orthopaedic Surgeons. Journal of the American academy of orthopaedic surgeons*. Available at: [https://journals.lww.com/jaaos/Fulltext/2005/01000/The\\_Biology\\_of\\_Bone\\_Grafting.10.aspx](https://journals.lww.com/jaaos/Fulltext/2005/01000/The_Biology_of_Bone_Grafting.10.aspx). (Accessed: 27 October 2020).

Khosla, S., Oursler, M. J. and Monroe, D. G. (2012). 'Estrogen and the skeleton'. *Trends in Endocrinology and Metabolism*. Elsevier Current Trends, pp. 576–581. doi: 10.1016/j.tem.2012.03.008.

Kim, J.-N., Lee, J.-Y., Shin, K.-J., Gil, Y.-C., Koh, K.-S. and Song, W.-C. (2015). 'Haversian system of compact bone and comparison between endosteal and periosteal sides using three-dimensional reconstruction in rat'. *Anatomy & Cell Biology*. Korean Association of Anatomists, 48 (4), p. 258. doi: 10.5115/ACB.2015.48.4.258.

Kim, K. T., Eo, M. Y., Nguyen, T. T. H. and Kim, S. M. (2019). 'General review of titanium toxicity'. *International Journal of Implant Dentistry*. Springer Science and Business Media LLC, 5 (1). doi: 10.1186/s40729-019-0162-x.

Kim, L. U., Kim, J W, A. and Kim, C. K. (2006). 'Effects of Molecular Structure of the Resins on the Volumetric Shrinkage and the Mechanical Strength of Dental Restorative Composites'. *Biomacromolecules*. American Chemical Society, 7 (9), pp. 2680–2687. doi: 10.1021/BM060453H.

Kodama, H. (1981). 'Automatic method for fabricating a three-dimensional plastic

model with photo-hardening polymer'. *RSci*, 52 (11), pp. 1770–1773. doi:  
10.1063/1.1136492.

Kohli, N., Sawadkar, P., Ho, S., Sharma, V., Snow, M., Powell, S., Woodruff, M. A.,  
Hook, L. and García-Gareta, E. (2020). 'Pre-screening the intrinsic angiogenic  
capacity of biomaterials in an optimised ex ovo chorioallantoic membrane model'.  
*Journal of Tissue Engineering*. SAGE Publications, 11. doi:  
10.1177/2041731420901621.

Kohli, N., Sharma, V., Orera, A., Sawadkar, P., Owji, N., Frost, O. G., Bailey, R. J.,  
Snow, M., Knowles, J. C., Blunn, G. W. and García-Gareta, E. (2021). 'Pro-  
angiogenic and osteogenic composite scaffolds of fibrin, alginate and calcium  
phosphate for bone tissue engineering':  
<https://doi.org/10.1177/20417314211005610>. SAGE Publications Sage UK: London,  
England, 12. doi: 10.1177/20417314211005610.

Komori, T. (2010). 'Regulation of osteoblast differentiation by Runx2'. *Advances in  
experimental medicine and biology*. Adv Exp Med Biol, 658, pp. 43–49. doi:  
10.1007/978-1-4419-1050-9\_5.

Koons, G. L., Diba, M. and Mikos, A. G. (2020). 'Materials design for bone-tissue  
engineering'. *Nature Reviews Materials*. Nature Research, pp. 584–603. doi:  
10.1038/s41578-020-0204-2.

Korpela, J., Kokkari, A., Korhonen, H., Malin, M., Närhi, T. and Seppälä, J. (2013).  
'Biodegradable and bioactive porous scaffold structures prepared using fused  
deposition modeling'. *Journal of biomedical materials research. Part B, Applied  
biomaterials*. J Biomed Mater Res B Appl Biomater, 101 (4), pp. 610–619. doi:

10.1002/JBM.B.32863.

Kowalska, A., Sokolowski, J. and Bociong, K. (2021). 'The Photoinitiators Used in Resin Based Dental Composite-A Review and Future Perspectives'. *Polymers*. *Polymers (Basel)*, 13 (3), pp. 1–17. doi: 10.3390/POLYM13030470.

Kram, V. and Young, M. F. (2013). 'Bone Matrix Proteoglycans in Skeletal Function'. in *Osteogenesis Imperfecta: A Translational Approach to Brittle Bone Disease*. Elsevier Inc., pp. 85–95. doi: 10.1016/B978-0-12-397165-4.00008-3.

Kruger, T. E., Miller, A. H., Godwin, A. K. and Wang, J. (2014). 'Bone Sialoprotein and Osteopontin in Bone Metastasis of Osteotropic Cancers'. *Critical reviews in oncology/hematology*. NIH Public Access, 89 (2), p. 330. doi: 10.1016/J.CRITREVONC.2013.08.013.

Ku, K.-L., Wu, Y.-S., Wang, C.-Y., Hong, D.-W., Chen, Z.-X., Huang, C.-A., Chu, I.-M. and Lai, P.-L. (2019). 'Incorporation of surface-modified hydroxyapatite into poly(methyl methacrylate) to improve biological activity and bone ingrowth'. *Royal Society Open Science*. The Royal Society, 6 (5). doi: 10.1098/RSOS.182060.

Kuang, J., Yan, X., Genders, A. J., Granata, C. and Bishop, D. J. (2018). 'An overview of technical considerations when using quantitative real-time PCR analysis of gene expression in human exercise research'. *PLoS ONE*. Public Library of Science, 13 (5). doi: 10.1371/JOURNAL.PONE.0196438.

Kumar, B. P., Venkatesh, V., Kumar, K. A. J., Yadav, B. Y. and Mohan, S. R. (2016). 'Mandibular Reconstruction: Overview'. *Journal of Maxillofacial and Oral Surgery*. Springer, pp. 425–441. doi: 10.1007/s12663-015-0766-5.



- Kumar, P., Dehiya, B. S. and Sindhu, A. (2018). *Bioceramics for Hard Tissue Engineering Applications: A Review. International Journal of Applied Engineering Research*. Available at: <http://www.ripublication.com> (Accessed: 25 January 2021).
- Kumar, P., Vinitha, B. and Fathima, G. (2013). 'Bone grafts in dentistry'. *Journal of Pharmacy & Bioallied Sciences*. Wolters Kluwer -- Medknow Publications, 5 (Suppl 1), p. S125. doi: 10.4103/0975-7406.113312.
- Kunze, K. N., Burnett, R. A., Wright-Chisem, J., Frank, R. M. and Chahla, J. (2020). 'Adipose-Derived Mesenchymal Stem Cell Treatments and Available Formulations'. *Current Reviews in Musculoskeletal Medicine*. Springer, 13 (3), p. 264. doi: 10.1007/S12178-020-09624-0.
- Kurtz, S. M., Kocagöz, S., Arnholt, C., Huet, R., Ueno, M. and Walter, W. L. (2014). 'Advances in zirconia toughened alumina biomaterials for total joint replacement'. *Journal of the Mechanical Behavior of Biomedical Materials*. Elsevier, 31, pp. 107–116. doi: 10.1016/j.jmbbm.2013.03.022.
- Lalevée, J., Dumur, F., Mayer, C. R., Gignes, D., Nasr, G., Tehfe, M.-A., Telitel, S., Morlet-Savary, F., Graff, B. and Fouassier, J. P. (2012). 'Photopolymerization of N-Vinylcarbazole Using Visible-Light Harvesting Iridium Complexes as Photoinitiators'. *Macromolecules*. American Chemical Society, 45 (10), pp. 4134–4141. doi: 10.1021/MA3005229.
- Lamort, A. S., Giopanou, I., Psallidas, I. and Stathopoulos, G. T. (2019). 'Osteopontin as a Link between Inflammation and Cancer: The Thorax in the Spotlight'. *Cells*. NLM (Medline). doi: 10.3390/cells8080815.
- Langdahl, B., Ferrari, S. and Dempster, D. W. (2016). 'Bone modeling and

remodeling: potential as therapeutic targets for the treatment of osteoporosis'.  
*Therapeutic Advances in Musculoskeletal Disease*. SAGE Publications, 8 (6), p. 225.  
doi: 10.1177/1759720X16670154.

Laub, D. R. (2015). 'Globalization of Craniofacial Plastic Surgery: Foreign Mission Programs for Cleft Lip and Palate'. *The Journal of Craniofacial Surgery*. Wolters Kluwer Health, 26 (4), p. 1015. doi: 10.1097/SCS.0000000000001690.

Lebeau, J., Efromson, J. P. and Lynch, M. D. (2020). 'A Review of the Biotechnological Production of Methacrylic Acid'. *Frontiers in Bioengineering and Biotechnology*. Frontiers Media SA, 8, p. 207. doi: 10.3389/FBIOE.2020.00207.

Lee, J. H., Parthiban, P., Jin, G. Z., Knowles, J. C. and Kim, H. W. (2021). 'Materials roles for promoting angiogenesis in tissue regeneration'. *Progress in Materials Science*. Pergamon, 117, p. 100732. doi: 10.1016/J.PMATSCI.2020.100732.

Lee, J., Hong, J., Jung, J., Shim, J., JH, O. and Cho, D. (2014). '3D printing of composite tissue with complex shape applied to ear regeneration'. *Biofabrication*. Biofabrication, 6 (2). doi: 10.1088/1758-5082/6/2/024103.

Lee, N. K., Sowa, H., Hinoi, E., Ferron, M., Ahn, J. D., Confavreux, C., Dacquin, R., Mee, P. J., McKee, M. D., Jung, D. Y., Zhang, Z., Kim, J. K., Mauvais-Jarvis, F., Ducy, P. and Karsenty, G. (2007). 'Endocrine Regulation of Energy Metabolism by the Skeleton'. *Cell*. NIH Public Access, 130 (3), pp. 456–469. doi: 10.1016/j.cell.2007.05.047.

Lello, S., Allen, P. and Haig, S. (2015). 'Aetiology of paediatric facial trauma at a UK District General Hospital'. *Oral Surgery*. Blackwell Publishing Ltd, 8 (4), pp. 208–216. doi: 10.1111/ors.12143.

Lethaus, B., Safi, Y., Ter Laak-Poort, M., Kloss-Brandstätter, A., Banki, F., Robbenmenke, C., Steinseifer, U. and Kessler, P. (2012). 'Cranioplasty with customized titanium and PEEK implants in a mechanical stress model'. *Journal of Neurotrauma*. Mary Ann Liebert, Inc. 140 Huguenot Street, 3rd Floor New Rochelle, NY 10801 USA , 29 (6), pp. 1077–1083. doi: 10.1089/neu.2011.1794.

Leventhal, G. S. (1951). 'Titanium, a metal for surgery.' *The Journal of bone and joint surgery. American volume*. doi: 10.2106/00004623-195133020-00021.

Lewis, L., Agalloco, J., Lambert, B., Madsen, R., Staples, M., Lambert, B. J., Mendelson, T. A. and Craven, M. D. (2011). 'Radiation and Ethylene Oxide Terminal Sterilization Experiences with Drug Eluting Stent Products'. *AAPS PharmSciTech*, 12 (4). doi: 10.1208/s12249-011-9644-8.

Ligon, S. C., Liska, R., Stampfl, J., Gurr, M. and Mülhaupt, R. (2017). 'Polymers for 3D Printing and Customized Additive Manufacturing'. *Chemical Reviews*. American Chemical Society, 117 (15), pp. 10212–10290. doi: 10.1021/acs.chemrev.7b00074.

Liska, R. (2002). 'Photoinitiators with functional groups. V. New water-soluble photoinitiators containing carbohydrate residues and copolymerizable derivatives thereof'. *Journal of Polymer Science Part A: Polymer Chemistry*. John Wiley & Sons, Ltd, 40 (10), pp. 1504–1518. doi: 10.1002/POLA.10232.

Little, C., Bawolin, N. and Chen, X. (2011). 'Mechanical properties of natural cartilage and tissue-engineered constructs'. *Tissue engineering. Part B, Reviews*. *Tissue Eng Part B Rev*, 17 (4), pp. 213–227. doi: 10.1089/TEN.TEB.2010.0572.

Liu, F. H., Lee, R. T., Lin, W. H. and Liao, Y. S. (2013). 'Selective laser sintering of bio-metal scaffold'. *Procedia CIRP*. Elsevier B.V., 5, pp. 83–87. doi:

10.1016/J.PROCIR.2013.01.017.

Liu, J. and Yan, C. (2018). '3D Printing of Scaffolds for Tissue Engineering'. *3D Printing*. IntechOpen. doi: 10.5772/INTECHOPEN.78145.

Liu, S., Qin, S., He, M., Zhou, D., Qin, Q. and Wang, H. (2020). 'Current applications of poly(lactic acid) composites in tissue engineering and drug delivery'. *Composites Part B: Engineering*. Elsevier Ltd, p. 108238. doi: 10.1016/j.compositesb.2020.108238.

Livak, K. and Schmittgen, T. (2001). 'Analysis of relative gene expression data using real-time quantitative PCR and the 2(-Delta Delta C(T)) Method'. *Methods (San Diego, Calif.)*. Methods, 25 (4), pp. 402–408. doi: 10.1006/METH.2001.1262.

Long, F. and Ornitz, D. M. (2013). 'Development of the endochondral skeleton'. *Cold Spring Harbor Perspectives in Biology*. Cold Spring Harbor Laboratory Press. doi: 10.1101/cshperspect.a008334.

Lu, J. X., Huang, Z. W., Tropiano, P., Clouet d'Orval, B., Remusat, M., Dejou, J., Proust, J. P. and Poitout, D. (2002). 'Human biological reactions at the interface between bone tissue and polymethylmethacrylate cement'. *Journal of Materials Science: Materials in Medicine*. Springer, 13 (8), pp. 803–809. doi: 10.1023/A:1016135410934.

Luca, A. Di, Ostrowska, B., Lorenzo-Moldero, I., Lepedda, A., Swieszkowski, W., Blitterswijk, C. Van and Moroni, L. (2016). 'Gradients in pore size enhance the osteogenic differentiation of human mesenchymal stromal cells in three-dimensional scaffolds'. *Scientific Reports*. Nature Publishing Group, 6. doi: 10.1038/SREP22898.

Di Lullo, G. A., Sweeney, S. M., Körkkö, J., Ala-Kokko, L. and San Antonio, J. D. (2002). 'Mapping the ligand-binding sites and disease-associated mutations on the most abundant protein in the human, type I collagen'. *Journal of Biological Chemistry*. American Society for Biochemistry and Molecular Biology, 277 (6), pp. 4223–4231. doi: 10.1074/jbc.M110709200.

Lv, Y., Wang, B., Liu, G., Tang, Y., Lu, E., Xie, K., Lan, C., Liu, J., Qin, Z. and Wang, L. (2021). 'Metal Material, Properties and Design Methods of Porous Biomedical Scaffolds for Additive Manufacturing: A Review'. *Frontiers in Bioengineering and Biotechnology*. Frontiers, 0, p. 194. doi: 10.3389/FBIOE.2021.641130.

Ma, H., Feng, C., Chang, J. and Wu, C. (2018). '3D-printed bioceramic scaffolds: From bone tissue engineering to tumor therapy'. *Acta Biomaterialia*. Acta Materialia Inc, pp. 37–59. doi: 10.1016/j.actbio.2018.08.026.

Ma, R. and Guo, D. (2019). 'Evaluating the bioactivity of a hydroxyapatite-incorporated polyetheretherketone biocomposite'. *Journal of Orthopaedic Surgery and Research 2019 14:1*. BioMed Central, 14 (1), pp. 1–13. doi: 10.1186/S13018-019-1069-1.

Mabrouk, M., Beherei, H. H. and Das, D. B. (2020). 'Recent progress in the fabrication techniques of 3D scaffolds for tissue engineering'. *Materials Science and Engineering: C*. Elsevier, 110, p. 110716. doi: 10.1016/J.MSEC.2020.110716.

Maher, S., Kolieb, E., Sabik, N. A., Abd-Elhalim, D., El-Serafi, A. T. and El-Wazir, Y. (2015). 'Comparison of the osteogenic differentiation potential of mesenchymal cells isolated from human bone marrow, umbilical cord blood and placenta derived stem cells'. *Beni-Suef University Journal of Basic and Applied Sciences*. Springer Science

and Business Media LLC, 4 (1), pp. 80–85. doi: 10.1016/j.bjbas.2015.02.011.

Mahmood, M. A. and Popescu, A. C. (2021). '3D printing at micro-level: Laser-induced forward transfer and two-photon polymerization'. *Polymers*, 13 (13), pp. 1–27. doi: 10.3390/polym13132034.

Mardas, N., Chadha, V. and Donos, N. (2010). 'Alveolar ridge preservation with guided bone regeneration and a synthetic bone substitute or a bovine-derived xenograft: a randomized, controlled clinical trial'. *Clinical Oral Implants Research*, 21 (7), pp. 688–698. doi: 10.1111/j.1600-0501.2010.01918.x.

Markstedt, K., Mantas, A., Tournier, I., Martínez Ávila, H., Hägg, D. and Gatenholm, P. (2015). '3D Bioprinting Human Chondrocytes with Nanocellulose-Alginate Bioink for Cartilage Tissue Engineering Applications'. *Biomacromolecules*. *Biomacromolecules*, 16 (5), pp. 1489–1496. doi: 10.1021/ACS.BIOMAC.5B00188.

Marshall, K. M., Kanczler, J. M. and Oreffo, R. O. (2020). 'Evolving applications of the egg: chorioallantoic membrane assay and ex vivo organotypic culture of materials for bone tissue engineering': <https://doi.org/10.1177/2041731420942734>. SAGE Publications Sage UK: London, England, 11. doi: 10.1177/2041731420942734.

Matassi, F., Nistri, L., Chicon Paez, D. and Innocenti, M. (2011). 'New biomaterials for bone regeneration.' *Clinical cases in mineral and bone metabolism: the official journal of the Italian Society of Osteoporosis, Mineral Metabolism, and Skeletal Diseases*. CIC Edizioni Internazionali, 8 (1), pp. 21–4. Available at: <http://www.ncbi.nlm.nih.gov/pubmed/22461799> (Accessed: 27 June 2019).

Matveeva, L., Efremova, M. and Baranets, I. (2018). 'STUDIES OF THE

MORPHOLOGY OF WATERPROOF COATINGS BASED ON URETHANE ISOCYANATE, ALKYL-PHENOL-FORMALDEHYDE RESIN AND DIBUTYLTIN DILAURATE USING THE HIGH-RESOLUTION OPTICAL MICROSCOPY TECHNIQUE'. *Architecture and Engineering*. Saint Petersburg State University of Architecture and Civil Engineering (SPSUACE), 3 (2), pp. 43–47. doi: 10.23968/2500-0055-2018-3-2-43-47.

McNerny, E. M. B., Gong, B., Morris, M. D. and Kohn, D. H. (2015). 'Bone fracture toughness and strength correlate with collagen cross-link maturity in a dose-controlled lathyrisms mouse model'. *Journal of Bone and Mineral Research*. John Wiley and Sons Inc., 30 (3), pp. 446–455. doi: 10.1002/jbmr.2356.

Meereis, C. T. W., Leal, F. B., Lima, G. S., De Carvalho, R. V., Piva, E. and Ogliari, F. A. (2014). 'BAPO as an alternative photoinitiator for the radical polymerization of dental resins'. *Dental Materials*. Elsevier Inc., 30 (9), pp. 945–953. doi: 10.1016/j.dental.2014.05.020.

Mehdawi, I. M. and Young, A. (2015). 'Antibacterial composite restorative materials for dental applications'. in *Biomaterials and Medical Device - Associated Infections*. Elsevier Inc., pp. 199–221. doi: 10.1533/9780857097224.2.199.

Mehdizadeh, H., Bayrak, E. S., Lu, C., Somo, S. I., Akar, B., Brey, E. M. and Cinar, A. (2015). 'Agent-based modeling of porous scaffold degradation and vascularization: Optimal scaffold design based on architecture and degradation dynamics'. *Acta Biomaterialia*. Elsevier, 27, pp. 167–178. doi: 10.1016/J.ACTBIO.2015.09.011.

Mencio, G. A. and Swiontkowski, M. F. (2014). *Green's Skeletal Trauma in Children:*

*Fifth Edition. Green's Skeletal Trauma in Children: Fifth Edition.* Elsevier Inc. doi:  
10.1016/C2011-0-05030-5.

Merckx, G., Tay, H., Monaco, M. Lo, Zandvoort, M. van, Spiegelaeere, W. De,  
Lambrichts, I. and Bronckaers, A. (2020). 'Chorioallantoic Membrane Assay as  
Model for Angiogenesis in Tissue Engineering: Focus on Stem Cells'.  
<https://home.liebertpub.com/teb>. Mary Ann Liebert, Inc., publishers 140 Huguenot  
Street, 3rd Floor New Rochelle, NY 10801 USA , 26 (6), pp. 519–539. doi:  
10.1089/TEN.TEB.2020.0048.

Meyer, H., Khalid, S. I., Dorafshar, A. H. and Byrne, R. W. (2020). 'The Materials  
Utilized in Cranial Reconstruction: Past, Current, and Future: A Review'. *Plastic  
Surgery*. SAGE Publications Ltd, p. 229255032092856. doi:  
10.1177/2292550320928560.

Middleton, J. C. and Tipton, A. J. (2000). 'Synthetic biodegradable polymers as  
orthopedic devices'. *Biomaterials*. Elsevier, 21 (23), pp. 2335–2346. doi:  
10.1016/S0142-9612(00)00101-0.

Mills, D., Tappa, K., Jammalamadaka, U., Weisman, J. and Woerner, J. (2017). 'The  
Use of 3D Printing in the Fabrication of Nasal Stents'. *Inventions 2018, Vol. 3, Page  
1*. Multidisciplinary Digital Publishing Institute, 3 (1), p. 1. doi:  
10.3390/INVENTIONS3010001.

Moad, G., Rizzardo, E. and Thang, S. H. (2008). 'Radical addition–fragmentation  
chemistry in polymer synthesis'. *Polymer*. Elsevier, 49 (5), pp. 1079–1131. doi:  
10.1016/J.POLYMER.2007.11.020.

Moldovan, M., Balazsi, R., Soanca, A., Roman, A., Sarosi, C., Prodan, D., Vlassa,



M., Cojocaru, I., Saceleanu, V. and Cristescu, I. (2019). 'Evaluation of the degree of conversion, residual monomers and mechanical properties of some light-cured dental resin composites'. *Materials*. MDPI AG, 12 (13). doi: 10.3390/ma12132109.

Mondschein, R., Kanitkar, A., Williams, C., Verbridge, S. and Long, T. (2017). 'Polymer structure-property requirements for stereolithographic 3D printing of soft tissue engineering scaffolds'. *Biomaterials*. Biomaterials, 140, pp. 170–188. doi: 10.1016/J.BIOMATERIALS.2017.06.005.

Morriss-Kay, G. (2016). 'The Craniofacial Region'. in *Kaufman's Atlas of Mouse Development Supplement*. Elsevier, pp. 207–218. doi: 10.1016/b978-0-12-800043-4.00016-6.

Moser, S. C. and van der Eerden, B. C. J. (2019). 'Osteocalcin — A versatile bone-derived hormone'. *Frontiers in Endocrinology*. Frontiers Media S.A. doi: 10.3389/fendo.2018.00794.

Mukhtarkhanov, M., Perveen, A. and Talamona, D. (2020). 'Application of stereolithography based 3D printing technology in investment casting'. *Micromachines*, 11 (10). doi: 10.3390/mi11100946.

Murariu, M. and Dubois, P. (2016). 'PLA composites: From production to properties'. *Advanced Drug Delivery Reviews*. Elsevier B.V., pp. 17–46. doi: 10.1016/j.addr.2016.04.003.

Musib, M., Jones, J., Chakote, K., Hayes, W. and Saha, S. (2012). 'Microhardness of bi-antibiotic-eluting bone cement scaffolds'. *Progress in Biomaterials*. Springer Nature, 1 (1), p. 3. doi: 10.1186/2194-0517-1-3.

Nair, L. S. and Laurencin, C. T. (2007). 'Biodegradable polymers as biomaterials'. *Progress in Polymer Science*. Pergamon, 32 (8–9), pp. 762–798. doi: 10.1016/J.PROGPOLYMSCI.2007.05.017.

Neumann, A. and Kevenhoerster, K. (2009). 'Biomaterials for craniofacial reconstruction.' *GMS current topics in otorhinolaryngology, head and neck surgery*. German Medical Science, 8, p. Doc08. doi: 10.3205/cto000060.

Neve, A., Corrado, A. and Cantatore, F. P. (2013). 'Osteocalcin: Skeletal and extra-skeletal effects'. *Journal of Cellular Physiology*. J Cell Physiol, 228 (6), pp. 1149–1153. doi: 10.1002/jcp.24278.

Nguyen, A. K., Goering, P. L., Elespuru, R. K., Das, S. S. and Narayan, R. J. (2020). 'The photoinitiator lithium phenyl (2,4,6-Trimethylbenzoyl) phosphinate with exposure to 405 nm light is cytotoxic to mammalian cells but not mutagenic in bacterial reverse mutation assays'. *Polymers*, 12 (7), pp. 1–13. doi: 10.3390/polym12071489.

Nguyen, P. D., Khechoyan, D. Y., Phillips, J. H. and Forrest, C. R. (2018). 'Custom CAD/CAM implants for complex craniofacial reconstruction in children: Our experience based on 136 cases ☆'. *Journal of Plastic, Reconstructive and Aesthetic Surgery*. Churchill Livingstone, 71 (11), pp. 1609–1617. doi: 10.1016/j.bjps.2018.07.016.

Ni, J., Ling, H., Zhang, S., Wang, Z., Peng, Z., Benyshek, C., Zan, R., Miri, A. K., Li, Z., Zhang, X., Lee, J., Lee, K. J., Kim, H. J., Tebon, P., Hoffman, T., Dokmeci, M. R., Ashammakhi, N., Li, X. and Khademhosseini, A. (2019). 'Three-dimensional printing of metals for biomedical applications'. *Materials Today Bio*. Elsevier, 3, p. 100024. doi: 10.1016/J.MTBIO.2019.100024.

Nikolova, M. P. and Chavali, M. S. (2019). 'Recent advances in biomaterials for 3D scaffolds: A review'. *Bioactive Materials*. KeAi Publishing, 4, p. 271. doi: 10.1016/J.BIOACTMAT.2019.10.005.

Nishimura, I., Hisanaga, R., Sato, T., Arano, T., Nomoto, S., Ikada, Y. and Yoshinari, M. (2015). 'Effect of osteogenic differentiation medium on proliferation and differentiation of human mesenchymal stem cells in three-dimensional culture with radial flow bioreactor'. *Regenerative Therapy*. Elsevier, 2, pp. 24–31. doi: 10.1016/J.RETH.2015.09.001.

Noori, A., Ashrafi, S., Vaez-Ghaemi, R., Hatamian-Zaremi, A. and Webster, T. (2017). 'A review of fibrin and fibrin composites for bone tissue engineering'. *International journal of nanomedicine*. Int J Nanomedicine, 12, pp. 4937–4961. doi: 10.2147/IJN.S124671.

Nowak-Sliwinska, P., Segura, T. and Iruela-Arispe, M. (2014). 'The chicken chorioallantoic membrane model in biology, medicine and bioengineering'. *Angiogenesis*. Angiogenesis, 17 (4), pp. 779–804. doi: 10.1007/S10456-014-9440-7.

Nyberg, E. L., Farris, A. L., Hung, B. P., Dias, M., Garcia, J. R., Dorafshar, A. H. and Grayson, W. L. (2017). '3D-Printing Technologies for Craniofacial Rehabilitation, Reconstruction, and Regeneration'. *Annals of Biomedical Engineering*. Springer New York LLC, 45 (1), pp. 45–57. doi: 10.1007/s10439-016-1668-5.

O'bryan, C. S., Bhattacharjee, T., Marshall, S. L., Sawyer, W. G. and Angelini, T. E. (2018). 'Commercially available microgels for 3D bioprinting'. doi: 10.1016/j.bprint.2018.e00037.

Ogata, Y. (2008). 'Bone sialoprotein and its transcriptional regulatory mechanism'.

*Journal of Periodontal Research*. John Wiley & Sons, Ltd, 43 (2), pp. 127–135. doi: 10.1111/j.1600-0765.2007.01014.x.

Ohgushi, H., Dohi, Y., Tamai, S. and Tabata, S. (1993). 'Osteogenic differentiation of marrow stromal stem cells in porous hydroxyapatite ceramics'. *Journal of Biomedical Materials Research*. J Biomed Mater Res, 27 (11), pp. 1401–1407. doi: 10.1002/jbm.820271107.

Ohtsuki, A., Goto, A. and Kaji, H. (2012). 'Visible-Light-Induced Reversible Complexation Mediated Living Radical Polymerization of Methacrylates with Organic Catalysts'. *Macromolecules*. American Chemical Society, 46 (1), pp. 96–102. doi: 10.1021/MA302244J.

Ortega, N., Behonick, D. J. and Werb, Z. (2004). 'Matrix remodeling during endochondral ossification'. *Trends in Cell Biology*. Elsevier Ltd, pp. 86–93. doi: 10.1016/j.tcb.2003.12.003.

Orti, V., Bousquet, P., Tramini, P., Gaitan, C., Mertens, B. and Cuisinier, F. (2016). 'Benefits of mineralized bone cortical allograft for immediate implant placement in extraction sites: An in vivo study in dogs'. *Journal of Periodontal and Implant Science*. Korean Academy of Periodontology, 46 (5), pp. 291–302. doi: 10.5051/jpis.2016.46.5.291.

Osorio, C. C., Escobar, L. M., González, M. C., Gamboa, L. F. and Chambrone, L. (2020). 'Evaluation of density, volume, height and rate of bone resorption of substitutes of autologous bone grafts for the repair of alveolar clefts in humans: A systematic review'. *Heliyon*. Elsevier Ltd, p. e04646. doi: 10.1016/j.heliyon.2020.e04646.

Owji, N., Aldaadaa, A., Cha, J.-R., Shakouri, T., García-Gareta, E., Kim, H.-W. and Knowles, J. C. (2019). 'Synthesis, Characterization, and 3D Printing of an Isosorbide-Based, Light-Curable, Degradable Polymer for Potential Application in Maxillofacial Reconstruction'. doi: 10.1021/acsbiomaterials.9b00884.

Özcan, M. and Hämmerle, C. (2012). 'Titanium as a reconstruction and implant material in dentistry: Advantages and pitfalls'. *Materials*. Multidisciplinary Digital Publishing Institute (MDPI), 5 (9), pp. 1528–1545. doi: 10.3390/ma5091528.

Pacifici, L., De Angelis, F., Orefici, A. and Cielo, A. (2016). 'Metals used in maxillofacial surgery'. *ORAL and Implantology*. CIC Edizioni Internazionali s.r.l., pp. 107–111. doi: 10.11138/orl/2016.9.1S.107.

Pacifici, L., DE Angelis, F., Orefici, A. and Cielo, A. (2016). 'Metals used in maxillofacial surgery.' *ORAL & implantology*. CIC Edizioni Internazionali, 9 (Suppl 1/2016 to N 4/2016), pp. 107–111. doi: 10.11138/orl/2016.9.1S.107.

Panina, Y., Germond, A., Masui, S. and Watanabe, T. M. (2018). 'Validation of Common Housekeeping Genes as Reference for qPCR Gene Expression Analysis During iPS Reprogramming Process'. *Scientific Reports 2018 8:1*. Nature Publishing Group, 8 (1), pp. 1–8. doi: 10.1038/s41598-018-26707-8.

Parithimarkalaignan, S. and Padmanabhan, T. V. (2013). 'Osseointegration: An update'. *Journal of Indian Prosthodontist Society*. Wolters Kluwer -- Medknow Publications, pp. 2–6. doi: 10.1007/s13191-013-0252-z.

Park, S., Bae, H. and Park, J. (2015). 'Osteogenic differentiation and gene expression profile of human dental follicle cells induced by human dental pulp cells'. *Journal of molecular histology*. *J Mol Histol*, 46 (1), pp. 93–106. doi:

10.1007/S10735-014-9604-1.

Paul, G. M., Rezaenia, A., Wen, P., Condoor, S., Parkar, N., King, W. and Korakianitis, T. (2018). 'Medical Applications for 3D Printing: Recent Developments.' *Missouri medicine*. Missouri State Medical Association, 115 (1), pp. 75–81. Available at: <http://www.ncbi.nlm.nih.gov/pubmed/30228688> (Accessed: 3 February 2021).

Persikov, A. V., Ramshaw, J. A. M. and Brodsky, B. (2005). 'Prediction of collagen stability from amino acid sequence'. *Journal of Biological Chemistry*. J Biol Chem, 280 (19), pp. 19343–19349. doi: 10.1074/jbc.M501657200.

Pina, S., Ribeiro, V. P., Marques, C. F., Maia, F. R., Silva, T. H., Reis, R. L. and Oliveira, J. M. (2019). 'Scaffolding strategies for tissue engineering and regenerative medicine applications'. *Materials*. MDPI AG. doi: 10.3390/ma12111824.

Polo-Corrales, L., Latorre-Esteves, M. and Ramirez-Vick, J. E. (2014). 'Scaffold design for bone regeneration'. *Journal of Nanoscience and Nanotechnology*. NIH Public Access, pp. 15–56. doi: 10.1166/jnn.2014.9127.

Poomathi, N., Singh, S., Prakash, C., Subramanian, A., Sahay, R., Cinappan, A. and Ramakrishna, S. (2020). '3D printing in tissue engineering: a state of the art review of technologies and biomaterials'. *Rapid Prototyping Journal*. Emerald Publishing Limited, 26 (7), pp. 1313–1334. doi: 10.1108/RPJ-08-2018-0217.

Prasadh, S. and Wong, R. C. W. (2018). 'Unraveling the mechanical strength of biomaterials used as a bone scaffold in oral and maxillofacial defects'. *Oral Science International*. No longer published by Elsevier, 15 (2), pp. 48–55. doi: 10.1016/S1348-8643(18)30005-3.

- Quan, H., Zhang, T., Xu, H., Luo, S., Nie, J. and Zhu, X. (2020). 'Photo-curing 3D printing technique and its challenges'. *Bioactive Materials*. KeAi Publishing, 5 (1), p. 110. doi: 10.1016/J.BIOACTMAT.2019.12.003.
- Raghavendra, P. and Pullaiah, T. (2018). 'Biomedical Imaging Role in Cellular and Molecular Diagnostics'. in *Advances in Cell and Molecular Diagnostics*. Elsevier, pp. 85–111. doi: 10.1016/b978-0-12-813679-9.00004-x.
- Rahaman, M. N., Day, D. E., Sonny Bal, B., Fu, Q., Jung, S. B., Bonewald, L. F. and Tomsia, A. P. (2011). 'Bioactive glass in tissue engineering'. *Acta Biomaterialia*. Elsevier, pp. 2355–2373. doi: 10.1016/j.actbio.2011.03.016.
- Rawlings, R. D. (1993). 'Bioactive glasses and glass-ceramics'. *Clinical Materials*. Elsevier, pp. 155–179. doi: 10.1016/0267-6605(93)90038-9.
- Rhee, S., Puetzer, J., Mason, B., Reinhart-King, C. and Bonassar, L. (2016). '3D Bioprinting of Spatially Heterogeneous Collagen Constructs for Cartilage Tissue Engineering'. *ACS biomaterials science & engineering*. ACS Biomater Sci Eng, 2 (10), pp. 1800–1805. doi: 10.1021/ACSBBIOMATERIALS.6B00288.
- Ricard-Blum, S. (2011). 'The Collagen Family'. *Cold Spring Harbor Perspectives in Biology*. Cold Spring Harbor Laboratory Press, 3 (1), pp. 1–19. doi: 10.1101/CSHPERSPECT.A004978.
- Roberts, T. T. and Rosenbaum, A. J. (2012). 'Bone grafts, bone substitutes and orthobiologics the bridge between basic science and clinical advancements in fracture healing'. *Organogenesis*. Taylor & Francis, 8 (4), pp. 114–124. doi: 10.4161/org.23306.

Rodella, L. F., Favero, G. and Labanca, M. (2011). 'Biomaterials in maxillofacial surgery: membranes and grafts.' *International journal of biomedical science : IJBS*. Master Publishing Group, 7 (2), pp. 81–8. Available at: <http://www.ncbi.nlm.nih.gov/pubmed/23675225> (Accessed: 13 May 2019).

Rodriguez, A. E. and Nowzari, H. (2019). 'The long-term risks and complications of bovine-derived xenografts: A case series'. *Journal of Indian Society of Periodontology*. Wolters Kluwer Medknow Publications, 23 (5), pp. 487–492. doi: 10.4103/jisp.jisp\_656\_18.

Rojbani, H., Nyan, M., Ohya, K. and Kasugai, S. (2011). 'Evaluation of the osteoconductivity of  $\alpha$ -tricalcium phosphate,  $\beta$ -tricalcium phosphate, and hydroxyapatite combined with or without simvastatin in rat calvarial defect'. *Journal of Biomedical Materials Research Part A*. John Wiley & Sons, Ltd, 98A (4), pp. 488–498. doi: 10.1002/jbm.a.33117.

Rosset, E. M. and Bradshaw, A. D. (2016). 'SPARC/osteonectin in mineralized tissue'. *Matrix Biology*. Elsevier B.V., pp. 78–87. doi: 10.1016/j.matbio.2016.02.001.

Rossi, M., Battafarano, G., Pepe, J., Minisola, S. and Del Fattore, A. (2019). 'The endocrine function of osteocalcin regulated by bone resorption: A lesson from reduced and increased bone mass diseases'. *International Journal of Molecular Sciences*. MDPI AG. doi: 10.3390/ijms20184502.

Rozila, I., Azari, P., Munirah, S., Safwani, W. K. Z. W., Gan, S. N., Azurah, A. G. N., Jahendran, J., Pinguang-Murphy, B. and Chua, K. H. (2016). 'Differential osteogenic potential of human adipose-derived stem cells co-cultured with human osteoblasts on polymeric microfiber scaffolds'. *Journal of Biomedical Materials Research Part A*.



John Wiley & Sons, Ltd, 104 (2), pp. 377–387. doi: 10.1002/JBM.A.35573.

Rutkovskiy, A., Stensløyken, K.-O. and Vaage, I. J. (2016). 'Osteoblast Differentiation at a Glance'. *Medical Science Monitor Basic Research*. International Scientific Information, Inc., 22, p. 95. doi: 10.12659/MSMBR.901142.

Ryabenkova, Y., Pinnock, A., Quadros, P., Goodchild, R., Möbus, G., Crawford, A., Hatton, P. and Miller, C. (2017). 'The relationship between particle morphology and rheological properties in injectable nano-hydroxyapatite bone graft substitutes'. *Materials science & engineering. C, Materials for biological applications*. Mater Sci Eng C Mater Biol Appl, 75, pp. 1083–1090. doi: 10.1016/J.MSEC.2017.02.170.

Saberianpour, S., Heidarzadeh, M., Geranmayeh, M. H., Hosseinkhani, H., Rahbarghazi, R. and Nouri, M. (2018). 'Tissue engineering strategies for the induction of angiogenesis using biomaterials'. *Journal of Biological Engineering*. BioMed Central, 12 (1). doi: 10.1186/S13036-018-0133-4.

Saini, M., Singh, Y., Arora, P., Arora, V. and Jain, K. (2015). 'Implant biomaterials: A comprehensive review.' *World journal of clinical cases*. Baishideng Publishing Group Inc, 3 (1), pp. 52–7. doi: 10.12998/wjcc.v3.i1.52.

Sandor, G. (2006). 'Elaine McClarence, Close to the Edge: Brånemark and the Development of Osseointegration, Quintessence Publishing Company, Chicago, Illinois (2006) 1-630-3223 ISBN: 1-85097-067-X Pages: 92 Illustrations: 83 Price: \$78.00 USD.' *Alpha Omegan*. doi: 10.1016/j.aodf.2006.10.008.

Sapru, B. L., Mohan, S. M. and Roy, S. K. (1999). 'IMPLANTS IN MAXILLOFACIAL SURGERY.' *Medical journal, Armed Forces India*. Elsevier, 55 (4), pp. 285–286. doi: 10.1016/S0377-1237(17)30348-9.

- Sartori, S., Silvestri, M., Forni, F., Cornaglia, A. I., Tesei, P. and Cattaneo, V. (2003). 'Ten-year follow-up in a maxillary sinus augmentation using anorganic bovine bone (Bio-Oss). A case report with histomorphometric evaluation'. *Clinical Oral Implants Research*. John Wiley & Sons, Ltd, 14 (3), pp. 369–372. doi: 10.1034/j.1600-0501.2003.140316.x.
- Sas, A., Pellikaan, P., Kolk, S., Marty, P., Scheerlinck, T. and Lenthe, G. H. van. (2019). 'Effect of anatomical variability on stress-shielding induced by short calcar-guided stems: Automated finite element analysis of 90 femora'. *Journal of Orthopaedic Research®*. John Wiley & Sons, Ltd, 37 (3), pp. 681–688. doi: 10.1002/JOR.24240.
- Saxon, D. J., Luke, A. M., Sajjad, H., Tolman, W. B. and Reineke, T. M. (2020). 'Next-generation polymers: Isosorbide as a renewable alternative'. *Progress in Polymer Science*. Pergamon, 101, p. 101196. doi: 10.1016/J.PROGPOLYMSCI.2019.101196.
- Schomann, T., Qunneis, F., Widera, D., Kaltschmidt, C. and Kaltschmidt, B. (2013). 'Improved method for Ex Ovo -cultivation of developing chicken embryos for human stem cell xenografts'. *Stem Cells International*. doi: 10.1155/2013/960958.
- Schubert, C., Langveld, M. C. Van and Donoso, L. A. (2014). 'Innovations in 3D printing: a 3D overview from optics to organs'. *The British journal of ophthalmology*. Br J Ophthalmol, 98 (2), pp. 159–161. doi: 10.1136/BJOPHTHALMOL-2013-304446.
- Sequeira, S., Fernandes, M. H., Neves, N. and Almeida, M. M. (2017). 'Development and characterization of zirconia–alumina composites for orthopedic implants'. *Ceramics International*. Elsevier Ltd, 43 (1), pp. 693–703. doi:

10.1016/j.ceramint.2016.09.216.

Setiawati, R. and Rahardjo, P. (2019). 'Bone Development and Growth'. in *Osteogenesis and Bone Regeneration*. IntechOpen. doi: 10.5772/intechopen.82452.

Shah, F. A., Thomsen, P. and Palmquist, A. (2019). 'Osseointegration and current interpretations of the bone-implant interface'. *Acta Biomaterialia*. Elsevier, 84, pp. 1–15. doi: 10.1016/J.ACTBIO.2018.11.018.

Shahrubudin, N., Koshy, P., Alipal, J., Kadir, M. H. A. and Lee, T. C. (2020). 'Challenges of 3D printing technology for manufacturing biomedical products: A case study of Malaysian manufacturing firms'. *Heliyon*. Elsevier, 6 (4), p. e03734. doi: 10.1016/J.HELİYON.2020.E03734.

Shaker, J. L. and Deftos, L. (2018). 'Calcium and Phosphate Homeostasis'. *Endocrine and Reproductive Physiology*. MDText.com, Inc., pp. 77-e1. Available at: <https://www.ncbi.nlm.nih.gov/books/NBK279023/> (Accessed: 9 August 2021).

Shakouri, T., Cha, J.-R., Owji, N., Haddow, P., Robinson, T. E., Patel, K. D., García-Gareta, E., Kim, H.-W. and Knowles, J. C. (2020). 'Comparative study of photoinitiators for the synthesis and 3D printing of a light-curable, degradable polymer for custom-fit hard tissue implants'. *Biomedical Materials*, 16 (1), p. 015007. doi: 10.1088/1748-605X/aba6d2.

Shand, J. (2018). 'Paediatric oral & maxillofacial surgery'. *Australian Dental Journal*. Blackwell Publishing, 63, pp. S69–S78. doi: 10.1111/adj.12592.

Sheikh, Z., Abdallah, M.-N., Hanafi, A. A., Misbahuddin, S., Rashid, H. and Glogauer, M. (2015). 'Mechanisms of in Vivo Degradation and Resorption of Calcium

Phosphate Based Biomaterials'. *Materials*. Multidisciplinary Digital Publishing Institute (MDPI), 8 (11), p. 7913. doi: 10.3390/MA8115430.

Sheikh, Z., Sima, C. and Glogauer, M. (2015). 'Bone replacement materials and techniques used for achieving vertical alveolar bone augmentation'. *Materials*. MDPI AG, 8 (6), pp. 2953–2993. doi: 10.3390/ma8062953.

Shirliff, V. J. and Hench, L. L. (2003). 'Bioactive materials for tissue engineering, regeneration and repair'. *Journal of Materials Science*. Springer, 38 (23), pp. 4697–4707. doi: 10.1023/A:1027414700111.

Shkarina, S., Shkarin, R., Weinhardt, V., Melnik, E., Vacun, G., Kluger, P., Loza, K., Epple, M., Ivlev, S. I., Baumbach, T., Surmeneva, M. A. and Surmenev, R. A. (2018). '3D biodegradable scaffolds of polycaprolactone with silicate-containing hydroxyapatite microparticles for bone tissue engineering: High-resolution tomography and in vitro study'. *Scientific Reports*. Nature Publishing Group, 8 (1). doi: 10.1038/s41598-018-27097-7.

Sidambe, A. (2014). 'Biocompatibility of Advanced Manufactured Titanium Implants—A Review'. *Materials*. MDPI AG, 7 (12), pp. 8168–8188. doi: 10.3390/ma7128168.

Simon, P., Mohan, J., Selvaraj, S., Saravanan, B. S. and Pari, P. (2014). 'Craniofacial Prosthetic Reconstruction Using Polymethyl Methacrylate Implant: A Case Report'. *Journal of Indian Prosthodontist Society*. Springer India, 14 (Suppl 1), pp. 303–307. doi: 10.1007/s13191-014-0361-3.

Smith, B. T., Shum, J., Wong, M., Mikos, A. G. and Young, S. (2015). 'Bone tissue engineering challenges in oral & Maxillofacial surgery'. in *Advances in Experimental*

*Medicine and Biology*. Springer New York LLC, pp. 57–78. doi: 10.1007/978-3-319-22345-2\_4.

Soares, C. J., Faria-E-Silva, A. L., Rodrigues, M. de P., Fernandes Vilela, A. B., Pfeifer, C. S., Tantbirojn, D. and Versluis, A. (2017). 'Polymerization shrinkage stress of composite resins and resin cements - What do we need to know?' *Brazilian Oral Research*. Sociedade Brasileira de Hematologia e Hemoterapia, pp. 49–63. doi: 10.1590/1807-3107BOR-2017.vol31.0062.

Sogal, A. and Tofe, A. J. (1999). 'Risk Assessment of Bovine Spongiform Encephalopathy Transmission Through Bone Graft Material Derived From Bovine Bone Used for Dental Applications'. *Journal of Periodontology*. Wiley, 70 (9), pp. 1053–1063. doi: 10.1902/jop.1999.70.9.1053.

Sokolova, V., Kostka, K., Shalumon, K. T., Prymak, O., Chen, J. P. and Epple, M. (2020). 'Synthesis and characterization of PLGA/HAP scaffolds with DNA-functionalised calcium phosphate nanoparticles for bone tissue engineering'. *Journal of Materials Science: Materials in Medicine*. Springer, 31 (11), pp. 1–12. doi: 10.1007/s10856-020-06442-1.

Song, R., Murphy, M., Li, C., Ting, K., Soo, C. and Zheng, Z. (2018). 'Current development of biodegradable polymeric materials for biomedical applications'. *Drug Design, Development and Therapy*. Dove Medical Press Ltd., pp. 3117–3145. doi: 10.2147/DDDT.S165440.

Stalling, S. S., Akintoye, S. O. and Nicoll, S. B. (2009). 'Development of photocrosslinked methylcellulose hydrogels for soft tissue reconstruction'. *Acta Biomaterialia*. Elsevier, 5 (6), pp. 1911–1918. doi: 10.1016/J.ACTBIO.2009.02.020.

- Stoddart, M. J., Craft, A. M., Pattappa, G. and Gardner, O. F. W. (2018). *Developmental biology and musculoskeletal tissue engineering: Principles and applications. Developmental Biology and Musculoskeletal Tissue Engineering: Principles and Applications*. Elsevier. doi: 10.1016/C2016-0-01519-X.
- Stylianou, N., Buchan, I. and Dunn, K. W. (2015). 'A review of the international Burn Injury Database (iBID) for England and Wales: descriptive analysis of burn injuries 2003-2011'. *BMJ open*. British Medical Journal Publishing Group, p. e006184. doi: 10.1136/bmjopen-2014-006184.
- Sun, H., Ye, F., Wang, J., Shi, Y., Tu, Z., Bao, J., Qin, M., Bu, H. and Li, Y. (2008). 'The Upregulation of Osteoblast Marker Genes in Mesenchymal Stem Cells Prove the Osteoinductivity of Hydroxyapatite/Tricalcium Phosphate Biomaterial'. *Transplantation Proceedings*. Elsevier, 40 (8), pp. 2645–2648. doi: 10.1016/J.TRANSPROCEED.2008.07.096.
- Suska, F., Kjeller, G., Tarnow, P., Hryha, E., Nyborg, L., Snis, A. and Palmquist, A. (2016). 'Electron Beam Melting Manufacturing Technology for Individually Manufactured Jaw Prosthesis: A Case Report'. *Journal of Oral and Maxillofacial Surgery*. W.B. Saunders, 74 (8), pp. 1706.e1-1706.e15. doi: 10.1016/j.joms.2016.03.046.
- Tamimi, F., Sheikh, Z. and Barralet, J. (2012). 'Dicalcium phosphate cements: Brushite and monetite'. *Acta Biomaterialia*. Elsevier, pp. 474–487. doi: 10.1016/j.actbio.2011.08.005.
- Tan, H.-L., Kheirandish-Gozal, L., Abel, F. and Gozal, D. (2016). 'Craniofacial Syndromes and Sleep-Related Breathing Disorders'. *Sleep medicine reviews*. NIH

Public Access, 27, p. 74. doi: 10.1016/J.SMRV.2015.05.010.

Tao, O., Kort-Mascort, J., Lin, Y., Pham, H. M., Charbonneau, A. M., ElKashty, O. A., Kinsella, J. M. and Tran, S. D. (2019). 'The applications of 3D printing for craniofacial tissue engineering'. *Micromachines*. MDPI AG. doi: 10.3390/mi10070480.

Tappa, K. and Jammalamadaka, U. (2018). 'Novel Biomaterials Used in Medical 3D Printing Techniques'. *Journal of Functional Biomaterials*. Multidisciplinary Digital Publishing Institute (MDPI), 9 (1). doi: 10.3390/JFB9010017.

Tarafder, S., Dernell, W., Bandyopadhyay, A. and Bose, S. (2015). 'SrO- and MgO-doped microwave sintered 3D printed tricalcium phosphate scaffolds: mechanical properties and in vivo osteogenesis in a rabbit model'. *Journal of biomedical materials research. Part B, Applied biomaterials*. J Biomed Mater Res B Appl Biomater, 103 (3), pp. 679–690. doi: 10.1002/JBM.B.33239.

Temple, H. T. and Malinin, T. I. (2008). 'Microparticulate Cortical Allograft: An Alternative to Autograft in the Treatment of Osseous Defects'. *The Open Orthopaedics Journal*. Bentham Science Publishers Ltd., 2 (1), pp. 91–96. doi: 10.2174/1874325000802010091.

Thrivikraman, G., Athirasala, A., Twohig, C., Boda, S. K. and Bertassoni, L. E. (2017). 'Biomaterials for Craniofacial Bone Regeneration'. *Dental Clinics of North America*. W.B. Saunders, pp. 835–856. doi: 10.1016/j.cden.2017.06.003.

Thuaksuban, N., Nuntanaranont, T. and Pripatnanont, P. (2010). 'A comparison of autogenous bone graft combined with deproteinized bovine bone and autogenous bone graft alone for treatment of alveolar cleft'. *International Journal of Oral and Maxillofacial Surgery*. Int J Oral Maxillofac Surg, 39 (12), pp. 1175–1180. doi:

10.1016/j.ijom.2010.07.008.

Tian, X. Y. and Chen, X. B. (2014). 'Effects of Cell Density on Mechanical Properties of Alginate Hydrogel Tissue Scaffolds'. *Journal of Biomimetics, Biomaterials and Tissue Engineering*. Trans Tech Publications Ltd, 19, pp. 77–85. doi: 10.4028/WWW.SCIENTIFIC.NET/JBBTE.19.77.

Tirkkonen, L., Haimi, S., Huttunen, S., Wolff, J., Pirhonen, E., Sándor, G. and Miettinen, S. (2013). 'Osteogenic medium is superior to growth factors in differentiation of human adipose stem cells towards bone-forming cells in 3D culture'. *European cells & materials*. Eur Cell Mater, 25, pp. 144–158. doi: 10.22203/ECM.V025A10.

Tulyaganov, D. U., Akbarov, A., Ziyadullaeva, N., Khabilov, B. and Baino, F. (2020). 'Injectable bioactive glass-based pastes for potential use in bone tissue repair'. *Biomedical Glasses*, 6 (1), pp. 23–33. doi: 10.1515/bglass-2020-0003.

Turnbull, G., Clarke, J., Picard, F., Riches, P., Jia, L., Han, F., Li, B. and Shu, W. (2018). '3D bioactive composite scaffolds for bone tissue engineering'. *Bioactive Materials*. Elsevier, 3 (3), pp. 278–314. doi: 10.1016/J.BIOACTMAT.2017.10.001.

Unterhofer, C., Wipplinger, C., Verius, M., Recheis, W., Thomé, C. and Ortler, M. (2017). 'Reconstruction of large cranial defects with poly-methyl-methacrylate (PMMA) using a rapid prototyping model and a new technique for intraoperative implant modeling'. *Neurologia i Neurochirurgia Polska*. Urban and Partner, 51 (3), pp. 214–220. doi: 10.1016/j.pjnns.2017.02.007.

Vanaei, S., Parizi, M. S., Vanaei, S., Saleemizadehparizi, F. and Vanaei, H. R. (2021). 'An Overview on Materials and Techniques in 3D Bioprinting Toward Biomedical



Application'. *Engineered Regeneration*. Elsevier, 2, pp. 1–18. doi:

10.1016/J.ENGREG.2020.12.001.

Ventola, C. L. (2014). 'Medical Applications for 3D Printing: Current and Projected Uses'. *Pharmacy and Therapeutics*. MediMedia, USA, 39 (10), p. 704. Available at: /pmc/articles/PMC4189697/ (Accessed: 4 August 2021).

Visscher, D. O., Farré-Guasch, E., Helder, M. N., Gibbs, S., Forouzanfar, T., van Zuijlen, P. P. and Wolff, J. (2016). 'Advances in Bioprinting Technologies for Craniofacial Reconstruction'. *Trends in Biotechnology*. Elsevier Current Trends, 34 (9), pp. 700–710. doi: 10.1016/J.TIBTECH.2016.04.001.

Wang, K., Ho, C. C., Zhang, C. and Wang, B. (2017). 'A Review on the 3D Printing of Functional Structures for Medical Phantoms and Regenerated Tissue and Organ Applications'. *Engineering*. Elsevier, 3 (5), pp. 653–662. doi:

10.1016/J.ENG.2017.05.013.

Wang, W. and Yeung, K. W. K. (2017). 'Bone grafts and biomaterials substitutes for bone defect repair: A review'. *Bioactive Materials*. KeAi Communications Co., pp. 224–247. doi: 10.1016/j.bioactmat.2017.05.007.

Wang, X., Zhang, L., Liu, Z., Zeng, Q., Jiang, G. and Yang, M. (2018). 'Probing the surface structure of hydroxyapatite through its interaction with hydroxyl: a first-principles study'. *RSC Advances*. The Royal Society of Chemistry, 8 (7), pp. 3716–3722. doi: 10.1039/C7RA13121F.

Wang, Y., Azais, T., Robin, M., Vallée, A., Catania, C., Legriel, P., Pehau-Arnaudet, G., Babonneau, F., Giraud-Guille, M. M. and Nassif, N. (2012). 'The predominant role of collagen in the nucleation, growth, structure and orientation of bone apatite'.

*Nature Materials*. Nature Publishing Group, 11 (8), pp. 724–733. doi:

10.1038/nmat3362.

Widmaier, E. P., Raff, H. & Strang, K. T. (2006). *Vander's human physiology*.

*Vander's human physiology, McGraw-Hill New York, NY*. Available at:

<http://repository.fue.edu.eg/xmlui/bitstream/handle/123456789/1784/9910.pdf?sequence=1> (Accessed: 24 September 2020).

Wiria, F., Leong, K., Chua, C. and Liu, Y. (2007). 'Poly-epsilon-

caprolactone/hydroxyapatite for tissue engineering scaffold fabrication via selective laser sintering'. *Acta biomaterialia*. *Acta Biomater*, 3 (1), pp. 1–12. doi:

10.1016/J.ACTBIO.2006.07.008.

Woodruff, M. A. and Hutmacher, D. W. (2010). 'The return of a forgotten polymer—

Polycaprolactone in the 21st century'. *Progress in Polymer Science*. Pergamon, 35 (10), pp. 1217–1256. doi: 10.1016/J.PROGPOLYMSCI.2010.04.002.

Wu, G.-H. and Hsu, S. (2015). 'Review: Polymeric-Based 3D Printing for Tissue

Engineering'. *Journal of Medical and Biological Engineering 2015 35:3*. Springer, 35 (3), pp. 285–292. doi: 10.1007/S40846-015-0038-3.

Wubneh, A., Tsekoura, E. K., Ayranci, C. and Uludağ, H. (2018). 'Current state of fabrication technologies and materials for bone tissue engineering'. *Acta*

*Biomaterialia*. Elsevier, 80, pp. 1–30. doi: 10.1016/J.ACTBIO.2018.09.031.

Xu, L. C. and Siedlecki, C. A. (2007). 'Effects of surface wettability and contact time on protein adhesion to biomaterial surfaces'. *Biomaterials*, 28 (22), pp. 3273–3283.

doi: 10.1016/j.biomaterials.2007.03.032.

Xueyong Deng, Bingxue Huang, Rui Hu, Liling Chen, Yingying Tang, Canhui Lu, Zhenming Chen, Wei Zhang and Ximu Zhang. (2021). '3D printing of robust and biocompatible poly(ethylene glycol)diacrylate/nano-hydroxyapatite composites via continuous liquid interface production'. *Journal of Materials Chemistry B*. Royal Society of Chemistry, 9 (5), pp. 1315–1324. doi: 10.1039/D0TB02182B.

Yadla, S., Campbell, P. G., Chitale, R., Maltenfort, M. G., Jabbour, P. and Sharan, A. D. (2011). 'Effect of early surgery, material, and method of flap preservation on cranioplasty infections: A systematic review'. *Neurosurgery*. Neurosurgery, pp. 1124–1130. doi: 10.1227/NEU.0b013e31820a5470.

Yadollahi, M., Behzadi Seyf-abadi, M. and Pazhuheian, F. (2019). 'Pattern of Maxillofacial Injuries and Determinants of Outcome in a Large Series of Patients admitted to a Level-I Trauma Center'. *Bulletin of Emergency and Trauma*. Armenian Green Publishing Co., 7 (2), pp. 176–182. doi: 10.29252/beat-070214.

Ye, W. P., Du, F. S., Jin, W. H., Yang, J. Y. and Xu, Y. (1997). 'In vitro degradation of poly(caprolactone), poly(lactide) and their block copolymers: influence of composition, temperature and morphology'. *Reactive and Functional Polymers*. Elsevier, 32 (2), pp. 161–168. doi: 10.1016/S1381-5148(96)00081-8.

Yu, D., Zhao, J., Wang, W., Qi, J. and Hu, Y. (2019). 'Mono-acrylated isosorbide as a bio-based monomer for the improvement of thermal and mechanical properties of poly(methyl methacrylate)'. *RSC Advances*. The Royal Society of Chemistry, 9 (61), pp. 35532–35538. doi: 10.1039/C9RA07548H.

Yuan, H., Fernandes, H., Habibovic, P., De Boer, J., Barradas, A. M. C., De Ruiter, A., Walsh, W. R., Van Blitterswijk, C. A. and De Bruijn, J. D. (2010). 'Osteoinductive

ceramics as a synthetic alternative to autologous bone grafting'. *Proceedings of the National Academy of Sciences of the United States of America*. National Academy of Sciences, 107 (31), pp. 13614–13619. doi: 10.1073/pnas.1003600107.

Yunus Basha, R., Sampath, S. K. and Doble, M. (2015). 'Design of biocomposite materials for bone tissue regeneration'. *Materials Science and Engineering C*. Elsevier Ltd, pp. 452–463. doi: 10.1016/j.msec.2015.07.016.

Zhang, A. P., Qu, X., Soman, P., Hribar, K. C., Lee, J. W., Chen, S. and He, S. (2012). 'Rapid Fabrication of Complex 3D Extracellular Microenvironments by Dynamic Optical Projection Stereolithography'. *Advanced Materials*. John Wiley & Sons, Ltd, 24 (31), pp. 4266–4270. doi: 10.1002/ADMA.201202024.

Zhang, J., Liu, Y., Chen, Y., Yuan, L., Liu, H., Wang, J., Liu, Q. and Zhang, Y. (2020). 'Adipose-Derived Stem Cells: Current Applications and Future Directions in the Regeneration of Multiple Tissues'. *Stem Cells International*. Hindawi Limited, 2020. doi: 10.1155/2020/8810813.

Zhang, J. and Xiao, P. (2018). 'Polymer Chemistry MINIREVIEW 3D printing of photopolymers'. *Polymer Chemistry*, 9. doi: 10.1039/c8py00157j.

Zhao, H., Chen, Q., Alam, A., Cui, J., Suen, K. C., Soo, A. P., Eguchi, S., Gu, J. and Ma, D. (2018). 'The role of osteopontin in the progression of solid organ tumour'. *Cell Death and Disease*. Nature Publishing Group, pp. 1–15. doi: 10.1038/s41419-018-0391-6.

Zhao, H. and Liang, W. (2017). 'A novel comby scaffold with improved mechanical strength for bone tissue engineering'. *Materials Letters*, 194, pp. 220–223. doi: 10.1016/j.matlet.2017.02.059.

Zhou, P., Shi, J.-M., Song, J.-E., Han, Y., Li, H.-J., Song, Y.-M., Feng, F., Wang, J.-L., Zhang, R. and Lan, F. (2021). 'Establishing a deeper understanding of the osteogenic differentiation of monolayer cultured human pluripotent stem cells using novel and detailed analyses'. *Stem Cell Research & Therapy* 2021 12:1. BioMed Central, 12 (1), pp. 1–16. doi: 10.1186/S13287-020-02085-9.

Zima, A., Czechowska, J., Siek, D., Olkowski, R., Noga, M., Lewandowska-Szumieł, M. and Ślósarczyk, A. (2017). 'How calcite and modified hydroxyapatite influence physicochemical properties and cytocompatibility of alpha-TCP based bone cements'. *Journal of Materials Science: Materials in Medicine*. Springer New York LLC, 28 (8), p. 117. doi: 10.1007/s10856-017-5934-3.